Neuronal oscillations: from single-unit activity to emergent dynamics and back

Belén de Sancristóbal Alonso

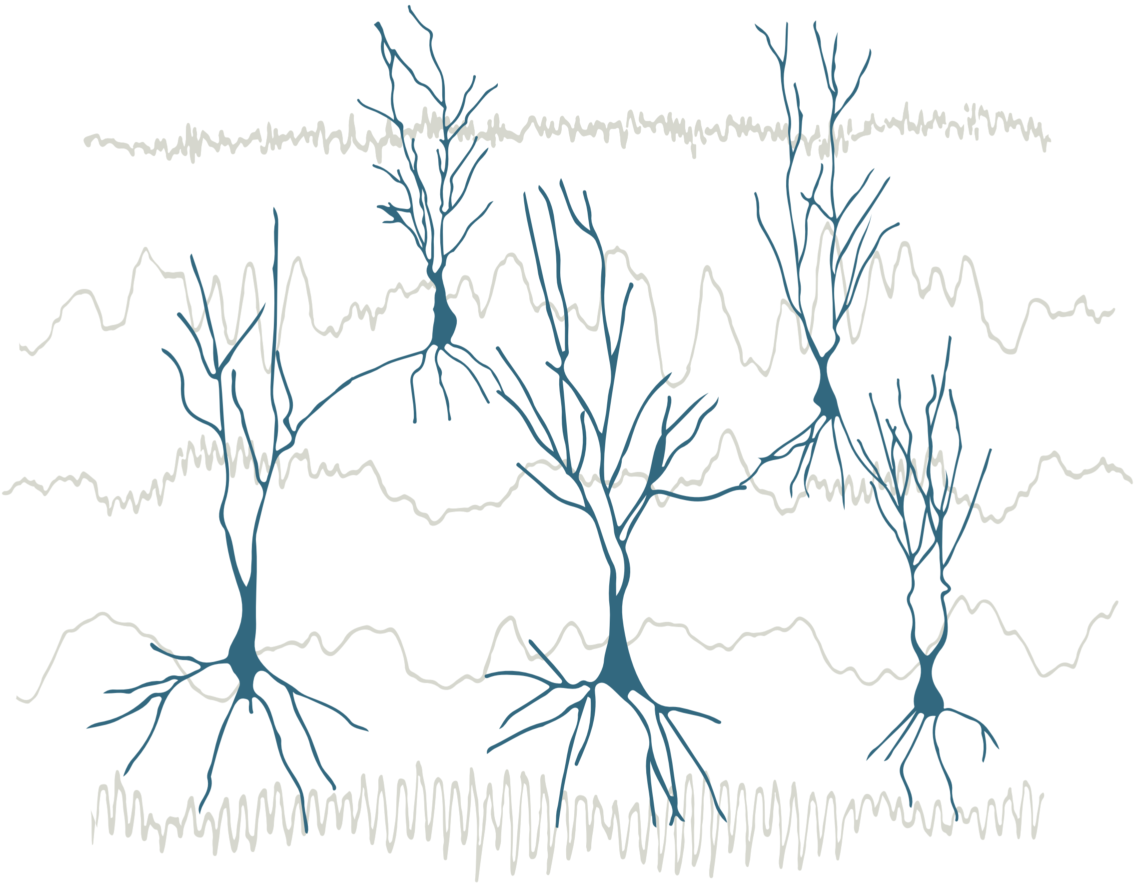

Neuronal oscillations: from single-unit activity to emergent dynamics and back

Ph. D. THESIS

Belén de Sancristóbal Alonso

July 2013

Ph. D. advisors: Jordi Garcia Ojalvo
and José María Sancho Herrero

Universitat Politècnica de Catalunya

Departament de Física i Enginyeria Nuclear

In nature, epiphenomena seldom remain epiphenomena for long; they are the raw material for evolutionary advances.

B. HUTCHEON AND Y. YAROM

Agraïments

Moltes persones m'han ajudat a trobar un equilibri durant aquests primers anys de recerca. Aquesta tesi ha estat possible gràcies al suport i a la mirada genial del Jordi. La seva vitalitat, bon humor i entusiasme, han estat sempre un motor per seguir endavant, insistir i buscar respostes aquí i allà.

I les he trobat, aquí amb el José María i la Mavi i el seu equip (la Lorena, la Bea, el Marcel i la María), que han enriquit de bon tros els meus coneixements. I allà, a Frankfurt, amb el Raúl, que sempre m'ha donat ànims perquè l'esforç no és en va i ajudat a valorar la meva forma d'avançar, que jo trobo tan lenta! I tots ell m'han permès conèixer gent magnífica, grans amics, amb qui he compartit molts moments: el cansament quan les coses no surten, l'alegria dels bons resultats i les nostres històries, amb les que arribàvem al laboratori (casaments, embarassos, viatges, lloguers, compres, política, crisis...). Tinc molt bons records del nostre gran equip Marta, Pau i Elena, Lorena, Jordi T, Jordi Z i Dani! Carme, Crina, Núria, Cristina i Toni! I Marta C i África: al final sí, a Alemanya només anava amb espanyoles. I darrerament han arribat nous fitxatges, just en la recta final d'aquesta tesi i, sincerament, heu aconseguit fer-la més lleugera, gràcies Marçal, Nara, Alessandro, Maciek i Letícia.

En l'altre plat de la balança, hi ha totes aquelles persones a qui un dia vaig dir "vull provar fer recerca, si no ho faig ara no ho faré mai". Olivia, Estel i Ana, em sembla mentida la quantitat d'anys que fa que ens coneixem i aprofito aquesta excusa per dir-vos que sense vosaltres m'hagués perdut una part important de la vida. Marc, aquest matí encara ens estàvem rient de l'estrès que porto a sobre, gràcies per fer les coses tan fàcils i tenir tanta paciència. Anna, que sempre em calmes i escoltes. Tània, estiguis on estiguis mai desapareixes. Mamá, siempre estás ahí y saberlo me ha ayudado mucho. Papá y Chari, que confiáis en mí y en que sabré hacerlo. Berta que siempre me apoyas y entiendes, y abuela por animarme tanto (sé que hoy aún te preguntas cuando acabaré de "estudiar").

L'estiu que vaig començar el doctorat va lligat al viatge als Balcans amb el Jordi i l'Anna, a la seva generositat i tendresa i a tot l'afecte que saben donar. Amb ells he conegut a la Mar, a la Laia, al Teo i al Fabi, que sumen bons records i sentiments allà on anem, des de Campelles al Poblenou, passant per Fonolleres! Jaume, Núria i Àngela, gràcies per la vostra acollida, Banyoles i els arrossos!

Fabi, haver arribat fins aquí és en gran mesura gràcies a tu, la portada només n'és una mostra visible. Gràcies per compartir-ho de tan a prop, per ajudar-me a gaudir del què m'envolta, del què faig i del què fem.

Oscil·lacions neuronals: de l'activitat d'unitats individuals a dinàmica emergent i viceversa

Resum: L'objectiu principal d'aquesta tesi és avançar en la comprensió del processament d'informació en xarxes neuronals en presència d'oscil·lacions subumbrals. La majoria de neurones propaguen la seva activitat elèctrica a través de sinapsis químiques que són activades, exclusivament, quan el corrent elèctric que les travessa supera un cert llindar. És per aquest motiu que les descàrregues ràpides i intenses produïdes al soma neuronal, els anomenats potencials d'acció, són considerades la unitat bàsica d'informació neuronal, és a dir, el senyal mínim i necessari per a iniciar la comunicació entre dues neurones. El codi neuronal és entès, doncs, com un llenguatge binari que expressa qualsevol missatge (estímul sensorial, memòries, etc.) en un tren de potencials d'acció. Tanmateix, cap funció cognitiva rau en la dinàmica d'una única neurona. Circuits de milers de neurones connectades entre sí donen lloc a determinats ritmes, palesos en registres d'activitat colectiva com els electroencefalogrames (EEG) o els potencials de camp local (LFP). Si els potencials d'acció de cada cèl·lula, desencadenats per fluctuacions estocàstiques de les corrents sinàptiques, no assolissin un cert grau de sincronia, no apareixeria aquesta periodicitat a nivell de xarxa.

Per tal de poder entendre si aquests ritmes intervenen en el codi neuronal hem estudiat tres situacions. Primer, en el Capítol 2, hem mostrat com una cadena oberta de neurones amb un potencial de membrana intrínsecament oscil·latori filtra un senyal periòdic arribant per un dels extrems. La resposta de cada neurona (pulsar o no pulsar) depèn de la seva fase, de forma que cada una d'elles rep un missatge filtrat per la precedent. A més, cada potencial d'acció presinàptic provoca un canvi de fase en la neurona postsinàptica que depèn de la seva posició en l'espai de fases. Els períodes d'entrada capaços de sincronitzar les oscil·lacions subumbrals són aquells que mantenen la fase d'arribada dels potencials d'acció fixa al llarg de la cadena. Per tal de què el missatge arribi intacte a la darrera neurona cal, a més a més, que aquesta fase permeti la descàrrega del voltatge transmembrana.

En segon cas, hem estudiat una xarxa neuronal amb connexions tant a veïns propers com de llarg abast, on les oscil·lacions subumbrals emergeixen de l'activitat col·lectiva reflectida en els corrents sinàptics (o equivalentment en el LFP). Les neurones inhibidores aporten un ritme a l'excitabilitat de la xarxa, és a dir, que els episodis en què la inhibició és baixa, la probabilitat d'una descàrrega global de la població neuronal és alta. En el Capítol 3 mostrem com aquest ritme implica l'aparició d'una bretxa en la freqüència de descàrrega de les neurones: o bé polsen espaiadament en el temps o bé en ràfegues d'elevada intensitat. La fase del LFP determina l'estat de la xarxa neuronal codificant l'activitat de la població: els mínims indiquen la descàrrega simultània de moltes neurones que, ocasionalment, han superat el llindar d'excitabilitat degut a un decreixement global de la inhibició, mentre que els màxims indiquen la coexistència de ràfegues en diferents punts de la xarxa degut a decreixements locals de la inhibició en estats globals d'excitació. Aquesta dinàmica és possible gràcies al domini de la inhibició sobre l'excitació.

En el Capítol 4 considerem acoblament entre dues xarxes neuronals per tal d'estudiar la interacció entre ritmes diferents. Les oscil·lacions indiquen recurrència en la sincronització de l'activitat col·lectiva, de manera que durant aquestes finestres temporals una població optimitza el seu impacte en una xarxa diana. Quan el ritme de la població receptora i el de l'emissora difereixen significativament, l'eficiència en la comunicació decreix, ja que les fases de màxima resposta de cada senyal LFP no mantenen una diferència constant entre elles.

Finalment, en el Capítol 5 hem estudiat com les oscil·lacions col·lectives pròpies de l'estat de son donen lloc al fenomen de coherència estocàstica. Per a una intensitat òptima del soroll, modulat per l'excitabilitat de la xarxa, el LFP assoleix una regularitat màxima donant lloc a un període refractari de la població neuronal.

En resum, aquesta Tesi mostra escenaris d'interacció entre els potencials d'acció, característics de la dinàmica de neurones individuals, i les oscil·lacions subumbrals, fruit de l'acoblament entre les cèl·lules i ubiqües en la dinàmica de poblacions neuronals. Els resultats obtinguts aporten funcionalitat a aquests ritmes emergents, agents sincronitzadors i moduladors de les descàrregues neuronals i reguladors de la comunicació entre xarxes neuronals.

Contents

Chapter 1
Introduction

Contents

1.1 The human brain

The nervous system contains two main moduli: the central nervous system (CNS) formed by the brain and spinal cord, and the peripheral nervous system (PNS) which consists of all the nerves outside the CNS connecting it to other parts of the body. The brain itself is divided into three anatomic parts: cerebrum, cerebellum and brain stem (see left picture in Figure 1.1). The cerebrum contains the two cerebral hemispheres, i.e. the *neocortex* or *cerebral cortex* of $\sim$3 mm thick, joined by a large white matter of myelinated axons, the *corpus callosum*; and two deeper structures, the *thalamus* and the *hypothalamus*, which are also halved (see right picture in Figure 1.1). The brain stem can be also decomposed in subareas: *midbrain*, *pons* and *medulla*.

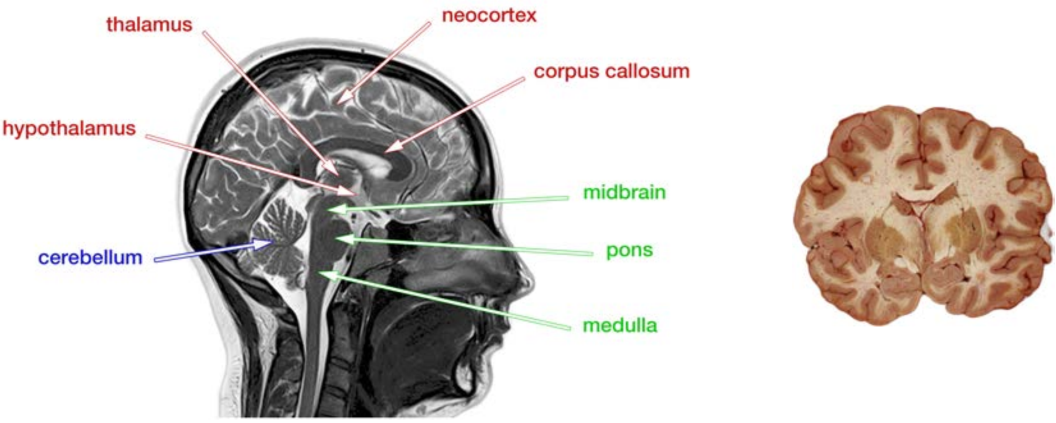

Figure 1.1: Left: MRI brain sagittal section. The subdivisions of the three main brain areas: the cerebrum (red), the cerebellum (blue) and the brain stem (green). Right: Section of the human cerebrum. The cortex is the outer layer in darker tone. From [Jones 2010].

The basic functional units of the brain are the nerve cells or *neurons* (Figure 1.2) which number up to 100 billion. The cortex is the region containing more such cells. We have approximately 25 billions of cortical neurons and the number of connections between them can reach 300 trillion. Neurons are excitable cells surrounded by a membrane crossed along its branched morphology by ionic currents –commonly of Na^+, K^+, Ca^{2+} and Cl^- ions–. Electrical pulses arriving at the contact sites between nerve cells, go up the dendrites to the soma, where neurons are able to summate inputs nonlinearly, and are conducted away from the soma through the axon. The cortex possess an enormous computational power due to the vast amount of neurons nested within it.

1.2 The cerebral cortex

The human brain holds a massive grey matter, named the *cerebral cortex*, composed of neuronal bodies and capable of higher functions than the rest of mammals. The cortex is split into the two interconnected hemispheres surrounding the earlier brain. In each hemisphere four lobes are identified: frontal, parietal, occipital and temporal (see left picture of Figure 1.3). The cortical tissue has a special structure arranged horizontally in six layers (see right picture of Figure 1.3) and vertically in columns in which neurons are

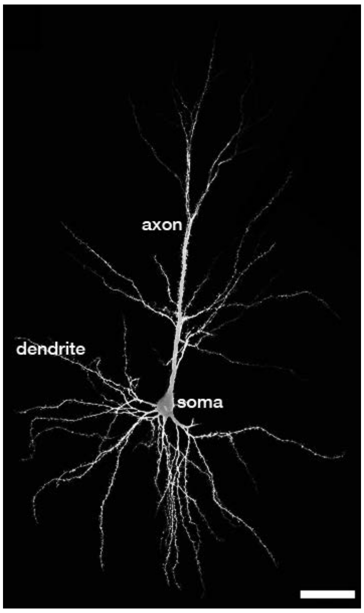

Figure 1.2: Neuronal morphology. Scale bar: 50 μm. Adapted from [Hao 2007].

interconnected along the cortical depth and share common external connectivity [Rakic 2008]. Each layer contains specific types of neurons, and those neurons that form a column have very similar receptive fields.

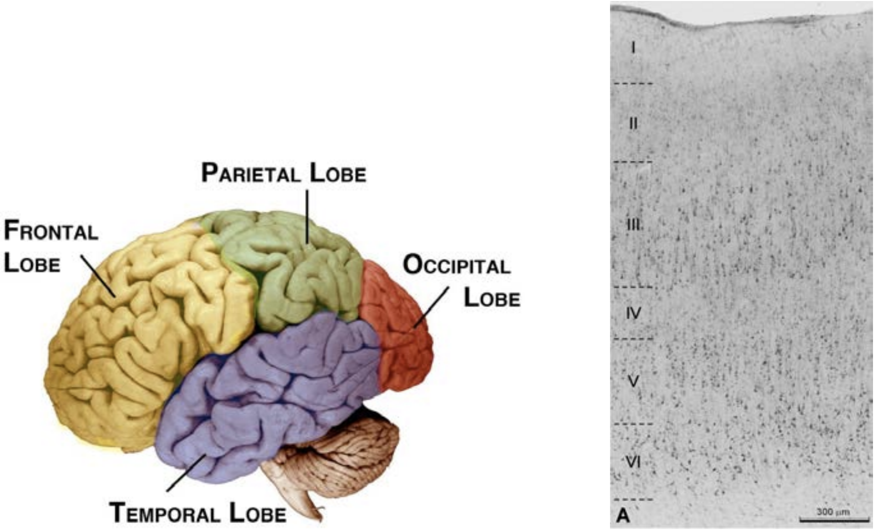

Figure 1.3: Left: The four lobes of the hemispheres. Right: Layered organization of the human temporal cortex. From [Yague 2006].

Neurons can make contacts with neighboring neurons, i.e. neurons in the next column or in a lower or upper layer, as well as with those neurons belonging to other cortical areas or to the opposite hemisphere. Connectivity, which is usually weak and sparse, shapes both local and distant circuits. Local circuits help coactivate the responses of interconnected neurons and synchronize them, so that their joint output may perturb a common target area more efficiently.

The connectivity between neurons is not fixed. Several activity-dependent mechanisms can reinforce or weaken the strength of such connections and the local circuitry is shaped accordingly.

The human cortex is divided into several areas of continuous networks of cortical columns, whose boundaries are not clear-cut. The connectivity between and within those regions is complex and partially known. Usually, cortical areas are defined according to their function. Despite the fact that spontaneous activity is recorded through the whole brain, specific cognitive tasks or stimulus features enhance the activity of neuronal circuits in particular regions.

1.3 Neurons

1.3.1 Basic description of neurons

Neurons are a specialized type of cell mainly found in the CNS. They are complex electrical devices specialized in intercellular communication. They are well-equipped by a variety of elements to accomplish this function: they contain molecules that are released and target neighboring neurons, numerous receptor sites cover their membrane in order to capture those chemical compounds, they are extensively branched and make multiple contacts with other neurons, and they possess a long conductive path named axon. This machinery is turned on at every *action potential* or *spike*, which is a fast and transient change (around 100 mV in 1 ms) in the voltage drop across the cell membrane (Figure 1.4).

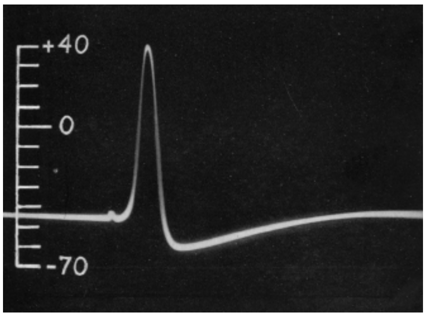

Figure 1.4: Action potential recorded by A. L. Hodgkin and A. F. Huxley from the squid giant axon, taking the electrode placed outside the axon as the voltage reference (0 mV). From [Hodgkin 1945].

This voltage difference is due to distinct concentrations of ions across the membrane, basically Na^+ and K^+ ions and negatively charged amino acids and proteins. Since the neuronal membrane is a lipid bilayer impermeable to ions, particles need ion channels to cross the membrane. At rest, when the neuron is not conducting impulses, the inside of the neuron carries a less positive charge than the outside and its voltage, called *resting membrane potential*, can range from -40 mV to -90 mV (taking the potential outside the membrane arbitrarily equal to zero). Electrically, the membrane is thus a capacitor separating the charges between the inner and outer surfaces.

This difference in ionic concentration can be maintained because the neuronal membrane is selectively permeable to only a few ions: it is most permeable to potassium, less to chlorine and much less to sodium. This is reflected in the different conductances of the ion channels. The neuron stays in a steady state by means of a membrane protein that pumps three Na^+ ions out of the cell and two K^+ ions inside for every ATP hydrolyzation. The Na^+-K^+ pump keeps the inner Na^+ concentration about 10 times lower than outside the cell, and the inner K^+ concentration about 20 times higher. This pump prevents Na^+ from accumulating within the cell and intracellular K^+ from dissipating outside the cell (something that occurs however during action potentials).

Due to this concentration gradient the Na^+ ions tend to diffuse inside the neuron, and the K^+ ions tend to escape from it. However, due to the higher permeability to K^+, many more K^+ ions leave the cell than Na^+ ions enter and the neuron is negatively charged which attracts the positive ions back to the neuron. In order to maintain a resting potential, the neuron is constantly consuming energy via the Na^+-K^+ pump. Besides, each ion channel is characterized by its *equilibrium* or *reversal potential*, at which no net transmembrane flux of the specific ion crosses the channel because a balance between the concentration gradient and the electric potential is reached. The *Nernst equation* provides the relation between this electrostatic potential, $\mathrm{V}_{\mathrm{ion}}$, and the concentration of an ion C in two regions:

$$V_{\mathrm{ion}} = \frac{RT}{zF} ln \left(\frac{C_{\mathrm{o}}}{C_{\mathrm{i}}} \right) \tag{1.1}$$

where R is the universal gas constant (8.314 J/Kmol), T is the temperature in Kelvin, z is the number of elementary charges of the ion and F is the Faraday constant (96.845 C/mol). C_{o} is the extracellular concentration and C_{i} the intracellular concentration of a particular ion.

The Nernst equation does not take into account the permeability of the membrane and the presence of several ionic species crossing it. Considering such situation, the resting membrane potential can be calculated via the

Goldman equation, which is written as follows -taking into account the most relevant ions-:

$$\Delta V = \frac{RT}{F} ln \left(\frac{P_{\mathrm{K}}[K^+]_{\mathrm{o}} + P_{\mathrm{Na}}[Na^+]_{\mathrm{o}} + P_{\mathrm{Cl}}[Cl^-]_{\mathrm{o}}}{P_{\mathrm{K}}[K^+]_{\mathrm{i}} + P_{\mathrm{Na}}[Na^+]_{\mathrm{i}} + P_{\mathrm{Cl}}[Cl^-]_{\mathrm{i}}} \right) \tag{1.2}$$

where $z = 1$ for those ions and P is the permeability of each ion in m/s.[†]

The relative permeability of the neuronal membrane to Na^+ and K^+ ions depends on the transmembrane voltage. These ion channels are known as *voltage-gated channels* because the membrane potential of the cell determines whether the channels are open or close. As mentioned above, at rest, the permeability to K^+ is the highest. However when the membrane is depolarized, the permeability to Na^+ increases and thus the membrane potential becomes more positive as more Na^+ ions enter the cell down the concentration gradient. Eventually the Na^+-K^+ pump restores the membrane potential to its resting level, actively maintaining the concentration gradient. Thus, neurons are excitable systems capable of modifying their membrane potential.

Neurons responding to external stimuli such as light, sound, or heat (*sensory neurons*) produce action potentials when exposed to them, while other neurons react upon the reception of action potentials coming from other neurons. Both input sources produce a flow of ions across the neuronal membrane. All neurons elicit a spike when the input is strong enough to bring them above a certain threshold and transiently makes the transmembrane potential positive. Otherwise the neuron only undergoes a depolarization of its membrane potential that increases with the strength of the input (see left plot in Figure 1.5). Interestingly, once the neuron fires, the amplitude of the action potential is independent of the input, like an *all-or-none* response. However the number of spikes fired per unit time, its *firing rate*, depends on the strength and duration of the input.

Other ionic channels are not responsible for the action potential generation. Instead, they are active at weak levels of input, and they cause rhythmic subthreshold fluctuations of the membrane potential (see right plot in Figure 1.5).

There are hundreds of different neuronal types in the brain (see left picture of Figure 1.6) that subserve different functions and exhibit a wide variety of electrical behaviors (see right picture of Figure 1.6). There are, however, some similarities regarding the biophysics of their membrane, the representation

---

[†] Fick's first law relates the diffusive flux per unit area per unit time J [mM/m^2·s] to the ionic concentration in the steady state as $J = P|C_{\mathrm{o}} - C_{\mathrm{i}}|$, where the concentration has dimensions of [mM/m^3]. The units of permeability P are then [m/s]. Standard permeability constants of neurons in the cat motor cortex are $P_{\mathrm{K}} = 10^{-7}$ cm/s, $P_{\mathrm{Na}} = 10^{-8}$ cm/s and $P_{\mathrm{Cl}} = 10^{-8}$ cm/s [Smith 2009].

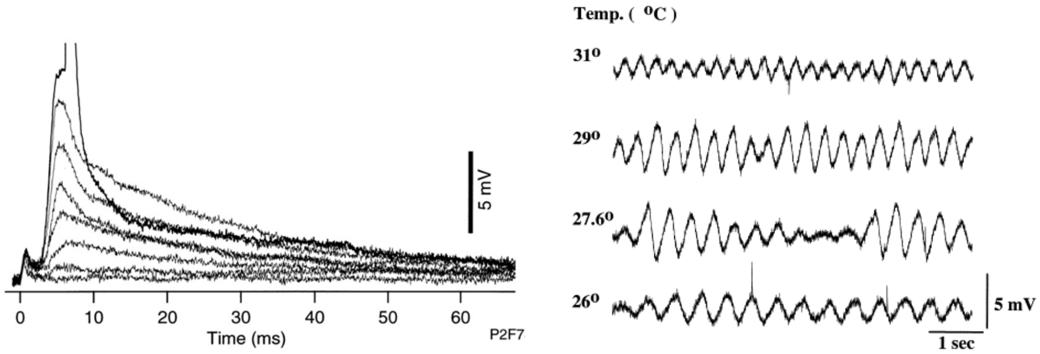

Figure 1.5: Left: Graded depolarization of parallel fibers in a pyramidal cell. From [Berman 1998]. Right: Intracellular recordings from neurons of the inferior olive nucleus. Lower bath temperature decreases the frequency of the spontaneous oscillations. From [Lampl 1997].

of information by means of spikes or their input-output relation or transfer function.

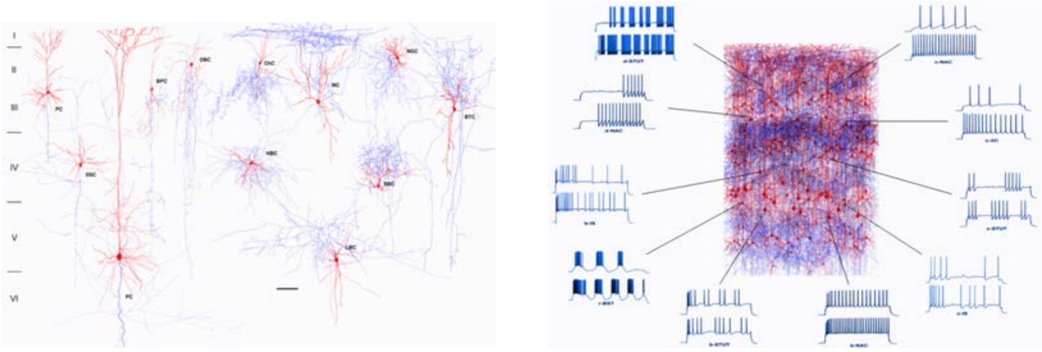

Figure 1.6: Left: Morphological classes of neurons according to their location in the neocortical layers. Right: Different electrical responses of neocortical neurons to injection of a constant current. From the presentation by Henry Markram, EPFL/BlueBrain: The Emergence of Intelligence in the Neocortical Microcircuit.

1.3.2 Neuron models

1.3.2.1 Hodgkin-Huxley model

A full mathematical description of single neurons including their particular variety of ion channels (usually more then ten types), axonal and dendritic tree is not possible due to the lack of a complete biochemical and morphological cell portrait. Some models omit the action potential generation or the axons and dendrites and keep only the soma. The first successful attempt to obtain biophysical equations for the neuronal membrane potential was attained by Hodgkin and Huxley at Cambridge in 1952, [Hodgkin 1952]. They performed a series of experiments on the squid giant axon (1000 times thicker than a typical mammalian axon) that helped them obtain the time and voltage dependence of the sodium and potassium conductances. Their empirical differential equations reproduce quantitatively the generation of action potentials with great accuracy.

Hodgkin and Huxley considered an electrical circuit equivalent to the neuronal membrane (Figure 1.8) in which the total current traversing the membrane is the sum of ionic currents and the capacitive current accounting for the storage of charges in the inner and outer surfaces of the membrane:

$$I_{\mathrm{ext}}(t) = I_{\mathrm{ionic}}(t) + C_{\mathrm{m}}\frac{dV_{\mathrm{m}}}{dt} \tag{1.3}$$

where C_{m} is the membrane capacitance (see Table 1.7 for experimental data on cortical neurons), V_{m} is the voltage difference between the outside and the inside of the neuron and I_{ext} is an external applied current. Hence, voltage changes reflect the storage and release of ionic charges on the two surfaces of the neuronal membrane.

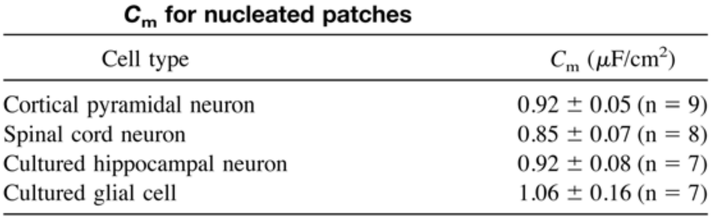

C_{m} for nucleated patches

Cell type	C_{m} (μF/cm^2)
Cortical pyramidal neuron	0.92 ± 0.05 (n = 9)
Spinal cord neuron	0.85 ± 0.07 (n = 8)
Cultured hippocampal neuron	0.92 ± 0.08 (n = 7)
Cultured glial cell	1.06 ± 0.16 (n = 7)

Table 1.7: Values (mean ± standard error) of the whole-cell capacitance, C_{m}, of four cell classes measured in nucleated patches[†] of 7-14-day-old Wistar rats. From [Gentet 2000].

Equation (1.3) is a non-linear differential equation describing the membrane voltage. I_{ionic} represents the sum of sodium and potassium conductance currents plus a leak current with a constant resistance primarily carried by chloride ions. Each of these currents, I_{Na}, I_{K} and I_{L}, shown in Figure 1.8, represents a large population of microscopic ion currents of the same type and is modeled following Ohm's law: $I_i = G_i(V_{\mathrm{m}} - E_i)$, where i is the ionic species and E_i is the equilibrium potential, given by V_{ion} in Equation (1.1), at which there is no net flow of ions i.

The ionic conductances G_i vary due to the opening and closing of the ion channels regulated by *gates*. Each gate can be in one of two possible

---

[†] Patch-clamp recording in which a piece of membrane is pulled out of the cell together with the nucleus. The external face of the membrane remains in contact with the extracellular medium and surrounds the nucleus, forming a blob [Migliore 2002].

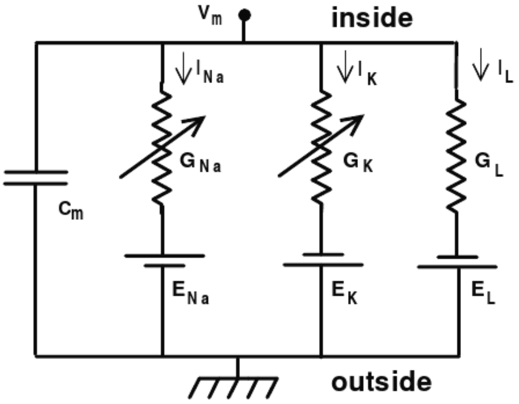

Figure 1.8: Electrical circuit diagram representing the modeled Hodgkin-Huxley neuron. The capacitor represents the dielectric properties of the membrane and the other branches containing the resistors represent the conductive properties of the cell. The arrows designate variable conductances due to the opening and closing of ionic channels. The batteries represent the electrochemical forces caused by the different ionic concentrations inside and outside the cell body. From [Nelson 1995].

states: *permissive* or *non-permissive* with a probability that depends on the membrane potential. Considering the large fraction of ion channels of a ionic species i, we can introduce a probability p_i for the fraction of gates of that population that are in the permissive state, and $1-p_i$ as the fraction of gates in the non-permissive state. When all the gates of species i are in the permissive state, $p_i = 1$ and the channel of i is open. The transition between these two states is governed by an ordinary first-order linear differential equation:

$$\frac{dp_i}{dt} = \alpha_i(V)(1 - p_i) - \beta_i(V)p_i \tag{1.4}$$

where α_i and β_i are voltage-dependent rate constants for the non-permissive-to-permissive and permissive-to-non-permissive transitions, respectively. Hodgkin and Huxley considered three different kinds of gates, m, n and h:

$$\begin{aligned} G_{\mathrm{Na}} &= \overline{g_{\mathrm{Na}}}\, p_m^3\, p_h \equiv \overline{g_{\mathrm{Na}}}\, m^3\, h && (1.5) \\ G_{\mathrm{K}} &= \overline{g_{\mathrm{K}}}\, p_n^4 \equiv \overline{g_{\mathrm{K}}}\, n^4 && (1.6) \end{aligned}$$

in which the powers are obtained by adjusting the functions to the experimental data (Figure 1.9).

The set of four equations of the Hodgkin-Huxley model then reads:

$$\begin{aligned}
C_{\mathrm{m}}\frac{dV_{\mathrm{m}}}{dt} &= I_{\mathrm{ext}} - \overline{g_{\mathrm{Na}}}\, m^3\, h\, (V_{\mathrm{m}} - E_{\mathrm{Na}}) - \overline{g_{\mathrm{K}}}\, n^4\, (V_{\mathrm{m}} - E_{\mathrm{K}}) - \\
&\quad -\overline{g_{\mathrm{L}}}\, (V_{\mathrm{m}} - E_{\mathrm{L}}) && (1.7)\\
\frac{dm}{dt} &= \alpha_m(V)(1-m) - \beta_m(V)m && (1.8)\\
\frac{dh}{dt} &= \alpha_h(V)(1-h) - \beta_h(V)h && (1.9)\\
\frac{dn}{dt} &= \alpha_n(V)(1-n) - \beta_n(V)n && (1.10)
\end{aligned}$$

and should be solved numerically due to the non-linear relationship between the conductances and the voltage. The voltage-dependent functions appearing in Equations (1.8)-(1.10) were valid at a temperature of 6.3 ^{o}C. At other temperatures a correcting factor, $3^{\frac{T-6.3}{10}}$, multiplies the right hand side of the gating-variable equations. Other models use this formalism to describe a larger variety of ionic conductances, and are all referred to as conductance-based models.

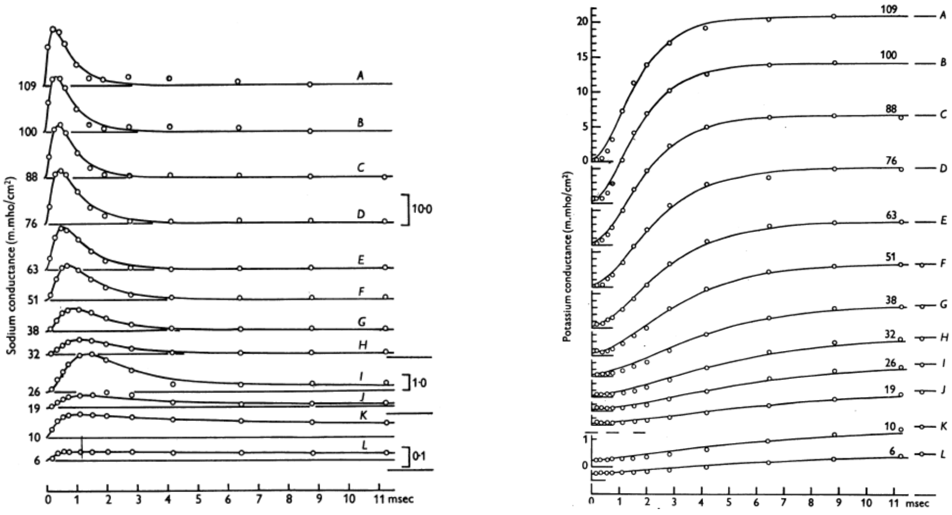

Figure 1.9: Rise of sodium (left) and potassium (right) conductances at different depolarizations. The circles are experimental results and the smooth curves are the theoretical curves. From [Hodgkin 1952].

1.3.2.2 FitzHugh-Nagumo model

The phase space of the Hodgkin-Huxley model is four dimensional (V_{m}, m, n, h) which makes intuitively hard to understand its dynamics. Other mathematical models, such as the FitzHugh-Nagumo, are simplifications of the

Hodgkin-Huxley model showing the basic mechanism of excitation without the electrochemical description of the ion channels:

$$\varepsilon \frac{du}{dt} = u(u-\lambda)(1-u) - v + I = f(u,v) \qquad (1.11)$$

$$\frac{dv}{dt} = u - \gamma v = g(u,v) \qquad (1.12)$$

where $0 < \lambda < 1$ and $\varepsilon \ll 1$. The latter condition makes the dynamics of v slower than u. In order to make a biophysical interpretation of this model, u is usually called a voltage-like variable, v the recovery variable and I represents the applied current.

The FitzHugh-Nagumo model can be analyzed geometrically in a two-dimensional space (u, v), called the *phase plane*. The stationary solution (also named *fixed* or *equilibrium point*), defined by $\frac{du}{dt} = 0$ and $\frac{dv}{dt} = 0$, corresponds to the value (or values) of u and v at which these two curves, named *nullclines*, intersect. The nullclines are the curves where the change of sign of the derivatives takes place, i.e. the functions $v(t)$ and $u(t)$ go from increasing to decreasing or vice versa. The first curve is a polynomial of third degree, $v = u(u-\lambda)(1-u) + I$ while the second one is a straight line $v = u/\gamma$. Depending on the values of the parameters, the model shows monostability, bistability, excitability, or oscillatory behavior.

In the monostability case there is only one stationary solution, i.e. one intersection point between the nullclines as shown in Figure 1.10(a, top left) describing a neuron completely at rest. In the bistability case the v-nullcline crosses the u-nullcline at three sites, Figure 1.10(a, bottom left). These intersection points are located in different branches of the u-nullcline and, thus, their stability differs. Figure 1.10(a, bottom left) shows two stable points at the solid segments of the u-nullcline and one unstable point at the dashed segment of the u-nullcline. The sign and magnitude of the functions $f(u,v)$ and $g(u,v)$ are represented by arrows in the phase plane, Figure 1.10(b), indicating the direction of the vector field that any trajectory will follow. Notice that in Figure 1.10(b) all vectors around the unstable solution, represented by a white circle, point away from it.

The excitable system, Figure 1.10(a, top right), also shows a monostable solution but a finite perturbation leads to a large excursion (thick line) through the phase plane that ends in the stable fix point again. The difference in time scale of the dynamics of u and v due to ε forces the system to follow the u-nullcline. In the oscillatory system, Figure 1.10(a, bottom right), only one solution appears but in this case it is an unstable equilibrium surrounded by a stable limit cycle that constrains the trajectory of the system.

Another mathematical advantage of the FitzHugh-Nagumo model with

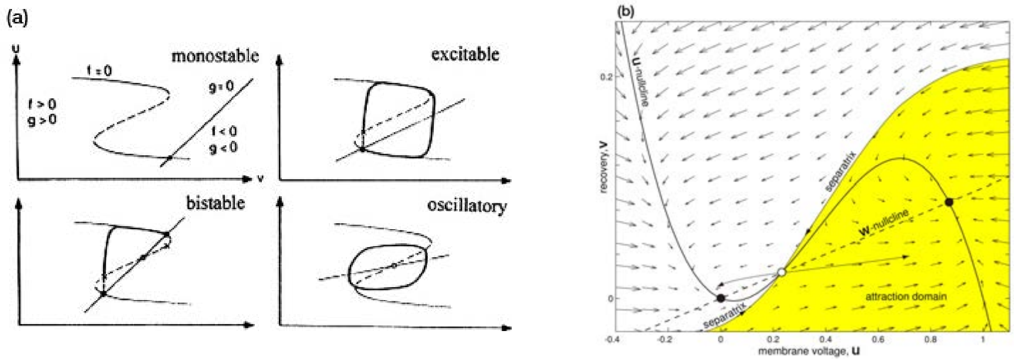

Figure 1.10: (a) Four solutions of the FitzHugh-Nagumo model represented by the intersection points between the nullclines $f(u,v) = 0$ and $g(u,v) = 0$, [Imbihl 2008]. (b) Phase plane of the FitzHugh-Nagumo model showing coexistence of two stable equilibria (black circles). The white circle is an unstable equilibrium. Adapted from [Izhikevich 2007].

respect to the Hodgkin-Huxley model is its reduced number of parameters, which allows to easily apply the *bifurcation theory*, which studies how solutions of a set of differential equations depend on the parameters. From Equations (1.11)-(1.12), we can directly draw a simple geometrical conclusion: keeping λ, ε and γ constant, varying I makes the u-nullcline move along the v-axis, whereas fixing λ, ε and I and varying γ changes the slope of the v-nullcline [Figure 1.11(a)-(c)]. Both modifications imply a change in the location of the equilibrium points and, thus, in their stability.

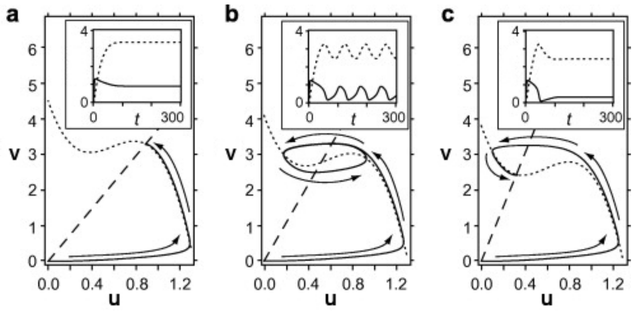

Figure 1.11: Phase portrait of a dynamical system, similar to the FitzHugh-Nagumo model, with a cubic u-nullcline (dotted line) and a straight v-nullcline (dashed line). An increase in the slope of the v-nullcline, from (a) to (c) goes through the oscillatory regime (b). The inset shows the time course of v (dotted curve) and u (solid curve). Adapted from [Takinoue 2009].

1.4 Synapses

1.4.1 Basic description of synapses

From the nerve cell body, the *soma*, numerous *dendrites* extend through the neuronal tissue making contacts with other neuron's dendrites. Besides, another protrusion, the *axon*, grows usually longer than the dendrites and also branches innervating a wide fraction of the brain (Figure 1.2). Dendrites usually receive signals while axons usually transmit them. However, there are also some examples of transmission between dendrites or from dendrite to axon. The number of contacts to each neuron determines the number of inputs that it can receive simultaneously, which can reach tens of thousands. The contact site is a small gap called the *synaptic cleft* of around 0.02 μm wide between the axolemma of one neuron, the *presynaptic neuron*, from where neurotransmitters diffuse, and the membrane of the *postsynaptic neuron*. The postsynaptic cell can also be a muscle fiber (a *myocyte*) or an organ-specific cell.

When an action potential is triggered it travels down the axon to all its ramification terminals where a local depolarization takes place, causing the opening of voltage-dependent calcium (Ca^{2+}) channels. Due to the influx of calcium ions, the storage vesicles containing neurotransmitters fuse with the membrane and release their content into the synaptic cleft in a submillisecond time scale. The neurotransmitters bind to postsynaptic proteins called *receptors*, which are embedded in the cell membrane. When the receptor captures one of those ligands it activates signal transduction, through which other messengers (like Ca^{2+} ions or cAMP and IP_3 molecules) propagate the signal into the cell eliciting a physiological response. Hence, electrical changes of the membrane serve as a signaling mechanism.

A synaptic input to a dendrite can be *excitatory* or *inhibitory*, meaning that the triggered electrical signal is a transient increase (excitatory postsynaptic potential, EPSP) or decrease (inhibitory postsynaptic potential, IPSP) of the membrane potential of the postsynaptic dendrite. All the synapses made by a neuron onto others are of the same type, either excitatory or inhibitory, so it is straightforward to divide neurons into those that are excitatory and those that are inhibitory. Most of the contacts on the dendritic tree are excitatory, the inhibitory contacts tend to be around the soma. The neuron sums the excitatory and inhibitory inputs arriving from different sites of the dendritic arbor at the *axon hillock* (a region between the soma and the axon rich in Na^+ channels, Figure 1.12) where they have propagated. In the axon hillock an action potential can be generated if the integration of all the inputs brings the membrane potential above threshold. In that case the Na^+ channels open and allow the entry of Na^+ ions, causing a depolarization of the membrane poten-

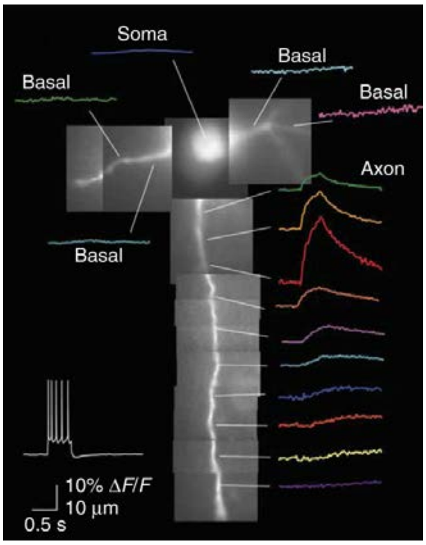

Figure 1.12: Fluorescent image (montage) of a layer 5 pyramidal neuron filled with the Na^{+}-sensitive dye SBFI (1 mM), with examples of the change in SBFI fluorescence at the indicated locations (colored traces) during action potentials (bottom, left) evoked by somatic current injection. The major changes in fluorescence occur at 25 μm from the soma, in the middle of the axon hillock. From [Kole 2008].

tial up to 40 mV. At this moment the Na^{+} channels close and the K^{+} channels open, letting the K^{+} flow out of the cell to the extracellular medium, following the electrochemical gradient and repolarizing the membrane potential. Finally the summed inputs are transmitted down the axon due to the passive spread of current to the adjacent segments. This current is prevented from going backwards due to a *refractory state* posterior to the action potential elicited in the preceding axonal segment. As mentioned in the previous section, the Na^{+}-K^{+} pump removes the excess of Na^{+} ions from the interior of the cell and infuses K^{+} ions inside the cell, restoring the resting concentrations.

Neurons that use γ-aminobutyric acid (GABA) and glutamate as neurotransmitters constitute the most important inhibition and excitation sources respectively. Receptors for these neurotransmitters are divided in two groups: ionotropic and metabotropic receptors. The first ones directly open sodium and potassium channels (excitatory) or chloride (inhibitory) occurring in the millisecond range, while the second ones activate a second messenger cascade, which eventually leads to ion channel opening, producing longer responses of seconds or even minutes. The main ionotropic receptors are AMPA (Figure 1.13, left) and NMDA for glutamate, and $GABA_A$ for GABA. On the other hand, common metabotropic receptors are *mGlu* for glutamate and $GABA_B$ for GABA. Most AMPA receptor channels are permeable to K^{+} and Na^{+} and have a linear current-voltage relationship, but other subtypes are permeable to Ca^{2+} and have a nonlinear current-voltage relationship (Figure 1.13, right). AMPA receptors activate rapidly and have decay time constants of roughly 3 ms. NMDA receptors are slow and have a nonlinear voltage dependence due to extracellular Mg^{2+} ions that block the channels at low depolarizing levels (in such case the EPSP is only triggered by AMPA activation). Hence, to open NMDA receptors, a certain level of depolarization of the postsynaptic membrane caused by simultaneous arrival of excitatory currents is needed in order to expel the Mg^{2+} ions.

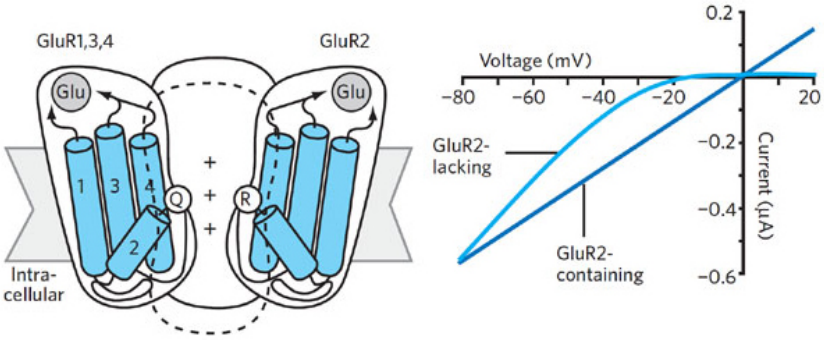

Figure 1.13: Left: Scheme of an AMPA receptor showing the assemble of tetrameric structures comprised of four subunits (GluR1, GluR2, GluR3 and GluR4). Right: Current-voltage (I-V) relationships for GluR2-lacking and GluR2-containing AMPA receptors are rectifying and linear, respectively. GluR2 renders the channel impermeable to calcium. From [Fleming 2010].

1.4.2 Modeled synapses

The activation of ionotropic receptors produces a ionic current that can be described using Ohm's law in a conductance-based formalism:

$$I_{\text{syn}}(t) = g_{\text{syn}}(t)(V(t) - E_{\text{syn}}) \tag{1.13}$$

where $g_{\text{syn}}(t)$ is the synaptic conductance and E_{syn} is the reversal potential of the synapse, at which a given neurotransmitter causes no net current flow of ions through that corresponding ion channel. For positive values of E_{syn} the synapse is depolarizing or excitatory ($E_{\text{syn}} = 0$ mV for glutamate receptors), otherwise it is hyperpolarizing or inhibitory ($E_{\text{syn}} =$ -70 mV for GABA-receptors).

Deterministic models of synaptic dynamics neglect the stochasticity of biological processes and give a description of the average behavior. For instance, the average state of the receptors can be described by a rate equation:

$$\frac{d\sigma(t)}{dt} = \alpha T(t)(1 - \sigma(t)) - \beta\sigma(t) \tag{1.14}$$

where $\sigma(t)$ is the number of open receptors relative to the total number of receptors, $T(t)$ is the time-varying neurotransmitter concentration, α is the rate of opening and β the rate of closing. The synaptic conductance can be expressed as $g_{\text{syn}}(t)=g_{\max}\sigma(t)$, where $g_{\max}$ is the peak conductance. If $T(t)$ is considered to be a Dirac delta function $\delta(t-t_j)$ occurring at every presynaptic spike time t_j, a solution for σ(t) is obtained [Destexhe 2004]:

$$\sigma(t) = \alpha \sum_j [1 - \sigma(t_j)] e^{-\beta(t-t_j)} \tag{1.15}$$

where the rise of $\sigma(t)$ is instantaneous and its amplitude depends on the concentration of closing receptors at that time, $1 - \sigma(t_j)$ [see Figure 1.14(a)]. This solution implements a saturation, because the rise of σ at t_j due to the delta-pulse release of neurotransmitters depends on the state of σ at that time, then decaying at $t > t_j$.

Another more realistic option is to consider that T occurs as a pulse [Destexhe 1994] such that $[T] = T_{\max}$ for $t_0 < t < t_1$. Solving Equation (1.14) we obtain:

$$\sigma(t - t_0) = \sigma_\infty + (\sigma(t_0) - \sigma_\infty) e^{[-(t-t_0)/\tau_\sigma]} \quad \text{for } t_0 < t < t_1 \tag{1.16}$$

where

$$\sigma_\infty = \frac{\alpha T_{\max}}{\alpha T_{\max} + \beta} \tag{1.17}$$

and

$$\tau_\sigma = \frac{1}{\alpha T_{\max} + \beta} \tag{1.18}$$

for a general initial condition $\sigma(\mathrm{t}_0)$. After the pulse $t > t_1$, when $[T] = 0$:

$$\sigma(t - t_0) = \sigma(t_1) e^{-\beta(t-t_1)} \quad \text{for } t > t_1 \tag{1.19}$$

An older model [Rall 1967] uses an alpha function to describe the evolution of the synaptic conductance due to an action potential [see Figure 1.14(b)].

In this case:

$$\sigma(t) = \sum_j \frac{t - t_j}{t_{\text{peak}}} \exp\left(-\frac{t - t_j - t_{\text{peak}}}{t_{\text{peak}}}\right) \tag{1.20}$$

which reaches its maximum at $t - t_j = t_{\text{peak}}$. This equation has a single time constant t_{peak}, therefore the rise and decay time are correlated and cannot be set independently. Instead we can use a sum of two exponentials, one for the rising and the other for the decay phase [see Figure 1.14(c)]:

$$\sigma(t) = f \sum_j \left(e^{-\frac{t-t_j}{\tau_{\text{decay}}}} - e^{-\frac{t-t_j}{\tau_{\text{rise}}}}\right) \tag{1.21}$$

Here σ peaks at $t_{\text{peak}} = t_j + \frac{\tau_{\text{decay}}\tau_{\text{rise}}}{\tau_{\text{decay}}-\tau_{\text{rise}}} \ln(\frac{\tau_{\text{decay}}}{\tau_{\text{rise}}})$. f is the normalization factor that ensures that σ ranges between 0 and 1:

$$f = \frac{1}{e^{-\frac{t_{\text{peak}}-t_j}{\tau_{\text{decay}}}} - e^{-\frac{t_{\text{peak}}-t_j}{\tau_{\text{rise}}}}} \tag{1.22}$$

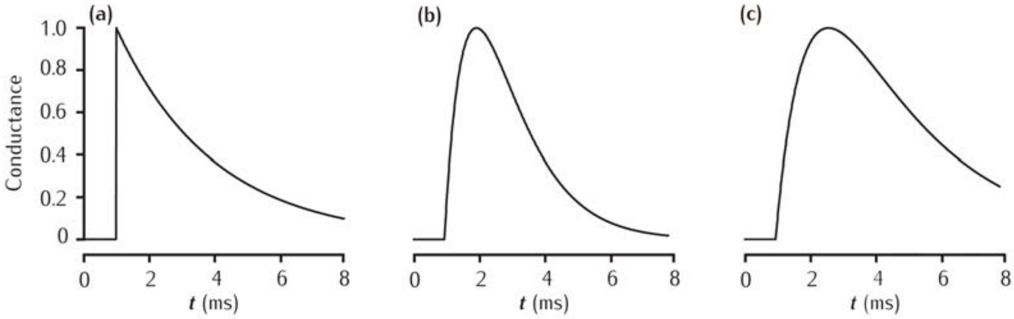

Figure 1.14: Waveforms for synaptic conductances: (a) exponential decay, Equation (1.15), (b) alpha function, Equation (1.20), and (c) dual exponential, Equation (1.21). From [Sterratt 2011].

One consequence of adopting Ohm's law to describe the relation between the synaptic current and the elicited postsynaptic potential (PSP), is the decrease in the membrane input resistance and membrane time constant (i.e. the time scale of the neuron's responsiveness to input changes) upon strong stimulation, which reduces and shortens the PSPs [Kumar 2008]. Postsynaptic potentials produced at individual excitatory synapses may be only a fraction of millivolts, which is far below the spiking threshold. Whether or not the summation of several postsynaptic potentials results in an action potential depends on the balance of excitation and inhibition. The strength of a synapse depends on the amount and duration of the neurotransmitters release.

The activation of a synapse is delayed a certain time after the presynaptic spike is fired. Moreover, depending on the nature of the synaptic coupling (excitatory to inhibitory, excitatory to excitatory, inhibitory to inhibitory or inhibitory to excitatory) and the location of the synapses (soma or dendrites), the conductance $g_{\max}$ varies. GABAergic terminals exceed non-GABAergic terminals at the soma, while at the dendrites non-GABAergic terminals outnumber GABAergic terminals [Benson 1996]. Synapses located at the dendrites trigger an inward current that travels through the dendrite to the soma. Therefore, the postsynaptic potential elicited locally at the dendrite spreads passively into the soma reducing its amplitude. Single inhibitory postsynaptic potentials are, thus, stronger than single excitatory potentials. This distribution of synapses avoids the buildup of excitation boosted by the more numerous excitatory neurons.

In addition to the chemical synapses explained above, electrical synapses or *gap junctions* have to be considered as well, although they have been only directly seen between inhibitory neurons in the neocortex [Gibson 1999]. These synapses have a low-resistance to the direct movement of ions between neurons and are very fast transmission channels leading to synchronization of membrane voltages both above and beneath threshold. Electrical junctions are permanently active and do not need an activation threshold but they are constrained to neighboring neurons (Figure 1.15).

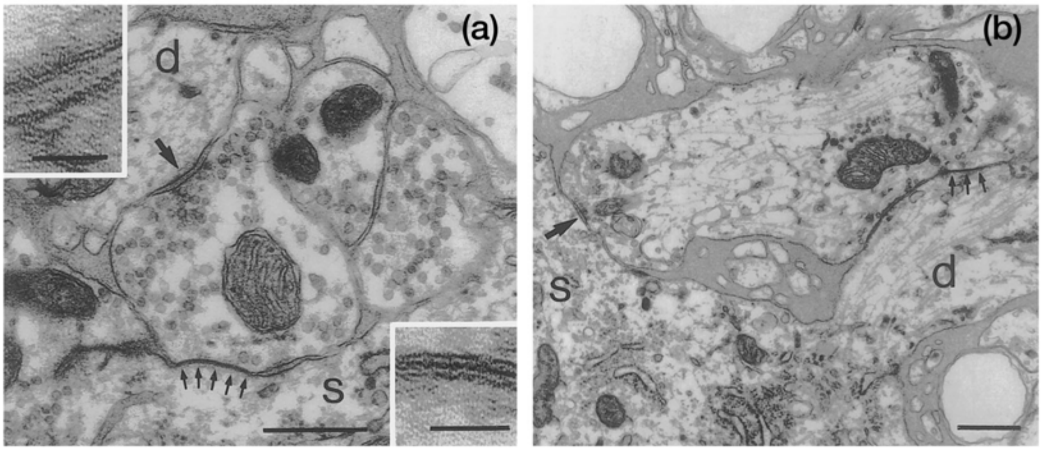

Figure 1.15: Electron micrographs of synaptic endings that establish both chemical (large arrow) and electrical gap junction contacts (small arrows). Insets in (a) illustrate chemical (top left) and gap junction (bottom right) contact zones. Nomenclature: d, dendrite; s, soma. Scale bars: (a) 0.25 μm (inset, 0.05 μm) and (b) 0.5μm. From [Graf 2003].

1.5 Neuronal Code

1.5.1 Encoding by individual neurons

Each neuron summates all the inputs coming from the bulk of synapses located in its dendritic tree. If the integration of EPSPs and IPSPs gives a net increase of the membrane potential above threshold, an action potential is emitted and transmitted through the axon. The series of spikes fired by a cortical neuron are highly irregular. The mean firing frequency of the *in vivo* neuronal response is reproducible under presentation of the same stimulus, however, the precise timing of the action potentials is not, as shown in Figure 1.16(left). On the other hand, neurons *in vitro* fire regularly in response to constant current injection (Figure 1.16, right).

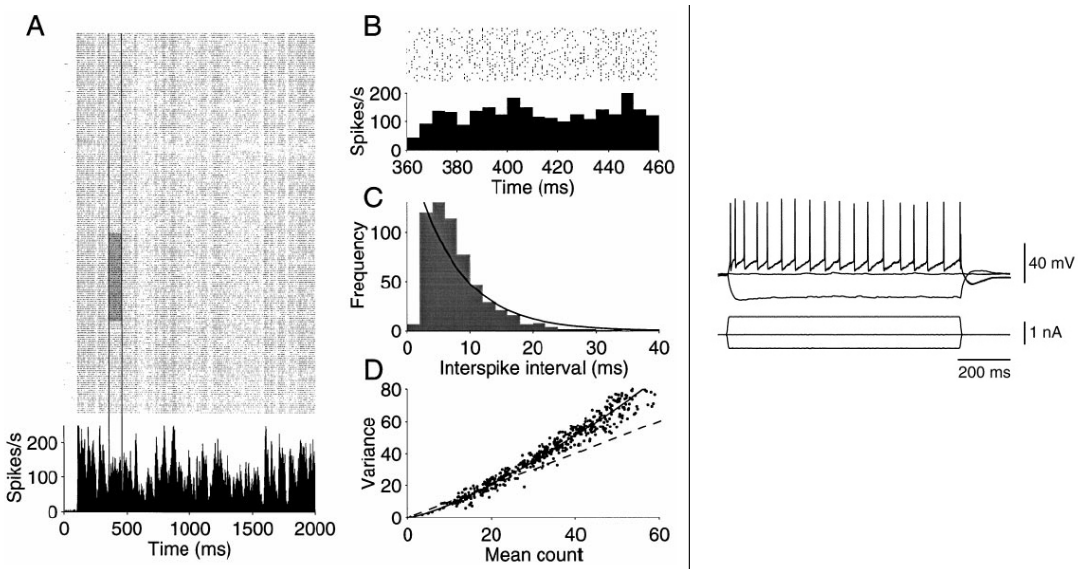

Figure 1.16: Left: (A) Raster plot and peristimulus time histogram for a neuron in the middle temporal visual area (MT or V5) for 210 presentations of the same 2 s-sequence of random moving dots with rapid fluctuations of luminance. Vertical lines delineate a period of fairly constant firing rate across trials. The shaded region is zoomed in (B) and contains 50 trials between 360 ms and 460 ms. (C) ISI frequency histogram from the 50 trials fitted by and exponential (solid curve) as expected from a Poisson distribution of events (spikes). (D) Plot of the coefficient of variation of the ISI distribution across 500 randomly chosen epochs from (A) lasting from 100 to 500 ms including from 50 to 200 adjacent trials. The best fitting power law (solid curve) is not predicted from a Poisson process (dashed line). From [Shadlen 1998]. Right: Response of a neuron in the basolateral amygdala to intracellular injection of a constant current. From [Kano 2005].

An interesting debate, opened in the early 90s, discusses whether this irregular timing of spikes carries relevant information (*temporal-coding* or *coincidence detection* hypothesis) or it is just noise and, thus, the information is conveyed in the spiking rate (*rate-coding* or *temporal integration* hypothesis) [deCharms 2000]. The difference between these two concepts lies within the relationship between the integration time over which neurons effectively summate synaptic potentials and the mean interspike interval. Temporal integration does not take into account the precise pattern of the spikes impinging the neuron and only temporal changes in the structure of the train of spikes can result in changes in the firing rate of the perturbed neuron [Figure 1.17(a)]. Coincidence detection requires a short integration time compared to the mean interspike interval, and only simultaneous postsynaptic potentials in a millisecond range are summated together as shown in Figure 1.17(b).

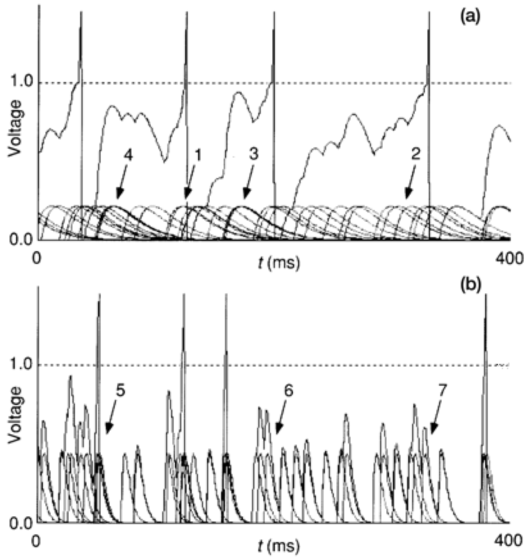

Figure 1.17: (a) Temporal integration of a train of EPSPs simulated by an alpha function with a time constant of 15 ms. In this case the majority of PSPs contribute to the generation of an action potential either when they are are synchronous in time (1) or not (2). Furthermore synchronous PSPs do not always trigger action potentials (3,4). (b) Coincidence detection of a train of EPSPs simulated by an alpha function with a time constant of 3 ms and a PSP size increased by a factor of two. Most PSPs do not contribute to spike triggering (6,7), only synchronous ones (5) are capable of triggering spikes. From [König 1996].

Other relevant differences between the two integration modes refer to the speed of cortical processing and the coefficient of variation of the interspike interval. As shown in Figure 1.17(a) the processing time of a temporal integrator is of the same order of magnitude as the interspike interval of its output. For the coincidence detector [Figure 1.17(b)] the processing time is only a fraction of the interspike interval of its output.

The irregularity of *in vivo* action potentials discharges is characterized by the interspike interval distribution. Neocortical neurons have a high degree of variability with a coefficient of variation CV[†] between 0.5 and 1 [Softky 1993]. Models of neurons performing temporal integration do not reproduce the high values of CV. The *integrate-and-fire* (IF) model summates successive EPSPs until the voltage reaches the firing threshold and then resets to zero:

$$C_\mathrm{m}\frac{dV}{dt} = I(t) \tag{1.23}$$

where $I(t)$ is the input current. In this model, arbitrarily small input constant currents eventually lead to a spike because the membrane voltage increases linearly with time, $V(t) = \frac{I}{C_\mathrm{m}}t$ (in this case the resting membrane potential has been arbitrarily taken equal to zero). Moreover the output spike train corresponding to a constant current is perfectly periodic. If $I(t)$ is a sequence of postsynaptic currents the IF-neuron will summate the inputs one after another irrespective of their temporal separation. If V_th is the spiking threshold and we consider a random train of pulses of size I_o and average firing rate f_o, for every group of n spikes, with n being the smallest integer larger than $\frac{C_\mathrm{m}V_\mathrm{th}}{I_\mathrm{o}}$, the IF-neuron will fire an action potential and its average firing rate will be $f_{\mathrm{o}/\mathrm{n}}$. As shown by [Tuckwell 1988], if the incoming pulses are Poisson distributed, the output train of pulses from an IF-neuron will be gamma distributed, Figure 1.18.

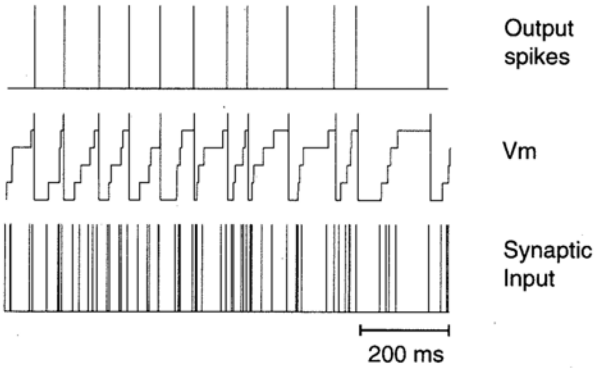

Figure 1.18: A Poisson train of spikes (bottom trace) with an ISI exponential distribution is injected to a IF-neuron (middle trace) producing a more regular output (top trace) with gamma distributed ISI. In this example, $n = 5$ (middle trace). From [Gabbiani 1998].

A leak channel represented by a resistance R is added to the model in

---

[†] The coefficient of variation CV $= \frac{\sigma}{\mu}$ of a sample of data $\{x_i\}_N$ is defined as the corrected sample standard deviation, $\sigma = \sqrt{\frac{1}{N-1}\sum_{i=1}^{N}(x_i-\mu)^2}$, normalized by the mean $\mu = \frac{1}{N}\sum_{i=1}^{N} x_i$.

order to account for a relaxation behavior of the membrane voltage after the integration of an input. This model, known as the *leaky integrate-and-fire* (LIF) model:

$$C_{\mathrm{m}}\frac{dV}{dt} = I(t) - \frac{V}{R} \tag{1.24}$$

exponentially decays to a steady-state voltage after switching off the injection of a constant current, $V(t) = IR(1 - e^{-\frac{t}{RC_{\mathrm{m}}}})$.

The time constant $\tau_{\mathrm{m}} = RC_{\mathrm{m}}$ of the LIF-neuron affects the coefficient of variation of the ISI of the output train of spikes. If more than one presynaptic spike is needed to elicit an action potential, $n > 1$, only synchronous presynaptic spikes will efficiently increase the membrane voltage towards the firing threshold because between presynaptic spikes the LIF-neuron relaxes according to τ_{m}. Large values of τ_{m} will make the output more regular because the neuron will convert randomly arriving presynaptic spikes into a single action potential. On the other hand, short τ_{m} increase the sensitivity to coincident spikes and turns the neuron into a coincident detector with greater CV.

For high input firing rates $f > \frac{1}{\tau_{\mathrm{m}}}$ the LIF-neuron is similar to the IF-neuron and acts much like a temporal integrator because the capacitor is not discharged significantly before it reaches the threshold. On the other hand, for low firing rates $f \ll \frac{1}{\tau_{\mathrm{m}}}$, the LIF-neuron can only integrate synchronous presynaptic spikes like a coincident detector and its output approximates a Poisson process in which $\mathrm{CV} = 1$. In order to reproduce high values of CV seen *in vivo* cortical recordings for high rates of synaptic input, we need either very small values of τ_{m} around a fraction of a millisecond (Figure 1.19, thin line labeled $\tau = 0.2$ ms), or high amplitude EPSPs such that the threshold is reached after only 1 or 2 presynaptic spikes (Figure 1.19, thin line labeled $N_{th} = 4$ or squares labeled $N_{th} = 1$).

Biologically plausible values in a motor neuron are, for instance, such that an EPSP is only 0.2-0.4 mV in amplitude, far below the spiking threshold that requires depolarizations of 10 mV or more from the resting potential [Kandel 2000]. The results obtained by the LIF-neuron with realistic parameters (lower curve in Figure 1.20) do not reproduce the experimental results for the variability in the interspike intervals of cortical neurons.

Softky et al. [Softky 1993] computed CV values for more detailed biophysical models and showed that experimental CV values can be reproduced if neurons are provided with fast mechanisms for repolarizing the membrane potential while they integrate the incoming presynaptic spikes. This case corresponds to the coincident detection mode that translates the variability of the spike trains impinging on the soma into the variability of the output ISI. They

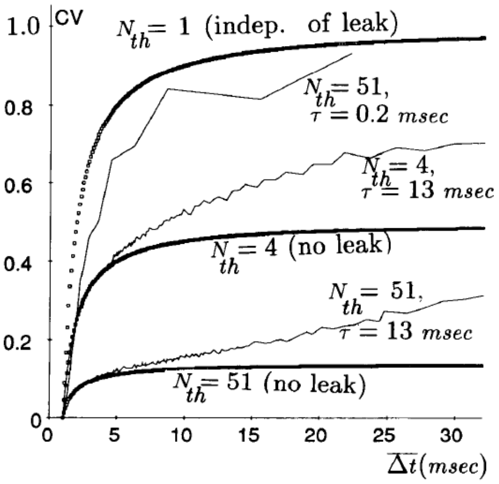

Figure 1.19: CV dependence on the mean period $\overline{\Delta t}$ –inverse of the mean firing rate– of the synaptic input for the integrate-and-fire model (squares) and the leaky integrate-and-fire model (thin lines) for a refractory period of 1 ms and for different values of the membrane time constant τ_{m} -τ in the figure- (relevant for the LIF-neuron) and different EPSP amplitudes given by n -N_{th} in the figure-. From [Softky 1993].

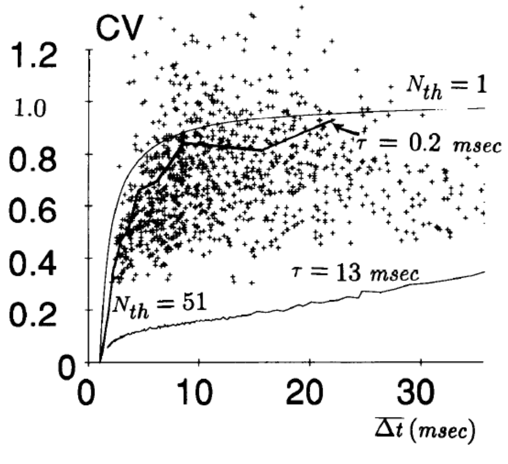

Figure 1.20: CV dependence on the mean period of the synaptic input $\overline{\Delta t}$ for simulated data from the leaky integrate-and-fire model (thin lines) for a refractory period of 1 ms and for experimental data from macaque cortical neurons (crosses). The lower curve corresponds to parameters in a plausible biological range. The middle curve corresponds to parameters out of the plausible biological range but reproducing the observed variability in high CVs. The upper curve corresponds to the extreme case of $n = 1$. In this figure τ_{m} and n are τ and N_{th} respectively. From [Softky 1993].

argued that sodium action potentials generated in distal dendrites ($\geq 100\ \mu m$ from the soma) demand indeed coincident presynaptic events [experimentally shown as the green traces in Figure 1.21(A)] and that those dendritic spikes, in turn, must arrive within a millisecond time window at the soma in order to trigger an action potential (red traces in Figure 1.21(A) and green circles of Figure 1.21(B), in comparison with the red circles). This effectively reduces the number of presynaptic spikes required to elicit a somatic action potential and brings the neuron closer to the coincident detector regime.

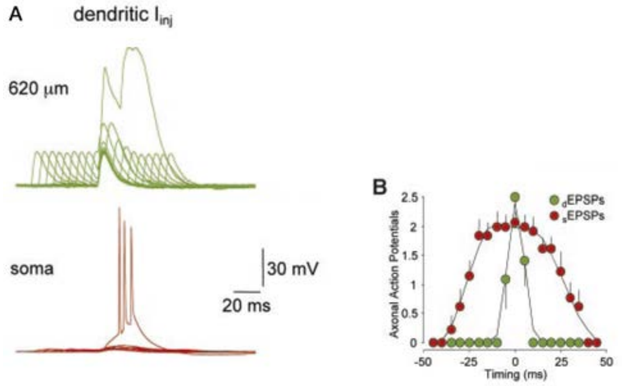

Figure 1.21: Current injections I_{inj} separated in time by 0 to 45 ms generate pairs of artificial EPSPs (aEPSPs) at distal dendritic sites of neocortical pyramidal neurons. (A) Summation of aEPSPs at 620 μm distance from soma (green) and response at the soma (red). Dendritic spikes are only generated when the aEPSPs are coincident in time (around 5 ms of separation). (B) Dendritic spikes forward-propagate to the soma where they elicit an action potential if they arrive near synchronous (green circles, B). Direct somatic excitation allows for a broader time distribution of aEPSPs for action potential generation (red circles, B). From [Williams 2002].

Many real neurons, however, have a CV greater than 1 because the number of spikes that a neuron receives is not constant in time. There are many other sources of variability not considered by the Poisson character of the input train of spikes, such as stochasticity in synaptic transmission[†] [Maass 1999] or network effects due to correlations among the inputs [Salinas 2000].

1.5.2 Balanced inhibition

The noisiness of the interspike intervals of neurons that are part of a network can emerge as a network effect when the mean membrane potential stays just below threshold, i.e. in the *subthreshold regime*. Shadlen [Shadlen 1994] pointed out the role of inhibition in increasing the ISI variability. Models that

---

[†] A spike arriving at a synapse triggers the release of neurotransmitters with a certain probability less than one.

take into account both excitation and inhibition producing an average zero net current are also known as *random walk models* or *diffusion processes* because fluctuations on the excitation-inhibition balance at the millisecond time scale cause a depolarization (or hyperpolarization) step on the postsynaptic neuron, following a random trajectory, provided there is a momentary drop in inhibition in combination with a simultaneous excess of excitation (or in the other direction) [Koch 1999].

Shadlen et al. [Shadlen 1994] argue that due to the intense bombardment of presynaptic spikes, a neuron behaving as coincident detector (as it is proposed in [Softky 1993]) will need unrealistic short membrane time constants. Therefore, neurons are more likely to act as temporal integrators, the spiking times not containing any information from the input. At the same time, fluctuations in the balance between excitation and inhibition will make the neurons fire randomly.

Without the inhibitory offset, excitatory spikes arriving from neighboring neurons at random times will cause an average constant depolarization in the postsynaptic neuron, leading to a tonic firing that is not observed in *in vivo* conditions. This paradox is partially solved by considering the balance of inhibition, which as mentioned, helps increase the CV of cortical spiking. Correlated fluctuations of the input coming from different presynaptic active neurons will increase the variance of the net synaptic current.

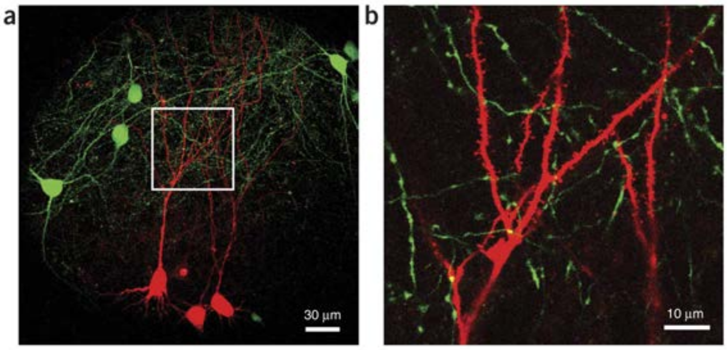

Figure 1.22: (a) GABAergic interneuron (green) and pyramidal neuron (red) of hippocampal slices. (b) Zoomed area showing synaptic contacts between inhibitory boutons and excitatory dendrites. From [Wierenga 2008].

In [Shadlen 1994] several experimental results are cited, supporting the hypothesis that inhibition can balance excitation despite the fact that excitatory neurons are more abundant than inhibitory neurons. They point out that whereas excitatory synapses can fail in the release of neurotransmitters, inhibitory synapses are more reliable and have a larger impact in the membrane voltage. Moreover, unlike excitatory neurons, inhibitory neurons make multiple contacts on the postsynaptic targets (Figure 1.22) and spike more synchronously due to electrical coupling [Galarreta 2001] and tend to have a higher firing rates (Figure 1.23). Hence, the biophysics of inhibitory neurons help to compensate their relative small number in order to balance excitation.

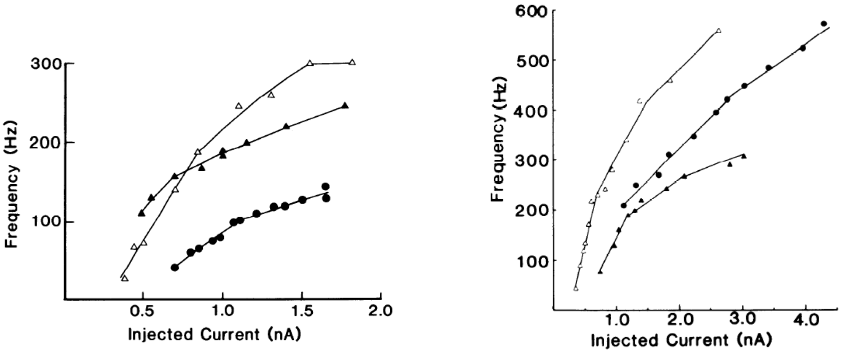

Figure 1.23: Frequency-current plots for three different regular-spiking neurons (left) and fast-spiking neurons (right). Regular-spiking neurons were identified as spiny pyramidal neurons (excitatory neurons) and fast-spiking were found to use GABA as their neurotransmitter (inhibitory neurons). From [McCormick 1985].

In a balanced network, neuronal irregular spiking is a network emergent property [van Vreeswijk 1996] and spurious correlations between the random synaptic inputs can cause a spike. The time response of neurons is fastened because the effective membrane resistance is reduced due to the opening of ion channels produced by the high synaptic bombardment -a state known as *high-conductance*-, leaving the question of the neuronal code somewhat unresolved because the requirement of a small individual time constant is then met.

Experimentally, Stevens and Zador [Stevens 1998a] have shown that the variability in the output of cortical neurons stimulated *in vitro* by a synthesized synaptic current composed of a mixture of excitatory and strong inhibitory currents is much less than the observed *in vivo*. In order to reproduce *in vivo* variability of cortical firing they had to introduce correlations among synaptic inputs such that at some intervals there was synchrony in the incoming spikes. This observations were later confirmed by the experiments of Harsch and Robinson [Harsch 2000] making more relevant the role of fluctuating inputs, in addition to the process of postsynaptic integration traditionally discussed, in the irregular nature of cortical spikes.

Correlation of excitation and inhibition shows significant effects in the firing rate of neurons because they affect fluctuations of the average input. For a given average firing rate of the excitatory and inhibitory inputs, the firing output of a postsynaptic balanced neuron can be more effectively tuned by input correlations than an unbalanced neuron. This is shown in Figure 1.24 for different correlation patterns of spike trains impinging on a leaky integrate-and-fire neuron model [Salinas 2001]. The Figure shows a balanced (red trace) and an unbalanced (green trace) input consisting of 160 excitatory and 40 inhibitory spike trains. The rate of inhibitory inputs was always 1.7 times the excitatory rate. In the upper row all spike trains are independent, in the second and third row two correlated activities are considered, namely synchrony and oscillations, respectively. In the lower row the correlations between pairs of excitatory inputs, pairs of inhibitory inputs and between excitatory and inhibitory pairs are equal. The balanced neuron is more sensitive to correlations than the unbalanced one, as shown by the relative difference with the independent case (broken lines).

In summary, probably both coding strategies, temporal integration (slow-time integration) and coincidence detection (fast-time integration), coexist in our brains in different areas in order to subserve specific functions [Kumar 2010]. Moreover the nature of the input seems to affect the chosen coding strategy. We have seen that, theoretically, neurons within a balanced network are more sensitive to the temporal pattern of the presynaptic spike trains of correlated inputs. In an experimental work, Mainen and Sejnowski [Mainen 1995] had isolated rat cortical neurons in a slice preparation blocking glutamate and $\mathrm{GABA_A}$ receptors. Two types of injected current, a pure constant DC current [Figure 1.25(A)] and a low-pass filtered Gaussian white noise added to the DC current [Figure 1.25(B)] evoked an unreliable and a high reliable spiking response, respectively. Hence, the timing of the outgoing neuronal spike train appears to be input-dependent even outside the network.

Concerning the neuronal code, information should be regarded as population activity averages and not only by temporal averages of single units.

1.5.3 Encoding by neuronal populations

As described in the previous section, stimuli appear to be encoded both by the spike count and the millisecond precision of the timing of individual spiking neurons. However information is typically encoded in the nervous system by populations of neurons. Is the population coding a sum of independent spike codes by single units or is there additional information in the correlation of the spike patterns? A sum of individual spikes will give a population rate measure but, is there any other information carried by the spike train besides the firing rate? A high population firing rate computed over a short time interval indicates either a high degree of synchrony between neurons or a high individual firing rate. Riehle and colleagues [Riehle 1997], had disentangled

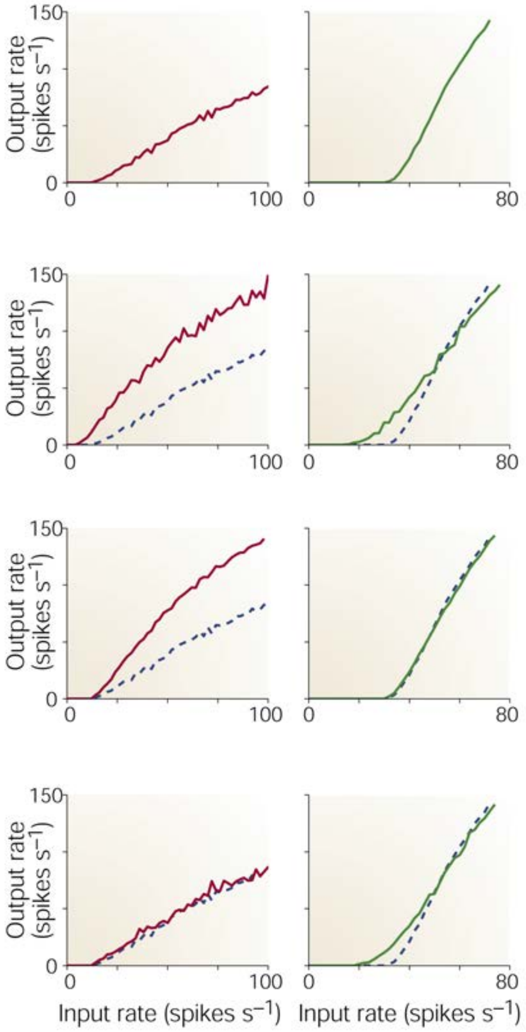

Figure 1.24: Input-output rate plots. Red and green traces correspond to responses of balanced and unbalanced neurons, respectively. Upper row: All input spike trains were independent. Second row: Excitatory inputs were synchronous, with 10% shared inputs. Third row: Inhibitory inputs oscillated with an amplitude equal to 50% of the mean rate. Lower row: All inputs were synchronous, with 10% shared inputs. For comparison, broken lines are the curves obtained with independent inputs (upper row). From [Salinas 2001].

these two causes in order to clarify the role of synchrony in behavior. In a motor task monkeys had to touch a target appearing in a screen after a delay of variable duration, following a preparatory signal that instructed the monkey to get ready. This delay was varied randomly from trial to trial and could take up to 600, 900, 1200 or 1500 ms. They found synchronization (within a 5 ms window) between pairs of neurons either when the target stimulus was presented or when it was expected. However, only in the former case, synchrony was accompanied by an increase in the discharge frequency of the

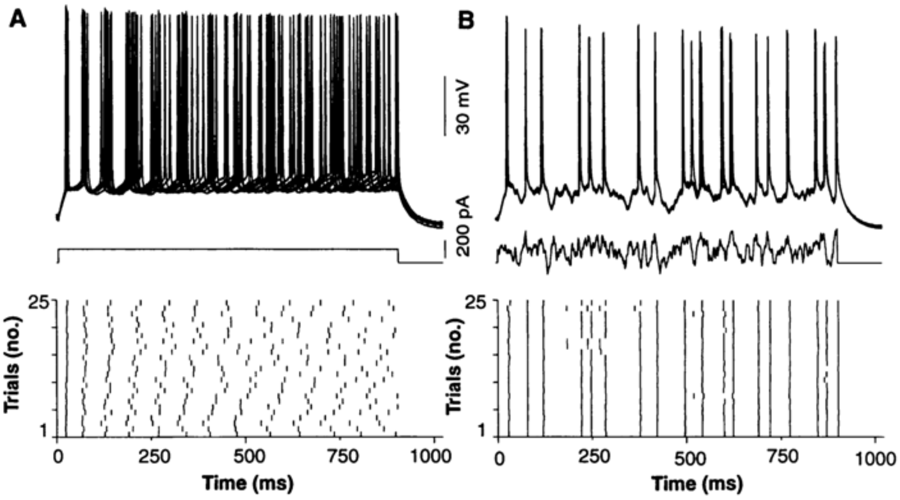

Figure 1.25: The upper row shows superimposed somatic voltage traces from 25 trials. The lower row shows the spiking times of a neuron over 25 trials. (A) DC constant current of 150 pA during 900 ms. (B) Gaussian white noise ($\mu = 150$ pA and $\sigma = 100$ pA) low-pass filtered with a time constant $\tau = 3$ ms. From [Mainen 1995]. Note the difference with *in vivo* Figure 1.16 in which synaptic transmission was not blocked.

neurons. This observation suggests that correlations are modulated by the animal internal state.

The importance of correlations in neuronal coding is highlighted by the binding problem, which looks for an explanation of how the brain can functionally link neuronal distributed activity. [Milner 1974] and [Von Der Malsburg 1981] proposed a mechanism for the common integration of features belonging to an object while separating the representation of another one which consisted in the selective synchronization of cell assemblies encoding the same stimulus. Such combination of distributed activities should be dynamically modulated by the stimulus and by the state of the subject, such as attentive state or decision making preceding a motor command.

Interesting studies [Fries 2001, Canolty 2010] have added new perspectives to the traditional view of the neuronal code. Even if there is total agreement that the spikes are the basic unit of neuronal information, slower relevant brain dynamics should also influence the way in which spikes are processed. Pascal Fries and collaborators have examined the role of oscillations coming out from the synchronized activity of cortical neurons in communication between brain areas. Specifically, in [Fries 2007] they study the effect of these oscillations in shaping the temporal pattern of activity. They conclude that, *"within the gamma cycle*[†] *, the excitatory input to a pyramidal cell is converted into*

[†] Rhythmic synchronization of a population of neurons within the 30 - 90 Hz frequency range.

a temporal code whereby the amplitude of excitation is recoded in the time of occurrence of output spikes relative to the gamma cycle, stronger inputs leading to earlier responses. Thus, amplitude values are converted into phase values that indicate by how much a discharge precedes the peak of a gamma cycle". Thus, the temporal code seems more plausible if the spiking times are related to the phase values of an ongoing oscillatory excitatory input, which might provide an internal clock.

1.6 Neuronal oscillations

One of the most well established observations in brain dynamics is the presence of sensory-evoked cortical oscillations [Gray 1989, Liu 2006, Buzsáki 2006]. Recordings obtained from microelectrodes introduced in the cortex show coherent oscillatory electrical signals named *local field potentials (LFPs).* The LFP is the low frequency component of the combined dendritic activity -subthreshold dynamics- of multiple neurons. It is a collective property of a neuronal ensemble and not a property of the individual neurons, providing a measure of the input to and local processing within an area. Therefore, the LFP reflects the activity of both the recurrent loops between excitatory and inhibitory neurons and the afferent pathways from other areas [Goense 2008]. Large amplitudes of the LFP are due to synchronous activity of the neurons within an area of radius $\sim$100 μm surrounding the recording electrode. However, usually there is no equivalent apparent rhythmicity in the spike trains -suprathreshold dynamics- of individual cells, which becomes only visible after data processing of spike trains of multiple single cells. The spike trains of the constituent neurons of a cortical region are typically irregular and sparse [Olshausen 2004, Brunel 2003b, Wolfe 2010].

The *multi-unit activity (MUA)*, which is the high frequency component of the electrical signal recorded from an electrode placed extracellularly, only captures fast events such as action potentials (which are smaller than recorded intracellularly) emitted by the surrounding neurons. In particular, just spikes elicited by the neurons with larger somas (i.e. large pyramidal cells) are measured [Goense 2008]. Both the LFP and MUA signals reveal the synchronized activity of local neurons, i.e. those found in the vicinity of the electrode's tip.

The frequency spectrum of the recorded local field potentials is related to the state of the brain (sleep/wake states, perceptual attention, disease states, etc. and sensory input-dependent states) and to particular anatomical areas. For instance, oscillations in the beta and gamma range -at frequencies between 15 to 30 Hz and 30 to 90 Hz respectively- are found in humans when they are in a state of focused attention or in response to acoustic or visual stimulation [Singer 1993]. During sleep and many behavioral states electrical signals recorded from the human cortex show frequency peaks in their power spectra, which otherwise decrease with frequency following approximately a $1/f^2$ power law [Buzsáki 2006]. However, the mechanisms underlying the appearance of rhythmic coherent activity of ensembles of neurons are not perfectly known and might be different in distinct areas. For instance, collective oscillations in the cortex can be driven by periodic input from the thalamus [Steriade 1984] or be independent of it [Silva 1991]. Self-sustained oscillations can rely on periodic firing neurons that synchronize through their synapses [Whittington 1995] or can arise as a network property despite the fact that the individual cells do not oscillate [Fries 2001].

Regardless of the source of generation of collective oscillations, a common feature is the presence of rhythmic synchronized depolarization of neuronal membrane potentials and of a recurrent loop of synaptic excitatory and inhibitory flow. These dynamics represent two sides of the same coin: an excited neuronal tissue is depolarized and neurons can eventually fire simultaneously, causing an avalanche of inhibition that terminates the firing until another excitatory synaptic flow activates. Such excitatory events bring the neurons closer to threshold, increasing the probability of firing due to small fluctuations in the input. Therefore, inhibition besides limiting excitation, controls the timing of action potentials by regulating the excitability of neurons [Klimesch 2007].

1.7 Neuronal circuits

Neurons are interconnected forming *neuronal circuits*, which are the meaningful units of information processing. The electrical activity of an isolated neuron cannot be related to a brain function. It is the collective activity of the single elements of a neuronal circuit that travels to other regions of the brain and directly contributes to a cortical task. Neurons wired together coordinate the spiking activity spatio-temporally.

Connected neurons can be close to each other ($<$1 mm) or far apart from one another ($>$1 mm). Some neurons within a neuronal circuit, the *principal or projection neurons*, send their axons to distant neurons whereas others, the *interneurons*, project only locally. In this way, different parts of the brain involved in different functions are also communicating. Principal neurons are excitatory and interneurons tend mostly to inhibit their neighbors (few interneurons are excitatory).

There is yet no exact anatomical map of the human brain, nor even of specific sensory areas or cortical columns. Connectivity between neurons is established by tracing the axons, dendrites, and synapses through complicated arbors [Figure 1.26(a,b)]. The human brain contains around 10^{11} neurons and 10^{15} connections between them, which are technically impossible to distinguish separately. However, as brain functions mainly rely on the coactivity of large populations of neurons not necessarily close in space, it is probably not required to know the precise wiring between individual neurons. Brain areas or neuronal populations, contrary to single neurons, have no clear anatomical boundaries.

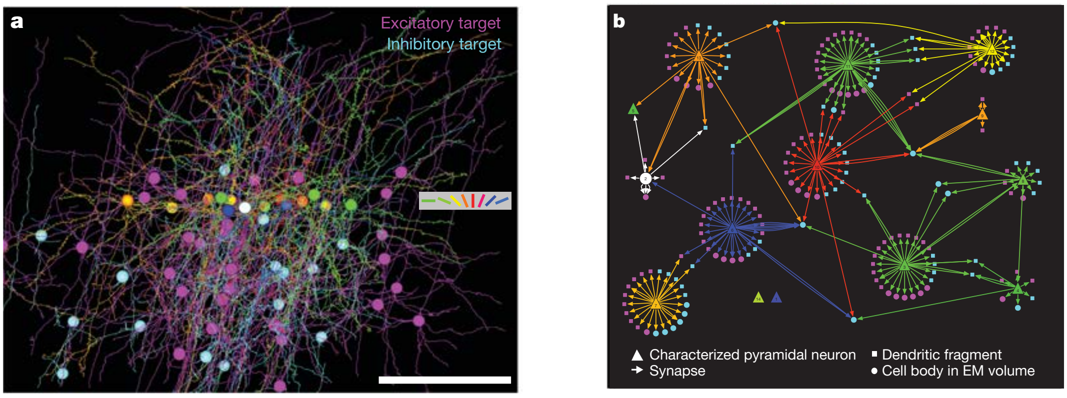

Figure 1.26: (a) Cell bodies, axons and dendrites of 14 neurons in the functionally calcium-imaged plane (colored according to their orientation preference) of the cat visual cortex. Dendrites and cell bodies of these neuron's excitatory (magenta) and inhibitory (cyan) postsynaptic targets within the volume (600 x 600 x 250 μm) are also shown. Obtained with electron microscopy (EM). Scale bar: 100 μm. (b) Directed network diagram of the functionally characterized cells and their targets. From [Bock 2011].

Another level of description, the functional connectivity (Figure 1.27, middle) *links* brain areas according to statistical dependencies between measured electrical signals -such as LFPs or fMRI-. Such correlations fluctuate over a wide range of time scales, while the anatomical connections (Figure 1.27, left) are stable over longer periods (from hours to days).

Analysis of correlations and coherence of experimental data shows that the functional connectivity approaches a small-world network [Stam 2004]. Small-world networks were first described by Watts and Strogatz [Watts 1998], as being highly clustered, i.e. with a high degree of short-range connections but with some long-range connections that shorten the path length (average distance between two nodes in the network). Intuitively this type of connectivity seems very suited for neuronal networks, because it shortens the time delay between topologically distant nodes and, at the same time, favors integration of information of nearest neighbors. The probability that two neighbors of the same node are connected between them is greater than for two nodes randomly selected. It is however not known if the structural connectivity is also a small-world network. Besides, the anatomical connections can be described at three scales: microscopic, mesoscopic and macroscopic. Each scale refers to the organization of individual neurons, neuronal populations, and brain regions respectively.

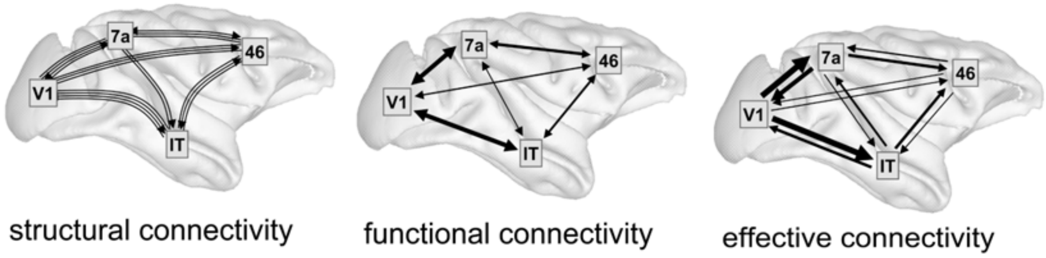

Figure 1.27: Scheme of the structural –axonal pathways connecting brain regions–, functional –statistical relations among brain regions– and effective –directed influences among brain regions– connectivity. The boxes denote specialized cortical regions: V1 (primary visual cortex), 7a (visual cortex in the parietal lobe), IT (visual cortex in the inferior temporal lobe) and 46 (an area of prefrontal cortex). From [Sporns 2010].

In analogy with the World-Wide Web network, scale-free functional neuronal networks have also been introduced [Eguíluz 2005]. In a scale-free network [Barabási 2004] the number of connections made by each node, its degree, is distributed heterogeneously with a few nodes, the hubs, connected to a high number of other nodes. The probability distribution $P(k)$ of the degree decays much slowly than a Poisson and follows a power law [Figure 1.28(B, bottom)]. This architecture is appealing when considering biological networks for two main reasons: on one hand Barbási and colleagues [Barabási 1999] found that large scale-free networks emerge when adding new nodes that attach preferentially to those existing nodes with a higher degree; on the other hand they have argued [Albert 2000] that this type of connectivity is more resistant to random injuries due to the existence of hubs present on the majority of links. These properties can be applied to a growing population such as neurons, which need to be robust to attacks in order to maintain their functionality, although it is little evidence that this is the case for real brains.

In addition to the structural and functional connectivity, there is a third level of connectivity, the effective connectivity (Figure 1.27, right) which unravels the direction of the flow of information between areas by means of causality measures. Unlike functional connectivity, in this case one can distinguish correlated activity between two electrodes's measurements due to direct interactions between the two brain areas from a similar effect caused by stimulus-locked transients in two disconnected areas.

Despite the lack of an anatomical map at the level of single neurons (the *connectome*), at the mesoscopic scale some magnetic resonance imaging (MRI)

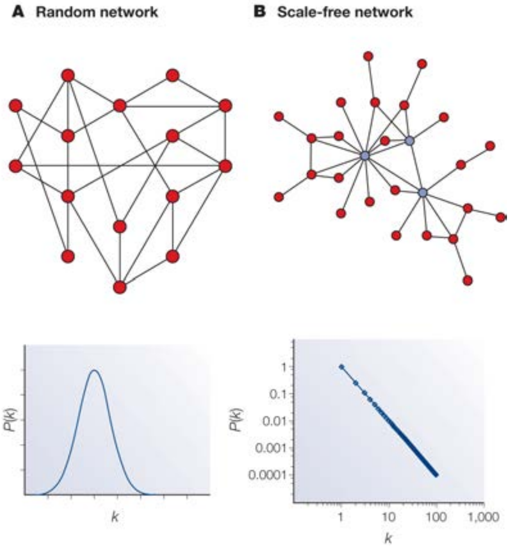

Figure 1.28: Graph of a random network (A, top) and a scale-free network (B, top) and their connectivity distribution function $P(k)$ (Ab, Bb) where k is the node degree -the number of connected nodes-. The random network, similar to the small-world network from [Watts 1998], follows a Poisson distribution of the connectivity (A, bottom), while the scale-free network has a power-law degree distribution (B, bottom). From [Barabási 2004].

experimental work points up its small-world features [He 2007, Schmitt 2008]. Hence, in Chapters 2, 3 and 4, we have considered populations of small-world connected neurons in which each cell has the same number of neighbors in average and the clustering is greater than in a random network (while the average path length is shorter) [Figure 1.28(A)]. The same structural connectivity was applied when connecting two neuronal networks. Therefore, nodes are here single-neurons and edges their axons (not modeled explicitly but time delays are being considered). Probably most functional relations between brain areas arise from their structural links, specially when considering time scales at which the anatomical connectivity remains constant. However, some dynamical properties appearing from a single network might not be structure-dependent and connectivity would not need to be imposed beforehand. For instance, the frequency content of an electrical signal coming out from the synaptic activity of neighboring neurons as measured by the LFP is very similar between a random network (Figure 1.29, black) and a quasi-regular network (Figure 1.29, gray).

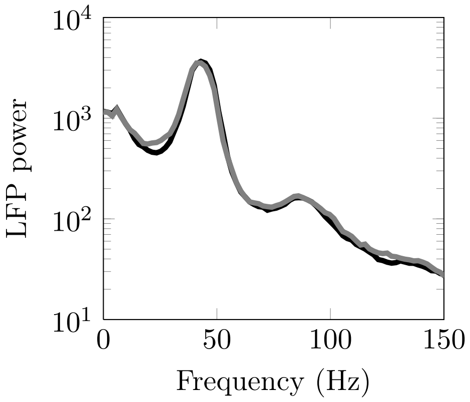

Figure 1.29: LFP power spectrum of a simulated LFP from a random (black) and quasi regular (gray) network of 2000 neurons averaged over 20 trials. Details of the model from which these simulations were obtained can be found in Appendix A.2.

We started our research with the aim of understanding the role of neuronal oscillations in communication between brain areas. We had an image in mind: the motion of undulating waves with spikes traveling through it; and many questions: how do these oscillations emerge, and how are they influenced by the neuronal discharges? The action potentials of a population of excitatory and inhibitory neurons generate an electrical oscillatory signal. Are these oscillations a mere representation of the collective dynamics or do they convey extra information? It turns out that this continuous oscillatory activity is expressing the level of excitability of a cell assembly. Each neuron spikes with higher probability at certain time windows. Both its firing rate and time of spiking depend on the phase of the neuronal oscillations. Although subthreshold neuronal oscillations are not synaptically transmitted, they shape local suprathreshold activity, and they also determine the synaptic effect of incoming inputs. We have studied the interactions between action potentials and both membrane voltage oscillations (Chapter 2) and neuronal oscillations of the synaptic current (Chapter 3). Excitatory events impinging on a cell assembly are also filtered by the ongoing local fluctuations. Intrinsic electrophysiological features and the input dynamics contribute to the frequency content of the neuronal oscillations.

How do the emergent neuronal oscillations regulate the coupling between distinct populations? The frequency and amplitude of the neuronal oscillations also reveal the strength of the population firing rate. A bidirectional coupling between cell assemblies, anatomically symmetric, can be effectively asymmetric, due to a frequency difference. How similar two neuronal pools need to be in order to achieve communication? Depending on the frequency detuning between two subthreshold oscillatory signals, a zero-lag synchronization or a leader-laggard configuration is obtained (Chapter 4). A consistent phase lag is achieved across different realizations of the same coupling scenario. This phase coherence is mediated by the interactions of the two populations and is subserved by the frequency detuning. If a particular perturbation drives a subset of neurons of the *emitter network* towards into spike-to-spike synchrony, the rhythmicity of the neuronal oscillations is enhanced and transmitted to the *receiver network*. The success in communication can be observed in the transient amplification of the neuronal oscillations of the second network, entrained to the emitter rhythm. Close enough to the frequency locking regime, the recurrent excitability windows of both populations are suitably locked and match the time delay. Thus, information transmission between neuronal networks also relies on the neuronal oscillations evoked by the spontaneous spiking activity.

Moreover, the sensitivity of neuronal oscillations to noise amplitude gives rise to non-linear phenomena such as coherence resonance (Chapter 5). The regularity of the slow-oscillations characteristic of deep sleep is tuned according to the firing activity level. These results show, once more, that the interplay between spiking activity and neuronal oscillations gives rise to new network properties.

In summary, the work presented in this Thesis intends to shed light on the role of neuronal oscillations in providing coding strategies of local spiking activity, in translating features of the external input into dynamic features of the neuronal network, and in assisting effective interactions of distinct brain areas.

CHAPTER 2

Action potential propagation in the presence of membrane subthreshold oscillations

---

Contents

2.1 Membrane subthreshold oscillations

Subthreshold oscillations are electrical signals recorded by an electrode in contact with a neural tissue, whose power spectrum is far from flat and whose mean value is below the firing threshold of the constituting cells. These signals are ubiquitous in the brain and usually come from the coordinated activity of many neurons, as mentioned in Section 1.6, but a precise relation with the individual neuronal membrane potentials or synaptic currents is still unknown. A simple mechanism for the generation of these rhythms would be the existence of a *central pattern generator* oscillating autonomously and entraining the rest of the population. However there is no experimental evidence of this kind of structure in the neocortex (this type of circuit is found, nevertheless, in the spinal cord and is related to motor behavior [Yuste 2005]).

Voltage oscillations have also been reported in the membrane of single neurons in the mammalian central nervous system [Alonso 1989, Lampl 1993] contributing to the emergence of brain rhythms. In this Chapter we will focus on these individual oscillations (Figure 2.1) whose origin is clearer than that of network oscillations. The main feature of these type of neurons is their resonant behavior, arising from the dynamics of various ionic channels, which makes the neuron's membrane voltage to oscillate above a certain injection current or when interacting with the rest of the network. This type of neuron help strengthen the oscillatory patterns of the neuronal population in which they are embedded.

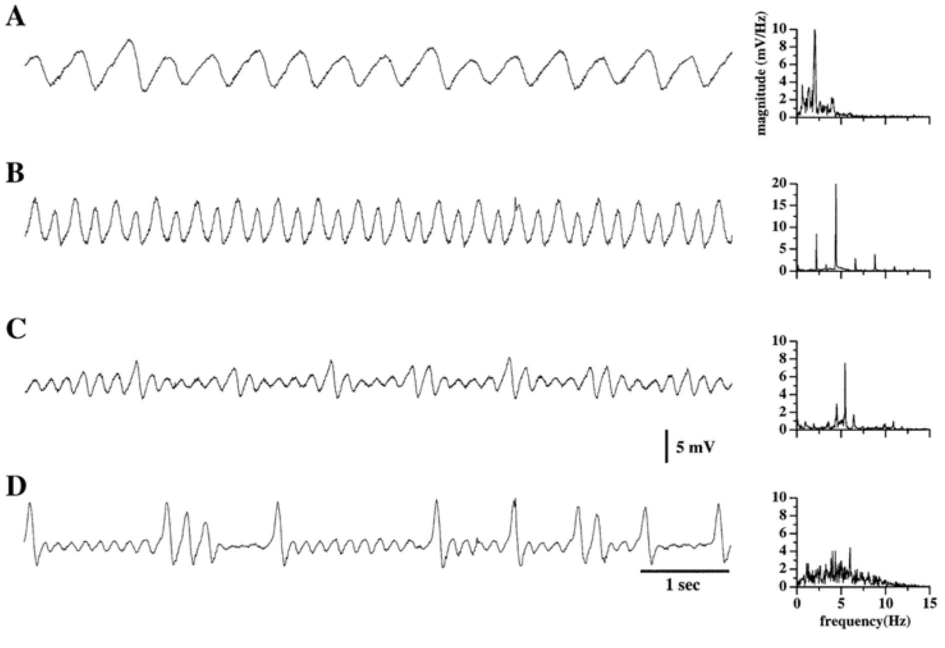

Figure 2.1: Left: Four intracellular recordings from four different slices of the inferior olivary nucleus. Right: Corresponding power spectra. From [Lampl 1997].

Resonances appear when the neuron combines low-pass and high-pass filter mechanisms. The result is a band-pass filter that attenuates frequencies outside a certain range [Hutcheon 2000]. Such neurons respond to a continuously-varying sine wave current (ZAP), with membrane oscillations that have largest amplitudes when the input frequency is within a certain band (determined by the low-pass and high-pass filter features). The passive properties of the neurons, i.e. those which are independent of the membrane voltage, such as its capacitance and leak conductance, are responsible for the low-pass filer. The high-pass filter is obtained by slowly activating ionic channels whose reversal potential is close to the minimum voltage required for their activation [Figure 2.2(a)] which therefore always tend to oppose membrane voltage changes with time scales longer than the membrane time constant. Other ionic channels amplify the resonance by having their reversal potential at high values of their activation curve [Figure 2.2(b)]. In this last case, the activated channels tend to rapidly enhance membrane voltage changes.

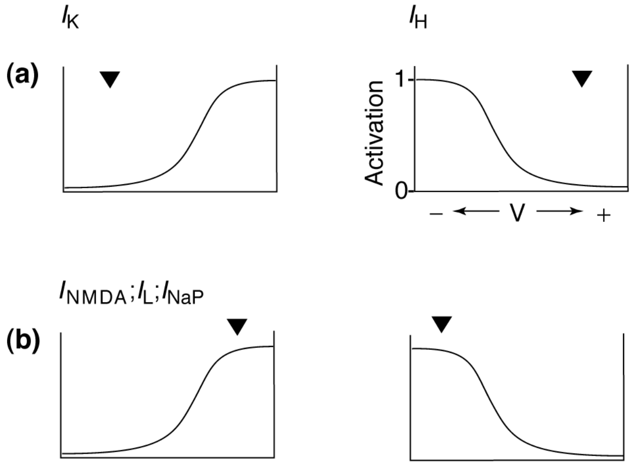

Figure 2.2: Schematic activation curves of different channels involved in the resonant behavior of neurons. The reversal potential is labeled with an arrowhead. The reversal potential is located at the beginning (a) or ending (b) of their activation curve by depolarization (left) or by hyperpolarization (right). From [Hutcheon 2000].

Neurons having these types of ionic channels are provided with frequency-specific responses even when the neurons do not display spontaneous subthreshold oscillations. Thus, inputs with a strong frequency component at the resonant frequency of the cell will trigger larger responses. For instance, firing-rate resonances have been found in the presence of an oscillating applied current [Richardson 2003, Brunel 2003a]. This oscillatory driving causes a periodic modulation of the firing rate, whose amplitude is maximal (for high enough background noise) when the driving frequency matches that of the subthreshold oscillation.

The excitability of these neurons is intrinsically modulated because the oscillations of the membrane potential lead to periodic changes of the distance to the spiking threshold. Therefore, the synaptic afferent currents are more effective at the peaks of the oscillation, where the distance to threshold is minimal. This rhythmic activity of the membrane potential allows to control the precise timing of action potentials. Subthreshold oscillations have been shown to shape spike-train patterns in cortical neurons by leading to spike clusters, thus influencing qualitatively the distribution of interspike intervals [Verechtchaguina 2004, Verechtchaguina 2007], and inducing correlations between them [Engel 2008]. The interaction between these oscillations and the synaptic input helps to synchronize the firing of a population of neurons by perturbing their phase nonlinearly.

Spikes in the membrane potential of neurons are considered to be the basic carriers of information in the nervous system [Rabinovich 2006]. In contrast, subthreshold activity, takes the form of fairly coherent oscillations that do not elicit neurotransmitter release, which are therefore not transmitted synaptically to neighboring neurons. In order to assign a functional role to subthreshold oscillations, their effect on the spike firing patterns have to be established. In this Chapter we will examine this question, in particular how a neuronal chain of neurons displaying membrane potential oscillations interacts with a propagating train of spikes.

2.2 Modeling single-neuron subthreshold oscillations: a modified FitzHugh-Nagumo model

We have used here a modified FitzHugh-Nagumo model reported by [Makarov 2001] displaying subthreshold oscillations of the membrane potential for particular values of the parameters (see Appendix A.1.1). The model is as follows:

$$\varepsilon\frac{\mathrm{d}u}{\mathrm{d}t} = u(u-a)(1-u)-v \tag{2.1}$$

$$\frac{\mathrm{d}v}{\mathrm{d}t} = g(u-b) \tag{2.2}$$

where ε is the ratio between the characteristic times of u and v. We consider that this parameter is much smaller than 1, so that the system relaxes rapidly to the u-nullcline. The function g is defined as:

$$g(u-b) = k_1(u-b)^2 + k_2\left(1-\exp\left[-\frac{u-b}{k_2}\right]\right) \tag{2.3}$$

In comparison with Equation (1.12), g does not depend on the slow variable v. The duration of the spikes can be tuned by the parameters k_1 and k_2, because k_1 and k_2 control the value of $\frac{\mathrm{d}v}{\mathrm{d}t}$ and, consequently, the time spent by the trajectory $\frac{\mathrm{d}u}{\mathrm{d}t} = 0$. The spikes in this model can be faster than in the standard model (see Section 1.3.2.2) and they do not interfere with the period of the membrane subthreshold oscillations. Note that the v-nullcline is just the straight line $u = b$, so that the equilibrium point is given by $u_o = b$ and $v_o = b(b - a)(1 - b)$.

2.2.1 Stability analysis of the modified FitzHugh-Nagumo model

In order to determine the stability of the fixed point as a function of the parameters we perform a local linear analysis of the system of Equations (2.1)-(2.2):

$$\frac{\mathrm{d}}{\mathrm{d}t}\begin{pmatrix} \bar{u} \\ \bar{v} \end{pmatrix} = \begin{pmatrix} \frac{1}{\varepsilon}\partial F/\partial u & \frac{1}{\varepsilon}\partial F/\partial v \\ \\ \partial G/\partial u & \partial G/\partial v \end{pmatrix}_{(u_o,v_o)} \begin{pmatrix} \bar{u} \\ \bar{v} \end{pmatrix} \tag{2.4}$$

where $F = u(u - a)(1 - u) - v$ and $G = g(u - b)$. $\bar{u} = u - u_o$ and $\bar{v} = v - v_o$ are the deviations from the equilibrium point. The matrix of the first-order partial derivatives is the Jacobian matrix of the system. The eigenvalues and the eigenvectors of this matrix, J,

$$J\vec{w} = \lambda\vec{w} \tag{2.5}$$

help us to write a general solution for the linear system in the form

$$\begin{pmatrix} \bar{u}(t) \\ \bar{v}(t) \end{pmatrix} = c_1 e^{\lambda_1 t}\vec{w_1} + c_2 e^{\lambda_2 t}\vec{w_2} \tag{2.6}$$

where λ_1 and λ_2 are the eigenvalues of the eigenvectors $\vec{w_1}$ and $\vec{w_2}$ and can be rewritten as:

$$\lambda_{1,2} = \frac{\tau \pm \sqrt{\tau^2 - 4\Delta}}{2} \tag{2.7}$$

where τ and Δ are the trace and the determinant of the Jacobian matrix, respectively. c_1 and c_2 are integration constants.

The sign of the eigenvalues depends on the values of τ and Δ, and determine the way the trajectories behave around the fixed point according to Equation (2.6). If both eigenvalues have negative real part the trajectory in the phase plane responds to a brief perturbation from the fixed stable point approaching it asymptotically and spiraling into it (if the two eigenvalues are complex) or sinking into it (if the eigenvalues are pure real). If the strength of the perturbation is larger than a certain threshold, both u and v undergo a large increase before returning to the fixed point. This trajectory represents an action potential and makes the system excitable. If at least one eigenvalue has positive real part, small perturbations are amplified and the system escapes the fixed point (unstable). Thus the necessary and sufficient condition for stability is $\Delta \geq 0$ and $\tau < 0$. This allows us to classify the equilibrium points besides their stability: if the eigenvalues are of the same sign we talk about *nodes*, if they have opposite signs they are called *saddles*, and if they are complex they are *foci*.

For the system of Equations (2.1)-(2.2), the determinant and the trace of the Jacobian matrix at the fixed point are:

$$\Delta = 1/\varepsilon, \tag{2.8}$$

$$\tau = \frac{1}{\varepsilon}(-b^3 + (1-a)\,b^2 - ab) \tag{2.9}$$

The choice of the parameters ε, a and b depends on the desired dynamical regime. We set $\varepsilon = 0.005$ and $a = 0.9$, as in [Makarov 2001], and vary b. Notice that Equation (2.2) does not depend on v (i.e. $\partial G/\partial v = 0$), therefore the trace τ of the Jacobian matrix in Equation (2.4) is just $\frac{1}{\varepsilon}\frac{\partial F}{\partial u}|_{(u_\mathrm{o},v_\mathrm{o})} = \frac{\partial \dot{u}}{\partial u}|_{(u_\mathrm{o},v_\mathrm{o})}$. If the parameter b is chosen to be equal to the value of u at the absolute minimum of the u-nullcline (remember that the u coordinate of the equilibrium point is $u_\mathrm{o} = b$), then $\tau = \frac{\partial \dot{u}}{\partial u}|_{(b,v_\mathrm{o}(b))} = 0$, which means that the eigenvalues have no real part. When the resting state undergoes a transition from stable (eigenvalues with negative real parts) to unstable (eigenvalues with positive real parts) focus giving rise to a small-amplitude limit cycle attractor, we talk about a supercritical Andronov-Hopf bifurcation. We then lose stability of the fixed point but gain stable oscillations. Near the supercritical Andronov-Hopf bifurcation the model generates –via a canard explosion[†] (see Figure 2.3)– low amplitude quasi-harmonic oscillations remaining excitable. In this case we have $b = \frac{1+a-\sqrt{1-a+a^2}}{3} = 0.315$, and by setting $b = 0.316$ we get $\tau > 0$. Now the real part of the eigenvalues is positive and a low amplitude stable limit cycle (a subthreshold oscillation) appears.

2.2.2 Time scale of subthreshold oscillations

The function $g(u-b)$ in Equation (2.2) controls the duration of spikes. In order to choose values for k_1 and k_2 we derive an approximate expression for the excitation, T_exc, and refractory, T_ref, intervals, looking at the slow motion equation of the u-nullcline $v = u(u-a)(1-u)$. We define the excitation interval

---

[†] Fast transition, due to a small parameter change, from a small amplitude limit cycle to a relaxation oscillation [Brøns 1991].

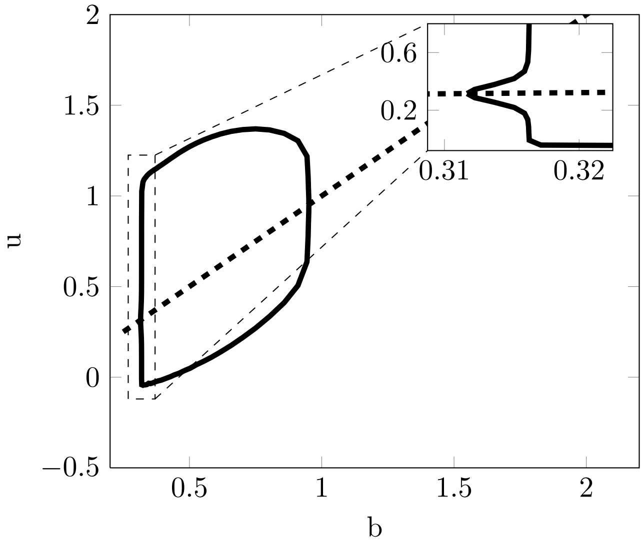

Figure 2.3: Bifurcation diagram of the fast variable u with respect to the parameter b, obtained with XPPAUT. The plot shows the appearance of a stable limit cycle with increasing b. The inset is a zoom of the small region around the bifurcation point, $b = 0.315$, showing the canard transition from the relaxation oscillator to the stable oscillator of small amplitude (subthreshold oscillations).

as the time spent going from point A to point B represented in Figure 2.4:

$$\int_{v_\mathrm{A}}^{v_\mathrm{B}} \mathrm{d}v = \int_0^{T_\mathrm{exc}} \frac{\mathrm{d}v}{\mathrm{d}t}\mathrm{d}t = v_\mathrm{A} - v_\mathrm{B} \tag{2.10}$$

where v_A and v_B are the ordinate values of the absolute minimum and maximum of the u-nullcline (for $\frac{\mathrm{d}v(u)}{\mathrm{d}u} = 0$), respectively. This equation can be solved by integrating Equation (2.2) between v_A and v_B, using as a first approximation $u(t) \approx 1$ [Makarov 2001]:

$$\int_0^{T_\mathrm{exc}} \frac{\mathrm{d}v}{\mathrm{d}t}\mathrm{d}t = \int_0^{T_\mathrm{exc}} g(u-b)\,\mathrm{d}t \simeq g(1-b)\cdot T_\mathrm{exc} \tag{2.11}$$

Solving $\frac{\mathrm{d}v(u)}{\mathrm{d}u} = -3u^2 + 2(1+a)u - a = 0$ to obtain the abscissas of the absolute minimum and maximum of the u-nullcline (i.e. u_A and u_B) and substituting again in the $v(u)$ equation, we obtain:

$$v_\mathrm{A} = v\left(\frac{1}{3}\left[(1+a) - \left(1-a+a^2\right)^{1/2}\right]\right), \tag{2.12}$$

$$v_\mathrm{B} = v\left(\frac{1}{3}\left[(1+a) + \left(1-a+a^2\right)^{1/2}\right]\right) \tag{2.13}$$

Since $v_{\mathrm{A}} - v_{\mathrm{B}} = g(1-b) \cdot T_{\mathrm{exc}}$:

$$\mathrm{T}_{\mathrm{exc}} = \frac{4\,(1-a+a^2)^{3/2}}{27g\,(1-b)}, \tag{2.14}$$

$$\mathrm{T}_{\mathrm{ref}} = -\frac{4\,(1-a+a^2)^{3/2}}{27g\,(-b)} \tag{2.15}$$

For the calculation of the refractory interval shown above, we have followed the same steps between point C and point D using $u(t) \approx 0$. The duration of a spike will be $\mathrm{T}_{\mathrm{exc}}$+$\mathrm{T}_{\mathrm{ref}}$, which depends on the parameters k_1 and k_2.

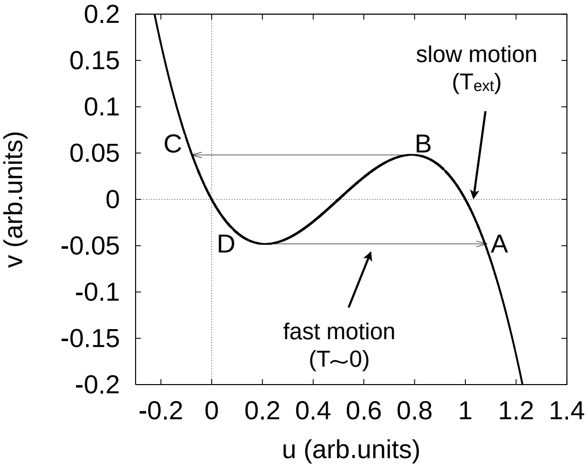

Figure 2.4: u-nullcline with a simplified phase plane trajectory representing a spike.

An expression for the period of the subthreshold oscillations can also be obtained solving the linear system [Equation (2.4)] at the Andronov-Hopf bifurcation (i.e. $b = 0.315$ for $a = 0.9$ and $\varepsilon = 0.005$, $\tau = 0$ and $\Delta = 1/\varepsilon$):

$$\frac{d}{dt}\begin{pmatrix} \bar{u} \\ \bar{v} \end{pmatrix} = \begin{pmatrix} 0 & -1/\varepsilon \\ 1 & 0 \end{pmatrix}\begin{pmatrix} \bar{u} \\ \bar{v} \end{pmatrix} \tag{2.16}$$

The eigenvalues of the Jacobian matrix are $\lambda_{1,2} = \pm i\sqrt{\Delta}$, and therefore the solution of the system, $\bar{u}(t)$ and $\bar{v}(t)$, is an harmonic oscillator with $\omega = \sqrt{\Delta} = 1/\sqrt{\varepsilon}$ and period $\mathrm{T}_{\mathrm{sth}} \approx 2\pi\sqrt{\varepsilon} \approx 0.44$.

In what follows we choose $k_1 = 7.0$ and $k_2 = 0.08$ as in [Makarov 2001]. The excitation and refractory period are then $\mathrm{T}_{\mathrm{exc}} \approx \mathrm{T}_{\mathrm{ref}} \approx 0.044$, what makes the duration of a spike shorter than the period of subthreshold oscillations, $\mathrm{T}_{\mathrm{sth}}$ (see right plot of Figure 2.5).

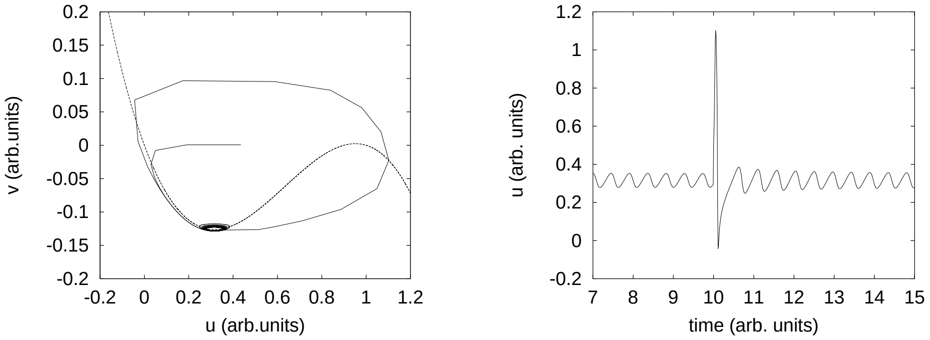

Figure 2.5: Left: Phase portrait for a FitzHugh-Nagumo neuron of Equations 2.1-2.2. Right: Membrane potential time course.

2.3 Spiking response in the presence of subthreshold oscillations

For the parameters given in the previous Sections, the neuron operates in an excitable regime whose basal state is a limit cycle, corresponding to the subthreshold oscillations (see left plot of Figure 2.5). Its excitable character implies that a large enough perturbation of the limit cycle leads to a pulsed response, which corresponds to an action potential. In contrast with neurons with a steady rest state, the response to perturbations of neurons with subthreshold oscillations is not equal at all times, but depends on the phase of the oscillation at which the perturbation is received [Volgushev 1998, Desmaisons 1999].

We have studied the response of the FitzHugh-Nagumo neuron described in Section 2.2 to incoming spikes that activate a synapse, allowing the flow of an inward current [Sancristóbal 2010a]. The synaptic current entering the neuron is given by Equations (1.13)-(1.14). The synaptic conductance g_{syn} determines the strength of the synapse; here we take $g_{\text{syn}} = 0.1$. The amplitude is chosen such that the neuron fires in response to the current pulses only for a specific range of phases of its subthreshold period. The synapse potential E_{syn} defines the type of synapse; here we consider $E_{\text{syn}} = 0.7$, which makes the connection excitatory. $\alpha = 44$ and $\beta = 22$ are set in order to keep the rise and decay times of $\sigma(\text{t})$ (i..e the fraction of open membrane receptors) smaller than the period of the subthreshold oscillations. The concentration of neurotransmitters *T(t)* released into the synaptic cleft is considered to behave as a pulse as described in Equations (1.16)-(1.19). Therefore, during a time $\tau_{\text{syn}} = 0.006$ after the arrival of a pre-synaptic spike at time t_{o}, *T(t)* remains constant and equal to $T_{\max} = 1$. Hence $T(t) = T_{\max}\theta(t_{\text{o}} + \tau_{\text{syn}} - t)\theta(t - t_{\text{o}})$.

Figure 2.6 shows the effect of two synaptic pulses arriving at two different time instants. Two distinct responses arise, depending on the phase of the subthreshold oscillation at the arrival of the perturbation.

The figure shows that depending on the phase of the subthreshold oscillations at the time the perturbation arrives, a spike is triggered (blue solid line in the figure) or not (red dashed line). We can understand this dual behavior as follows. As the fraction of active receptors $\sigma(\mathrm{t})$ increases upon the arrival of the synaptic pulse, the u-nullcline [defined by $\dot{u} = 0$, thin black line with cubic shape in Figure 2.6(b)] moves upwards and towards increasing u in such a way that it now intersects the v-nullcline [defined by $\dot{v} = 0$, thin vertical black line in Figure 2.6(b)] at the stable branch of the u-nullcline, and the unstable fixed point stabilizes temporarily. If this happens when the system lies along the part of the limit cycle represented by a thick empty line in Figure 2.6(c), the perturbation will quickly relax back to the oscillatory attractor. On the other hand, if at the time at which the perturbation arrives the neuron is in the part of the limit cycle represented by a thick solid line in Figure 2.6(c), the trajectory finds itself temporarily beyond the excitation threshold, and a spike is triggered before the u-nullcline returns to its original location.

If the subthreshold oscillation is intrinsic to the neuron, rather than entrained by a periodic forcing, its phase will be affected by the incoming spikes, thus conditioning the future response of the neuron to subsequent perturbations. This can be observed in Figure 2.6(a) in the different time voltage courses after perturbing the neuron at distinct phases. In order to quantify this phase-dependent behavior, we define the phase of the subthreshold oscillations by rescaling the state variables as follows:

$$\tilde{u} = 2\frac{u - u_{\mathrm{min}}}{u_{\mathrm{max}} - u_{\mathrm{min}}} - 1 \tag{2.17}$$

$$\tilde{v} = 2\frac{v - v_{\mathrm{min}}}{v_{\mathrm{max}} - v_{\mathrm{min}}} - 1 \tag{2.18}$$

where the subindices ‘max’ and ‘min’ stand for the maximum and minimum values of the voltage and recovery variables within a period of the subthreshold oscillations. In the $(\tilde{u}, \tilde{v})$ plane, an isolated neuron describes a circle of radius 1 centered at the origin. We will represent this trajectory by means of a single phase variable, $\phi = \arctan(\tilde{v}/\tilde{u})$. The origin of the phase variable occurs when $\tilde{v} = 0$, corresponding to half the amplitude of the v-interval covered by the limit cycle according to Equation (2.18) [see horizontal dashed line in Figure 2.6(c)]. Note that this definition of phase can only be applied when the neuron has had enough time to relax to the limit cycle after a perturbation.

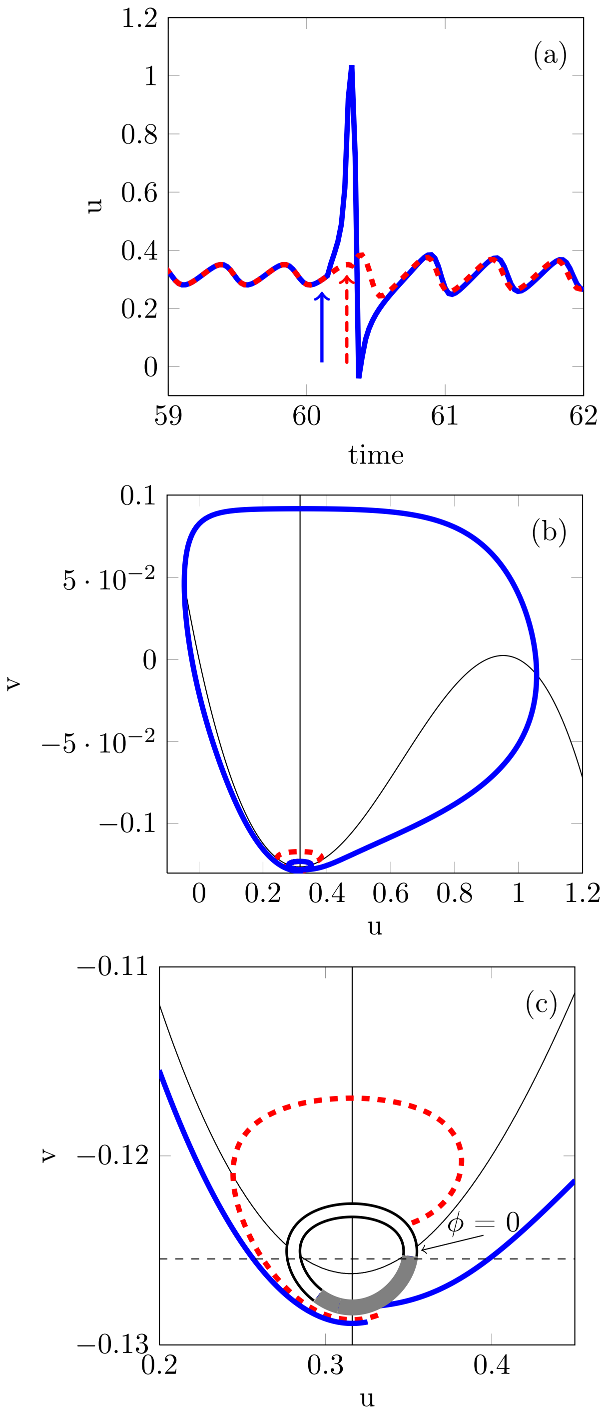

Figure 2.6: Response of a neuron with subthreshold oscillations to input synaptic spikes. (a) Time series of the voltage variable of the response neuron for input spikes arriving from the driving neuron at two different times. (b) Phase portrait of the two trajectories shown in plot (a). The black lines depict the nullclines of Equations (2.1)-(2.2). (c) Zoomed area around the limit cycle shown in plot (b), indicating the phase origin chosen (horizontal dashed line crossing the limit cycle) and the region where a spike is elicited (thick solid line on the limit cycle) or not (thick empty line on the limit cycle).

We can plot now the amplitude of the voltage response, i.e. the post-synaptic potential (PSP), resulting from the perturbation [see Figure 2.6(a)] as a function of the phase of the subthreshold oscillation at the instant at which the perturbation starts to act upon the neuron. The result is shown in Figure 2.7(a), and reveals a range of input phases (termed *non-spike-triggering phases* in what follows, white region in the horizontal bar above the plot) for which the perturbation is not able to produce a spike (red dashed line in Figure 2.6), while spikes are generated (blue solid line in Figure 2.6) for other phases (called *spike-triggering phases* below, grey region in the horizontal bar above the plot). Note that the transition between these two regions is sharp. For slower synapses [dashed and dot-dashed lines in Figure 2.7(a,b)] the range of spike-triggering phases increases because the trajectory leaves the stable limit cycle for a longer time. The neuron then has more time to reach the excitation threshold before relaxing to the limit cycle again.

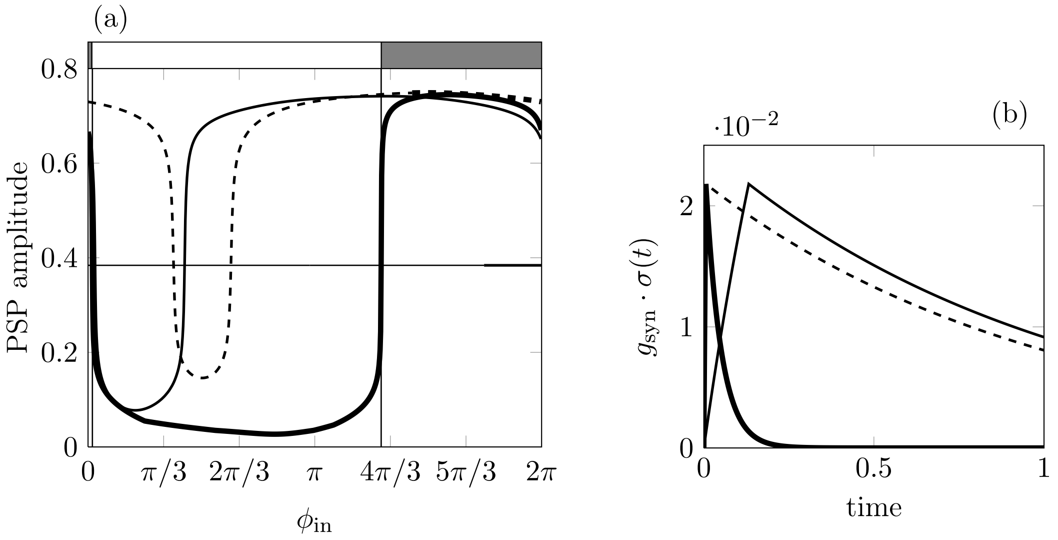

Figure 2.7: (a) Phase dependence of the neuronal response. Amplitude of the post-synaptic potential resulting from the input spike arriving at different phases ϕ_{in} of the subthreshold oscillation. (b) Synaptic time course upon activation at time zero. The solid thick line corresponds to the baseline parameter values used given in this Section ($\alpha = 44$ and $\beta = 22$). The dashed and solid thin lines represent situations in which the synapse is slower (one parameter change in each case, $\alpha = 2$ and $\beta = 1$, respectively). The rest of synapse parameters are tuned such that the peak of the synaptic pulse, $g_{\text{syn}}\sigma_{\max}$, is kept constant either due to a larger value of $g_{\text{syn}} = 1.833$ (dashed line) or of $\tau_{\text{syn}} = 0.011$ (thin solid line). The horizontal bar above plot (a) represents, for the baseline parameters (solid black line) regions of spike-triggering phases (see text) in dark grey, while non-spike-triggering phases are represented in white; this notation is the one used in the upcoming figures. Note that the transition between the spike-triggering and non-spike-triggering phases depends on the dynamics of the synapse, σ(t). Slower synapses are less phase-specific.

The above-described selective response to a single presynaptic spike with respect to its arrival phase suggests that the neuron should also respond selectively with respect to the period of an input spike train. Do subthreshold oscillations allow a neuron to select which incoming trains of spikes it reacts to on the basis of their firing rate? In order to address this question we have measured the response of the FitzHugh-Nagumo model neuron to a periodic synaptic pulse train considering different frequencies [Sancristóbal 2010a]. We have computed the percentage of those perturbations that elicit a spike in the neuron, which we term *success rate*. Figure 2.8 shows the dependence of the success rate on the period of the input spike train, and reveals a non-monotonic dependence of the spiking efficiency of the neuron on the timing at which it receives the stimulus.

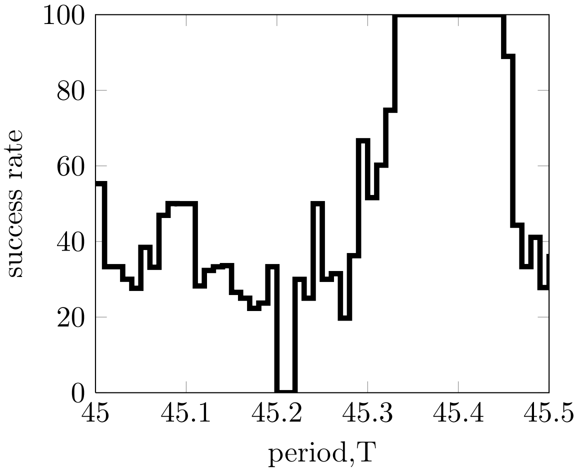

Figure 2.8: Success rate versus period of the input spike train. The success rate is measured as the percentage of successful spike transmission events calculated over 1000 external pulses, removing an initial transient time of ∼ 1400 units of time. An average success rate is calculated over 10 different realizations, changing the initial conditions of u and v randomly in a region bounded by the limit cycle.

A success rate smaller than 100% corresponds to an average interspike interval of the output that is greater than the input period, and shows that the neuron acts as a filter to some external periods. This filtering behavior is reminiscent of the one exhibited by the membrane potential of these neurons with respect to the frequency of a sinusoidal modulation of the applied current, [Puil 1994, Gutfreund 1995, Hutcheon 1996, Pike 2000, Hutcheon 2000]. Here, however, we are examining the spiking response of the neuron instead of the modulation of the membrane potential, and the driving signal is a spike train, instead of a harmonic modulation of the applied current.

The response profile shown in Figure 2.8 indicates that for most periods of the spike train there is at least a partial response of the neuron, in spite of the broad range of non-spike-triggering phases exhibited by the system in the case of an isolated perturbation.

2.3.1 Phase transition curve (PTC)

Given the mutual influence between spikes and subthreshold oscillations described above, success in the response of a neuron to a periodic spike train requires that (i) each pulse in the train elicits a spike, and (ii) this spike resets the phase of the oscillation in such a way that the following pulse will encounter the neuron at the 'right' phase again. In order to understand this phase resetting, we quantify the phase response of the neuron in terms of a phase transition curve (PTC) [Glass 1988, Winfree 2001] in which the phase a time T after the perturbation (T being the period of the input spike train), $\phi_{\mathrm{out,T}}$, is plotted versus the phase at the perturbation time instant, ϕ_{in}. PTCs allows us to establish an iterative map describing the evolution of the phase in response to successive pulses in the train. From the analysis of the steady-state behavior of this map we can establish the response of the neuron to the input spike train: for certain ranges of periods the phase quickly reaches a steady state in which perturbations always lead to spikes; for others the phase reaches values (stationary or part of a dynamical attractor) in which spikes are not triggered. In that way, the phase-response map provides a framework that helps us understand the resonance profile arising from subthreshold oscillations.

Phase-response curves have been previously used to study the response of both oscillatory [Hansel 1995, Galán 2005, Gutkin 2005] and excitable [Rabinovitch 1994] neurons to time-varying stimuli. Here we show that in neurons with subthreshold oscillations, due to the distinct response depending on the value of the phase at the time of the perturbation, the corresponding phase-response curve has a non-standard discontinuity that leads to complex phase dynamics. A similar discontinuity has been studied in neurons without subthreshold oscillations [Coombes 2000]. In our case, the different dynamical regimes of the phase response can be associated with different types of response of the neuron to the input spike train, constituting a dynamical scaffold that underlies the resonant behavior of the system.

The PTC of this FitzHugh-Nagumo neuron is constructed as follows: starting from the neuron operating in the stable limit cycle, we run simulations for each value of ϕ_{in}, until T units of time after the perturbation. Varying the instant of the perturbation over a subthreshold period, we cover a full cycle of input phases ϕ_{in}. From these simulations we obtain the maximum membrane voltage (PSP amplitude of Figure 2.7), and also the values of u and v a time T after activating the synapse. Provided T is large enough to allow the neuron to relax to the limit cycle between consecutive spikes, we can compute $\phi_{\text{out,T}}$ from Equations (2.17)-(2.18), and interpret it as a phase on the limit cycle. This leads to the PTC shown in Figure 2.9(a).

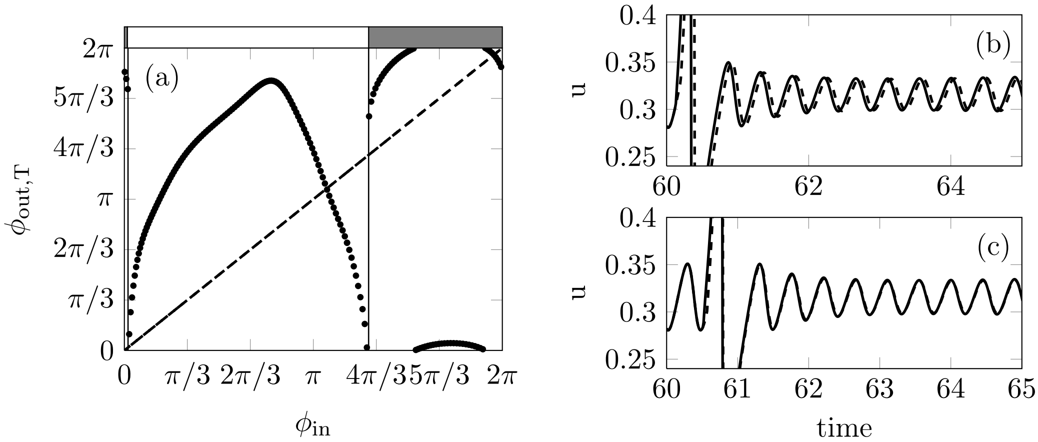

Figure 2.9: (a) Phase transition curve (PTC) showing the response phase $\phi_{\text{out,T}}$ a time T after the spike is received, versus the phase ϕ_{in} of the subthreshold oscillation at that instant. The vertical lines mark the boundary between the spike-triggering (shaded area) and non-spike-triggering regions. The dashed diagonal line corresponds to the situation $\phi_{\text{in}} = \phi_{\text{out}}$. In this case $T = 45$. The right column shows the time evolution of the voltage variable for two input phases for the cases of phase insensitivity –just above $5\pi/3$– (b) and phase resetting –just above $4\pi/3$– (c).

The results of Figure 2.7 allow us to identify the ranges of input phase values for which the perturbation elicits an action potential (spike-triggering input phases, see solid blue line in Figure 2.6) and those for which the perturbation quickly relaxes back to the limit cycle without triggering a pulse (non-spike-triggering input phases, see red dashed line in Figure 2.6). These phase intervals are represented by gray and white horizonal bars, respectively, above Figure 2.9(a). This figure shows that the response phase depends strongly on whether or not the perturbation triggers a spike. In particular, the PTC exhibits a discontinuity where this behavioral change occurs. We note that the range of spike-triggering phases (and thus the shape of the PTC) depends on the intensity of the perturbation, which is given by the strength of the chemical synapse, g_{syn}. For large enough g_{syn} (not the case considered here) the firing is no longer modulated by the subthreshold oscillations.

The slope of the PTC shown in Figure 2.9(a) indicates the level of phase sensitivity to variations in the input phase. In particular, the non-spike-triggering region exhibits areas of hypersensitivity (for ϕ_{in} slightly larger than zero and around π) for which a small variation in the input phase leads to a large change in the output phase. In the spike-triggering region, on the other hand, we can distinguish a horizontal segment around $5\pi/3$ corresponding to a situation of *phase insensitivity*, in which the output phase practically does not change in response of variations in the input phase. This situation is depicted in Figure 2.9(b), which shows the time evolution of the voltage variable in response to two input spikes slightly separated in time: at any instant after reaching the stationary limit cycle, the phase difference of this two traces is similar to the input phase difference. Around $4\pi/3$ the PTC is nearly parallel to the diagonal, corresponding to *phase resetting*: at any instant after reaching the stationary limit cycle, the phases of these two traces are equal regardless of the input phase difference [see Figure 2.9(c)]. Phase resetting is also observed in the non-spike-triggering region, in the area around $\pi/3 \lesssim \phi_{\text{in}} \lesssim 2\pi/3$.

2.3.2 Iterative maps and phase response to a spike train

Once we have obtained the phase transition curve for a given time T, we can easily determine the phase dynamics in response to a spike train of period T, by constructing the associated iterated map according to $\phi^i_{\text{out}} = \phi^{i+1}_{\text{in}}$ at every iteration i. The rationale behind this procedure is that iterations of the map would lead to the values of the subsequent phases that the response neuron exhibits at each time a new spike arrives. In that way, if the iterated map has a stable fixed point (given by an intersection point between the PTC and the diagonal at which the absolute value of the derivative of the PTC is smaller than one) that is globally attracting, this means that the neuron eventually reaches a constant value of the phase at every time a spike arrives, irrespective of the initial phase. An instance of this situation is shown in Figure 2.10(a), which depicts two trajectories starting from two different initial phases (squares) and ending in the same fixed phase (circle). In this particular case, the final phase is located at the spike-triggering region, and thus for the period T of that particular PTC, the neuron will exhibit a perfect 1:1 response to the input spike train. This leads to 100% success rate if the transients are ignored, as can be seen in Figure 2.10(e) for $T = 45.37$, which is the value used in plot (a). In this situation, the transitory starting spikes seem to prepare the phase of the neuron to the reach its stationary value. Since stable fixed points require the derivative of the PTC to be smaller than 1 in absolute value, they tend to occur around the flat areas of the PTC within the spike-triggering region described in Section 2.3.1, which correspond to situations of phase insensitivity. Therefore, phase insensitivity accounts for the successful propagation of the pulse train driving the response neuron. This result is in agreement with the experimental observation in [Lampl 1993] where subthreshold oscillations subserve the precise timing of information processing. When T varies, the PTC shifts vertically (with a slight distortion due to the nonlinear character of the subthreshold oscillation). Different T's

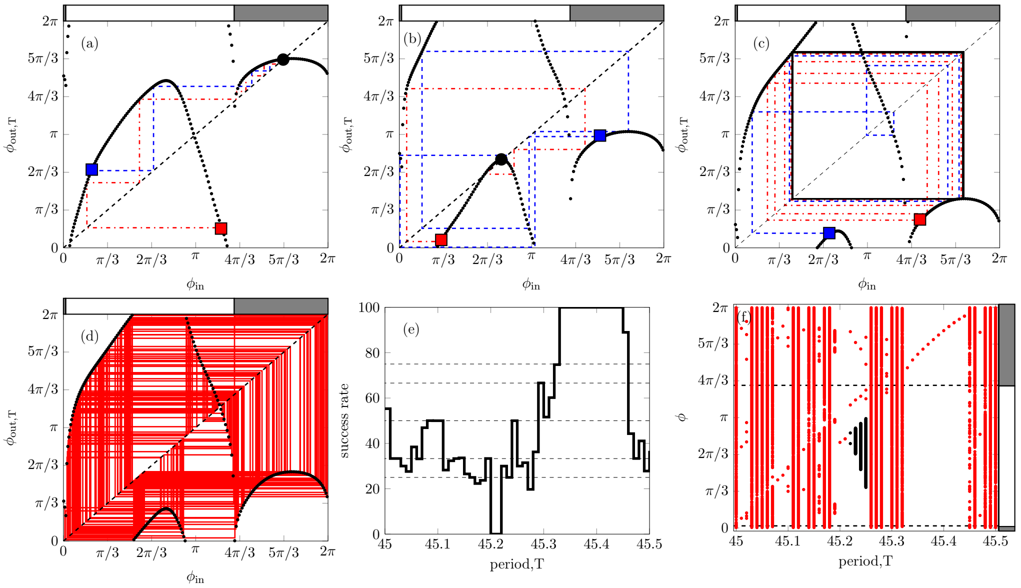

Figure 2.10: Iterated map and resonance response of the neuron. Plots (a-d) depict the phase transition curve (PTC) for four different values of T, for which the phase dynamics are qualitatively different. (a) $T = 45.37$ (single stable fixed point within the spike-triggering region). (b) $T = 45.20$ (single stable fixed point within the non-spike-triggering region). (c) $T = 45.08$ (period-2 limit cycle). (d) $T = 45.07$ (chaotic regime). (e) Success rate versus the period T of the spike train (from Figure 2.8). The horizontal dashed lines denote different $n : m$ responses. (f) Bifurcation diagram showing the phase attractors of the iterated map as a function of T. The dots (black online) are obtained when increasing T, and the circles (red online) when decreasing T. The dashed line separates the spike-triggering from the non-spike-triggering region as in Figure 2.9.

lead to different intersection points between the PTC and the diagonal, with distinct stability properties. Figure 2.10(b) shows the case of $T = 45.20$, for which the system has again a single stable fixed point, this time within the non-spike-triggering region. Therefore, for this particular value of T the iterated map predicts that the neuron will not respond (after a transient) to any of the input spikes, leading to a 0% success rate, as can be seen in Figure 2.10(e).

The iterative map thus predicts a filtering behavior of the spiking period of the neuron with respect to the period of the input pulse train, with values of T for which the neuron responds to all spikes in the train and other values of T for which it responds to none of the input spikes. But these are not the only possible behaviors of the system. When the map has no stable fixed points, it can exhibit a periodic behavior, such shown in Figure 2.10(c). In that case, the system oscillates between two phases, one in the spike-triggering region and the other in the non-spike-triggering one, leading to 1:2 response and subsequently to a 50% success rate [see Figure 2.10(e) for $T = 45.08$, which is the value used in plot (c)].

For other values of T the map exhibits higher periods, and even chaotic behavior, as shown in Figure 2.10(d) for $T = 45.07$. In that case the response of the neuron is not periodic (although it could be, depending on how the chaotic attractor is partitioned between the spike-triggering and non-spike-triggering regions). In those situations the success rate does not correspond to a $n : m$ response.

The behavior of the iterated map for varying T can be summarized in the bifurcation diagram plotted in Figure 2.10(f), which shows the phases of the subthreshold oscillations at the times at which a spike is received, for different periods of the spike train. The diagram shows regions of fixed-point, periodic, and chaotic behavior, which exhibit an exact correspondence with the success rate given in Figure 2.10(e), measured from simulations of the full model. As mentioned before, the extreme cases of 100% and 0% success rate correspond to stable fixed points. When all the fixed points are unstable we can observe either a periodic orbit or a chaotic orbit on the PTC map. The former case may entail 1:2 locking behavior (leading to 50% success rate), 1:3 locking (leading to 33% success rate), and even 2:3 locking (leading to 66% success rate). These well-defined locking regions are depicted in Figure 2.10(e) by horizontal dashed lines. Chaotic orbits show different success rates values without a defined spiking period. Similar phase-locking response patterns have been previously observed experimentally in excitable cardiac cells [Chialvo 1987], and studied theoretically in an excitable neuron model [Coombes 2000]. In some cases we obtain two distinct sets of stationary ϕ values for the same value of T [black dots and red circles in Figure 2.10(f)], depending on the direction of which T is being scanned. This fact reveals the existence of different coexistent attractors that are reached from different initial phases.

The response dynamics of a neuron with subthreshold oscillations to a train of input spikes is seen to be very rich, and the iterated map described above is able to characterize all dynamical regimes exhibited by the system. Our phase response approach shows that, at least for the model and parameters considered here, the range of input spike-train periods for which the neuron does not respond at all is very small. This lack of responsiveness arises when the stationary phase dynamics falls within the range of input phases for which spikes are not triggered, something that happens rarely, only when a single stable fixed point appears in the non-spike-triggering region [$T = 45.2$ in Figure 2.10(e,f)]. Most frequently the neuron exhibits a dynamical phase attractor that goes in and out of the spike-triggering zone, which leads to an increase (a multiple, if the phase attractor is periodic) of the spike train period. Perfect 1:1 response is obtained when the period T is such that the iterated map has a single stable fixed point in the spike-triggering region [Figure 2.10(a)]. The range of periods covered in the resonance plot shown in Figure 2.10(e) is approximately equal to the period of the subthreshold oscillations ($T_{\mathrm{sth}} \approx 0.44$ for the neuronal parameters considered here). The resonance profile shown in the plot will be repeated with that period, provided T is large enough for the neuron to have enough time to relax to the limit cycle between spikes, as mentioned above. The minimum period for which this happens is $T \approx 45$, which is the value considered here. For shorter periods the neuron never reaches the limit cycle after each perturbation and it is not possible to define a phase variable from the rescaled variables defined in Equations (2.17)-(2.18), as described above. In that case, the phase response approach presented above is no longer valid, and one must rely on pure numerical simulations to establish the phase response, which still exhibits a resonant behavior. These results are reported in [Sancristóbal 2010a].

2.4 Propagation of spikes through a neuronal chain

In a simple coupling scheme, we have studied how the single-neuron resonant behavior to a train of action potentials with a defined period affects propagation of this input, by using a chain of identical FitzHugh-Nagumo neurons with subthreshold oscillations. Such a situation might be expected to arise in the transmission of sensory or motor signals through cascades of neuronal populations (each of which is represented here by a single FitzHugh-Nagumo model [Ghosh 2008]) along the corresponding neuronal pathways. The existence of subthreshold oscillations in neurons involved in sensory processing and motor response, such as those found in the inferior olivary nuclei [Llinás 1986], olfactory bulb [Desmaisons 1999], and dorsal root ganglia [Amir 1999] makes this scenario plausible.

We have considered a chain of 20 neurons preceded by a first neuron perturbed by an external periodic train of spikes as described in Section 2.3. Neurons are coupled by unidirectional chemical synapses activated by the firing activity of this first presynaptic neuron. This initial neuron always fires an action potential in response of the perturbation, whereas the response of the rest of neurons is sensitive to their phase (see Figure 2.7). A picture describing this situation is shown in Figure 2.11.

Figure 2.12 shows the success rate as a function of the period T of the input pulse train, for neurons located increasingly further down the chain. The resonant behavior is maintained, in fact becoming sharper, as the train propagates. This effect can be understood as follows. For the cases when

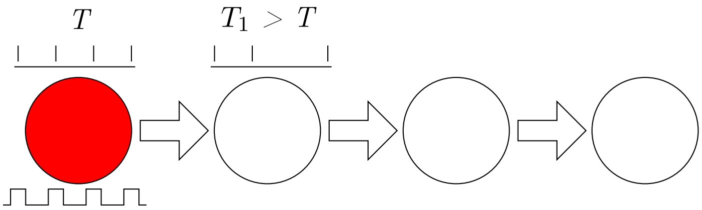

Figure 2.11: Schematic representation of the modeled neuronal chain. Circles represent neurons, vertical ticks mark the spikes elicited by each cell and the unidirectional arrows represent the chemical directed synapses between two consecutive neurons. The red neuron is the first presynaptic neuron in the chain and always spikes in response to an external train of pulses of period T.

the success rate of the first response neuron (neuron 1, solid thin line in Figure 2.12) is smaller than 100%, the instantaneous spike period increases. Since the response period of the next neuron can only be at most equal to (and in fact frequently it is smaller than) its input, the success rate with respect to the original spike train must be reduced (or at most remain constant) upon propagation. As the 1:1 region located around $T = 45.2$ is relatively small, eventually all the periods for which the success rate is not 100% for the first neuron will decay to zero far enough down the chain.

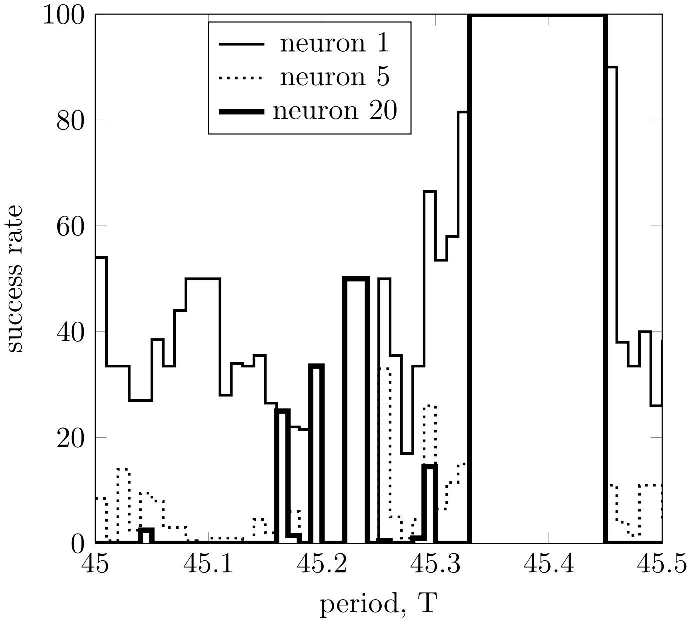

Figure 2.12: Success rate profile for neurons $i = 0$ (solid thin line), $i = 5$ (dashed line), and $i = 20$ (solid thick line). The trace for $i = 1$ is equivalent to Figure 2.8.

2.5 Conclusions

We have introduced a method to characterize the response of a neuron with subthreshold oscillations to a periodic train of synaptic pulses, based on analyzing the phase response of the neuron to the input pulses. To that end, we have obtained iterated maps that govern the behavior of the phase of the subthreshold oscillation at the times when the subsequent spikes are received. The iterated maps, which arise from the phase transition curve of the neuron, may exhibit stable, period and chaotic behavior, depending on the period of the spike train. These behaviors are able to explain the response of the neuron for varying input periods, which exhibits a resonant behavior.

Our results show that subthreshold oscillations provide an efficient mechanism to control propagation of spike trains. In that way, a neuronal chain with sufficient length is able to convert an heterogenous neural response to a presynaptic train of spikes into a quasi all-or-none response, which enables a way of classifying a wide variety of inputs: spiking with the same external period, no spiking at all, or transformation of the signal period. This type of classification might provide a useful framework that could underlie information processing capabilities of neuronal systems, such as firing-frequency-based selective communication [Izhikevich 2003, Balenzuela 2007], and communication through coherence [Fries 2005, Womelsdorf 2007].

The mechanism proposed here requires that there is a feedback between the input spikes and the subthreshold oscillations: subthreshold oscillations must dictate whether an input synaptic pulse can elicit a pulse or not, and in turn successful spikes must reset the subthreshold oscillations adequate to prepare the phase to receive and respond adequately to the next spike. When this feedback is broken, for instance in the presence of electrical coupling between the neurons, which is very efficient in synchronizing the phases of the subthreshold oscillations throughout the chain, thus increasing its inertia in front of spikes, the resonant behavior is quickly lost [Sancristóbal 2010b].

In summary, subthreshold oscillations allow for the precise timing of action potentials and filter out those periodic signals that do not lead to spike synchronization. Therefore, subthreshold oscillations provide a mechanism of rate coding [König 1996] due to their slow time-scale, that can discern input periods accurately. In this study, some assumptions are oversimplifications of a real neural assembly and we cannot generalize this information processing mechanism. For instance, the unidirectional chain connectivity (Figure 2.11) and the fact that a single presynaptic spike can elicit an action potential at appropriate phases [Figure 2.6(a)] are relatively far from realistic physiological conditions. However, our results shed light into the functional role of subthreshold oscillations and their interplay with the spikes, which are the information bins of the neural code. Moreover, synaptically induced membrane potential oscillations are ubiquitous in the brain and are a common fingerprint of the peak frequencies observed in EEG and LFP power spectrum. In the following chapters we will examine these oscillations in a more realistic scenario.

Chapter 3

Interplay between single action potentials and collective gamma neuronal oscillations

Contents

3.1 Firing activity of an isolated single neuron

We have mentioned in Section 2.1 that particular ion channels can cause subthreshold membrane potential oscillations either in isolated neurons or triggered by presynaptic activity within a network. Other channels provide the mechanisms to elicit suprathreshold responses, i.e. action potentials. Basically, the generation of action potentials requires an influx of sodium ions, Na^+, followed by a potassium efflux as described in Section 1.3.1. These events are mediated by voltage-gated ion channels, whose permeability depends on the membrane potential difference between the inside and the outside of the cell, according to the ionic concentration gradients. The dynamics of such channels is very rich, and their opening and closing time constants are heterogeneous. Thus, the type and distribution of ionic channels across the membrane of a neuron determine its excitability behavior in response to a stimulus. This behavior can be experimentally tested by injecting a pulsed,

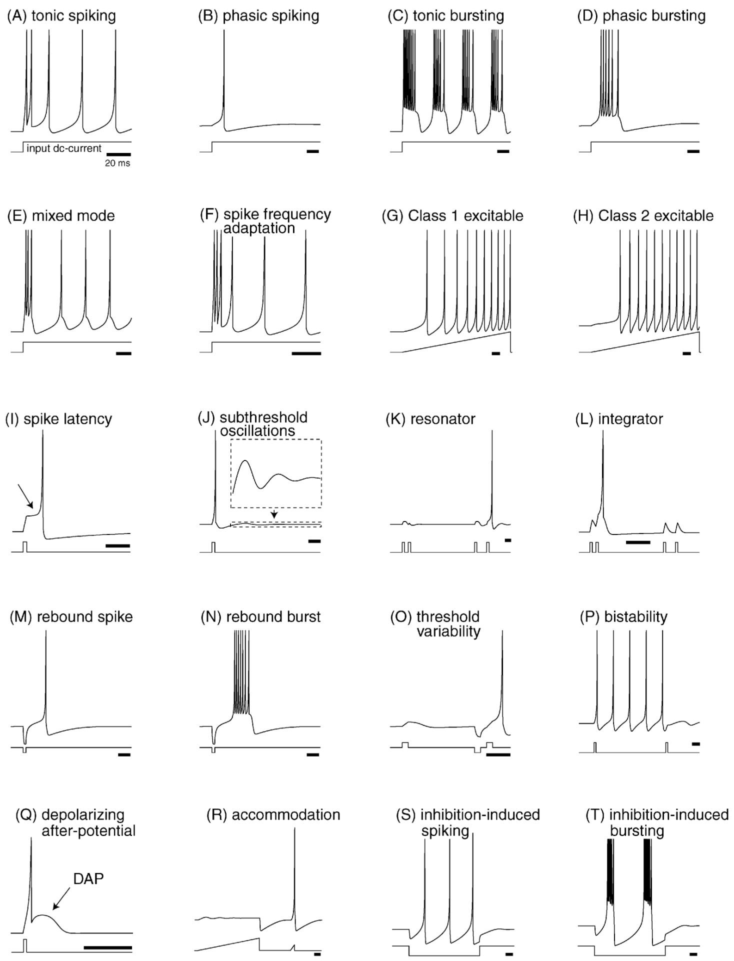

Figure 3.1: Variety of discharge patterns obtained from the Izhikevich model with different parameters. The horizontal bars denote 20 ms time interval. From [Izhikevich 2004].

constant, or ramp current, as shown in Figure 3.1. In the latter case (Figure 3.1G-H) one observes how the membrane potential changes as the input amplitude increases, eventually switching from a resting excitable state to an oscillating (tonic firing) state. Mathematically, this transition is described as a bifurcation of the membrane potential from a stable fixed point to a periodic orbit exhibiting distinct discharge patterns.

Depending on how the firing frequency within the oscillatory regime behaves near the bifurcation, neuronal excitability can be classified into *type I* or *type II* [Rinzel 1989]. In Figure 3.2 we show the cell's firing rate behavior in the two cases (and for an excitatory and an inhibitory neuron as discussed below) under constant injection current, for increasing values of the current. In type I excitability, the frequency increases continuously from zero as the bifurcation is crossed [Figure 3.2(a)]. Type II neurons [Figure 3.2(b)] on the other hand, exhibit a discontinuous jump in frequency as the tonic regime is entered, and their range of firing frequencies is quite narrow compared to type I neurons, which can achieve arbitrarily low frequencies [Izhikevich 2007].

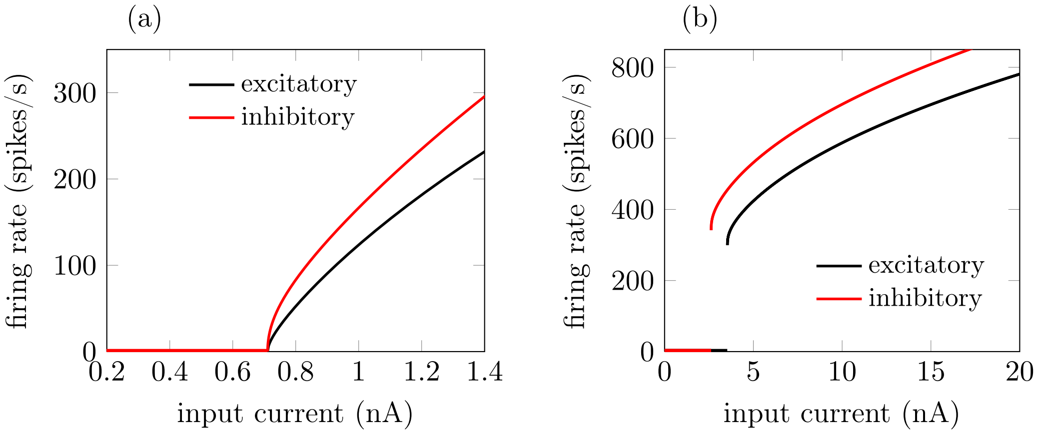

Figure 3.2: Characteristic *f*-*I* curves of type I (a) and type II (b) conductance-based excitatory (black) and inhibitory (red) neurons in isolation, obtained with the XPPAUT software [Ermentrout 2002]. Details of the type I model are given in Appendix A.2.1.

These different behaviors are associated with distinct bifurcations. In type I excitability, the periodic orbit emerges due to the collision of a stable fixed point (the resting state) and an unstable equilibrium point, occurring on top of an invariant circle (SNIC bifurcation) [see Figure 3.3(a)]. Type II excitability, on the other hand, can arise in three different ways: via a subcritical or a supercritical Hopf bifurcation [see Figure 3.3(b)], or through a saddle-node bifurcation *outside* the invariant circle [Rué 2011]. The integrate-and-fire and conductance-based models used in the literature to describe cortical networks are usually of type I [Wang 1996, El Boustani 2007].

The phase response can also be used as a criterion to distinguish between excitability classes: when operating in a tonic regime, type I neurons always advance their phase (defined with respect to their spiking period) when perturbed by a brief depolarizing pulse [see Figure 3.4(a)], while type II neurons can either advance or delay their phase depending on the instant of perturbation relative to the period of oscillation [Hansel 1995] [see Figure 3.4(b)].

Within a network, the input pulses come from other neurons, and therefore synchronized presynaptic spikes impinging on one periodic firing neuron might slow down or speed up its rhythm depending on the type of neuronal excitability. However, regular periodic firing patterns happen rarely *in vivo*; we have seen in Section 1.5.1 that the coefficient of variation of interspike intervals (ISIs) in the cortical neurons is typically larger than 1

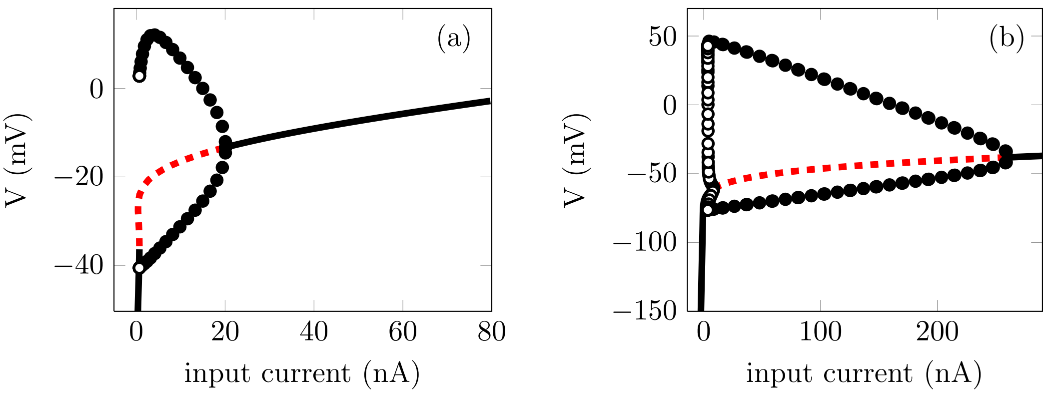

Figure 3.3: Bifurcation diagram of type I (a) and type II (b) conductance-based excitatory neurons in isolation, obtained with the XPPAUT software [Ermentrout 2002] and using Maurizio De Pittà's code *plotautobd.m* version 1.0 [de Pittà 2009]. Lines represent the equilibrium continuation curves (solid black means stable, dashed red means unstable). Orbits are plotted as black circles (filled circle means stable, empty circle unstable).

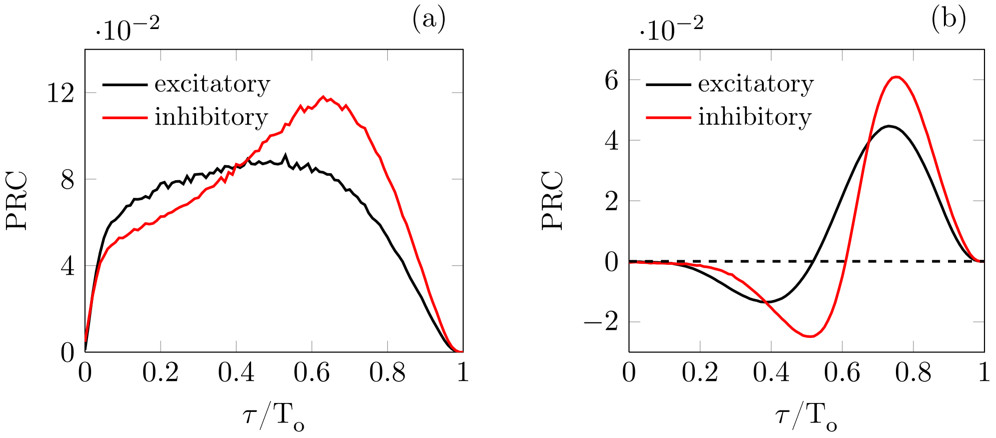

Figure 3.4: Phase response curves for (a) a type I excitatory (inhibitory) neuron and (b) a type II excitatory (inhibitory) neuron, representing the phase change in the spiking response of the neuron to a depolarizing pulse, as a function of the phase of the input (normalized to the spiking period T_o of the neuron). In (a), the excitatory (inhibitory) neuron is spiking tonically at an unperturbed period of 8.09 ms (6.00 ms), and receives the injection of a constant current of 1.0 nA. In (b), the excitatory (inhibitory) neuron fires every 2.36 ms (1.88 ms) and is subject to a constant current of 5 nA. The PRCs, obtained with the XPPAUT software [Ermentrout 2002], are defined as $1 - T(\tau)/T_o$, where $T(\tau)$ is the period after perturbing at time τ.

[Shinomoto 1999, Shinomoto 2005], corresponding to a nearly exponential distribution of ISIs. Usually, rhythmic electrical activity emerges from the recurrent synaptic activity in the network, rather than from spike-to-spike synchrony.

It has been experimentally observed [Softky 1993] that the high synaptic bombardment acting upon cortical neurons is far from being constant, leading to stochastic fluctuations that affect these neurons *in vivo*. When embedded in a population, neurons are subject to synaptic input that fluctuates in time. Even when the firing of the presynaptic neurons projecting to a given postsynaptic cell is uncorrelated between them, the total input current is Gaussian distributed [Roxin 2011]. Thus, neither the single-neuron frequency-current curve (f-I curve) nor the phase response can perfectly describe the firing behavior of single neurons when they are embedded in a network, which is not periodic but rather sparse and random.

From a single-neuron perspective, both the f-I and phase response curves have been widely studied and related to the kind of bifurcation that takes the cells from rest to tonic firing, as mentioned above. The f-I curves of the excitatory and inhibitory neurons helps to determine how the synaptic connection strength has to be tuned in order to balance excitation with inhibition, in agreement with the firing rates of each population. Moreover, as we will see in the next Section, type I neurons tend to fire faster within the network than in isolation.

3.2 Firing activity of a neuron embedded in a network

3.2.1 Input fluctuations and network gamma oscillations

Due to the high number of cells (nodes) and synapses (edges) involved in biological neuronal networks, computational neuroscience always deals with a small representation of the brain tissue, such as cortical columns, subareas of the cortical layers or a subset of neurons that represents a small piece of the brain. In all cases, a relative small number of neurons and their connections can be modeled, and the input coming from outside this network, arising from the activity of a far higher number of cells, is described as stochastic process. According to [Destexhe 2001], the *high-conductance state* is well reproduced by modeling the synaptic background activity as time varying synaptic conductances that follow an Ornstein-Uhlenbeck stochastic process.

Usually, an assumption about the dynamics of the external input (not arising from the modeled neurons) has to be made. Commonly, the incoming neuronal spike trains are considered to follow a Poisson distribution, which corresponds to the spiking times being independent of the previous history of events within each train [Zacksenhouse 2008]. The input to each neuron is the sum of many of these point processes, whose firing rate is jointly varying in time, also following a stochastic process. The cross-correlation of a given number of these inhomogeneous Poisson processes, also known as doubly stochastic Poisson processes, is equal to the cross-correlation of the instantaneous underlying rates, see [Brette 2009] for a complete demonstration. Therefore, in order to account for correlations between synaptic inputs, spike trains can be generated as inhomogeneous Poisson process with the same time varying rate. The average population activity, $\lambda(t)$, of a high number of these neurons will correspond to an Ornstein-Uhlenbeck process for an autocorrelation function with an exponential decay [Mazzoni 2008]:

$$\frac{d\lambda}{dt} = -\lambda(t) + \sigma \left(\sqrt{\frac{2}{\tau}} \right) \xi(t) \ , \qquad (3.1)$$

where σ is the standard deviation of the noisy process, leading to a *1/f* power spectrum for the λ time series that is flat up to a cut-off frequency $f = \frac{1}{2\pi\tau}$ Hz. $\xi(t)$ is a Gaussian white noise and $\lambda(t)$ is a measure of the input intensity to the network. Despite the fact that the time course of the instantaneous rate is generated by an unique Ornstein-Uhlenbeck process, the specific spike train impinging on each neuron is a different Poisson process, according to the rejection sampling (or spike thinning) technique to generate observations from a single distribution [Kuhn 2003].

From the modeled network other sources of synaptic input arise, i.e. the recurrent excitation and inhibition. When the induced spiking activity is large enough to percolate the network, the internal synaptic currents exhibit a fast cyclic behavior, alternating epochs of high excitation followed by high inhibition, due to the rhythmic synchronization of GABAergic cells (see Section 1.4.1) via their recurrent connections. Cortical oscillations thus arise as a collective phenomenon, which does not require individual-neuron firings to be oscillatory themselves. These global oscillations are discernible in averaged population activities such as the local field potential (LFP), whose troughs (or peaks, depending on the relative position of the recording electrode and the generating current dipoles) correspond to the minima of the synaptic inhibitory flow. In these temporal windows neurons are more likely to spike, producing an increase in the excitatory synaptic current, followed by a new burst of inhibition. These oscillations, at frequencies in the beta (12-30 Hz) and gamma (30-90 Hz) ranges, are experimentally seen in the cortex upon sensory stimulation [Buzsáki 2004]. Specifically, gamma-band synchronization has received special consideration, as it is hypothesized to be a mechanism for the dynamic generation of functional cell assemblies and for the flexible communication between brain areas (for a review, see [Singer 1999, Fries 2009]).

The net oscillatory synaptic current leads to a rhythmic behavior in averaged population measures such as the LFP (see Section 1.6 for a definition) and the time-resolved firing rate of the population (defined as the total number of spikes per unit time in the population divided by the number of neurons). This rhythmic activity is shown in Figure 3.5(a) and 3.5(d), respectively. The LFP power spectrum (see Appendix B.2) is depicted by solid lines in Figure 3.5(b), revealing a frequency peak whose precise position is determined by the GABAergic synaptic time constants and the synaptic strengths, as well as by the characteristics of the input [Henrie 2005].

For a range of biologically plausible parameters, a frequency peak in the LFP power spectrum appears in the gamma range (30–90 Hz). In particular, for the parameters given in Tables A.1 and A.2, the frequency peak of the LFP spectrum is located around 45 Hz for an external stimulation of time-averaged rate $\langle \lambda(t) \rangle_{\mathrm{t}} = 8500$ spikes/s. When the effective coupling between neurons is low, because either the induced spiking activity or the synaptic conductances are weak, the collective rhythm disappears from the LFP power spectrum, as shown by the dashed line in Figure 3.5(b). The low-frequency components are caused by the correlations in the synaptic input [Destexhe 2001, Szymon 2013].

Similarly to the local field potential, the global firing rate exhibits a marked peak at ~ 45 Hz in its spectrum [Figure 3.5(e)]. This rhythmicity reflects epochs of synchronization between subsets of neurons. Despite the collective rhythmic dynamics [Figure 3.5(d)], single neurons display strongly irregular individual spiking [Figure 3.5(c)], firing mostly in a sparse and single-spike mode occasionally accompanied by a high-frequency tonic firing, which nevertheless can be compatible with population rhythmic activity at gamma frequencies.

The recurrent connections between the excitatory and inhibitory population lead to rhythmicity in the synaptic current impinging on a neuron, composed by a succession of floods of excitation and of inhibition. These oscillations are a collective phenomenon arising from the interactions among neurons, and their frequency can be slowed down with increasing GABA synaptic duration. In that way, gamma oscillations in the firing rate activity and LFP signal arise naturally from the recurrent connections between excitatory and inhibitory neurons, when the synaptic conductances are adjusted to balance excitation with inhibition.

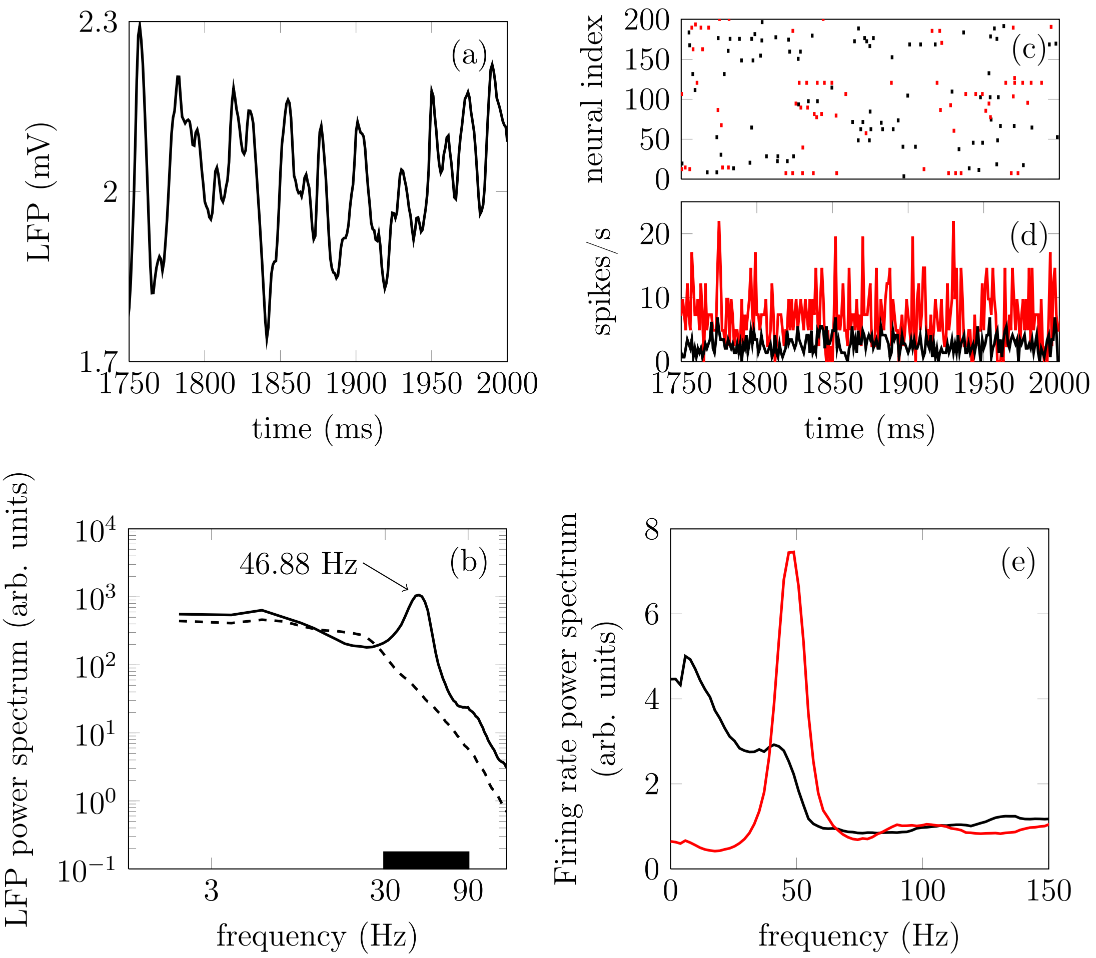

Figure 3.5: Collective oscillations in a type-I-neuron network. (a) LFP time trace in a 250 ms interval for an external mean rate of 8500 spikes/s. (b) Averaged LFP power spectrum for an external mean rate of 8500 spikes/s (solid line) and 5000 spikes/s (dashed line). The black bar delimits the gamma band (30 Hz–90 Hz). (c) Raster plot of 200 neurons for the same 250-ms interval. (d) Time-resolved firing rate of the whole population, and (e) the corresponding power spectrum for the excitatory (black) and inhibitory (red) neurons.

3.2.2 Distribution of individual firing rates within the network

The input arriving on a cortical area *in vivo* is the sum of the synaptic currents coming from all possible sources, which include recurrent excitation and inhibition (generated by the nearby network) as discussed above, and afferent pathways terminating onto this neuronal population (generated by distant cells with long-range axons). Each cortical neuron receives presynaptic potentials through 10 000 synapses on average. Therefore, despite the sparse activity of cortical neurons [Wolfe 2010], synchronized activity enables barrages of action potentials at high firing rates. This high spontaneous background activity is continuously activating the synapses, thus reducing the neuronal membrane resistance (5-40 MΩ) and shifting the membrane potential closer to the spiking threshold. Fluctuations of the synaptic current impinging on a neuron randomly bring the neuron above threshold, leading to a highly variable individual firing rate. In contrast to the *in vitro* recordings in which the synaptic bombardment is much lower, *in vivo* activity is often called the *high-conductance state* [Destexhe 2003].

In Section 1.5 we discussed the possible information codes concealed in the *in vivo* irregular train of spikes. It has been experimentally shown, both in isolated cortical neurons *in vitro* [Bryant 1976, Mainen 1995] and *in vivo* in the visual system of the fly [de Ruyter van Steveninck 1997], that the spikes fired by a single neuron are more reliable in time across trials when the injected (or presented) input is dynamic (see Figure 1.25)[†] . Therefore, the precise time at which a spike is elicited is highly dependent on the temporal pattern of events composing the stimulus. In order to understand this sensitivity to input transients we modeled a type I cortical network and analyzed the input-output relationships.

At first, the natural variability of the synaptic current driving neurons embedded in a network gives rise to an effective f-I curve (Figure 3.6, circles). Given the above-mentioned fluctuating character of the synaptic current received by the neurons within the network, the f-I response is quantified here as a function of the mean synaptic current received by the neuron between two consecutive spikes (interspike interval, or ISI). The inverse of this quantity is plotted in Figure 3.6 (circles), comparing its behavior with the corresponding f-I curves of the isolated neurons (solid lines). Note however the limitations of this comparison, as the mean synaptic current over an ISI differs from the actual fluctuating input received by a cell, specially for long periods. It is precisely in the range of low frequencies where both curves differ most. For instance, the firing rate in the resting state region departs from zero close to the bifurcation, due to the appearance of noise-induced spikes throughout the network. Differences between the firing rate of a network-embedded neuron and its characteristic f-I curve in isolation also exist in the tonic regime above 0.8 nA, as can be seen in Figure 3.6. We can understand this from the fact that, due to the synaptic bombardment, neurons within a network are persistently perturbed, and consequently their firing rates are altered. The characteristic phase response curve (PRC) of type I neurons [see Figure 3.4(a)] reveals a phase advance for any perturbation time within a period. Thus, when a type

---

[†] In contrast, variability shown in Figure 1.16 measured in the middle temporal visual area (MT) of behaving monkeys [Shadlen 1998], could be enhanced by the monkeys attentive state, which modulates neuronal firing rate across trials [Barberini 2001].

I neuron has just spiked and is excited again by a presynaptic potential its period is reduced (and thus its firing rate is increased). This explains why the firing rate of type I neurons embedded in a network, and thus continually perturbed by presynaptic activation, is above the f-I curve of an isolated neuron with tonic firing.

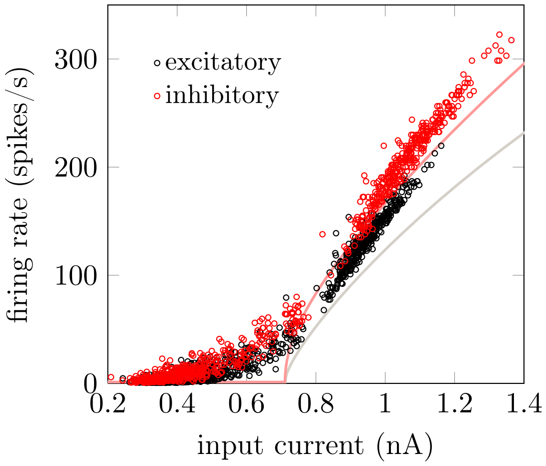

Figure 3.6: Equivalent f-I curve for neurons embedded in the network (circles) representing the instantaneous firing rate versus the net synaptic current averaged over the corresponding inter-spike interval, for an excitatory (black) and inhibitory (red) neuron. The single-neuron f-I curves are also shown in solid lines for comparison. $\langle\lambda(t)\rangle_t = 8500$ spikes/s.

It is worth noting that the firing rate discontinuity shown in Figure 3.6 (circles) is an emergent network property. Within a network, type I neurons display two clearly defined groups of inter-spike intervals, in a sort of population-level bimodality that does not exist for individual neurons in isolation. Thus, there is a striking difference in the spiking activity exhibited by the type I cells once embedded in a network compared to their intrinsic f-I curve. To better resolve the firing mode differences and their origin, we first characterize the distribution of instantaneous firing rates, and then we describe the relation of firing behavior to the input and LFP dynamics.

To characterize the distribution of instantaneous firing rates of individual neurons within the network, we compute their histogram for the parameter values given in Section A.2, which lead to synchronous irregular firing [see Figures 3.5(c,d)] with global oscillations in the gamma range [Figures 3.5(b,e)]. The distribution of instantaneous firing rates is bimodal [Figure 3.7(a)], indicating the prevalence of two firing modes, with high-firing-rate events (short ISIs) reflecting bursts of spiking activity, interspersed with short-firing-rate events (long ISIs). This effect arises from the network dynamics and cannot be predicted from the characteristic f-I curves of type I isolated neurons, which are continuous and hence do not forbid any particular range of firing rates

(Figure 3.6; note the gap in the circles, which occurs in network-embedded neurons). This bimodal response was also observed in a network of LIF neurons [Roxin 2011], when the inhibitory population firing rate exceeded the excitatory population rate. We will address the origin of this bimodal behavior at the end of this section.

The high-firing-rate peak in Figure 3.7(a) arises from the spikes of the network-induced bursts (see upper cloud in Figure 3.6). The low-firing-rate events are more frequent than the high-firing-rate ones (64% of the interspike intervals of the excitatory population across 20 trials lie below ~58.31 spikes/s [see arrows in Figure 3.7(a)]). In other words, more neurons are simultaneously found in a silent state or low-firing mode.

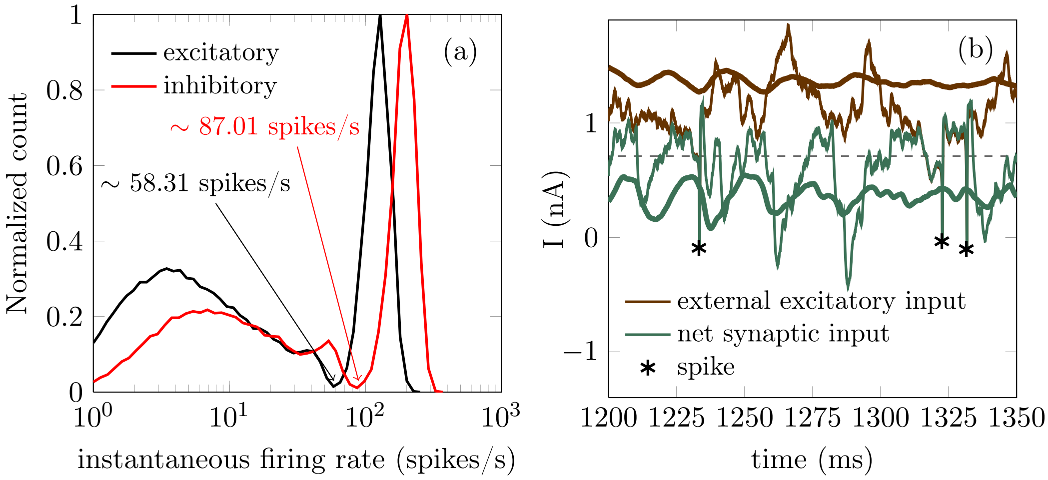

Figure 3.7: Modeled network with a GABAergic decay time constant $\tau^d_{\text{GABA}} = 5$ ms [see Equation (1.21)]. (a) Histogram of instantaneous firing rates of both excitatory (black) and inhibitory (red) neurons. The arrows point at the minimum of the distribution separating the fast and slow firing mode. (b) Time trace of the external excitatory current (brown lines) and the net synaptic current (green lines) acting upon the excitatory neurons. The thick lines are averages over the entire excitatory population, whereas the thin lines correspond to the current impinging on a single neuron. The asterisks label the spiking times of this neuron. The horizontal dashed line marks the spiking threshold, i.e. the value of I at the bifurcation of Figure 3.6.

In order to understand the genesis of this bimodal firing behavior, we now examine the time evolution of the synaptic currents acting upon the excitatory population (which by definition determines the dynamics of the LFP, see Appendix A.4). Figure 3.7(b) shows the time traces of the external excitatory input (brown lines) and the net synaptic current (green lines). This latter current accounts for both the excitatory component (arising from the external and the recurrent excitatory spikes) and the inhibitory component (arising from the recurrent inhibitory spikes). The thick lines are population averages over the excitatory neurons, whereas the thin lines represent the current values impinging locally on a given neuron. As shown in this figure, the average external synaptic input (thick brown line) lies well above the spiking threshold (horizontal dashed line), whereas the average net synaptic current (thick green line) is below the spiking threshold, due to the inhibitory flow that counteracts the strong external excitation. Therefore, the current impinging on a neuron [thin green line, corresponding to the I_{SYN} term of Equation (A.4), which is the sum of all synaptic contributions of the form Equation (1.13)] is typically below threshold. Thus neurons spike rarely, only when the excitation-inhibition balance is lost during a certain time window, in which the external input brings the neuron above threshold [see asterisks in Figure 3.7(b)]. From the definition of the brown and green thin lines it follows that, in those intervals in which both traces are quasi-superimposed, inhibition is zero because the excitatory current nearly equals the total synaptic input, I_{SYN}. From time to time these intervals are long enough for several spikes to occur in quick succession, giving rise to periods of high-firing rate (for instance around ∼1325 ms). On the other hand, if the excitation-inhibition balance is briefly lost, an isolated spike is elicited only if inhibition is low enough (as we will see in detail in Section 3.3.2), giving rise to low-firing-rate events (for instance at ∼1230 ms). Therefore the combined dynamics of excitation and inhibition is the basis of the bimodal distribution of instantaneous firing rates.

According to the previous discussion, the ratio of fast to slow firing events is determined by the characteristic timescale of the periods in which the excitation-inhibition balance is lost. In order to verify this reasoning, we now analyze the behavior of the network for a longer value of the decay time constant τ^d_{GABA} of the GABAergic synapses, see Equation (1.21). Increasing τ^d_{GABA} to 30 ms leads to a disappearance of the gamma rhythm [compare the thick green lines in Figures 3.7(b) and 3.8(b)] [Fisahn 1998, Heistek 2010]. Since the inhibitory currents are slower, in this case the periods in which the excitation-inhibition balance is lost are longer, giving rise to an increase in the number of fast spiking events [see asterisks in Figure 3.8(b)]. This is quantified in Figure 3.8(a), which shows that high firing rates are much more frequent than low firing ones. Thus the inhibition decay time, τ^d_{GABA}, determines the principal individual firing rate mode (mostly single-spike for fast inhibition and bursty for slow inhibition).

As long as inhibitory neurons fire more intensely than the excitatory ones to compensate for their relative small number, the network settles in a non-periodic firing state with a significant gamma band component. At frequencies closer or below the gamma LFP peak the external drive is balanced by inhibition, which leads to a low-firing mode that arises separated from the more “natural” fast-firing mode (given by the single-neuron f-I curve) by a gap of

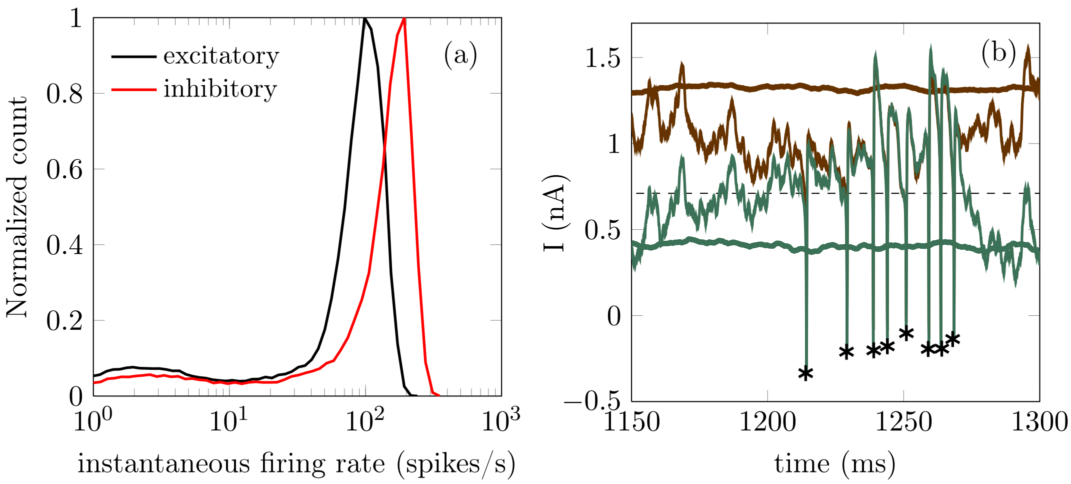

Figure 3.8: Modeled network with $\tau^{d}_{\mathrm{GABA}} = 30$ ms. (a) Histogram of instantaneous firing-rates of both excitatory (black) and inhibitory (red) neurons. (b) Time trace of the external excitatory current (brown lines) and the net synaptic current (green lines) acting upon the excitatory neurons. See caption of Figure 3.7 for a description of the plots.

quasi-forbidden instantaneous firing rates. This leads to a discontinuity in the firing rates of the neurons, similar to what happens in single type II neurons but that does not occur in type I neurons in isolation. Thus, this firing-rate discontinuity constitutes an emerging dynamical property of the network.

Bimodal distributions of instantaneous firing rates are found experimentally in both the auditory cortex [Shih 2011] and the visual cortex [DeBusk 1997, Snider 1998]. Other modeling works have also shown a bimodal distribution of ISIs [Wang 1998] using intrinsically bursting neurons, in contrast with our case in which the bimodality appears naturally from the balanced network as in [Roxin 2011]. Moreover, in [Bereshpolova 2011] the recorded single unit activity through different awake brain states, shows that during alert periods some particular neuronal types reduce their bursting with respect to the non alert periods. In agreement with our results, the alert state corresponds to higher power in the gamma range.

3.3 Coding strategies behind a bimodal firing pattern

The type I network oscillating in the gamma range [Figure 3.7(a)] clearly has a sparse activity, in agreement with the sparse coding of sensory inputs [Olshausen 2004, Wolfe 2010] (see Table 3.9). We now ask how the bimodality between slow and fast spiking regimes, with a band of forbidden firing rates,

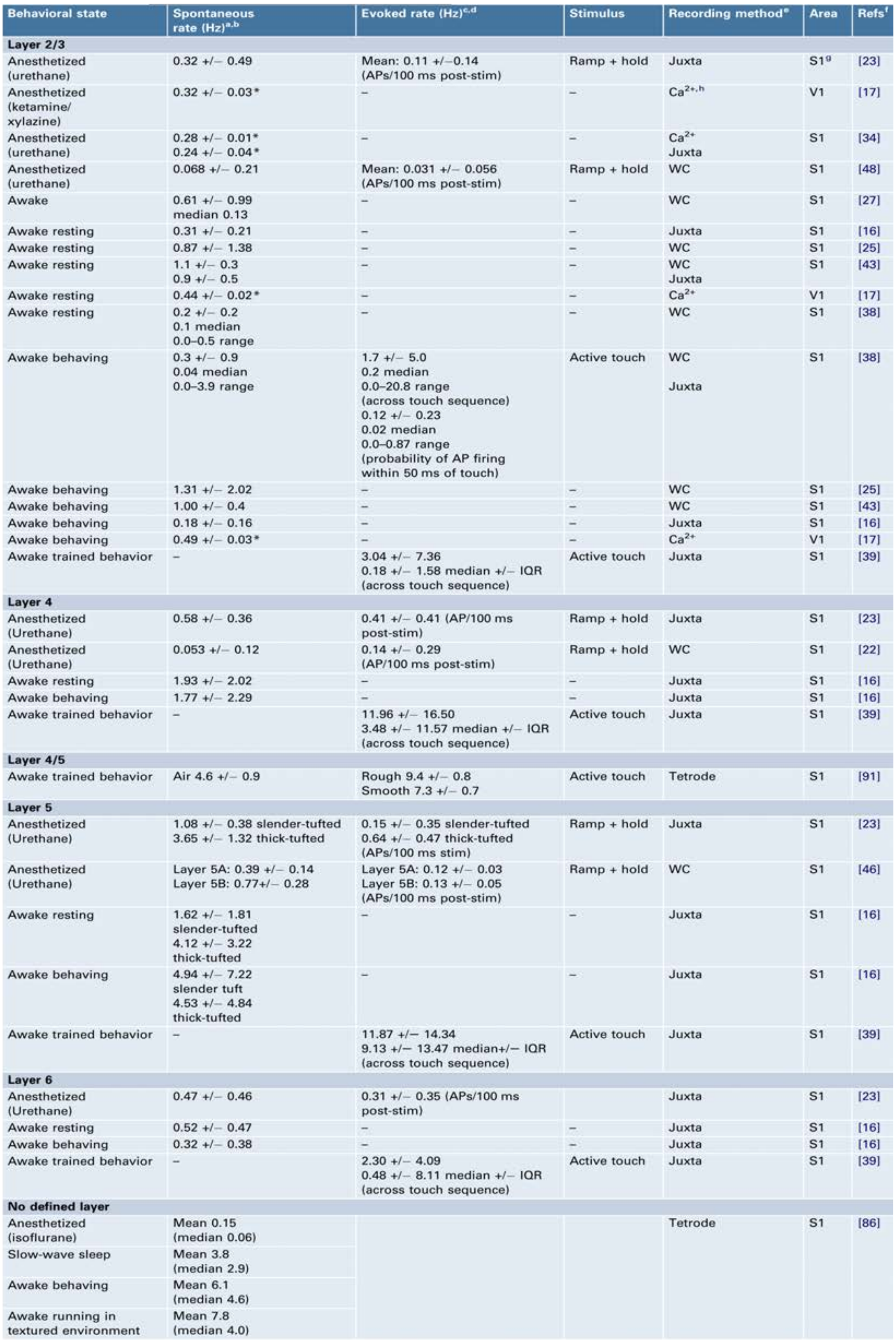

Behavioral state	Spontaneous rate (Hz)[a,b]	Evoked rate (Hz)[c,d]	Stimulus	Recording method[e]	Area	Refs[f]
Layer 2/3						
Anesthetized (urethane)	0.32 +/– 0.49	Mean: 0.11 +/–0.14 (APs/100 ms post-stim)	Ramp + hold	Juxta	S1[g]	[23]
Anesthetized (ketamine/ xylazine)	0.32 +/– 0.03*	–	–	Ca^{2+}[h]	V1	[17]
Anesthetized (urethane)	0.28 +/– 0.01* 0.24 +/– 0.04*	–	–	Ca^{2+} Juxta	S1	[34]
Anesthetized (urethane)	0.068 +/– 0.21	Mean: 0.031 +/– 0.056 (APs/100 ms post-stim)	Ramp + hold	WC	S1	[48]
Awake	0.61 +/– 0.99 median 0.13	–	–	WC	S1	[27]
Awake resting	0.31 +/– 0.21	–	–	Juxta	S1	[16]
Awake resting	0.87 +/– 1.38	–	–	WC	S1	[25]
Awake resting	1.1 +/– 0.3 0.9 +/– 0.5	–	–	WC Juxta	S1	[43]
Awake resting	0.44 +/– 0.02*	–	–	Ca^{2+}	V1	[17]
Awake resting	0.2 +/– 0.2 0.1 median 0.0–0.5 range	–	–	WC	S1	[38]
Awake behaving	0.3 +/– 0.9 0.04 median 0.0–3.9 range	1.7 +/– 5.0 0.2 median 0.0–20.8 range (across touch sequence) 0.12 +/– 0.23 0.02 median 0.0–0.87 range (probability of AP firing within 50 ms of touch)	Active touch	WC Juxta	S1	[38]
Awake behaving	1.31 +/– 2.02	–	–	WC	S1	[25]
Awake behaving	1.00 +/– 0.4	–	–	WC	S1	[43]
Awake behaving	0.18 +/– 0.16	–	–	Juxta	S1	[16]
Awake behaving	0.49 +/– 0.03*	–	–	Ca^{2+}	V1	[17]
Awake trained behavior	–	3.04 +/– 7.36 0.18 +/– 1.58 median +/– IQR (across touch sequence)	Active touch	Juxta	S1	[39]
Layer 4						
Anesthetized (Urethane)	0.58 +/– 0.36	0.41 +/– 0.41 (AP/100 ms post-stim)	Ramp + hold	Juxta	S1	[23]
Anesthetized (Urethane)	0.053 +/– 0.12	0.14 +/– 0.29 (AP/100 ms post-stim)	Ramp + hold	WC	S1	[22]
Awake resting	1.93 +/– 2.02	–	–	Juxta	S1	[16]
Awake behaving	1.77 +/– 2.29	–	–	Juxta	S1	[16]
Awake trained behavior	–	11.96 +/– 16.50 3.48 +/– 11.57 median +/– IQR (across touch sequence)	Active touch	Juxta	S1	[39]
Layer 4/5						
Awake trained behavior	Air 4.6 +/– 0.9	Rough 9.4 +/– 0.8 Smooth 7.3 +/– 0.7	Active touch	Tetrode	S1	[91]
Layer 5						
Anesthetized (Urethane)	1.08 +/– 0.38 slender-tufted 3.65 +/– 1.32 thick-tufted	0.15 +/– 0.35 slender-tufted 0.64 +/– 0.47 thick-tufted (APs/100 ms stim)	Ramp + hold	Juxta	S1	[23]
Anesthetized (Urethane)	Layer 5A: 0.39 +/– 0.14 Layer 5B: 0.77+/– 0.28	Layer 5A: 0.12 +/– 0.03 Layer 5B: 0.13 +/– 0.05 (APs/100 ms post-stim)	Ramp + hold	WC	S1	[46]
Awake resting	1.62 +/– 1.81 slender-tufted 4.12 +/– 3.22 thick-tufted	–	–	Juxta	S1	[16]
Awake behaving	4.94 +/– 7.22 slender tuft 4.53 +/– 4.84 thick-tufted	–	–	Juxta	S1	[16]
Awake trained behavior	–	11.87 +/– 14.34 9.13 +/– 13.47 median+/– IQR (across touch sequence)	Active touch	Juxta	S1	[39]
Layer 6						
Anesthetized (Urethane)	0.47 +/– 0.46	0.31 +/– 0.35 (APs/100 ms post-stim)		Juxta	S1	[23]
Awake resting	0.52 +/– 0.47	–	–	Juxta	S1	[16]
Awake behaving	0.32 +/– 0.38	–	–	Juxta	S1	[16]
Awake trained behavior	–	2.30 +/– 4.09 0.48 +/– 8.11 median +/– IQR (across touch sequence)	Active touch	Juxta	S1	[39]
No defined layer						
Anesthetized (isoflurane)	Mean 0.15 (median 0.06)			Tetrode	S1	[86]
Slow-wave sleep	Mean 3.8 (median 2.9)					
Awake behaving	Mean 6.1 (median 4.6)					
Awake running in textured environment	Mean 7.8 (median 4.0)					

Table 3.9: Compendium of spiking activity in sensory cortex. Details are given in [Barth 2012].

affects the coding capabilities of the neuronal network. To address this question, we establish how the individual firing rate depends on the external input to the population [brown lines in Figure 3.7(b)], rather than on the internal synaptic current (as shown in Figure 3.6). As mentioned above, the external input is modeled by a set of Poissonian spike trains perturbing each neuron, mimicking either an external sensory input representing a stimulus or neuronal activity arriving from other areas. The time course of the external firing rate is an Ornstein-Uhlenbeck process, see Equation (3.1). Upon arrival of an external spike an AMPA synapse (see Section 1.4.1) is activated, numerically meaning that the I_{syn} term changes according to the function $\sigma(t)$ [Equation (1.21)], and the neuron integrates the input giving rise to a postsynatic potential (PSP). If the rate of the external input is high, many spikes come in rapid succession and the sum of all the triggered PSPs can lead to an action potential, provided that inhibition is weak enough.

3.3.1 Rate coding for high single-neuron firing rates

Figures 3.10(a1-c1) show the firing rate of the excitatory neurons as a function of the mean external firing rate, averaged over the corresponding ISI, $\langle\lambda(t)\rangle_{\mathrm{ISI}}$, for which the instantaneous firing rate is calculated for three different GABAergic synaptic durations, all of them generating LFP oscillations in the gamma range. All three plots clearly reveal the bimodal character of the firing rate distribution described above. Two clouds of data points are clearly discernible, corresponding to distinct ISIs. The lower cloud is associated with longer firing periods. Naturally, the instantaneous external rate of that low-firing-rate state converges to the time-averaged value of the external rate ($\langle\lambda(t)\rangle_{\mathrm{t}}$, marked by a vertical dashed line in the three plots), due to the large periods over which that mean is calculated. On the other hand, the cloud at the top exhibits a clear correlation with the external rate, which provides for a standard mechanism of *rate coding*: the higher the external rate is, the faster the resulting firing rate of the neurons in the network. Accordingly, for external rates clearly above the mean external rate the network only responds with high-frequency firing, following the f-I curve of the individual neurons (i.e. operating in a rate coding mode). For moderate external rates, on the other hand, the distribution of firing rates is bimodal, with low-firing and high-firing events coexisting for the same value of the external rate.

The scatter plots shown in Figure 3.10 also allow us to further investigate the origin of the firing-rate gap evident in those plots (and in Figure 3.6 above). The origin of this gap is in the recovery time of the network following an increase of inhibition, due to the fact that firing rates that match the duration of network depression are forbidden. To verify that expectation, we compare

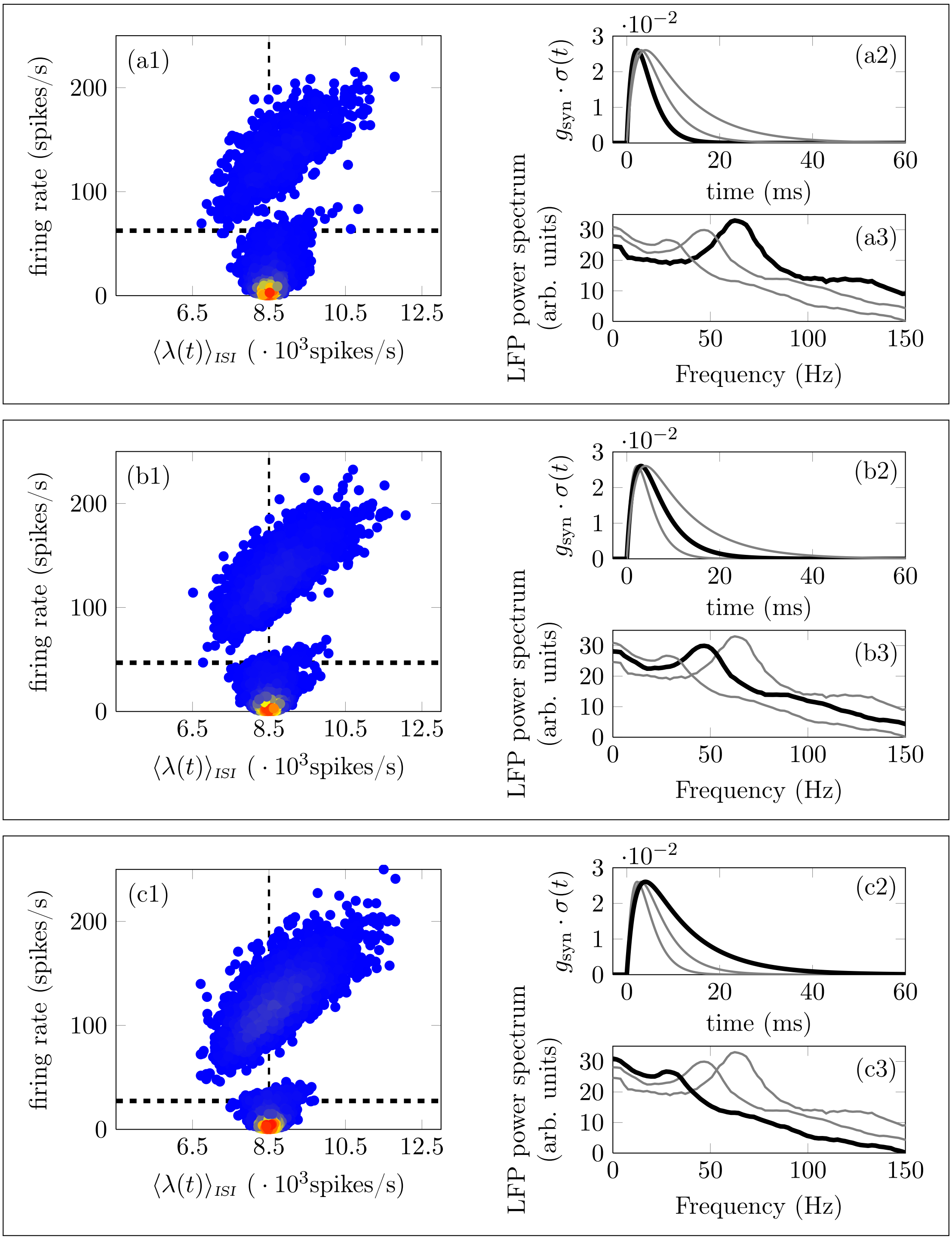

Figure 3.10: (1) Instantaneous firing rates of the excitatory neurons across 20 trials as a function of the external firing rate averaged over each corresponding ISI, $\langle\lambda(t)\rangle_{\text{ISI}} \sim \langle\lambda(t)\rangle_{\text{t}}$. The mean rate of the external spike train is $\langle\lambda(t)\rangle_{\text{t}} = 8500$ spikes/s and is marked with a vertical dashed line. (2) Temporal evolution of the inhibitory conductance $g_{\text{syn}}(\text{t})$. (3) LFP power spectrum. The thick dashed horizontal line is placed at the frequency-gamma peak of the LFP power spectrum (a3-c3), thus likening *Hz* to *spikes/s*. We consider three GABAergic decay time constant, τ^d_{GABA} *(next page)*:

the behavior of the network for different values of the decay time constant τ^d_{GABA} of the GABAergic synapses, while keeping the IPSP amplitude and AMPA synapses constant. Our results show that longer inhibition (growing from panel (a) to panel (c) in Figure 3.10) increases the range of forbidden firing periods, because the probability of spiking after an inhibitory barrage is lower during a longer time interval.

Figures 3.10(a2-c2) show the temporal evolution of the inhibitory conductance $g_{\text{syn}}(t)$ (see Section 1.4.2) for each of the τ^d_{GABA} values, highlighting in dark the time trace for the precise τ^d_{GABA} used in the corresponding scatter plot. As τ^d_{GABA} increases, $g_{\text{syn}}(t)$ is significant during a longer time interval. Accordingly, the low-firing mode reduces its area because the slower inhibitory synapses forbid the shortest ISIs within this mode that match the duration of the inhibitory barrage, which also causes slower gamma rhythms, as can be seen in Figures 3.10(a3-c3) and thick dashed horizontal line in Figures 3.10(a1-c1). However if inhibition is not too strong, due to weak excitatory drive –for instance at low $\langle\lambda(t)\rangle_{\text{ISI}}$ values–, shorter ISIs are allowed. Therefore, the low-firing state is the result of a competition between the external slow fluctuations and the recurrent inhibition, whose oscillating frequency decreases with increasing GABA synaptic decay time [see Figure 3.10(a2,3-c2,3)]. This leads to the counterintuitive discontinuity in the firing rate of type I neurons described above.

Figures 3.10(a1-c1) show a redundancy of instantaneous firing rates of single neurons in response to intermediate input strengths, $\langle\lambda(t)\rangle_{\text{ISI}} \sim \langle\lambda(t)\rangle_{\text{t}}$, which suggest that the two spiking rates encode different information characteristics at these input amplitudes. Moreover, we have seen that neurons behave like all-or-none detectors of rapid stimulus fluctuations (because they are measured over short ISIs), with instantaneous firing rates faster than the LFP gamma peak [above the thick dashed horizontal line in Figures 3.10(a1-c1)] encoding for the fast dynamics of the incoming synaptic activity.

3.3.2 Phase coding at intermediate input strengths

We have seen that, even though the firing rate of the individual neurons is far from being tonic, the probability of firing across the network varies rhythmi-

---

Figure 3.10 *(previous page)*: (a) $\tau^d_{\text{GABA}} = 2.5$ ms, (b) $\tau^d_{\text{GABA}} = 5.0$ ms (used in the rest of the simulations presented, unless stated otherwise) and (c) $\tau^d_{\text{GABA}} = 10$ ms. The local density of firing events within each cloud is represented by a normalized color scale (with red corresponding to high values and dark blue to low values) in order to emphasize that the slow firing mode predominates.

cally in time with a frequency around 45 Hz [Figure 3.5(e)]. As mentioned in Section 3.2.1 above, this rhythm is generated by recurrent excitatory and inhibitory connections, and is revealed in the LFP [Figure 3.5(a)] and firing-rate dynamics [Figure 3.5(d)]. Both the synaptic flow (apparent in the LFP) and the spiking activity are mutually interacting, given that a decrease in synaptic inhibition triggers an increase in the mean firing activity of the network. This causal relationship implies that the peaks of the population firing activity and the troughs of the LFP are displaced in time within the millisecond range, controlled by the synaptic delay.

To further characterize the effect of the global rhythm on the firing activity, we have computed spike triggered averages (STA) across trials of both the LFP and the inhibitory synaptic current, I_{GABA}, acting upon each neuron (see Appendix B.1). The LFP carries information about the global synaptic activity affecting the excitatory neurons of the population [see Equation (A.14)], and is therefore a measure of the global activity of the network. In contrast, I_{GABA} only accounts for the inhibitory synaptic current impinging on an neuron from the firing activity of its presynaptic inhibitory neurons, and is thus a local measure. We have considered the STA in a time window of 70 ms around a spike (50 ms pre-spike and 20 ms post-spike). Furthermore, to avoid having a previous spike from the same neuron fall within the time window being considered, we have only taken into account spikes at least 50 ms apart. When computing the STA we have classified the spikes, according to the bimodal distribution of instantaneous firing rates shown in Figure 3.7(a), as slow or fast firing events, the latter corresponding to network-induced bursts. Within the fast firing mode we selected the first spike of each burst, since we are interested in the events leading to burst initiation. We now discuss separately the mechanisms underlying the generation of the slow and fast firing modes and their relationship with the phase of the global oscillations.

Fast firing mode. As shown by the thick lines in Figures 3.11(a1,b1), the high-frequency regime appears when the inhibitory synaptic current I_{GABA} impinging on a neuron (i.e. its *local* inhibition) is close to zero for a relatively large time interval right after $t = 0$. In other words, the presynaptic inhibitory neurons must be silent for a long enough period of time after the neuron fires, in order for a burst to be initiated. In those conditions, it is more probable that the excitatory external input brings the neuron above the spiking threshold for a sustained amount of time, giving rise to a fast spiking period.

For the excitatory neurons this occurs preferentially at a high level of *global* inhibition, i.e. at the maxima of the LFP [thick line in Figure 3.11(a2)]. These two events, a maximum of the global inhibition (i.e. of the LFP) and a minimum of the local inhibition (i.e. of $|I_{\mathrm{GABA}}|$), occur simultaneously, since it

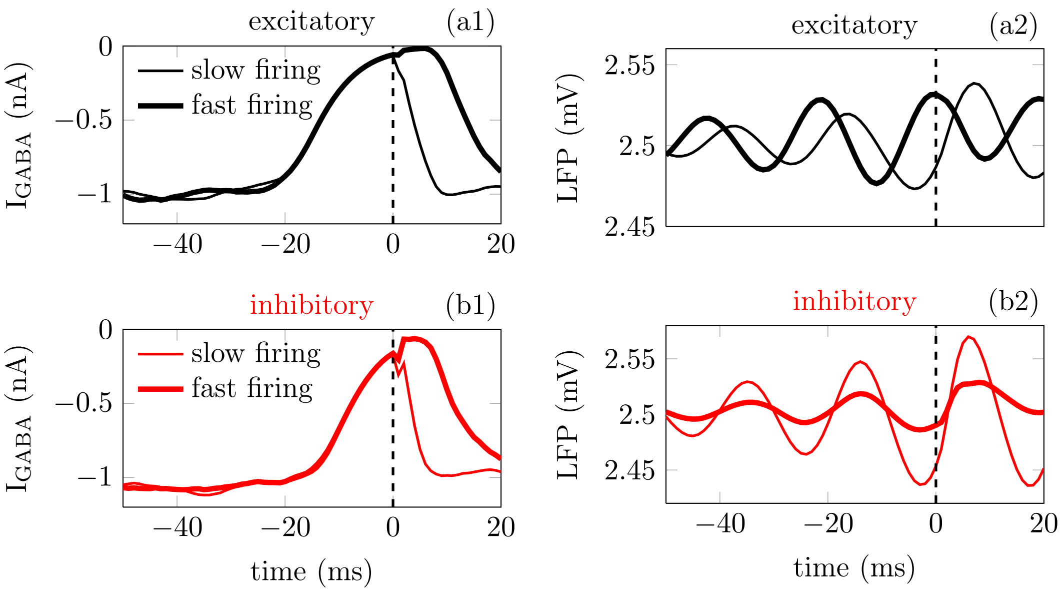

Figure 3.11: Spike-triggered averages (STA) of the synaptic inhibitory current impinging each individual cell (a1,b1) and of the LFP (a2,b2). Spikes from ISIs larger than 50 ms are considered. The thin lines correspond to those spikes prior to a long ISI (slow firing mode), while the thick lines correspond to the short ISIs (fast firing mode). These plots are obtained from a single trial, and the frontier between long and short ISIs is set at 17.14 ms (58.31 spikes/s) for the excitatory neurons and at 11.49 ms (87.01 spikes/s) for the inhibitory neurons, according to Figure 3.7(a). The vertical dashed line is the reference time at which a spike is elicited.

is when global inhibition is strong that some neurons can be locally surrounded by strongly inactivated inhibitory neurons. During this time interval, those neurons fire in bursts due to the external excitation, before all the inhibitory neurons become excited and prevent the firing of the rest of the population. A scheme of the interplay between local inhibition and global activation leading to the fast firing mode is shown in Figure 3.12(b). In contrast with the excitatory neurons, in inhibitory neurons the initiation of the fast firing mode does not depend so strongly on the level of global inhibition [thick line in Figure 3.11(b2)]. We hypothesize that these neurons, which have a smaller membrane time constant than the excitatory ones (see Appendix A.2.1), react rapidly to the external excitatory fluctuations and spike regardless of the level of global inhibition, provided their presynaptic inhibitory current is zero [thick line in Figure 3.11(b1)].

Slow firing mode. The low-frequency regime, on the other hand, takes place when the local inhibitory current, I_{GABA}, impinging on the neuron is momentarily zero, as shown by the thin line in Figure 3.11(a1,b1). The rapid increase of inhibition following a spike (at $t = 0$, dashed line) prevents the

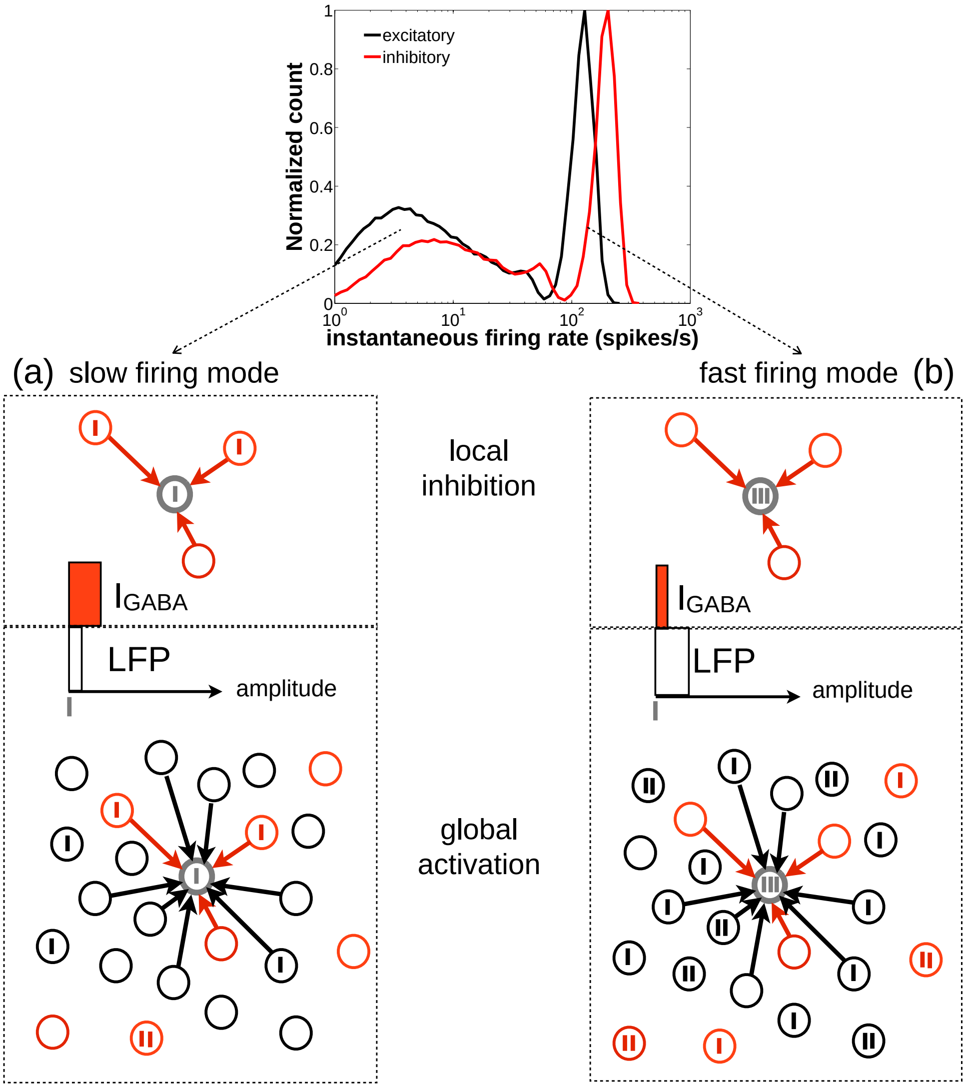

Figure 3.12: Scheme of the network spiking activity underlying slow (a) and fast (b) firing modes of a given neuron in the network (represented by the gray circle). Vertical thick ticks inside the circles represent spikes. The black and red circles represent excitatory and inhibitory neurons, respectively. For simplicity, only contacts to the grey neuron are represented (black arrows). In the top panel of A (slow firing mode), the reference neuron (in grey) is surrounded by presynaptic inhibitory neurons that are starting to fire (i.e. the level of I_{GABA}, represented by a horizontal red bar, is moderate). The global activity of the network (bottom panel, represented by a white horizontal bar) is low and the earliest inhibitory spikes prevent the cells from bursting. In the top panel of B (fast firing mode) the neuron is surrounded by inactive inhibitory neurons (i.e. the level of I_{GABA} is low), whose silence is driven by the high activity of the rest of the inhibitory population (reflected in a high level of the LFP).

neuron from spiking again. This happens at low levels of global inhibition, i.e. close to the minima of the LFP [thin line in Figures 3.11(b1,b2)]. Immediately after a spike the firing activity of the population increases, and thus the local inhibition grows as well, increasing the distance of individual neurons to threshold [see the scheme of Figure 3.12(a)].

The STA analysis discussed above shows that the simultaneous occurrence of slow instantaneous rates at both the excitatory and inhibitory populations is only possible near the minima of the LFP [thin lines in Figures 3.11(b1,b2)], whereas fast instantaneous rates can only be simultaneously present in both populations at the maxima of the LFP [thick lines in Figures 3.11(b1,b2)].

Given the described interaction between the individual firing modes and the rhythmic network dynamics, one can ask whether a partial representation of the input is coded in the spiking timing of cells relative to the phase of the population oscillation.We now address this question by proceeding to filter the LFP signal around the gamma frequency peak (47±5 Hz) and assign an instantaneous phase to the LFP time series via the analytical signal approach (Hilbert phase) [Le Van Quyen 2001]. Thus, the LFP phase corresponds here to the angle of the complex Hilbert transform of the LFP signal. A histogram of the LFP phase values at which the neurons spike is shown in Figure 3.13, with π corresponding to the LFP troughs (vertical dashed line in the figure).

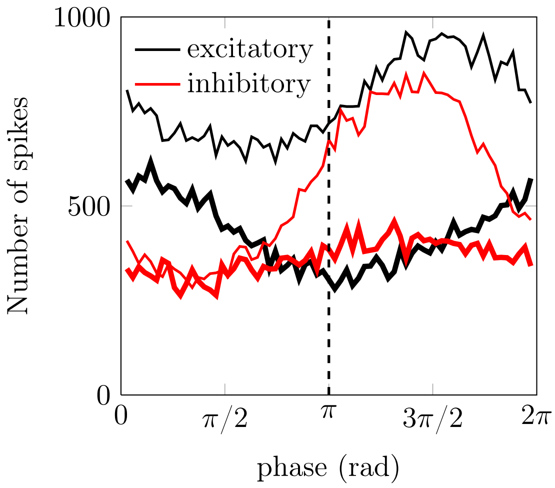

Figure 3.13: Distribution of LFP phase values at which neurons spike. The plot distinguishes between spikes flanking ISIs with fast (thick lines) and slow (thin lines) firing modes, for both excitatory (black) and inhibitory (red) neurons. Measures were performed over the same data used in Figure 3.11. The dashed line marks the π phase that corresponds to the LFP minimum.

Spike firings are widely distributed over the 2π cycle of the LFP phase because, as seen from the raster plot of Figure 3.5(c), the firing activity is noisy and the correlation between neurons is weak, due to their low coupling and the absence of a common drive. We have performed the spike-LFP phase locking analysis for both high-firing (thick lines) and low-firing (think lines) events, taking only into account the first spikes of short and long ISIs, respectively. Figure 3.13 shows that the slow firing regime of the inhibitory neurons (red thin line) is more sensitive to the LFP phase than the fast firing regime (red thick line), resulting in a more pronounced locking to the troughs of the LFP, with a delay ≥ 2 ms due to the mean synaptic delay. The high-firing mode of the excitatory neurons (black thick line), on the other hand, is phase-locked with no delay to the LFP peaks around 0 (note that no synaptic delay is considered in the external train of spikes, which as mentioned above controls the high-firing regime).

3.4 Conclusions

In Section 3.3.1 we have shown that the fast fluctuations of the excitatory external rate induce high instantaneous firing rates, and thus this mode encodes the fast dynamics of the input. In Section 3.3.2 we have additionally shown that the occurrence of spikes relative to the LFP phase depends on the firing mode. In particular, the high-frequency mode appears with higher probability when inhibition is maximal (the LFP phase is 0) and the low-frequency mode appears when inhibition is minimal (at the rising LFP phases near π). This constitutes a mechanism of phase coding that complements the rate-coding mechanism depicted in Figure 3.10, according to which fast external fluctuations were unambiguously encoded by a high-frequency bursting activity of the neurons. Therefore, the redundancy in the internal representation of external rates at $\langle\lambda(t)\rangle_{\mathrm{ISI}} \sim \langle\lambda(t)\rangle_{\mathrm{t}}$, by the single-neuron firing rates (i.e. 1/ISI), is resolved by the implementation of a phase code, in which the spiking times reveal the LFP phase. This allows the network to encode for the phase of the global oscillations, since in each one of the two modes the locking of the individual spikes to the gamma rhythm is different, as described in Section 3.3.2.

In conclusion, the balance of an excitatory synaptic current by a strong inhibitory current yields a discontinuity in the firing rate of individual neurons forming a neuronal network. The highest instantaneous rates encode fast fluctuations of the external stimulus, while the spiking times of the network occurring at moderate fluctuations of the input with respect to the mean encode the phase of the LFP. Therefore neuronal networks can efficiently implement two coding strategies: (i) a rate code for the fast bursting mode, sensitive to rapid changes in the processing of stimuli, and (ii) a phase code for the slower input fluctuations, according to which isolated spikes occur at the troughs of the LFP, whereas bursts of frequency higher than the gamma peak of the global oscillations arise at the peaks of the LFP. This second feature might contribute to an internal cortical representation of the input. In summary, these results show that cortical population activity depends non-trivially on the dynamical properties of the underlying neurons, and that global population measures shape the firing dynamics of the constituent cells, allowing for multiple encoding mechanisms to be implemented in networks with balanced excitation and inhibition [Sancristóbal 2013b].

Chapter 4

Interactions between collective neuronal oscillations in the gamma range

Contents

4.1 Coordinated rhythmicity in the cortex

The extracellular potential recorded from the cortex, either directly from the tissue or from the scalp, displays a variety of coexisting rhythms that are activated by distinct brain states [Buzsáki 2004]. By way of example, slow rhythms (less than 1 Hz) predominate under anesthesia and sleep [Steriade 1993a, Steriade 1993b], whereas fast rhythms (within the so-called gamma range, 30 Hz–90 Hz) appear during cognitive behavior [Tallon-Baudry 1997, Pulvermüller 1997, Gruber 1999] and perception [Gray 989b]. The mechanisms underlying the origin of these oscillatory signals and their functional role are both still a matter of debate, but published research provides evidence that electrical signals recorded from the brain are not an epiphenomenon.

In order to understand the functional significance of macroscopic cortical oscillations (arising from the activity of thousands of neurons), electroencephalography (EEG) or magnetoencephalography (MEG) recordings showing the enhancement of certain rhythms following stimulation is not sufficient.

The appearance of certain task-related EEG rhythms points out which cortical areas are involved in the performance of an action (see Figure 4.1), but does not tell us whether or not oscillations are secondary effects of neuronal activity.

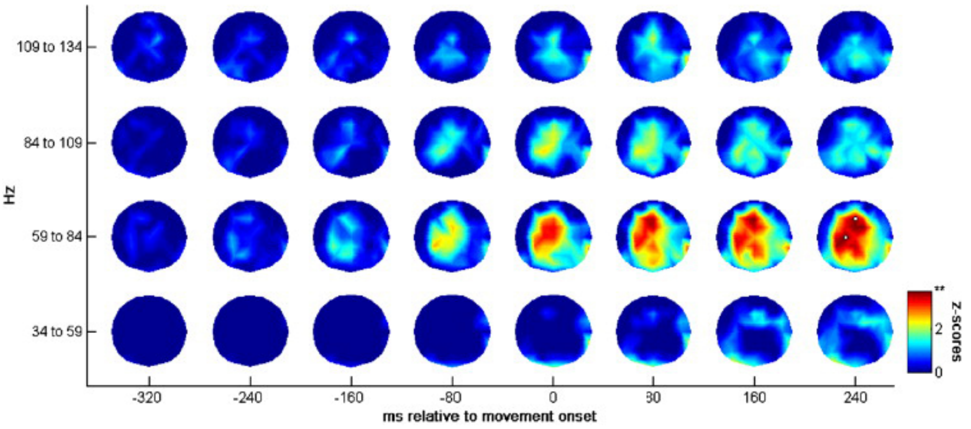

Figure 4.1: Spectral power change (Z-score) of EEG recordings in the high gamma range during an arm reaching task. From [Ball 2008].

The most prominent advantage of oscillatory signals is that they allow for a clock-like signal of the brain activity. At each frequency, a period T is defined and the time of occurrence of the action potentials can be internally interpreted as phases, $2\pi\frac{t}{T}$. In Section 3.3.2 we have seen that, within a neuronal network, bursts of spikes of high frequencies are elicited at local field potential (LFP) phases that are different from the phases at which single spikes are fired. Therefore, if two cell assemblies are structurally connected the signal traveling from one of them to the other (i.e. the presynaptic action potentials) carries the information about the presynaptic LFP phase. Moreover, because the postsynaptic LFP can also be defined in terms of a phase, we can understand modulations of the relative phases of two neuronal populations as regulation mechanisms of the effective communication between them. As introduced in Section 1.6, the LFP registers the synaptic activity surrounding the vicinity of the tip of the electrode resting on the tissue. Thus, fluctuations of the LFP reveal fluctuations in the synaptic currents which ultimately excite or inhibit the neurons. In our model [see Equation (A.14)], the troughs of the LFP (or equivalently the π-LFP phase) represent minima of the GABAergic inhibitory current, when most of the single spikes are triggered synchronously and when most neurons are closer to the spiking threshold. A population receiving this suprathreshold activity, whose rhythm is not influenced by the sending population and whose phases vary independently, will not respond with a corresponding firing activity if it does not receive the excitatory input consistently at its peaks of excitability (i.e. at the π-LFP phase).

Actually, it has been hypothesized that these recurrent periods of temporary spike synchronization provide a method of enhancing the effective connectivity across neuronal ensembles [Harris 2003]. Within that scenario, interactions among neuronal populations could be modulated in time, with this modulation representing information to be transmitted, and the routing of that information could be coordinated across different brain areas, in order to subserve coherent brain functions. This mechanism is referred to as *communication through coherence* (CTC) [Fries 2005]. Provided that it is verified that the brain benefits from CTC, neuronal oscillations will certainly accomplish an important function in coordinating brain-processed information, which is key to perception.

The CTC hypothesis relies on the fact that, as mentioned above, the collective oscillations affecting a neuronal population lead to a periodic modulation of the excitability of the participating neurons, whose firing is most likely to occur only within specific (and periodically repeating) time windows gated by the global cycle. When two oscillating populations of neurons have a well-defined phase relationship between their collective oscillations, conditions can be reached for which spikes sent by one population will reach the other population at the appropriate time window, and will do so systematically, thus leading to an effective transmission of information between the two groups of neurons. The two oscillators must thus operate in a coordinated manner for CTC to occur.

The coherent dynamics of coupled oscillators is a long-standing scientific question, starting with Christian Huygens' observation in 1665 of two pendulum clocks swinging in synchrony. Since then an extensive body of work has shown that coupled rhythms are ubiquitous in nature, from the macroscopic beating of pacemaker cells in the heart [Verheijck 1998] to the mammalian circadian clock [Yamaguchi 2003]. The mechanisms generating the oscillatory dynamics and the nature of the coupling take many forms. In the case of Huygens's clocks, the two oscillators are basically indistinguishable and they influence each other continuously and identically, i.e. they interact via a symmetric bidirectional coupling. On the other hand, the most common way through which neurons connect to each other, namely chemical synaptic coupling, is unidirectional and pulsed: the synapse is only active when the membrane voltage of the presynaptic neuron exceeds a certain threshold, triggering the release of neurotransmitters that will travel to and affect the postsynaptic neuron. An additional source of complexity in the study of synchronization between neuronal rhythms stems from the fact that the oscillations in neuronal assemblies emerge collectively from the activity of a large number of coupled *non-oscillatory* neurons. For these reasons, the standard approach to study the synchronization and coherent dynamics of coupled oscillators [Pikovsky 2001] cannot be applied to the CTC scenario in a straightforward way.

In this Chapter we will address the plausibility of the CTC hypothesis in a network model of connectivity. We consider two networks of 2000 neurons each, described by a conductance-based model [Sancristóbal 2013b]. Modeling assumptions similar to those of Chapter 3 are done: (1) the population is divided into 80% excitatory and 20% inhibitory neurons; (2) only AMPA and GABAergic chemical synapses are considered and (3) all neurons are driven above threshold by an external Poisson spike train, representing the thalamocortical input coming from non-simulated neurons [see Appendix A.2]. The high firing activity triggered in the inhibitory population elicits a strong recurrent inhibition capable of balancing excitation, and therefore neurons fire sparsely and irregularly, mostly fluctuating below threshold. This process, in which the inhibitory current follows the excitatory current leading in turn to another surge in inhibitory current, results in an oscillating LFP [Brunel 2003b]. All synaptic couplings in the model are considered to be subject to delay, which are shorter within a network and larger between networks. Furthermore, only excitatory neurons project onto neurons from another population. Unlike the network architecture used in Chapter 3 in which the neurons were randomly coupled, the networks considered in this Chapter show a certain degree of clustering (see Appendix A.2.2).

4.2 Modulation of neuronal oscillations in an isolated neuronal population

Experimental studies have revealed the importance of inhibitory neurons in generating gamma rhythms [Whittington 1995, Fisahn 1998]. These oscillations arise at the level of neuronal populations despite irregular single-unit discharges [Softky 1993, Stevens 1998b]. Computational models have shown that collective oscillations and highly irregular firing by single neurons are indeed compatible in noisy networks with strong recurrent inhibition [Brunel 2003b, Geisler 2005, Sancristóbal 2013b]. In this case, the oscillations emerge from the transient synchronized activity of neuronal assemblies, and thus can only be detected by population measures such as the local field potential (LFP) and multi-unit activity (MUA).

We first describe the LFP and multi-unit activity from the excitatory/inhibitory population (eMUA/iMUA) of a single network of 2000 neurons [see Appendix A.2.1 for a full description of the model] in order to discuss the characteristics of the power spectra of the neuronal populations in isolation. Figures 4.2(a) and (c) show the power spectrum of the LFP and MUA signals for increasing values of the GABAergic synaptic decay time, τ^{d}_{GABA}. Larger values of τ^{d}_{GABA} give rise to slower oscillations [Whittington 1995], as revealed by a shift of the gamma frequency peak towards the left. Changing of τ^{d}_{GABA} from 5 to 11 ms covers a frequency shift of $\sim$ 20 Hz from 43 to 27 Hz, and thus allowing to scan the peak frequency from middle gamma to high beta. A similar effect has been experimentally observed in the visual cortex when the contrast of the stimulus decreases [Ray 2010]. We also notice that the peaks of the iMUA spectra shows a good correlation with those of the LFP. eMUA, however, only follows the peaks of the iMUA for $\tau^{d}_{\mathrm{GABA}} = 5$, 6, and 7 ms.

In order to filter out the low-frequency contribution of the signals, we normalize the power spectra of Figures 4.2(a,c) with respect to the case of a vanishingly small gamma rhythm ($\tau^{d}_{\mathrm{GABA}} = 11$ ms), Figures 4.2(b,d). This measure, known as *power spectrum modulation*, was previously seen to increase in the gamma range (for the case of the LFP) for increasing stimulus contrast [Henrie 2005]. This behavior is attributed to the raise of the average firing rate of the lateral geniculate nucleus (LGN) with increasing contrast [Kaplan 1987]. Accordingly, most computational studies [Brunel 2003b, Mazzoni 2008] have modeled a variance in contrast by means of a change in the rate of the external spike train, $\langle\lambda(t)\rangle$, exciting the population [see Equation (A.5)]. As shown in Figure 4.2(a) below, activity measures such as the LFP, registered during the awake state, have a complex power spectrum characterized by $1/f^{\alpha}$-like profiles, where f denotes the frequency. Therefore, slower rhythms greatly contribute to the collective dynamics and modulate the amplitude of faster ones [Buzsáki 2012].

However, varying the external firing rate produces changes in the average LFP, thereby mixing the effect of the external signal with that of the intrinsic dynamics of the population. To avoid this, we have used τ^{d}_{GABA} instead of the external firing rate to tune the network oscillation frequency. Both strong external input to an area and low intrinsic (or stimulus-driven) τ^{d}_{GABA} are consistent with an intense firing activity of the neuronal population, and in principle also with changes on the mean LFP. Therefore, both parameters have a similar effect on the network properties, despite the fact that one of them (the external firing rate) acts upon the excitatory synaptic current and the other one (τ^{d}_{GABA}) affects the inhibitory current. In the present Chapter we have varied the inhibitory synaptic conductances together with τ^{d}_{GABA}, in order to maintain the amplitude of the inhibitory postsynaptic potential constant. Thus, different values of τ^{d}_{GABA} produce different gamma frequency peaks without substantially varying the mean LFP [see Figures 4.3(a) and (b)]. In contrast, similar frequency increments caused by the external rate

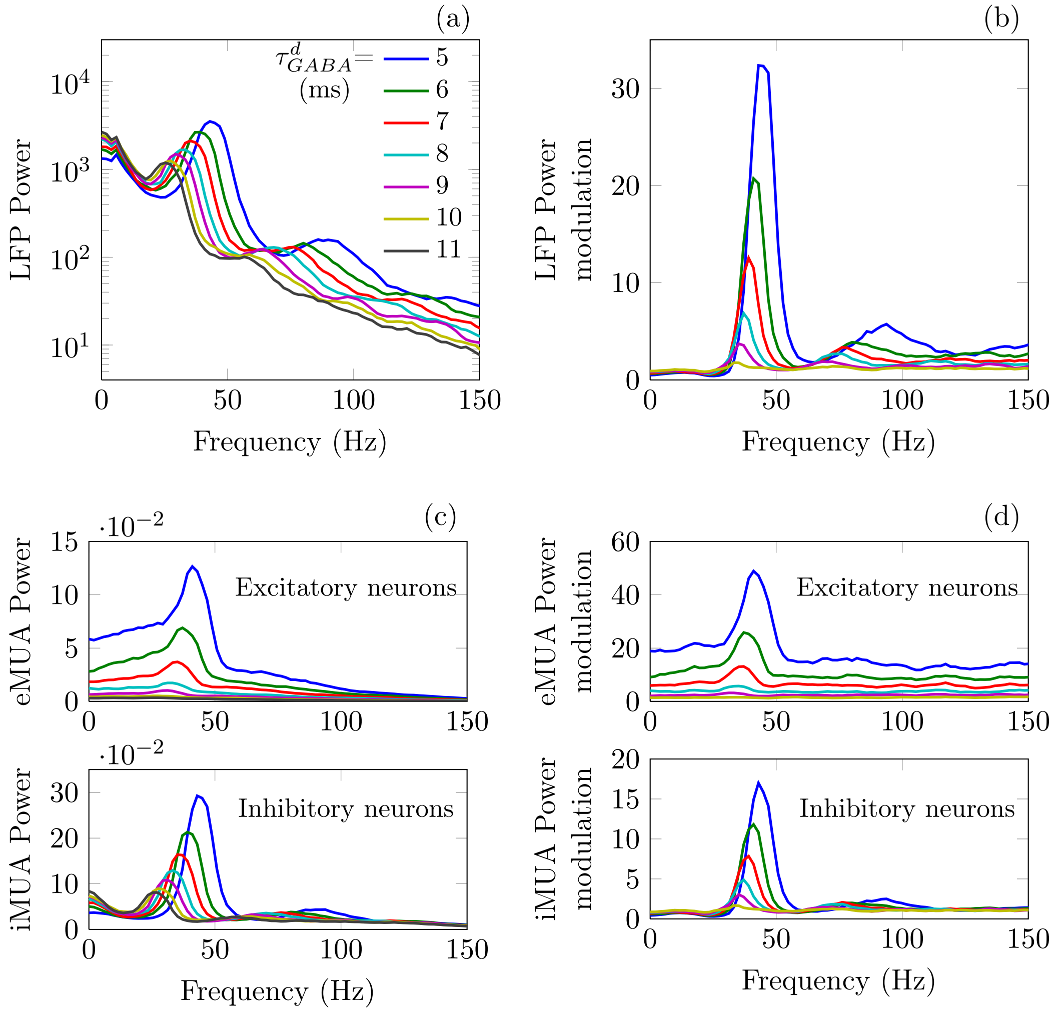

Figure 4.2: (a) LFP power spectrum and (c) MUA power spectrum (for the excitatory population in the top panel and the inhibitory population in the bottom panel) of the neuronal network for different values of the GABAergic synaptic decay time, τ^d_{GABA}. (b) and (d) show the corresponding power spectrum modulation with respect to the results at τ^d_{GABA}=11 ms.

lead to substantial changes in the mean LFP [see Figures 4.3(c) and (d)].

Our use of τ^d_{GABA} as the control parameter determining the frequency of one population does not presume, however, the existence of a patched distribution of IPSCs throughout the cortex. Neither do we assume that neuronal assemblies separated a few micrometers have widely distinct inhibitory dynamics. Nevertheless, previous works have revealed a wide heterogeneity among inhibitory neurons [Buhl 1994, Kang 1994, Puia 1994, Kawaguchi 1997, Houston 2009], suggesting that modulation of the dynamics of those cell types could provide a mechanism to control the gamma rhythm.

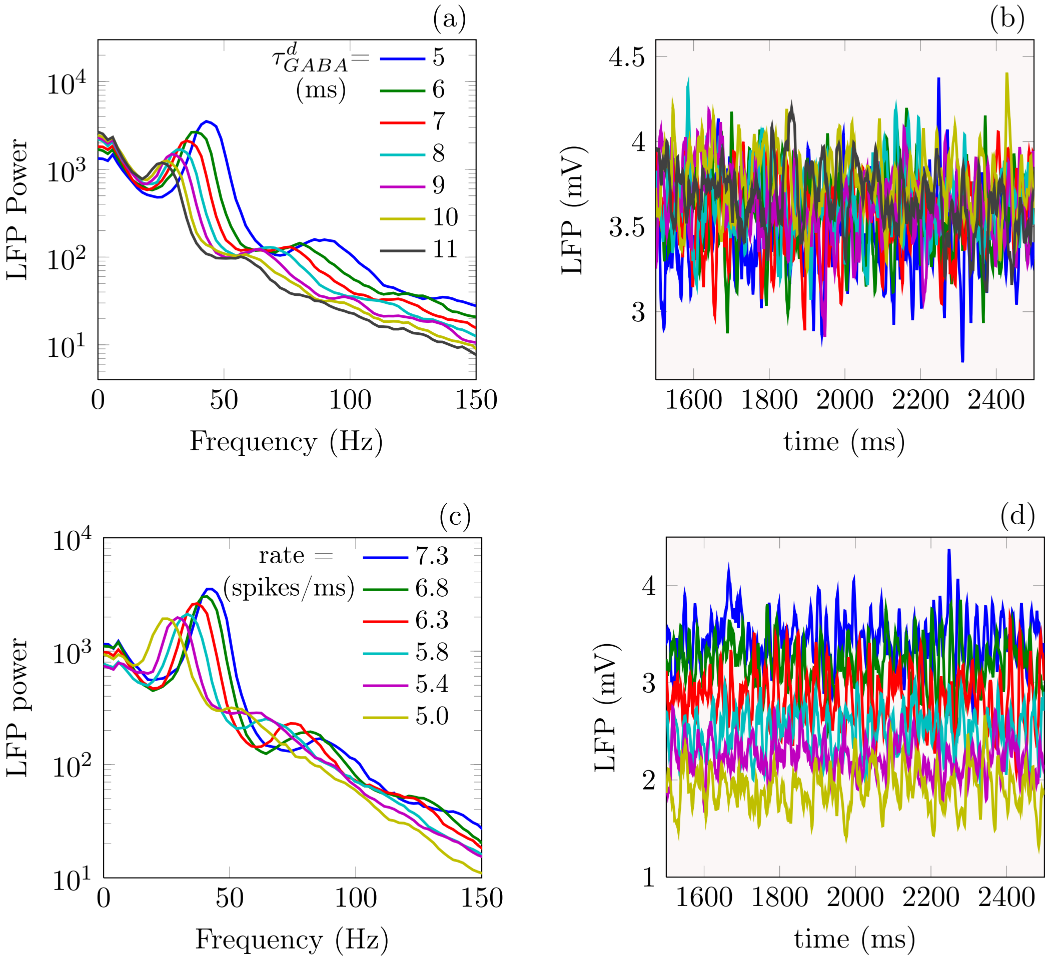

Figure 4.3: LFP power spectrum of the neuronal network for different values of (a) the GABAergic synaptic decay time τ^d_{GABA} and (c) the mean external rate $\langle\lambda(t)\rangle_T$. Plot (a) corresponds to Figure 4.2(a). The corresponding LFP time traces over 1 s are plotted in panels (b) and (d) respectively.

Finally, the control of the oscillation frequency allows us to study the interaction of different cortical rhythms.

4.3 Coupled neuronal networks

As mentioned above, we consider two neuronal populations coupled bidirectionally only by excitatory synapses. We surmise that 60% of the excitatory neurons of each network project to 10% of neurons from the other pool. The connectivity between networks exhibits the same degree of clustering as the connectivity within a network (see Appendix A.2.2). Therefore, exciting a subpopulation of adjacent excitatory neurons from an area triggers a response in a well-defined subpopulation of neighboring neurons in the receiving area.

The LFP [see Equation (A.14)] mainly accounts for the summation of synaptic currents impinging on the neurons close to the vicinity of the tip of the electrode, thus defining a recording volume of tissue from an area with a radius of at least 250-500 μm [Berens 2010]. These currents arise from the spiking activity of neurons close to this integrated area, hence from short-range connections, and from neurons at farther distances making long-range connections (mainly excitatory neurons). Phase locking between two signals is achieved by means of the synaptic connections across areas. Since the output from an area arises from the action potentials generated within its excitatory neurons, the synaptic current received by the second area is close to the presynaptic excitatory multi-unit activity (eMUA). Thus, at peak frequencies of the presynaptic eMUA power spectrum [see Figure 4.2(c) top panel], the postsynaptic neurons receive a barrage of spikes that can eventually trigger synchronization between the firing of the two populations.

As predicted by the CTC hypothesis, particular phase relations between neuronal oscillations enhance the response of a brain area (e.g. a cortical column) to presynaptic inputs coming from another area. If this situation is sustained in time and across multiple presentations of the same stimulus, two neuronal populations can share information about different features of the same perceptual object, and disregard information related to other stimuli. An important constraint for this to happen is the matching of the phase difference ($\Delta\phi$), synaptic time delay (τ_{syn}) and frequency (f) of the oscillations, which should fulfill the condition $\Delta\phi = 2\pi f \tau_{\mathrm{syn}}$ [see Figure 4.4(a)]. When this relationship holds, spikes fired in the emitting population at a specific phase of the signal (for instance at the troughs of the LFP, which correspond to the maxima of excitability) arrive at the receiving area at the same phase (and thus at the same excitability maximum), triggering a maximal response in the receiving area. On the contrary, if $\Delta\phi$ does not fulfill the relationship given above (or if it randomly varies), effective communication will not be achieved.

We consider here two mutually coupled neuronal networks at different gamma frequencies (Figure 4.5), studying how phase coherence depends on this frequency detuning. In all simulations the decay time in one of the two populations (referred to as fast population in what follows) is always held constant at $\tau^{d}_{\mathrm{GABA,f}} = 5$ ms (blue LFP traces in Figure 4.5). In the other population (slow population) the decay time $\tau^{d}_{\mathrm{GABA,s}}$ is varied from 5 ms to 11 ms (two cases are shown as turquoise and gray traces in Figure 4.5).

We characterize the rhythm in each population as the frequency in the gamma range at which the power spectrum amplitude is maximal (γ-frequency peak from now on) and we plotted it in Figure 4.6 as circles. Empty circles

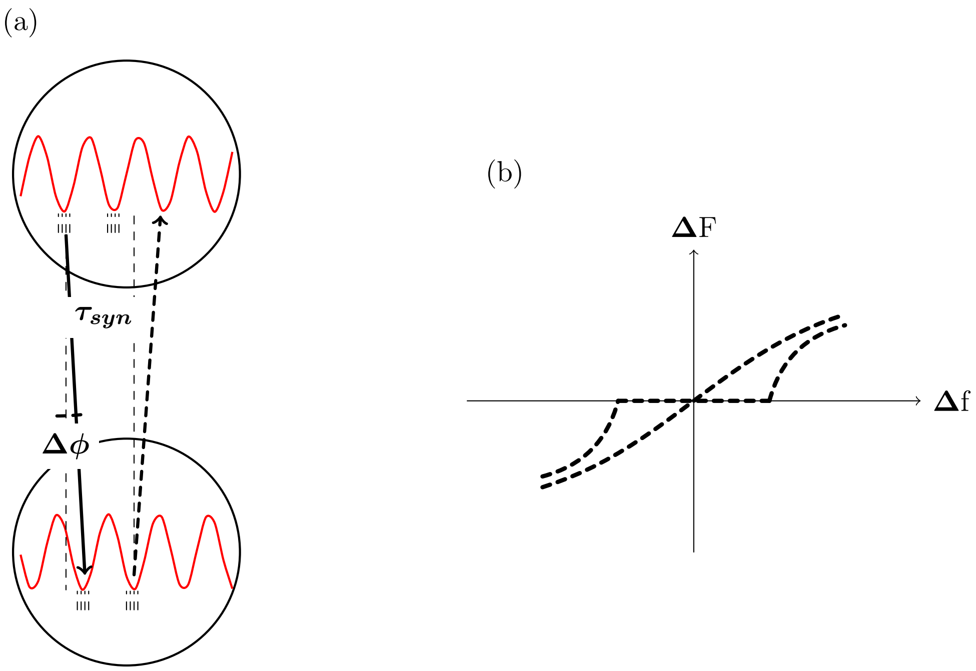

Figure 4.4: (a) The two networks are represented by circles and the synaptic bidirectional coupling by thin arrows. The LFP signal filtered at a frequency f is plotted in red. At the bottom of the LFP troughs (peaks of excitability in our case), the vertical ticks stand for the elicited spikes. Each bundle of spikes reaches the other population after a synaptic delay, τ_{syn}. If the difference in phase settled by the synaptic coupling, $\Delta\phi$, satisfies the relationship $\Delta\phi = 2\pi f \tau_{\text{syn}}$, an effective communication (like the one represented in this figure) is achieved. Scheme based on [Fries 2005]. (b) Frequency detuning before, Δf, and after, ΔF the coupling of two oscillators. For the dashed curve, only at relatively small Δf values, a frequency locking region is revealed by the coupling (for more information see [Pikovsky 2001]). In contrast, the solid curve does not show frequency locking, even at small Δf.

(filled circles) correspond to the fast (slow) population. The frequency detuning in the absence of coupling (which corresponds to the vertical distance between the blue circles in Figure 4.6 and to the Δf magnitude in Figure 4.4) is only equal to zero for two identical networks, i.e. $\tau^d_{\text{GABA,f}} = \tau^d_{\text{GABA,s}}$, and corresponds to the Δf magnitude in Figure 4.4(b). The excitatory interareal connectivity enhances the spiking activity of each population, and thereby speeds up the LFP and MUA oscillations. As a consequence of the longer duration of the GABAergic synapses, the slow population has weaker spiking activity (note the decrease in the MUA power spectrum amplitude of Figure 4.2(c) as $\tau^d_{\text{GABA,s}}$ increases), and the excitatory input from the slow to the fast population is reduced. Since the fast population fires more spikes per unit time, its effect on to the slow population is stronger than in the reverse direction. Therefore, the frequency shift towards faster gamma rhythms

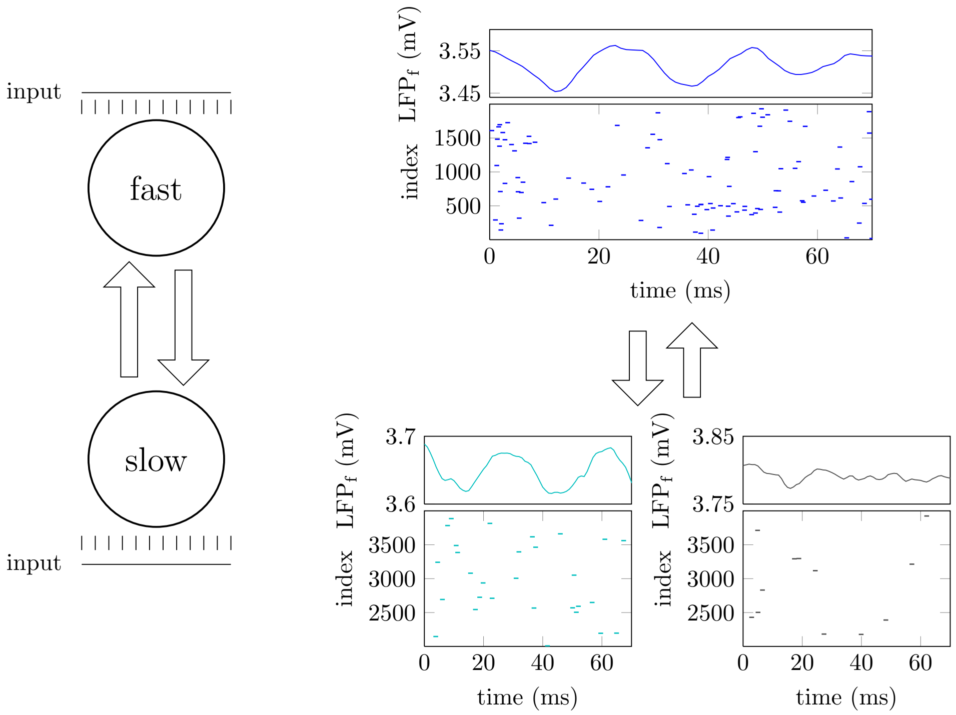

Figure 4.5: Left: The two neuronal networks are represented by circles and the synaptic coupling by arrows. The vertical ticks next to each circle stand for the external Poisson train of spikes, whose mean firing rate is qualitatively plotted with a line at the right of the *input* label, i.e. $\langle\lambda(t)\rangle$. Top-right: Raster plot and LFP for the fast population ($\tau^d_{\mathrm{GABA,f}} =$ 5 ms). Bottom: Raster plot and LFP for two different behaviors of the slow population at $\tau^d_{\mathrm{GABA,s}} = 8$ ms (left) and $\tau^d_{\mathrm{GABA,s}} = 11$ ms (right) showing distinct gamma-rhythms and firing intensities. LFPs are averaged over 200 trials.

caused in the slow population is larger than the one produced in the fast population (compare gap between filled circles and empty circles). As a result, the excitatory interaction between areas promotes a decrease in the frequency detuning [vertical distance, in Hz, between the red circles of Figure 4.6, which corresponds to the ΔF magnitude in Figure 4.4(b)].

As shown in Figure 4.6, no frequency-locking region appears due to the coupling between the two networks. The gamma peak of the fast population (empty red circles in Figure 4.6) remains at frequencies larger than the one of the slow population (filled red circles in Figure 4.6) for all values of $\tau^d_{\mathrm{GABA,s}}$. Given the lack of frequency locking, one might expect that two neuronal populations would not exhibit phase coherence (unless their intrinsic frequencies were identical). This expectation does indeed hold for the case of coupled self-sustained oscillators with a well-defined period, whose phase difference outside the frequency synchronization region varies in time [Pikovsky 2001]. The complex spectrum of our neuronal oscillations, how-

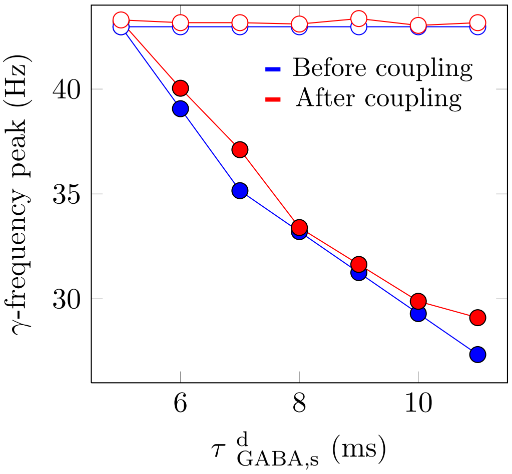

Figure 4.6: The frequency at the maximum peak in the gamma region (30 Hz - 90 Hz) of the LFP power spectrum is plotted against $\tau^d_{\mathrm{GABA,s}}$ for the two networks before (blue circles) and after (red circles) coupling averaged across 200 trials. Filled and empty circles correspond to the slow and fast population, respectively.

ever, allows for partial phase coherence to arise in specific frequency regions, in particular around the gamma band. Coherence measures are independent of the amplitude of the power spectrum and quantify, between 0 and 1, how consistent the phase difference $\Delta\phi$ is between pairs of oscillations. This is shown in Figure 4.7, which display in a colormap the phase coherence between the LFPs (a) and eMUAs (b) of the two populations for increasing frequency detuning between them (horizontally) and at different frequencies (vertically). We use here the eMUA signal, a measure of the spiking activity of the excitatory neurons, because the synapses between neurons belonging to different networks are always excitatory. In agreement with experiments [Schoffelen 2005, Womelsdorf 2007, Ray 2010, Bosman 2012], phase coherence is highest in the gamma range, and even in that region is only partial [perfect coherence would correspond to a value of 1 given our definition of phase coherence, see Equation (B.2)].

The connectivity between areas is, by construction, bidirectional, in the sense that interareal synaptic strengths are equal and the number of neurons from the receiving area being affected by a neuron in the sending area is the same, irrespective of the directionality of the coupling. However, the effect on one area on the other is asymmetric unless the firing activity of the two areas is the same (i.e. unless $\tau^d_{\mathrm{GABA,f}} = \tau^d_{\mathrm{GABA,s}}$) [Sancristobal2013b]. We have increased the gamma frequency peak of one of the areas by slowing down the inhibitory postsynaptic currents (IPSCs), i.e. by increasing the GABAergic synaptic decay time, τ^d_{GABA}. This parameter change produces a decrease in the firing activity, since longer IPSCs make the neurons unresponsive for longer periods of time. The phase coherence between the LFPs and eMUAs (defined in Appendix B.3) of the two networks for varying τ^d_{GABA} (and thus for varying frequency detuning) shown in Figure 4.7, was computed under the same structural connectivity through all Δf values.

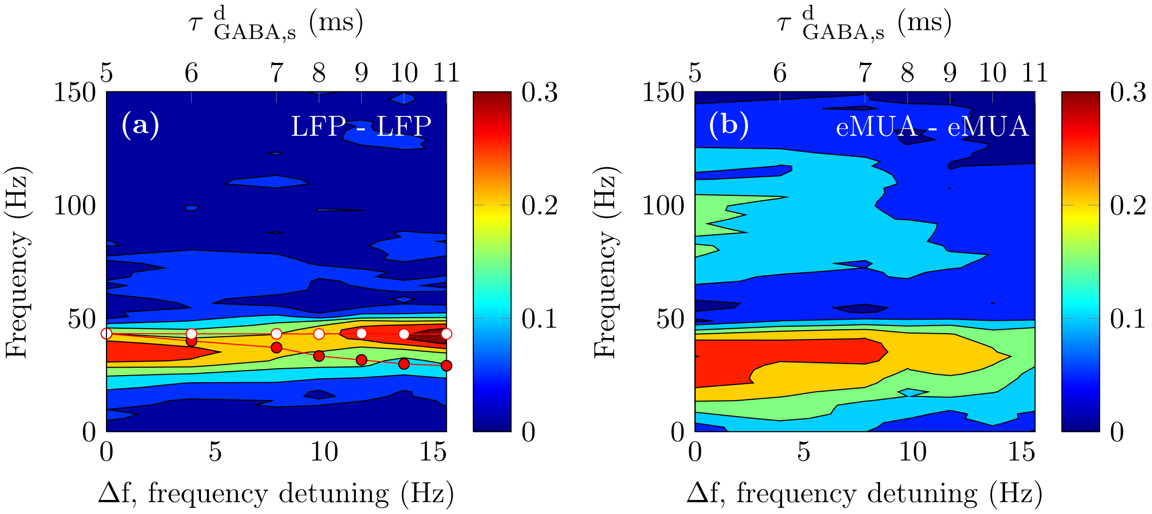

Figure 4.7: Phase coherence, in color code, as a function of frequency (y-axis) and of the intrinsic frequency detuning Δf (bottom x-axis), which is controlled by varying $\tau^d_{\mathrm{GABA,s}}$ (top x-axis), between the LFPs (a) and eMUAs (b) of the two populations. The intrinsic frequency detuning is the difference between the empty and filled blue circles of Figure 4.6. The red circles correspond to Figure 4.6.

A comparison between Figures 4.7(a) and 4.7(b) reveals a difference between the phase coherence of the LFP and eMUA signals. While the eMUA-eMUA phase coherence decreases continuously with increasing frequency detuning, the LFP-LFP phase coherence first decreases and then increases again for large detunings. Coherence measures, such as partial coherence, between individual pairs of spike trains have been used [Brillinger 1992, Brillinger 1994] to unravel direct interaction between neurons caused by common input. Here, we do not go in depth into the statistical dependencies between spike trains and we have instead studied the phase relationship between neuronal populations according to histograms of the fired action potentials.

In the frequency region where phase coherence exists, we have also quantified the phase lag between the oscillations which also reveals this contrasting behavior (see Figure 4.8, which shows the histogram of phase differences, $\Delta\phi$, between the two pairs of signals across three groups of 200 trials). In each case, the histogram is plotted for the frequency at which the phase coherence is optimal. The figure shows that while there is a relatively well defined phase difference between the LFP signals for increasing $\tau^d_{\mathrm{GABA,s}}$ (top row in

Figure 4.8), the distribution becomes broader for large $\tau^{d}_{\mathrm{GABA,s}}$ (and hence large detuning) in the case of the eMUA signals. An arrow is superimposed to the histograms, whose direction indicates the mean $\Delta\phi$ and whose length is inversely proportional to the standard deviation of the angle distribution and thus, is a measure of phase coherence at this frequency (i.e. the larger the arrow the greater the phase coherence).

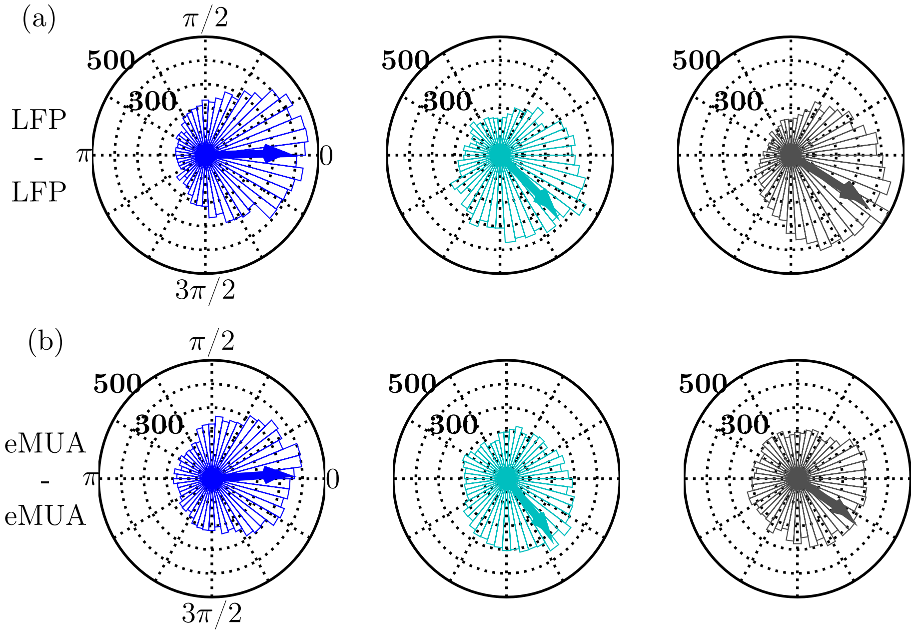

Figure 4.8: Angle histogram of the phase difference between the LFPs (a) and eMUAs (b) of the fast ($\tau^{d}_{\mathrm{GABA,f}} = 5$ ms) and slow oscillations [$\tau^{d}_{\mathrm{GABA,s}} = 5$ ms (left), 8 ms (middle), 11 ms (right)]. For each $\tau^{d}_{\mathrm{GABA,s}}$, the phase differences are computed at the frequency at which the LFP-LFP (a) and eMUA-eMUA (b) phase coherence are maximal across three groups of independent 200 trials. The thick arrows represent the mean values of the histogram (multiplied by a factor 5), which length is inversely proportional to the standard deviation, and thus, to the phase coherence at this frequency.

In order to grasp the origin of the different behavior of the phase coherence for the LFP and eMUA signals, we computed the effective time delay τ_e (see Appendix B.3) between the two pairs of signals as $\tau_e = \Delta\phi/2\pi f_{\max}$, where $\Delta\phi$ is again the phase difference at the frequency $f_{\max}$ of maximum phase coherence. The results are shown in Figure 4.9 for increasing frequency detuning Δf, and reveal that the two local maxima of phase coherence occurring at small and large detuning [Figure 4.7(a)] correspond to two different values of τ_e. Specifically, at small frequency detuning the LFP gamma rhythms of the two populations oscillate in phase ($\tau_e \simeq 0$), while at large frequency detuning there is a phase shift that matches the average synaptic delay time between the populations ($\tau_e \simeq 2$ ms), (see Appendix A.2.2). Thus Figure 4.9(a) reveals two scenarios: *simultaneous (*or *zero-lag) synchronization* between the LFPs for small frequency detuning, and a *leader-laggard regime* for large detunings, with the slow oscillation (laggard) following the fast one (leader) with a lag equal to the time it takes the neuronal signals to travel from the emitter to the receiver population (the synaptic delay). In the latter case, despite the fact that the structural connectivity is bidirectional, the functional connectivity is closer to a unidirectional coupling since the slow excitatory population fires at a lower firing rate than the fast excitatory population, as explained before. The effective time delay τ_e is then given by the synaptic delay, because the fast population drives the slow one, which adjusts passively its LFP phase to the leader.

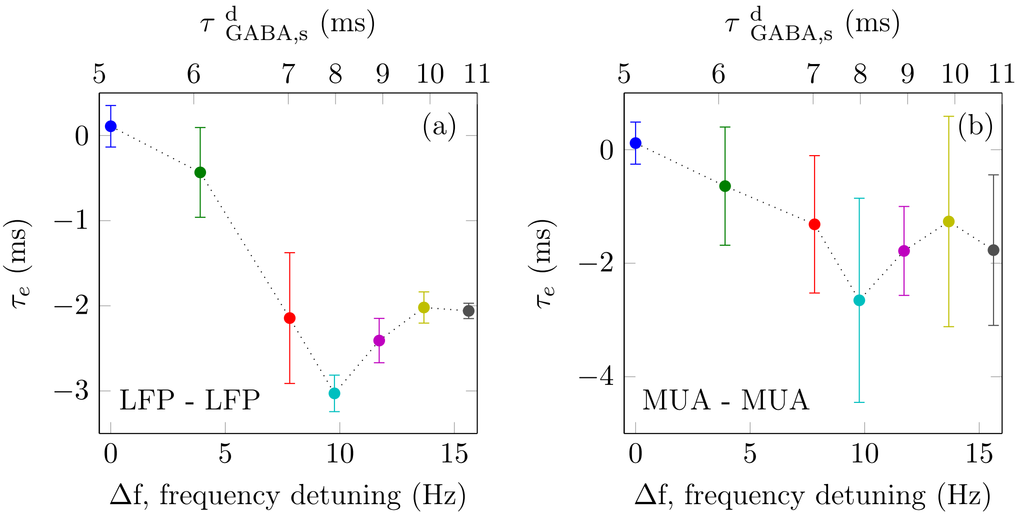

Figure 4.9: The effective time delay, τ_e, computed at the frequency of maximum phase coherence of Figures 4.7(a) and (b), is shown as a function of the intrinsic frequency detuning (bottom x-axis), which is controlled by varying $\tau^{d}_{\mathrm{GABA,s}}$ (top x-axis), between the LFPs (a) and eMUAs (b) of the two populations. The mean and sample standard deviation are computed across three groups of independent 200 trials.

In the presence of strong frequency detuning ΔF after coupling, the frequency at the maximum of the LFP-LFP phase coherence, ∼43 Hz, is close to the γ-frequency peak of the LFP power spectrum of the leader population [see red empty circles in Figure 4.7(a)]. However, in this situation the slow rhythm still dominates the oscillatory dynamics of the laggard population (see red filled circles of Figure 4.6), even though the LFP phases of the populations are partially synchronized at the maximum frequency of the leader population. Importantly, the eMUA activity of each population is locked in almost anti-phase to its own LFP signal at the gamma frequency peak (i.e. the spikes of each excitatory population fire preferentially closer to the troughs of its LFP).

Figure 4.10(a) shows an histogram of the phase difference between the LFP and eMUA of the slow population computed at the frequency of maximum LFP-eMUA phase coherence. At this frequency, and for any given value of $\tau^{d}_{\mathrm{GABA,s}}$, the eMUA is shifted $\sim 3\pi/4$ with respect to the LFP. In Figure 4.10(b) the filtered LFP and eMUA signals (blue and red traces respectively) around the frequency of maximum LFP-eMUA phase coherence for two values of $\tau^{d}_{\mathrm{GABA,s}}$=5 ms are shown. Despite the fluctuations in the phase shift between the blue and red traces [LFP-eMUA phase coherence is below 1 and decreases with increasing $\tau^{d}_{\mathrm{GABA,s}}$ as shown by the broadness of the phase histogram in (a)], we can observe the almost anti-phase synchronization between these two signals.

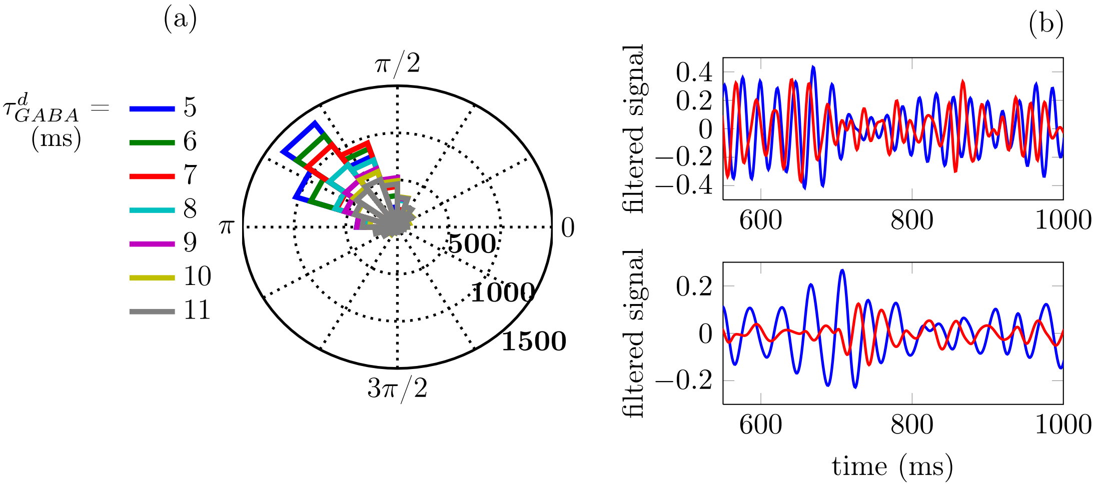

Figure 4.10: (a) Angle histogram of the phase difference between the LFP and eMUA at different $\tau^{d}_{\mathrm{GABA,s}}$ values of the slow population at the frequency of maximum LFP-eMUA phase coherence. (b) Two filtered LFP and eMUA signals (blue and red traces respectively) around the frequency of maximum LFP-eMUA phase coherence for $\tau^{d}_{\mathrm{GABA,s}}$=5 ms (top) and $\tau^{d}_{\mathrm{GABA,s}}$=11 ms (bottom).

The lack of gamma frequency locking in the leader-laggard regime prevents the LFP synchronization from triggering eMUA synchronization. Accordingly, the eMUA-eMUA phase coherence [Figure 4.7(b)] shows the loss of synchronization between the excitatory spikes of the two populations as the frequency detuning increases. On the other hand, at low frequency detunings both the LFP-LFP and eMUA-eMUA show synchronization with significant phase coherence at zero-lag, as shown by the blue and green circles in Figure 4.9. In summary, low frequency detuning entails zero-lag LFP synchronization, while higher frequency detuning leads to a non-zero phase lag. In the latter case the population with the smallest τ^{d}_{GABA}, and thus with the highest firing rate and fastest dynamics, becomes the leader. Besides, as the difference in τ^{d}_{GABA}

increases, the AMPA synapses from the leader to the laggard area are less effective and the eMUA-eMUA phase coherence drops to zero.

4.4 Communication between two neuronal populations

In the previous Section 4.3, we have numerically studied the emergence of phase coherence between two neuronal networks exhibiting oscillations at varying frequency peaks in the gamma band (with different τ^d_{GABA}). Experimental results [Ray 2010] show that neuronal assemblies in V1 cortex are entrained to different gamma rhythms for stimuli of varying contrast. It is well known that general interacting oscillators with well defined frequencies are able to synchronize their rhythms, thus leading to phase coherence, provided that their intrinsic frequencies are similar enough [Pikovsky 2001]. Conversely, given a strength of interaction there is a maximum frequency detuning above which coupling-induced frequency locking is forbidden (see Figure 4.4(b)). However, we have seen in the previous Section that in the case of neuronal oscillatory signals phase coherence appears despite a mismatch in the peak frequencies, due to their broad-band power spectrum [see Figure 4.7(a)].

In order to establish the conditions that lead to an efficient communication and its relation to the phase coherence maps, we have carried out the following test. First we increase, during a 100 ms window, the rate of the external Poissonian spike train impinging on around 160 long-range excitatory neurons from the emitter population [see sketch from Figure 4.5]. In those conditions, neurons belonging to that subpopulation fire synchronously, locked to the corresponding LFP (note that the troughs of the LFP coincide with the activity peaks of the raster plot in Figure 4.11). We average the response of the receiver population across 200 trials, taking as time reference the first local peak of the fast oscillations after the onset of the perturbation [see maximum LFP value at 0 ms in the blue trace of Figure 4.11(right)]. The LFP can be considered as the carrier of the information conveyed by the action potentials measured by the MUA. Since we are only taking into account chemical synapses, spikes are the only electrical activity that is shared between the two modeled networks. The phase relationship achieved by the two LFP signals is meant to regulate the effectiveness of communication [Fries 2005]. In particular, an unreliable phase difference will always lead to a failure in communication, in what can be called *non-communication through non-coherence* [Bosman 2012]. Moreover, depending on the phase difference $\Delta\phi$ between two coherent LFPs the response of the unperturbed network will replicate to a certain extent the response of the other network to a perturbation.

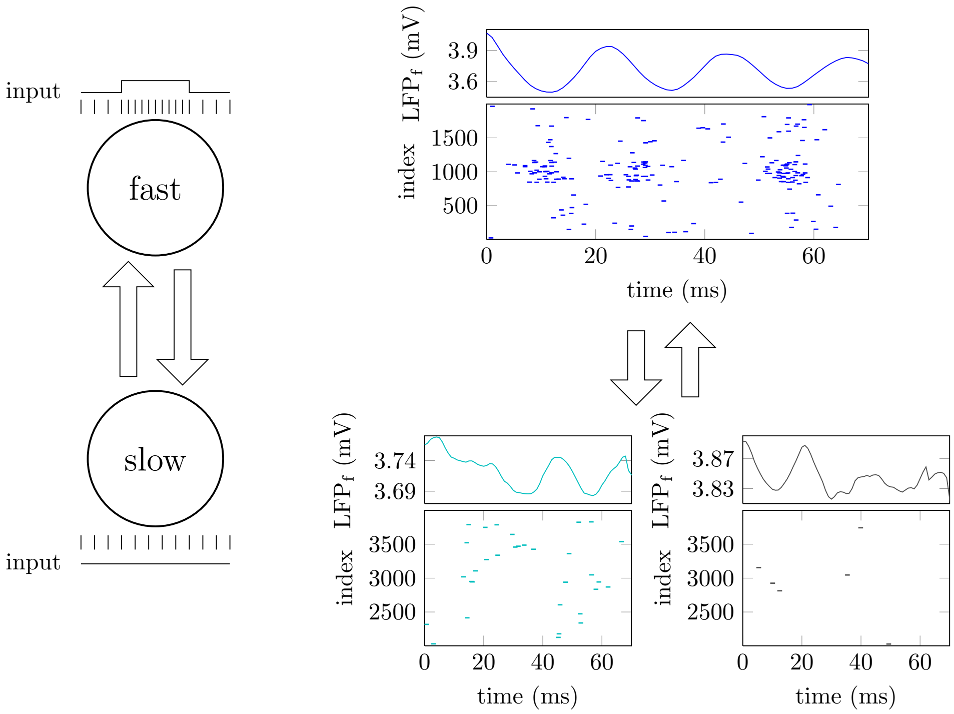

Figure 4.11: Left: The two neuronal networks are represented by circles and the synaptic coupling by arrows. The vertical ticks next to each circle stand for the external Poisson train of spikes, whose mean firing rate is qualitatively plotted with a line at the right of the *input* label, i.e. $\langle\lambda(t)\rangle$. Top-right: Raster plot and LFP for the fast population ($\tau^{d}_{\mathrm{GABA,f}} = 5$ ms). Bottom: Raster plot and LFP for two different behaviors of the slow population at $\tau^{d}_{\mathrm{GABA,s}} = 8$ ms (left) and $\tau^{d}_{\mathrm{GABA,s}} = 11$ ms (right) showing distinct gamma-rhythms and levels of spike-to-spike synchrony. LFPs are averaged over 200 trials.

Above a certain level of phase coherence, provided the phase difference between the peaks of the signals from the two neuronal pools matches the synaptic delay, we expect that the firing activity of the receiver population (slow population) will thus copy the dynamics of the emitter population (fast population). In order for this to happen reciprocally between the two populations, phase coherence should occur at zero lag. Therefore, reciprocal information transmission between two populations will only be successful if an appropriate causal relationship between them exists in the two directions of communication. Figure 4.12(a) shows the averaged LFP time traces of the fast population (upper panel) and the slow population (decreasing values of $\tau^{d}_{\mathrm{GABA,s}}$ correspond to downward narrow panels) averaged across 200 trials and taking as time reference the first local peak of the fast oscillations after the onset of the perturbation. The time lag between the first maxima of the fast LFP and the slow LFP reveals, again, a transition from zero lag synchronization (blue trace in the narrow (lower) panel compared with upper blue traces) to a leader-laggard configuration (gray trace in the narrow panel compared with upper blue traces). When the fast population is perturbed, hence becoming the emitter population, its amplitude of oscillation increases [upper blue traces in Figure 4.12(b)] due to an increase in spike-to-spike synchrony (blue raster plot in Figure 4.5, right). The same applies to the receiver population [narrow panels in Figure 4.12(b)], which is entrained to the gamma frequency of the emitter in agreement with [Roberts 2013]. In particular, for high frequency detunings (gray –$\tau^d_{\mathrm{GABA,s}} = 11$ ms– and yellow –$\tau^d_{\mathrm{GABA,s}} = 10$ ms– traces for instance), the increase in the oscillatory behavior, i.e, the signal-to-noise ratio, of the LFP [compare Figure 4.12(a) and (b)] is clearly manifested. Naturally, at intermediate frequency detunings (turquoise trace –$\tau^d_{\mathrm{GABA,s}} = 8$ ms–) that led to small LFP-LFP phase coherence [Figure 4.7(a)], this effect diminishes.

The same comparison can be done between the eMUA signals before [Figure 4.13(a)] and after [Figure 4.13(b)] perturbing the emitter population. Note that both the LFP and eMUA signal amplitudes from the fast population are highest at 0 ms in Figures 4.12-4.13, as the time traces have been aligned to the first LFP (MUA) peak within the perturbation interval. For $\tau^d_{\mathrm{GABA,s}} > 7$ ms, the eMUA-eMUA phase coherence drops [Figure 4.7(b)]. Thus, the eMUA traces from the receiver population at large frequency detunings (narrow panels from turquoise to gray) show a transient increase in their amplitude [Figure 4.13(b)] but, in high contrast with the corresponding signals at lower frequency detunings (narrow panels from blue to red), the faster rhythm of the emitter population is not sustained.

Comparing the blue upper traces [top panels of Figures 4.12(b)-4.13(b)] with the blue trace in the narrow (lower) bottom panels, corresponding to the simulation with $\tau^d_{\mathrm{GABA,f}} = \tau^d_{\mathrm{GABA,s}} = 5$ ms, we observe an increase in oscillation amplitude for both the LFP and eMUA of the perturbed population (upper blue traces). Therefore, the fast network better modulates its output to the external train of action potentials by highly synchronizing its spiking times to the troughs of the LFP (see raster plot in Figure 4.5, top right). Due to the increasing frequency detuning at large $\tau^d_{\mathrm{GABA,s}}$ (Figure 4.6), and to the fact that the highest LFP-LFP phase coherence in that case occurs at the frequency of the fast network as a consequence of the leader-laggard regime [Figure 4.7(a)], the raw signals are not convenient for analyzing modulation at this frequency band. Since phase coherence is bounded, causality should be better tested as a function of the frequency. Figure 4.14(a,b) shows the time traces corresponding to the lower (narrow) panels in Figure 4.12(b) and Figure 4.13(b) respectively, band-pass filtered in the gamma range (20 Hz $-$ 70 Hz). Similarly to Figure 4.7(a), the minimum modulation also occurs at the minimum of LFP-LFP phase coherence, around $\tau^d_{\mathrm{GABA,s}} = 8$ ms [see turquoise

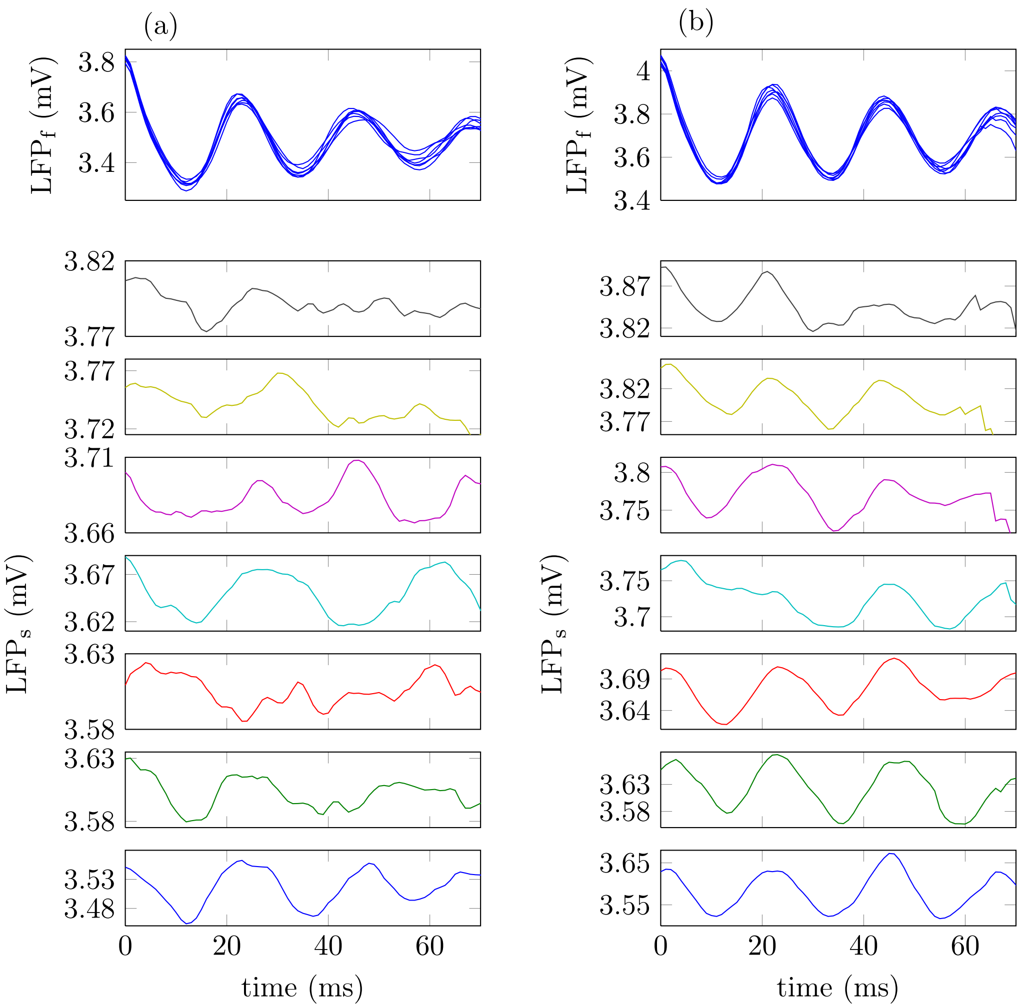

Figure 4.12: LFP traces before (a) and after (b) the perturbation applied to the fast population according to Figure 4.11. The blue LFP traces on the top panel correspond to the fast population at each $\tau^d_{\mathrm{GABA,s}}$. No major statistical changes are observed because this population is hold at constant $\tau^d_{\mathrm{GABA,f}} = 5$ ms. The narrow (lower) panels correspond to the LFP traces of the slow population at decreasing 1 ms-step $\tau^d_{\mathrm{GABA,s}}$ from top (11 ms) to bottom (5 ms). Therefore, frequency detuning also decreases from top to bottom. LFP are averaged across 200 trials. Colors as in Figure 4.10(a).

LFP trace in Figure 4.14(a)]. Moreover, the decrease in eMUA-eMUA phase coherence with increasing $\tau^d_{\mathrm{GABA,s}}$ (i.e. increasing detuning) shown in Figure 4.7(b), is also revealed by the modulation drop of the MUA signal [see dark grey MUA trace in Figure 4.14(b)].

Note that here we only study the modulatory effect of the fast population on the slow one, but similar results can be expected in the opposite direction. To prove a causal relationship between the activity of neuronal assemblies, we have compared the response of an area to an increase in the external in-

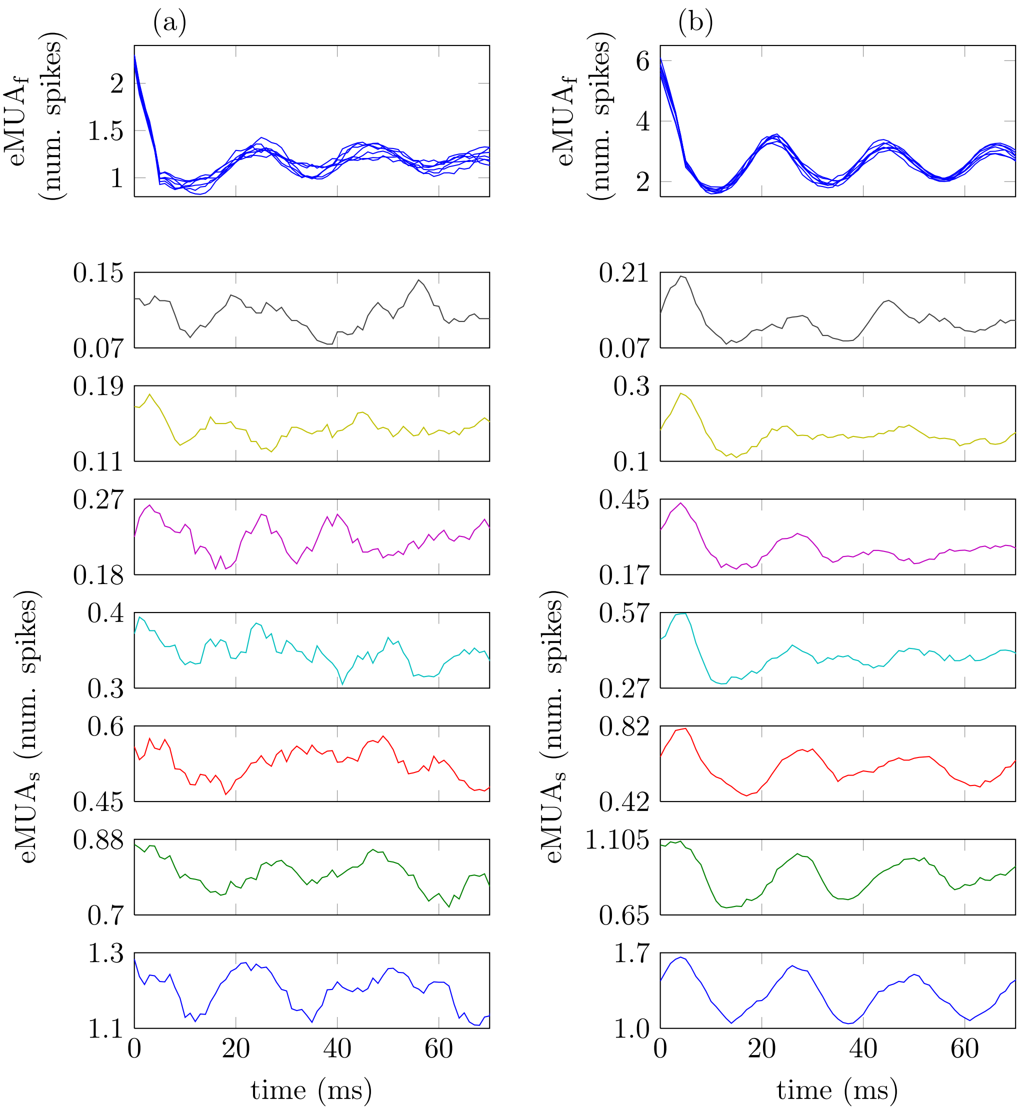

Figure 4.13: eMUA traces before (a) and after (b) the perturbation applied to the fast population according to Figure 4.11. The blue eMUA traces on the top panel correspond to the fast population at each $\tau^d_{\mathrm{GABA,s}}$. No major statistical changes are observed because this population is hold at constant $\tau^d_{\mathrm{GABA,f}} = 5$ ms. The narrow (lower) panels correspond to the MUA traces of the slow population at decreasing 1 ms-step $\tau^d_{\mathrm{GABA,s}}$ from top (11 ms) to bottom (5 ms). Therefore, frequency detuning also decreases from top to bottom. eMUA are averaged across 200 trials. Colors as in Figure 4.10(a).

put of the other area at the frequency of maximum phase coherence. Our results reveal an important requirement for the CTC hypothesis, namely that only in-phase synchronization of the LFP provides a scenario for communication across areas, otherwise phase coherence contributes to modulate the time course of the two LFPs without enabling an effective routing of information.

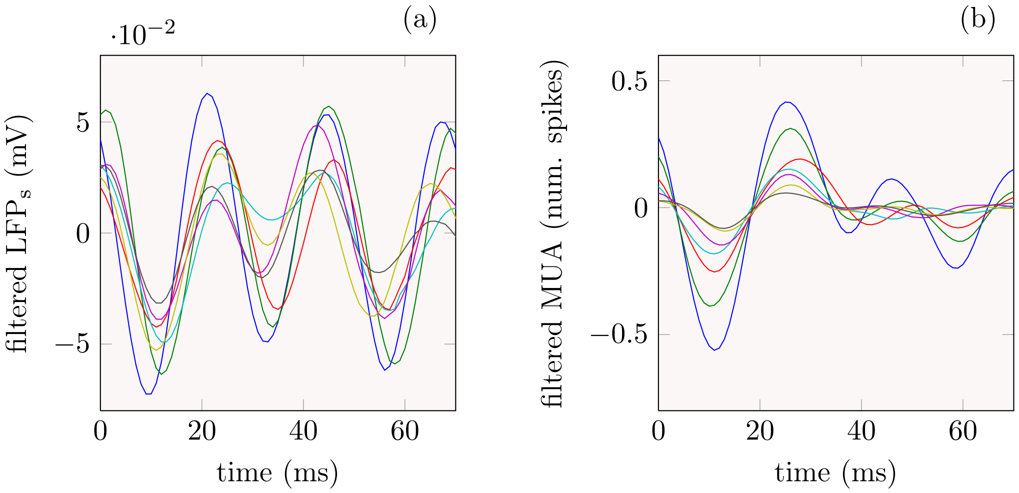

Figure 4.14: LFP (a) and eMUA (b) time traces for the receiver population, band-pass filtered in the range 20 Hz − 70 Hz, during the first 70 ms of the perturbation time interval. Note that the high-pass filter centers the signal around zero, thus leading to meaningless negative numbers of spikes in (b). Colors as in Figure 4.10(a).

4.5 Conclusions

An important aspect of cortical interactions is that a change in one parameter triggers multiple effects, making it difficult to isolate a single perturbation. For instance, a change in the gamma frequency rhythm of a neuronal population can be triggered, among other variables, by a change in the external synaptic input or in the synaptic time constants. In turn, this involves a variation in the firing activity of the population. In particular, in this chapter, we have seen that larger durations of the inhibitory synapses entail two related effects: a decrease in the firing activity of the neuronal population and a slowing down of the gamma rhythm of the LFP and MUA. Therefore, the effective connectivity across cell assemblies, which can be roughly quantified as the number of presynaptic spikes per unit of time arriving from another network, differs from the structural implemented connectivity as τ^d_{GABA} increases. Specifically, the synapses going from a slower to a faster population become less active than in the opposite direction as τ^d_{GABA} increases. As a matter of fact, the two extreme scenarios considered here, (i) $\tau^d_{\mathrm{GABA,f}} = \tau^d_{\mathrm{GABA,s}}$ and (ii) $\tau^d_{\mathrm{GABA,f}} \gg \tau^d_{\mathrm{GABA,s}}$, can be viewed respectively as (i) two hierarchically similar cortical networks with equivalent lateral connections, and (ii) two hierarchically different networks in which the feedforward and feedback connections are asymmetric. These functional pathways are usually referred to as *bottom-up* and *top-down*. It has been experimentally observed that the bottom-up stream triggers activity in upward areas. while the top-down stream primarily modulates downward signals [Desimone 1995] (for a complete review see [Knudsen 2007, Bastos 2012]).

The mechanisms behind the combination of sensory information processing with attention, memory and other cognitive tasks requires coordinated communication between different cortical areas. Our model shows a graded effective connectivity across networks that is endogenous to the system. We do not claim that our one-parameter control (i.e. τ^d_{GABA}) of the mutual influence between populations explains plastic cortical interactions, but consider it instead as a simple procedure to study the communication through coherence hypothesis [Fries 2005]. We observe that CTC naturally appears between networks with close gamma frequency rhythms with a zero-lag phase synchronization of both the LFP and eMUA signals, despite a non-zero synaptic delay. In this case, an input coming from other brain areas impinging on a neuronal population triggers an equivalent spiking response in the neighboring population. On the other hand, networks showing a significant frequency detuning between their gamma rhythms only succeed in synchronizing their LFPs with a phase-lag that matches the synaptic delay. The slower oscillation is then enslaved to the faster oscillation following a leader-laggard configuration. In those conditions, the maximum firing activity of the laggard neuronal population, locked to the troughs of its LFP, arrive at low levels of excitation of the leader network unable to drive these neurons above the spiking threshold, thus preventing backward communication. The eMUA from both populations is weakly coherent and action potentials fail to propagate.

In a neuronal context, communication (regarded as the successful transmission of information) requires that the spiking response is triggered through all the pathway in a communication cascade. Otherwise, in the absence of suprathreshold activity, only a modulatory effect is achieved by the elicited post-synaptic potentials between two directly connected networks. In summary, we observe that the CTC hypothesis holds between two mutually coupled similar neuronal networks undergoing LFP-LFP and eMUA-eMUA zero-lag synchronization. On the other hand, for different gamma rhythms of the two populations, phase coherence is only achieved between the LFP signals at non-zero phase-lag, in such a way that the leader population applies a phase modulatory effect on the laggard population without generating a suprathreshold response, which prevents successful communication.

We are currently studying another regime in which the neuronal firing rate does not decrease so dramatically with increasing τ_{GABA} (compare raster plots in Figure 4.5). An intriguing question is whether the drop in eMUA-eMUA phase coherence [Figure 4.7(b)] is mainly due to this reduction of the spiking activity of single neurons or to the frequency detuning. Clearly, a low number of excitatory spikes per gamma cycle entails a decrease in eMUA amplitude, contributing to poorly defined oscillations and, therefore, to a decrease in coherence. New results [Sancristóbal 2013a] point out that frequency detuning is also modulating the level of phase coherence between coupled neuronal populations, since the spikes from the slow population cycle skip the LFP rhythm of the faster population. Moreover, a leader-laggard configuration also appears at large detunings.

CHAPTER 5

Slow UP/DOWN neuronal oscillations

Contents

5.1 The slow rhythm of the sleep state

During sleep, cortical networks display slow oscillations (<1 Hz) [Steriade 1993b] that predominate over the gamma oscillatory pattern (30 Hz - 90 Hz), typical of the attentive state. Previously, we have mainly referred to the gamma rhythm as the major fingerprint of the local cortical activity displayed by recurrent populations of excitatory and inhibitory neurons. In particular, we have shown in this Thesis that the gamma frequency band is involved in the coding of information processed by a neuronal population (see Chapter 3) and in establishing effective communication between interacting populations (see Chapter 4). Thus, the rich variety of tasks performed during the awake state (which are undoubtedly related to the concept of *consciousness*) makes the gamma rhythm functionally relevant for its implication in the internal cortical coordination of stimulus-driven activity.

In contrast with the fast activity usually observed in the awake state, *in vitro* and *in vivo* cortical recordings, both during anesthetized-states and sleep, reveal slow dynamics of the local field potential (LFP). Contrary to the multi-unit activity (MUA) recorded in the awake state [see Figure 3.5(c)], the sleep state is characterized by highly synchronized depolarization states of elevated firing activity, interspersed by periods of quiescence on the order of seconds. The membrane potential of individual neurons also shows slow oscillations frequency-locked to the global LFP activity. Unlike the features described in the precedent chapters, during sleep, neuronal cells coordinate in time both their suprathreshold [Figure 5.1(a,top)] and subthreshold activity [Figure 5.1(a,bottom)-(b)], alternating between the so-called UP and DOWN states. The former are characterized by a depolarization of the membrane voltage towards the spiking threshold (around ∼10 mV) and a sustained firing activity of the neurons. In the DOWN states, neurons are basically silent and exhibit a highly hyperpolarized membrane voltage.

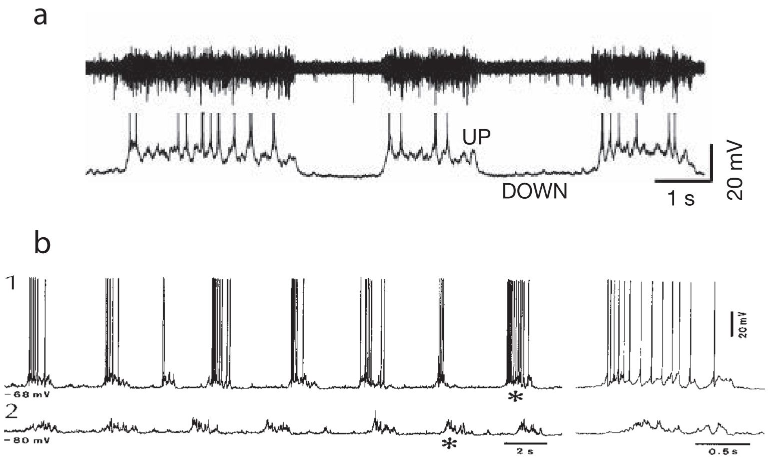

Figure 5.1: (a) *In vitro* extracellular (top) and intracellular (bottom) recordings from layer V of ferret prefrontal cortical slices. The extracellular recordings capture the fast dynamics of the action potentials fired by a group of neurons close to the tip of the electrode. From [Shu 2003]. (b) *In vivo* intracellular recordings of a cortical regular-spiking neuron of an anesthetized cat in (1) the resting state (∼0.3-0.4 Hz) and (2) upon injection of an hyperpolarizing current of -1 nA. The depolarized events marked with an asterisk are expanded in the right panels. From [Steriade 1993b].

The fact that UP and DOWN states exist also *in vitro*, suggests that these dynamics are self-sustained, appearing locally without requiring large-scale cortical interactions nor external stimulation: the recurrent connectivity between neurons is sufficient for the emergence of this bistable behavior. The initiation of the UP state can be triggered by the spontaneously synchronous firing of a few excitatory neurons, and the further propagation of an excitatory synaptic current to all the network. The build-up of local activity increases the population firing rate. In turn, specific ionic channels across the neuronal membrane account for its depolarization. The termination of the UP state can be induced by the increase of inhibitory activity during the UP state but extra mechanisms should explain the DOWN state duration, because it lasts longer than the GABA-receptor-mediated inhibition [Buzsáki 2006]. For instance, it has been proposed that frequency adaptation of neurons by activation of potassium channels that reduce the sensitiveness to synaptic inputs [Sanchez-Vives 2000, Compte 2003] can account for the UP-DOWN transition. It is debated whether synaptic plasticity causing fatigue of the synapses is also involved in this process [Holcman 2006, Mejias 2010]. Another important cause of entrance in the DOWN state is the decrease of input resistance during the UP state (i.e. stronger currents are needed to depolarize the membrane).

The computational model that we have used to study *in vitro* UP and DOWN dynamics was proposed by [Compte 2003], which reproduces the results from [Sanchez-Vives 2000]. In that experimental work, the authors studied the origins of the slow oscillatory period in ferret visual and prefrontal cortical slices by locally injecting successive pulses of glutamate (see Section 1.4.1). In response to this excitatory agonist, a collective discharge was triggered, only interacting with the intrinsic oscillatory activity as long as the period between two glutamate injections differed sufficiently from the natural period Figure 5.2(b). The straightforward conclusion was the existence of a refractory period that prevented the population from being immediately excited [see bottom trace in Figure 5.2(a), where an excitatory pulse too close to the spontaneous collective firing of the neurons is unable to trigger another burst of activity]. At the same time, intracellular recordings revealed that after an UP state individual neurons underwent an afterhyperpolarization (AHP) of duration equal to the DOWN state [Figure 5.2(c)]. Neurons showed a reduced sensitiveness to excitatory pulses of 0.1 nA injected intracellularly during the AHP period [Figure 5.2(d)] indicating an increase in membrane input resistance (i.e. a decrease in input conductance). The reversal potential of the AHP was close to ~ -87 mV, which led to the hypothesis that potassium conductances were being activated. Interestingly, blocking inhibitory synapses (i.e. GABA receptors) did not prevent the generation of the slow UP and DOWN activity. Therefore, we have chosen a model that accounts for the intrinsic mechanisms of UP termination rather than for synaptic mechanisms.

5.2 Features of the simulated UP and DOWN dynamics

We have reproduced the UP and DOWN dynamics in a modeled network described in [Compte 2003]. Both the excitatory and inhibitory neurons are

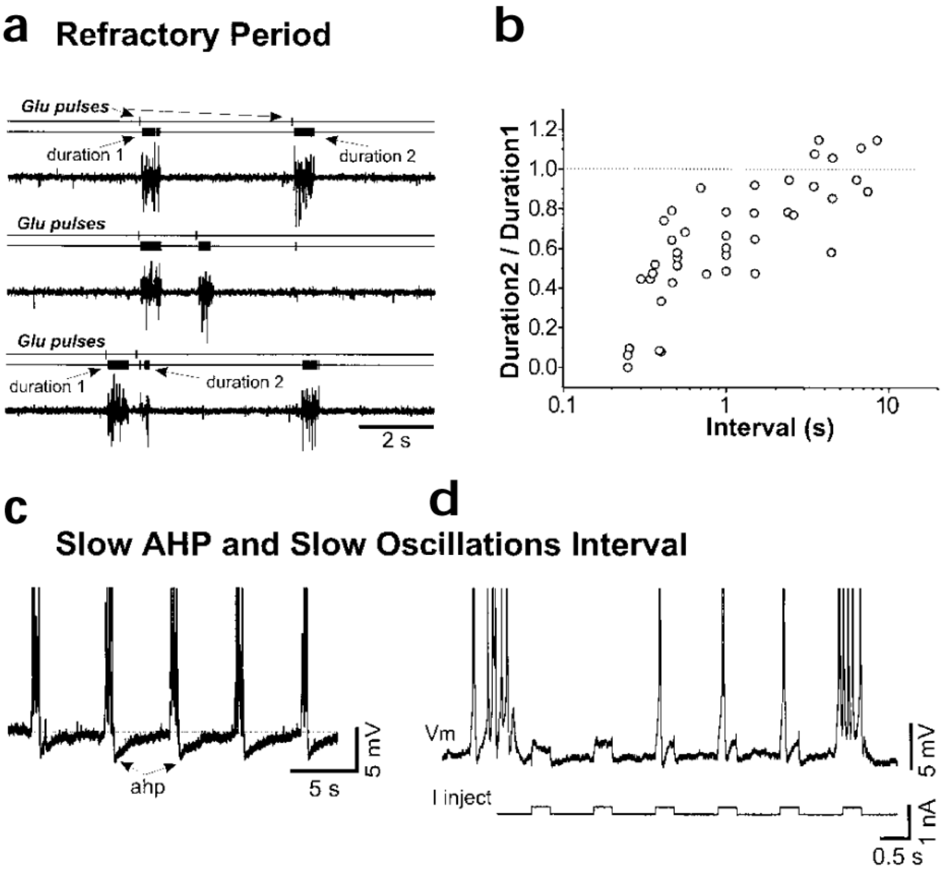

Figure 5.2: (a) Injection of glutamate pulses at three distinct periods (ticks in the upper traces of each set). The triggered action potentials (middle traces of each set) and the extracellular signal (bottom traces of each set) are shown. Note that a spontaneous burst of activity is indistinguishable from a glutamate-induced one (lower set). (b) The duration of a glutamate-induced UP state increases with the duration of the interval between stimulus injection. (c) Long afterhyperpolarizations (AHP) following UP states are seen in intracellular recordings. (d) The AHP is characterized by a lower response to depolarizing inputs. From [Sanchez-Vives 2000].

described by a conductance-based model. The inhibitory neurons are simple Hodgkin-Huxley-like cells in which only a leak current and the sodium and potassium channels for action potential generation are considered (see Section 1.3.2.1). The excitatory neurons are composed of two compartments, one for the soma and one for an effective dendrite, with a high diversity of ionic channels needed to reproduce the intracellular recordings shown in Figure 5.1. The coupling between all neurons shows a certain clustering, favoring short connections, but no synaptic delay is introduced in the transmission of action potentials. Details are given in Appendix A.3.1.

Some parameters of the model are distributed across neurons, making the population heterogeneous. In the excitatory population, this causes spontaneous firing rates below ∼1 Hz. The inhibitory population only fires due to the excitatory recurrent input from the excitatory neurons. An external Poissonian excitatory train of spikes impinges on every neuron, to account for the activity of neurons not belonging to the simulated network. Therefore, local measures of the electrical activity within the network correspond to only a subpopulation of the whole cortical slice.

The UP and DOWN dynamics described in the previous Section are not observed in an isolated cell. Without recurrent connections some neurons are in an excitable state but do not fire unless a synaptic coupling is introduced [see blue trace in Figure 5.3(a)], and other neurons are in a stable limit cycle firing quasi-periodically [see black and magenta traces in Figure 5.3(a)]. In this case, all neuronal discharges occur asynchronously and no net collective behavior can be registered. However, within the network, neurons engage synchronously in a slow oscillation [see Figure 5.3(b)], which is an emergent property of the network.

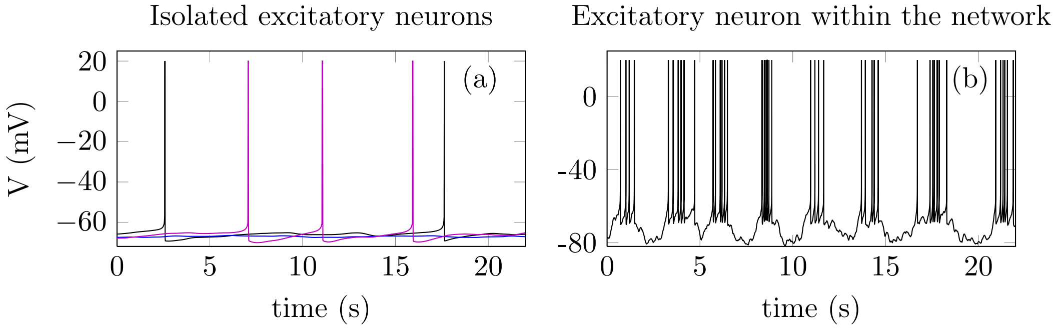

Figure 5.3: Membrane voltage traces for (a) three excitatory isolated modeled neurons and (b) one modeled neuron embedded in the network.

As in the previous Chapters 3 and 4, the local field potential (LFP) defined by Equation (A.14), represents the collective activity of the network. We obtain the spiking times of each neuron and the LFP time series of a subarea composed of 150 adjacent excitatory neurons. A clear advantage of the single-neuron network models is that we can simultaneously obtain precise information of the dynamics of all neurons. Experimentally, available data of individual neurons is reduced to few cells and is obtained indirectly from extracellular recordings (intracellular recordings are more challenging to perform). The extracellular signals account for the activity of multiple neurons, and thus spike sorting algorithms must be used to separate out the activity of single units. Figure 5.4 shows a numerically obtained raster plot and the corresponding LFP time trace, whose amplitude is scaled in order to emphasize the phase locking between increases in the firing activity and the LFP.

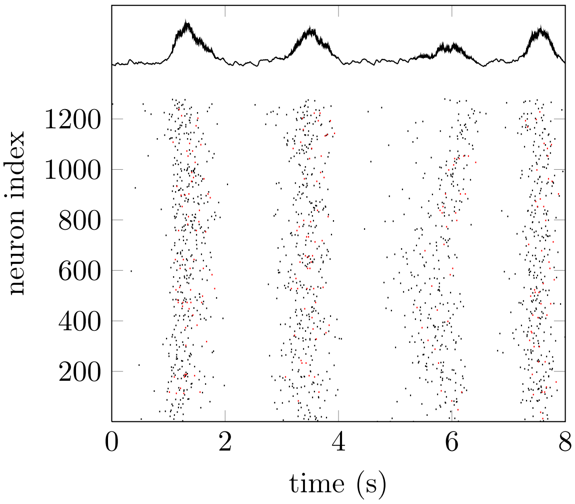

Figure 5.4: Raster plot for the spiking times of a subpopulation of excitatory (black) and inhibitory (red) neurons. A magnification of the corresponding LFP (blue trace) is plotted on top to better reveal the phase locking between increases in the LFP and collective firing activity.

Our results are compared with experimental studies where the MUA is usually defined as the high-filtered raw data registered by an extracellularly located electrode [McCormick 2003]. Since the action potentials have fast time courses [see Section 1.3.1], they are the major contributors to the high-pass filtered electrical signal [Sanchez-Vives 2010]. In contrast, the LFP is often viewed as the low-pass filter of the same raw data, as it captures the slower dynamics of the activation and deactivation of synapses (see Figure 5.5, left). In our modeling study the synaptic terms also represent the fast discharges, which depend on the voltage membrane [Equations (A.9) and (A.10)], as can be seen in the fast ripples at the maxima of the LFP in Figure 5.4. Therefore the MUA activity is shown as the high-pass filter (low frequency cutoff = 200 Hz) of the simulated LFP [Figure 5.5(a)]. Note that since the simulated LFP is a positive-defined magnitude [Equation (A.14)], modeled UP states are shown as upward shifts of potential while experimental UP states appear as downward shifts of potential since the reference electrode (0 mV) is placed outside the neuronal membrane.

The membrane voltage time course of three simulated neurons –two excitatory (black) and one inhibitory (red)– are shown in Figure 5.6(b). Despite the heterogeneity in the dynamics of individual neurons, a collective period can be defined as clearly revealed by the LFP trace in Figure 5.6(a).

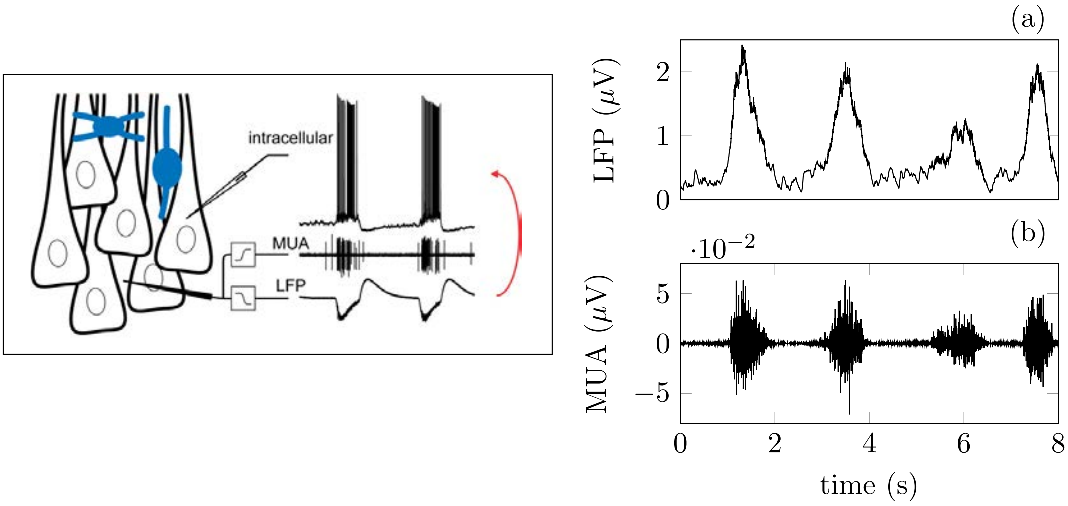

Figure 5.5: Left: Scheme showing excitatory pyramidal neurons (black) and inhibitory neurons (blue). Intracellular recordings (top time trace) and extracellular recordings, separated into the high-pass filtered (MUA, middle trace) and low-pass filtered (LFP, bottom trace) components. The red arrow indicates the positive feedback effect of the LFP on the neuronal activity. From [Mann 2010]. Right: (a) LFP time trace as in Figure 5.4 (real scale) and (b) MUA trace defined as the high-pass filter of the LFP.

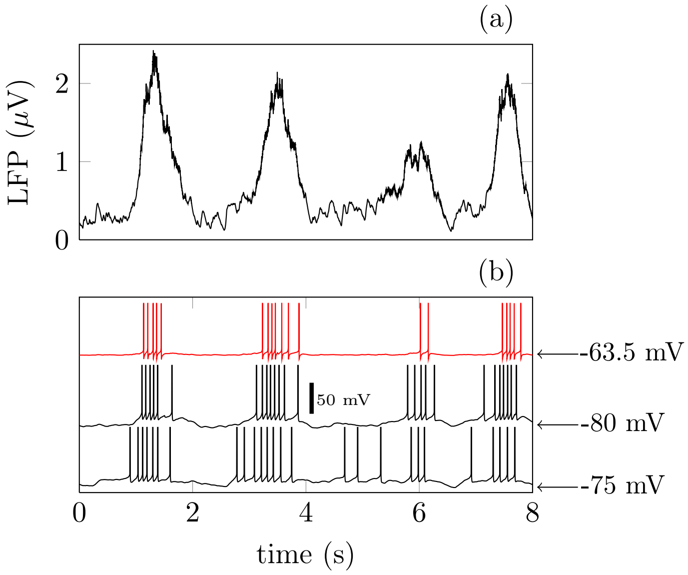

Figure 5.6: (a) LFP time trace as in Figure 5.5(a) and (b) membrane voltage time series for two excitatory neurons (black) and one inhibitory neuron (red) shifted vertically to better identify the traces.

5.3 Stochastic coherence of UP and DOWN states

Stochastic process are of great importance in biological systems. Random fluctuations are ubiquitous in the dynamics of neuronal variables. For instance, the ionic channels spread through the cell membrane (see Section 1.3.1) open and close randomly, and a large amount of them have to be taken into account in order to model a deterministic averaged behavior (see Section 1.3.2.1). Other stochastic processes of neuronal networks are the synaptic release of neurotransmitters and the firing activity of single neurons.

Due to the irregularity in the spiking activity, the synaptic input to neurons is clearly noisy. Each neuron receives from its neighbors a certain amount of presynaptic spikes, which are randomly distributed in time. The noisiness of this input can be measured by means of the coefficient of variation (CV) of the interspike interval (ISI) of the neuronal activity. As shown in Figure 5.7, the CV increases with the extracellular concentration of potassium $[\mathrm{K}^+]_\mathrm{o}$, which controls the firing activity of the network (the relationship between $[\mathrm{K}^+]_\mathrm{o}$ and the excitability of the network will be explained below). Therefore, $[\mathrm{K}^+]_\mathrm{o}$ provides a measure of the amplitude of neuronal noise. Low levels of excitability ($[\mathrm{K}^+]_\mathrm{o} < 2.5$ mM), at which neurons rarely discharge, cannot trigger UP and DOWN dynamics since, in the system, the source of noise, $[\mathrm{K}^+]_\mathrm{o}$, is also the trigger of the oscillatory behavior. We expect that a neuronal network entrained to UP and DOWN cyclic dynamics by a stochastic process exhibits stochastic coherence (also known as coherence resonance).

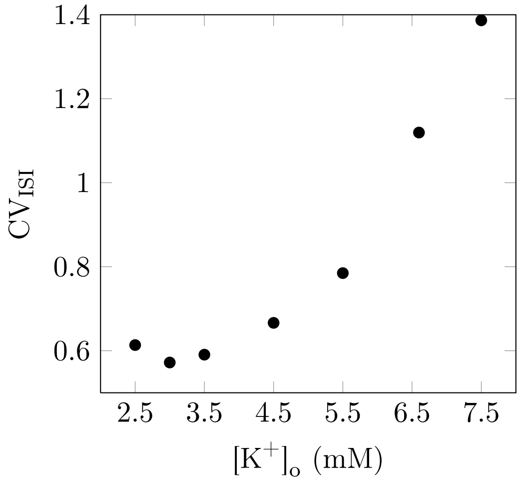

Figure 5.7: Coefficient of variation, CV, of the interspike interval, ISI, of the excitatory neurons calculated over the UP states, as a function of $[\mathrm{K}^+]_\mathrm{o}$.

This phenomenon has been described in autonomous oscillators, whose dynamics show a maximal regularity at a certain noise amplitude. Stochastic coherence was first reported in [Pikovsky 1997], where the authors studied a FitzHugh-Nagumo model in the excitable regime. A sufficient large input forced the neuron to pulse, making a large trajectory in the phase space [see Figure 1.10(a)]. In the model, the neuron fired randomly because it was driven by a Gaussian white noise of amplitude D. For both small and large values of D, the train of noise-induced pulses, or action potentials, was highly irregular. The maximal regularity was obtained at intermediate noise amplitudes, which endowed the system with a particular rhythm without the need of periodic external forcing. Stochastic coherence provides a mechanism of generating quasi-regular oscillations in a system that is intrinsically non-oscillating [Lindner 2004].

The time needed for the system to escape from the resting state (i.e. the activation time) depends both on its distance to the firing threshold and on the noise amplitude. Weaker noises (small D) cause longer activation times and a Poissonian-like train of spikes. On the contrary, stronger noises (large D) cause smaller activation times and the time between subsequent pulses [i.e. the interspike interval (ISI)] depends on the duration of a spike because noise moves the neuron away from the stable fixed point as soon as it reaches it. On the other hand, the duration of a spike in the FitzHugh-Nagumo version used in Chapter 2, was written as a sum of Equations (2.14) and (2.15) which depended on the intrinsic parameters of the model. Likewise, in [Pikovsky 1997], the time spent by the neuron in the excited state after being perturbed above threshold does not depend strongly on D. However, intense noise also causes fluctuations in the excursion time, whose variance is proportional to D^2 [Hilborn 2004]. Therefore, only intermediate noise amplitudes can make the noise-induced oscillatory period close to the constant duration of an action potential (plus the refractory time), while bounding its fluctuations to small values.

The Morris-Lecar (ML) neuronal model was shown to exhibit [Han 1999] coherence resonance when Gaussian noise is added to the membrane voltage differential equation. Moreover, two ML-neurons electrically coupled in this regime, with uncorrelated noise and different noise amplitudes $D_1 \neq D_2$, were frequency locked in the range where $D_1 \sim D_2$, which was wider for higher coupling strengths. This behavior resembles Figure 4.4(b), which compares the frequency detuning of two oscillators before and after coupling. In the neuronal network introduced in the previous Section, the source of noise appears in the synaptic coupling between neurons, and thus D is fairly equal between cells. In contrast with the previous studies, where the stochastic coherence is a local phenomenon, in the UP and DOWN dynamics neurons do not oscillate in the absence of coupling [see Figure 5.3(a)], and stochastic coherence emerges as a collective phenomenon.

Similar to the FitzHugh-Nagumo neuron discussed above, two time scales can be identified in our neuronal network when operating in an UP/DOWN regime: firstly, the time needed for the initiation of the UP state (analogously to the initiation of a single spike), which relies on the strength of the presynaptic activity and thus, on the noise amplitude, and secondly, the duration of the UP and DOWN cycle (analogously to the duration of a single spike), which is largely dependent on the dynamics of the K^+-channels generating the afterhyperpolarization.

5.3.1 Regularity of the slow oscillations in the modeled network

We have carried out simulations of the described network (see Appendix A.3.3) at varying values of the extracellular potassium concentration $[\mathrm{K}^+]_\mathrm{o}$. We know from the Nernst equation [see Equation (1.1)], that the ratio between extra and intracellular concentrations of an ion determines the equilibrium potential of the channels permeable to that ionic species (i.e. greater external than internal concentrations imply positive reversal potentials) (see Appendix A.3.2). Besides, less negative potassium reversal potential V_K get the neurons closer to the spiking threshold. Hence, we have tuned the excitability of neurons (and, thus, the neuronal noise) by increasing the extracellular potassium concentration $[\mathrm{K}^+]_\mathrm{o}$, from 2.5 mM (weak noise) to 7.5 mM (strong noise) (see Table 5.8 for physiological typical concentration values of mammalian neurons).

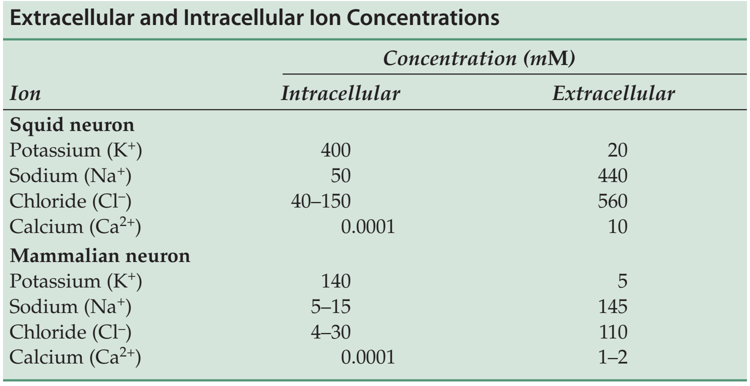

Extracellular and Intracellular Ion Concentrations

	Concentration (mM)	
Ion	*Intracellular*	*Extracellular*
Squid neuron		
Potassium (K^+)	400	20
Sodium (Na^+)	50	440
Chloride (Cl^-)	40–150	560
Calcium (Ca^{2+})	0.0001	10
Mammalian neuron		
Potassium (K^+)	140	5
Sodium (Na^+)	5–15	145
Chloride (Cl^-)	4–30	110
Calcium (Ca^{2+})	0.0001	1–2

Table 5.8: Extracellular and intracellular concentration of potassium, sodium, chloride and calcium ions for the large nerve cell of the squid axon and for a typical mammalian neuron. From [Purves, D et al. 2004].

In an interval of 10 min, we have computed the number of spikes in every UP state divided by its duration and by the number of neurons, i.e. the population averaged firing rate. Figure 5.9(a) shows the rise of this firing activity for increasing $[K^+]_o$ for both the excitatory and inhibitory population. Note that for high levels of excitability, inhibition overcomes excitation avoiding epileptic behavior. Together with Figure 5.7, Figure 5.9(a) reveals that the firing activity of the network is an indicator of the noise amplitude. Differently from other studies [Han 1999, Horikawa 2001], we consider here a network-endogenous noise rather than a white noise added to the membrane voltage.

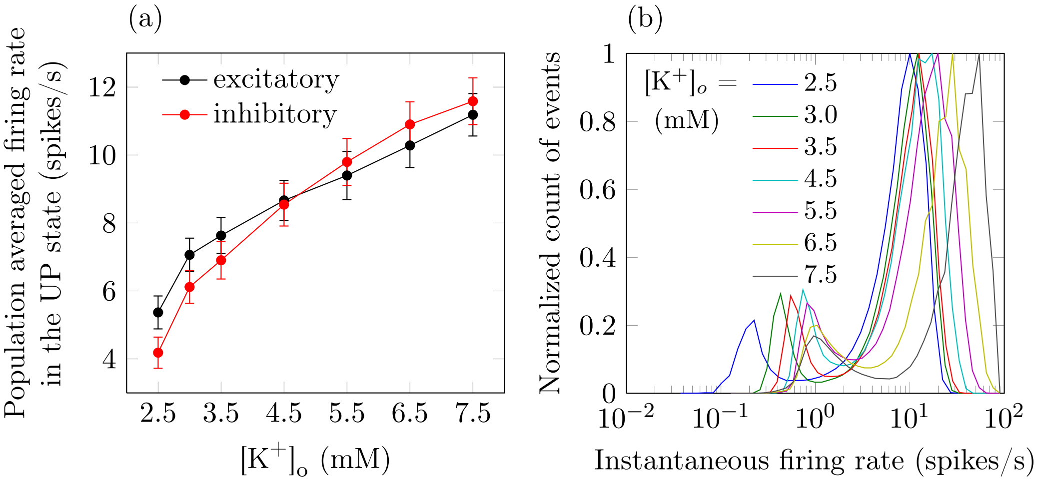

Figure 5.9: (a) Firing rate of the excitatory (black) and inhibitory (red) neurons averaged across the population and over the UP state duration, as a function of $[K^+]_o$. (b) Normalized histogram of the instantaneous firing rate of the excitatory neurons for different values of $[K^+]_o$.

We have computed the instantaneous spiking rate (i.e. the inverse of the interspike interval) of the excitatory neurons. A histogram of these values normalized to its maximum is shown in Figure 5.9(b) for different $[K^+]_o$. The bimodal distribution captures the UP and DOWN dynamics. The right peak corresponds to the mean instantaneous firing rate in the UP state, which shifts towards higher values with increasing $[K^+]_o$, indicating that the discharges in the UP state are sped up by the extracellular potassium. The left peak indicates the presence of long periods in which the neurons are silent, the DOWN states.

We have mentioned that high values of extracellular potassium depolarize the voltage membrane, thus promoting intense spiking. As the neuron discharges repeatedly, more sodium ions enter the cell and the intracellular $[Na^+]$ increases, triggering the build-up of the Na^+-dependent K^+-adaptive channel I_{KNa} [see Appendix A.3.1], which are expressed throughout the brain

[Bhattacharjee 2005b]. Both the intense background synaptic activity and firing rate at high $[K^+]_o$ exhausts the neuron, which enters a slow afterhyperpolarization period. Figure 5.10(a) shows first that, at $[K^+]_o$=7.5 mM, the intracellular $[Na^+]$ increases faster, second that the neuron is more depolarized, and finally that its firing rate in the UP states is larger than at $[K^+]_o$=3.5 mM. In the former case, the membrane input resistance has decayed so fast that the cells cease to spike soon and the period of the UP and DOWN cycle decreases [Figure 5.10(b)].

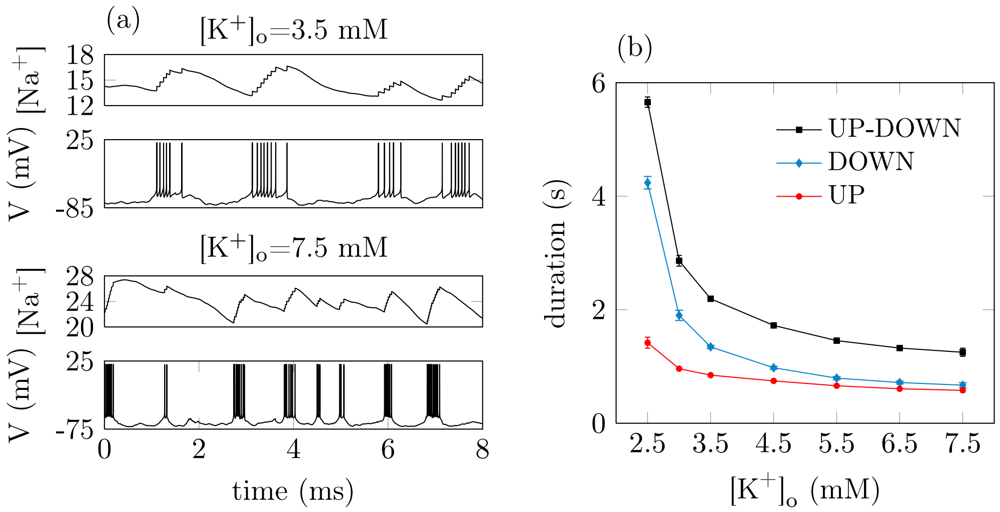

Figure 5.10: (a) Voltage membrane and intracellular $[Na^+]$ (in mM) time course for $[K^+]_o$=3.5 mM and $[K^+]_o$=7.5 mM. (b) Duration of the UP and DOWN cycle (i.e. inverse of the frequency of the slow oscillation), the UP and the DOWN states, as a function of the extracellular potassium concentration, $[K^+]_o$. Error bars correspond to the sampled standard deviation across groups of 100 events in 10 min simulated time.

In order to quantify the regularity of the slow oscillations we have used the coefficient of variation (CV) (introduced in Section 1.5.1), defined as

$$CV = \frac{\sigma}{\mu} \tag{5.1}$$

where σ is the corrected sample standard deviation of the duration of the UP and DOWN cycle and μ is its mean. The instantaneous period of the slow oscillation is given by the sum of durations of UP and DOWN adjacent states. Figure 5.11 shows a minimum of the CV at $[K^+]_o = 4.5$ mM, which corresponds to a maximum of regularity of the cycle. At low and high levels of noise, caused by low and high $[K^+]_o$ respectively, fluctuations around the mean UP-DOWN interval increase (larger CV). The CV behavior is not symmetric with respect to 4.5 mM, due to the change in the inhibition-excitation balance shown in Figure 5.9(a). When the inhibitory population dominates the electrical activity ($[K^+]_o > 4.5$ mM) the duration of the cycle is largely controlled by inhibition, which is not affected by the Na^+-dependent K^+ channel [see Equation (A.8)]. The membrane voltage of an inhibitory neuron at $[K^+]_o = 7.5$ mM (red trace in the top right panel of Figure 5.11) shows that this type of neuron fires during longer time intervals than the excitatory neurons. Whereas at $[K^+]_o = 3.5$ mM, the firing windows of the inhibitory neuron (red trace in the bottom right panel of Figure 5.11) are restricted to the activity of the excitatory neurons.

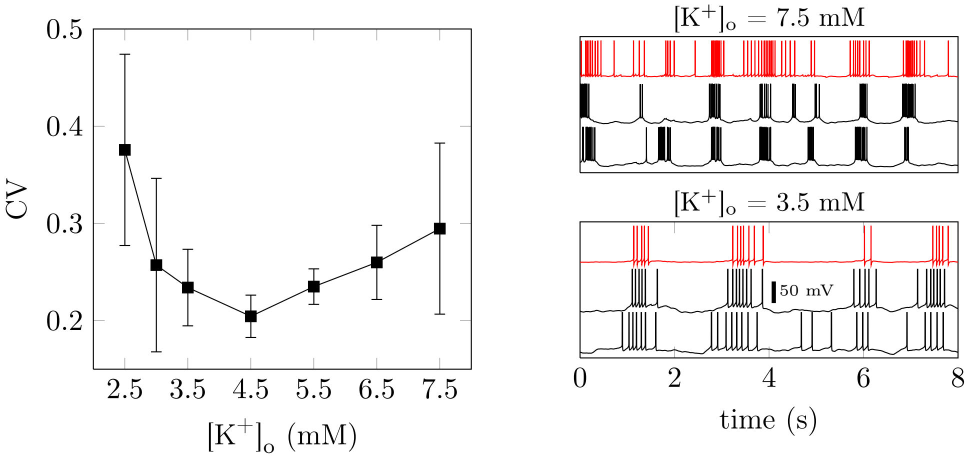

Figure 5.11: Coefficient of variation of the UP and DOWN cycle at different values of the extracellular potassium concentration $[K^+]_o$. The time traces of two excitatory neurons (black) and one inhibitory neuron (red) are shown on the right of the figure for $[K^+]_o = 3.5$ mM and 7.5 mM. Error bars correspond to the sampled standard deviation across groups of 100 events in 10 min simulated time.

In summary, at low levels of extracellular potassium concentration ($[K^+]_o < 4.5$ mM) excitation exceeds inhibition, but the depolarization of neurons is low enough to provide moderate firing rates. In the limit of small $[K^+]_o$, the slow collective oscillations (mean period ∼6 s) are irregular and the cycle of UP-DOWN states is determined by the dynamics of the Na^+-dependent K^+-adaptive channel. At high $[K^+]_o$, the slow collective oscillations (mean period ∼1.3 s) are less irregular and the cycle of UP-DOWN states is also controlled by the build up of inhibition which is not influenced by the Na^+-dependent K^+-adaptive channel. Between these two situations, the slow oscillations achieve a maximum of regularity. The simulated network clearly exhibits stochastic coherence and we next examine whether this phenomenon is observed in real cortical slices of interconnected neurons.

5.3.2 Regularity of the slow oscillation in cortical slices

UP and DOWN transitions have been measured *in vitro* in visual cortical slices under different experimental conditions [Sanchez-Vives 2000, Shu 2003, Cossart 2003]. In order to test our prediction, i.e. that coherence resonance should be observed in a real neuronal network varying its population activity, experiments were carried out in the Sanchez-Vives Lab by B. Rebollo (details are given in Appendix B.4). Spontaneous slow oscillations were registered in slices of ferret visual cortex (Figure 5.12, left) at an extracellular potassium concentration of 3.5 mM. From this control condition, $[K^+]_o$ was decreased to 2 mM and further increased up to 7 mM in steps of 1 mM. An extracellular unfiltered electrical signal was obtained by means of a tungsten electrode and amplified [Figure 5.12(b), right]. This activity corresponds to the modeled LFP. In the absence of single-unit recordings, MUA was described as the power change of the LFP at frequencies greater than 200 Hz [Reig 2010]. The MUA [Figure 5.12(a), right] was used to detect the transitions between the two UP and DOWN states and to determine their duration (see Appendix B.4), as well as the cycle of the slow oscillation, defined by the sum of an UP and a consecutive DOWN state, see Figure 5.13(a) similar to Figure 5.10(b).

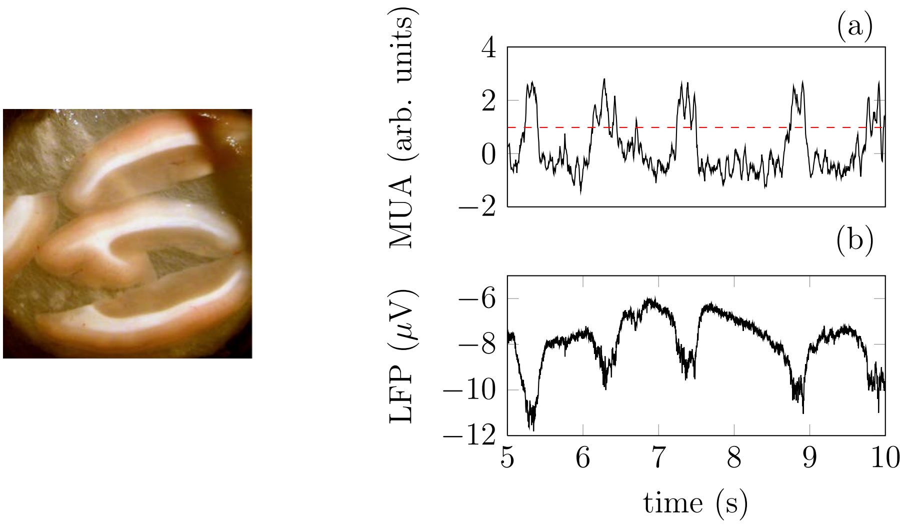

Figure 5.12: Left: Coronal slices of ferret visual cortex. Right: (a) Experimental MUA (black trace) and detection threshold for the UP states (dashed red line). (b) Registered LFP from a ferret visual cortical slice (left). $[K^+]_o = 3.5$ mM. The measures were obtained by B. Rebollo from the Sanchez-Vives Lab.

The existence of stochastic coherence at the population level was observed in the *in vitro* experiments [Figure 5.13(b)]. Therefore, population activity appears here as a collective parameter that controls the regularity of the collective rhythm. For an optimal value of firing, the network produces quasiregular signals -defined by the LFP or the multi-unit activity (MUA)- interspersed by the DOWN states, at a characteristic time scale of the network.

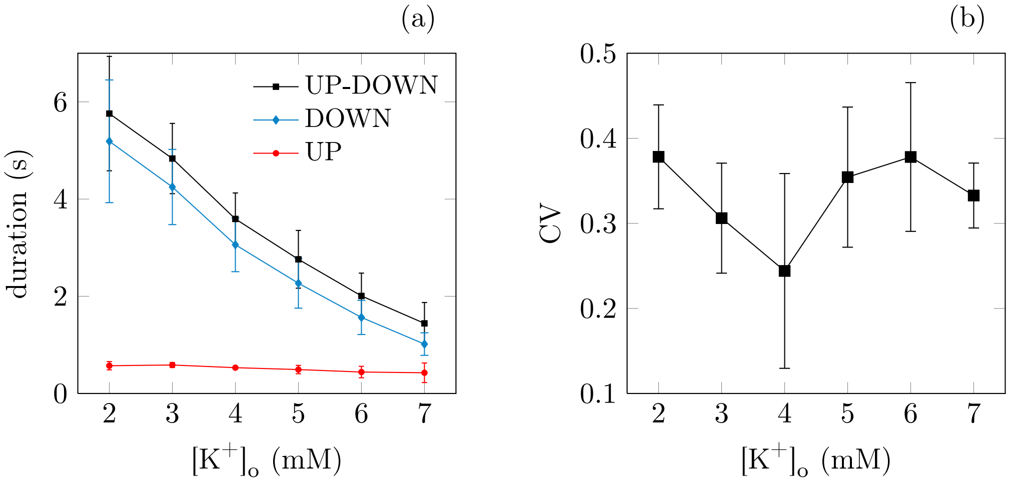

Figure 5.13: (a) Duration of the UP and DOWN cycle and the UP and the DOWN states, as a function of the extracellular potassium concentration, [K$^+$]$_o$, measured in two ferret visual slices. The analysis was performed by L. Perez-Mendez from the Sanchez-Vives Lab. (b) Coefficient of variation of the UP and DOWN cycle at different values of the extracellular potassium concentration [K$^+$]$_o$. Error bars correspond to the corrected sample standard deviation across groups of 200 events. The length of the data segments could vary depending on the quality of the register.

5.4 Conclusions

The dynamical properties of networks with UP and DOWN dynamics, namely the presence of excitation events (UP states) interspersed among quiescent periods (DOWN states), suggested the possibility that the coherence resonance phenomenon would be present in a collective excitable system. According to this scenario, an optimal noise amplitude would maximize the rhythmicity of the UP and DOWN cycle. Since these slow oscillations are a network-emerging property, modulation of their regularity could provide a mechanism of control of cortical information processing. The source of noise considered here is the firing activity of neurons, enhanced by increasing the excitability of the network. In *in vitro* experiments this could be done by adding more potassium ions to the extracellular medium.

Both the network model and the experimental recordings confirm that slow UP and DOWN rhythms are regulated by the amount of noise and achieve an optimal periodicity at a certain value of noise amplitude [Sancristóbal 2013d].

The onset of the UP state was induced by the recurrent firing activity of excitatory neurons, which is again controlled by the noise strength. However, the termination of the UP states was governed by $[\mathrm{K}^+]$-dependent-adapting channels that were insensitive to noise variations in the studied range of varying parameters (i.e. $[\mathrm{K}^+]_\mathrm{o}$). At low levels of $[\mathrm{K}^+]_\mathrm{o}$ the probability of eliciting an UP state is low, and their occurrence fluctuated strongly on time giving rise to a high variability of DOWN durations. On the other hand high levels of $[\mathrm{K}^+]_\mathrm{o}$, could evoke the UP state at a wider set of stages of the adaptive currents (i.e. the system could be excited again closer to the UP termination). Between both cases, the UP states were consistently evoked at the same phase of the DOWN state, and a recurrent collective period emerged. In agreement with the sleep-awake transitions, in more excitable states eventually the slow oscillations are replaced by faster rhythms.

Chapter 6
Summary of results and Perspectives

Contents

6.1 Role of neuronal oscillations

The rich variety of functions that our brain performs are the result of neuronal processes. Therefore, the best characterization of the elusive concept of *mind*, from consciousness to emotions, should emerge from the firing activity of neurons. However, it is yet unknown how both internal thoughts and stimuli from the external environment are coded in the brain. Like the binary language of computers, neurons use at least an all-or-none code (to spike or not to spike) to communicate between each other, and we aim to understand how the message is built.

If we observe a simple bar displayed on a screen, some neurons in the primary visual cortex (V1), tuned to respond to this precise orientation, will fire [Hubel 1959]. Moreover, if this bar is colored, other neurons will also discharge -the problem might not be so easy as neurons are selective to multiple features, for a review see [Shapley 2011]-. Therefore, two groups of discharging neurons must cooperate in such a way that we perceive a unique object, and not a colored spot and a separate bar at different locations of the screen. We know that these cell assemblies send their action potentials to each other through feed-back and feed-forward projections, but we do not know how to identify the colored bar from the registered electrical signal. Fortunately, the brain does.

Spontaneously, our brain always tries to make sense of perceptions, although we are only aware of it when something is unexpected. We will notice the absence of a book on the bedside table as soon as we enter in the bedroom because, only then, the every-day prediction is not confirmed in our brain. Seeing is not only perceiving but a complex process in which memory and feelings are also involved. Thus, higher levels of cognition also require the interplay of different cortical areas in a coherent manner. Dispersed neuronal circuits readily engage in communication to combine information (coming from both the outside and the inside of the brain) concerning a single stimulus without mixing non-related data. In the *Lincoln in Dalivision* painting (Figure 6.1) Dalí plays with two identities: naked Gala contemplating the sea through a window, and Lincoln's portrait, apparent by half-closing the eyes. As long as they are superimposed, we cannot clearly see Gala and Lincoln simultaneously, although the same visual input is entering the retina.

Figure 6.1: Lincoln in Dalivision litography by Salvador Dalí, 1977.

Neuronal oscillations, also called brain rhythms [Buzsáki 2006], are proposed as a mechanism to coordinate subpopulations of anatomically distant neurons. Extracellular recordings such as the local field potential (LFP) and recordings on the scalp such as the electroencephalogram (EEG) are oscillatory [Buzsáki 2004, Uhlhaas 2009]. The first evidence for a functional role of these subthreshold oscillations was their capacity to synchronize spikes from irregular firing neurons [Gray 1989, Henrie 2005], thus making their impact on target neurons more efficient [MacLeod 1998]. Neurons were also found to fire at particular phases of the oscillations, possibly providing a phase encoding mechanism [Jacobs 2007]. Therefore, oscillations can be interpreted as fluctuations of the spiking probability in a local area and as carriers of the informative spikes. Moreover, [Schoffelen 2005] showed that magnetoencephalography (MEG) measures from the motor cortex and activity in a spinal neuronal group (indirectly measured through muscle fibers) oscillated coherently in the gamma range (30 Hz - 90 Hz) when a motor task was expected to be done. Accordingly, a consistent phase difference was established between cell assemblies involved in an action that the subject was about to perform.

Despite the lack of direct empirical evidence for a functional role of neuronal oscillations, the aforementioned work has motivated interesting speculations. For instance, the *communication through coherence* hypothesis [Fries 2005] proposes that dynamic changes in the relative phase of oscillations modulates the coupling efficacy between areas. Furthermore, spike synchrony mediated through transient neuronal oscillations is suggested to conveniently tune interactions among neuronal groups as a solution to the *binding problem* [Singer 1999].

In the previous chapters I have presented our work on communication mediated by simulated neuronal oscillations. We have studied three scenarios: subthreshold membrane oscillations (Chapter 2), emergent gamma oscillations in the awake state (Chapter 3 and 4) and slow cortical oscillations in the sleep state (Chapter 5). Next, I will summarize the main findings of our research.

6.2 Summary of results

6.2.1 Action potential propagation in the presence of individual subthreshold oscillations

We used a FitzHugh-Nagumo model [Makarov 2001] to describe the subthreshold oscillations in the membrane potential of single neurons. This voltage modulation made the neurons fluctuate between different depolarization levels, and hence different excitability levels, determined by the distance to threshold. When a current pulse of moderate amplitude was injected, the response of the neuron was graded depending on the phase at which the perturbation was applied. The model parameters were tuned so that the cell was only responsive (elicited an action potential) near the peaks of the oscillation (spike-triggering, in contrast with the non-spike-triggering region), Figure 2.6(c).

We aligned several neurons in a chain, which only received synaptic input from the preceding neuron as shown in Figure 2.11. The first neuron in the array was forced to spike periodically at different frequencies (only this neuron was not phase-sensitive) and we measured the number of spikes elicited by the rest of neurons. In that way, each cell provided a read-out of the message at different stages of the pathway, and any failure in the propagation of a spike would be amplified. The success of information transmission was defined as the percentage of action potentials fired by the last neuron with respect to the initial train of spikes, i.e. *success rate*. This quantity varied with the period of the original signal. Therefore, at some frequencies all spikes were propagated along the chain and at others the last neuron fired at lower rates (even not firing at all).

In order to understand how the subthreshold oscillations were modulating spike propagation we numerically inferred the phase transition curves (PTCs) of the model for the range of input periods T [Figure 3.4(a)]. A presynaptic spike arriving at a given phase ϕ_{in} could send the membrane voltage to either the spike-triggering or the non-spike-triggering region after T units of time ($\phi_{\mathrm{out,T}}$). Superposing iterative maps on the PTC we could visualize the pathway in the phase plane ϕ_{in} versus $\phi_{\mathrm{out,T}}$ [Figure 2.10(a)-(d)]. Only those PTCs with a stable fixed point in the spike-triggering region led to phase dynamics that, after a transient, corresponded to an action potential at every T. Thus, the read-out of every neuron was identical. For input spike trains at periods that do not involve PTCs with stable fixed points, the read-out of every neuron was different, increasing the mean period at each stage of the chain. For long enough chains, the initial message (conveyed in the suprathreshold activity) eventually vanished (solid thick line in Figure 2.12).

Although this scenario involves some assumptions that are not physiologically plausible, such as a single presynaptic potential triggering a spike or the one-dimensional arrangement of neurons, it provides a simple understanding of the ability of subthreshold oscillations to filter signals. From a more realistic point of view, each neuron in the described array could represent a population of neurons, and its membrane subthreshold oscillation could be the electrical signal emerging from the collective activity of the neurons within this population. Then, in a unidirectional synaptic pathway of a hierarchical organization of areas, the first population will be passively reproducing the input. However, all subsequent identical populations will actively select which inputs are relevant, due to their oscillatory behavior. Interestingly, it is the interaction of all neurons (or populations) that modifies the final message to account only for regular periodic signals. The results presented in Chapter 3 have been published in [Sancristóbal 2010a] and were preceded by a previous research reported in [Sancristóbal 2008, Sancristóbal 2010b].

Before directly addressing communication between simulated neuronal pools (Chapter 5), we studied the properties of neurons embedded in a neuronal network and the emergence of collective behavior at the level of one population of neurons (Chapter 4).

6.2.2 Interplay between single action potentials and collective gamma neuronal oscillations

We modeled a cortical population of neurons at the single-neuron level using a conductance-based formalism [Gutfreund 1995]. The network showed a certain degree of clustering [Litwin-Kumar 2012] but all connections had the same synaptic delay. This sort of spatial preference for closer neurons enhanced the number of common neighbors and favored reverberation of the spiking activity by synchronizing presynaptic potentials. The neuronal model was of type I, i.e. above a certain amplitude of the injected current, isolated neurons spiked at infinitely low frequencies [Figure 3.2(a)]. However, when embedded in a network, neurons showed a discontinuity in their firing rates (Figure 3.6).

The external excitatory synaptic current, which mimics afferent long-range connections coming from other regions of the brain, was balanced by the recurrent inhibitory flow. Therefore, on average, the synaptic current was subthreshold. Occasionally, inhibition failed to compensate excitation, either because it dropped to zero (inhibitory presynaptic neurons are momentarily silent) or because the recurrent excitation increased (excitatory presynaptic neurons discharge). This dynamics drove the neurons irregularly and rarely above threshold. However, recurrent connections merged single-unit activity into an oscillatory synaptic activity of growth and decay of inhibition (or equivalently, an oscillatory activity of decay and growth of spiking activity). At the network level two measures revealed this rhythmicity: the subthreshold LFP [Figures 3.5(a,b)] and the suprathreshold mean population firing rate [Figures 3.5(d,e)]. The gamma-frequency peak of the power spectrum of these signals was mainly determined by the decay time of the GABAergic synapses τ^d_{GABA}.

Without inhibition neurons will be excessively active, their firing rate increasing enormously. Time windows during which local inhibition (i.e. the activity of the presynaptic inhibitory neurons of a given cell) was zero, made the neuron fire at a high rate. Otherwise, neurons fired single spikes. Hence, instantaneous firing activity of individual neurons was found to be bimodal [Figure 3.7(a)] with the bursts of spikes occurring preferentially at the peaks of the LFP and the isolated spikes at the troughs of the LFP (Figure 3.13). For slower inhibitory synapses, the fast spiking regime surpassed the slow spiking regime, and the range of forbidden rates increased because the longer time course of inhibition expanded the effective refractory period of the neurons (Figure 3.10).

We confirmed that a phase code associated with the dynamics of neuronal oscillations is plausible, as two different spiking modes at the single-cell level occurred at distinct phases of the LFP. Moreover, as a consequence of these oscillations, neurons were not allowed to fire at a certain range of firing rates and varying the gamma rhythm of these oscillations clearly controlled this gap. Again neuronal oscillations, naturally emerged from the recurrent connections across neurons, dynamically participated in coordinating single-unit activity.

An important issue is whether neuronal oscillations arising from the activity of distinct areas can influence each other through synaptic connections. Spikes (the information synaptically transmitted) give rise to neuronal oscillations in a recurrent network of excitation and inhibition provided that they are rhythmically synchronized. Due to the difficulty of tracking the activity of a large amount of single cells, measurements of collective behavior contain more information than the sum of single-unit recordings. Thus, correlations between local field potentials reflect the non-linear neuron-to-neuron interaction within an area and across areas. The results presented in Chapter 4 have been published in [Sancristóbal 2013b]. We next summarize the results obtained in this second paradigm of connectivity.

6.2.3 Interactions between local collective neuronal oscillations in the gamma range

We coupled two neuronal networks such as the one in Chapter 3 through long-range connections. The synaptic delay between cells from different populations were longer than within one population, but less than a quarter of the cycle. Each network contributed to the gamma frequency peak of the power spectrum of both its LFP and MUA. Spikes arriving from an area could trigger a response in another area depending on the phase of the oscillation at which they arrived (similar to the phase-sensitive response of Chapter 2). Therefore, by means of the coupling, two networks should maintain a difference in phase that matches the synaptic delay in order to maximize communication (i.e. action potentials arrive at the peaks of excitability). Since a phase can be defined for any period $\theta(t) = \frac{2\pi}{T}t + \theta_o$, the problem of how two neuronal oscillations are reciprocally influenced is multiplexed in several frequencies over the same connection. At any frequency, we calculated the phase coherence and the corresponding phase difference between LFPs and MUAs.

Each neuronal network showed phase-locking between its MUA and LFP, spikes being preferentially elicited near the troughs of the LFP (the maxima of spiking probability). Thus, these two neuronal oscillations showed significant phase coherence in the gamma range, fluctuating close to anti-phase. Two identical networks achieved zero-lag synchronization of their LFP signals [Figure 4.7(a) and 4.9(a) where $\tau^{d}_{\mathrm{GABA,s}} < 8$ ms], which was the needed condition for mutual communication. Synchronized barrages of spikes (elicited at the troughs of the presynaptic LFP) arrived close to the troughs of the postsynaptic LFP, thus triggering a maximal suprathreshold response and the MUAs also become phase-locked at zero lag [Figure 4.7(b) and 4.9(b)].

When the natural rhythms became too distinct, and the synaptic coupling was not enough to bring them closer, the two LFPs followed a leader-laggard configuration. The fastest LFP, which arose from the network with higher population firing rate, enslaved the dynamics of the slower one, which followed with a time shift equal to the synaptic delay [Figure 4.7(a) and 4.9(a) with $\tau^{d}_{\mathrm{GABA,s}} > 8$ ms]. At the gamma frequency of the fast LFP, only the spikes traveling from the fast to the slow population arrived close to the troughs of the LFP. Interestingly, the LFP-LFP phase coherence achieved at large frequency detunings was not translated into MUA-MUA phase coherence [Figure 4.7(b)]. The inter-areal coupling was able to modulate the LFP relative phase but without affecting suprathreshold activity expressed in the MUA. The gamma frequency peak of the neuronal oscillations, caused by the inhibitory-excitatory loop, determined a period for the peaks of excitability. The LFP and MUA filtered at other frequencies did not convey this same information. Therefore, when the two gamma rhythms are different enough, the MUA signals are non-coherent.

In order to test whether coherence led to communication we studied a simple paradigm in which communication was understood as the degree of reproducibility of a message, taken in the spiking activity. The fast population was perturbed by increasing the rate of the external presynaptic spikes impinging on a subpopulation during a certain time window. In response, these neurons spiked in synchrony increasing the regularity and modulation of the LFP and MUA (larger amplitude of the signals) and enhancing their efficiency on the target subpopulation. We analyzed the modulation of the LFP and MUA from the slow network during this interval. We observed that the modulation of the MUA signal decayed towards its control level (without the perturbation) as the frequency detuning increased whereas the rise in the LFP oscillatory behavior was not dependent on the frequency detuning (similar to phase coherence). Despite the LFP-LFP phase coherence results, communication only appeared at zero-lag synchronization, possible at small frequency detunings.

6.2.4 Slow UP/DOWN neuronal oscillations

In vitro experiments allow for the analysis of local networks (i.e. composed of a reduced number of connections, all synapses coming from neurons within the same brain area). Electrical activity recorded from cortical slices reveals that smaller neuronal circuits also generate spontaneous activity provided a certain level of excitability. UP and DOWN dynamics have been observed in both *in vivo* [Steriade 1993b, Lampl 1999] and *in vitro* [Sanchez-Vives 2000, Shu 2003] recordings, with the slow oscillations in the latter being more regular. In Chapter 5 we tested, in a modeled cortical network [Compte 2003] and in ferret visual cortical slices, whether the noise amplitude modulated such periodicity of the slow oscillations. The single-unit model took into account a K^+ adaptive channel, which become activated with increased intracellular sodium concentration, and contributed to adaptation of firing rate and to slow afterhyperpolarization at intense firing rates [Bhattacharjee 2005a]. Since the UP and DOWN dynamics exhibit these two time scales: one governing the initiation of the UP state and thus, sensitive to noise-induced excitation, and a second one governing the duration of the DOWN state and hence, dependent on the dynamics of the Na^+-dependent K^+-adaptive channel, a coherence resonance phenomenon appeared (Figure 5.11 and 5.13).

The noise amplitude was determined by the firing rate activity of the population [Figure 5.9(a)] and was controlled by the extracellular potassium concentration (Figure 5.7). For an optimal value of the firing rate, the network produced quasiregular LFP and MUA signals. These results shed light on the self-regulation of cortical dynamics across different states of excitability, and revealed a coherence resonance phenomenon for the emergence of a maximum level of regular dynamics. The temporal scale of this state determined a well-defined collective refractory period. Moreover, this study revealed a possible explanation for the variable regularity detected under different experimental conditions in vitro or under different brain states in vivo [Deco 2009].

6.3 Perspectives

The work presented in this thesis has also encouraged further research. In particular we have currently started to explore the relationship between long synaptic delays and the established phase shift between neuronal oscillations. [Bush 1996] showed that two cortical oscillations were able to synchronize at zero-lag as long as the synaptic delay between two identical networks was small (less than a quarter of the period). For higher delays, synchronization was disrupted. However, in our case we have studied phase coherence as a function of the frequency, which is specially relevant for signals with a complex power spectrum and with different gamma peaks. Transitions between in-phase and anti-phase appear in the gamma range according to the ratio between the synaptic delay and the inverse of the frequency. We believe that it is important to understand whether these two cases enable two routes of information transmission. We are currently analyzing results in which a shift in the gamma peak does not occur with a decay in the network firing rate.

Another interesting issue is how the interaction between distinct cell assemblies is regulated. We have found that the difference in the gamma frequency rhythms of two neuronal oscillations determines the amplitude of phase coherence and, thus, the efficiency of communication. It should be explored whether this mechanism is used by the cortex to coordinate activity in different areas and how it is dynamically achieved. For instance, disinhibition of feedback connections from associative areas down to primary sensory areas has been proposed to act behind synesthetic experiences. In this way a specific input, such as a sound, forward propagates to convergence areas where feedback inhibition is depressed and cannot avoid activation of another sensory modality, such as color, and any note is simultaneously perceived with some color [Grossenbacher 2001]. Are these coactivated areas forced to communicate because their reciprocal coupling is not inhibited? Synesthetes inevitably perceive a feature that is not present in the external stimulus and, thus, belong to their internal cortical activity. Could a change in the rhythmicity of one of this areas induce a loss of communication and recover a normal perception? Experimental collaborations should help to evaluate which is the most feasible way of testing our theoretical predictions.

We will also extend our work on UP and DOWN dynamics in two directions. On the one hand, we will investigate whether coherence resonance is being used by the *in vivo* brain to have some control over its state. For instance, in an anesthesia-awake transition, with the build up of cortical activity, we expect to find a maximum of regularity of the slow oscillations before entering the high-conductance state. On the other hand, we will study the gamma rhythm in the UP state and its disruption caused by perturbing the balance between excitation and inhibition. It is proposed that Down syndrome is mainly due to a a decrease in neuronal connectivity [Dierssen 2006]. The model presented in Appendix A.3 [Compte 2003], will allow us to selectively modify the synaptic conductances (excitatory-excitatory, excitatory-inhibitory, inhibitory-inhibitory and inhibitory-excitatory) in order to reveal their effect on the generation of gamma oscillations.

Appendix A

Models

A.1 Membrane subthreshold oscillations

A.1.1 Description of the FitzHugh-Nagumo neuronal model

We summarize here the model used in Chapter 2 and described throughout Section 2.2. In dimensionless units the model reads [Makarov 2001, Sancristóbal 2008]:

$$\varepsilon \frac{du}{dt} = u(u-a)(1-u) - v - I_{\text{syn}} \tag{A.1}$$

$$\frac{dv}{dt} = g(u-b) \tag{A.2}$$

where u represents the voltage variable and v the recovery variable. The parameter ε is the ratio between the characteristic times of u and v; here we choose $\varepsilon = 0.005$. The values of a and b are chosen such that the system operates near the Andronov-Hopf bifurcation ($a = 0.9$ and $b = 0.316$).

The function $g(u)$ has the form

$$g(u) = k_1 u^2 + k_2 \left(1 - \exp\left[-\frac{u}{k_2}\right]\right) \tag{A.3}$$

The duration of the spikes can be tuned by the parameters k_1 and k_2. We choose $k_1 = 7.0$ and $k_2 = 0.08$, for which the duration of the spikes is of the same order of magnitude as the period of the subthreshold oscillations, which is $T_{\text{sth}} = 2\pi\sqrt{\varepsilon} \approx 0.44$ near the Andronov-Hopf bifurcation point for an isolated neuron.

A.1.2 Description of the synaptic coupling

The synaptic current entering the neuron is given by Equation (1.13). The peak of the synaptic conductance, set to $g_{\max} = 0.1$, is chosen such that the neuron fires in response to the current pulses only for a specific range of phases of its subthreshold period. The synapse reversal potential $E_s = 0.7$, makes the connection excitatory. The fraction of open receptors $\sigma(t)$ follows the Equation (1.14), where $\alpha = 44$ and $\beta = 22$ are set in order to keep the rise and decay times of σ smaller than the period of the subthreshold oscillations. The function $T(t) = T_{\max}\theta(T_0 + \tau_{\text{syn}} - t)\theta(t - T_0)$ is the concentration of neurotransmitters released into the synaptic cleft, which is considered to have a constant value $T_{\max} = 1$ during a time $\tau_{\text{syn}} = 0.006$ after receiving a presynaptic spike at time T_0.

A.2 Collective gamma neuronal oscillations

A.2.1 Description of the conductance-based neuronal model

The dynamical equation for the neuronal membrane voltage used in Chapter 3 and 4 is given by a conductance-based model:

$$C_{\text{m}}\frac{dV}{dt} = -g_{\text{K}}n^4\left(V - V_{\text{K}}\right) - g_{\text{Na}}m^3h\left(V - V_{\text{Na}}\right) - g_{\text{L}}\left(V - V_{\text{L}}\right) - I_{\text{SYN}} \quad \text{(A.4)}$$

where $g_{\text{K}}, g_{\text{Na}}$ and g_{L} are the maximum conductances for the potassium, sodium and the leak current, respectively, and I_{SYN} is the synaptic current coming from the neighboring neurons impinging on a neuronal cell. For the three different synaptic sources studied here (i.e. GABAergic and AMPA synapses from the simulated inhibitory and excitatory neurons respectively, and AMPA synapses from the simulated external Poissonian train of spikes), I_{SYN} is the sum of three I_{syn}-like terms, Equation (1.13). The dynamics of the potassium and sodium channels is represented by the time-varying x probabilities that a channel is open:

$$\frac{dx}{dt} = \phi\left[\alpha_x(V)(1 - x) - \beta_x(V)x\right] \ ,$$

where x stands for n in the case of the potassium current, and for m and h in the case of the sodium current. $\alpha(V)$ and $\beta(V)$ are voltage-dependent rate constants, and ϕ is the temperature factor, defined by $\phi = 3^{(T-6.3)/10}$, where T is measured in degrees Celsius.

The rate functions α and β for each gating variable are:

$$\begin{aligned} \alpha_n(V) &= 0.01\frac{V + 20}{1 - e^{-(V+20)/10}} \\ \beta_n(V) &= 0.125e^{-(V+30)/80} \end{aligned}$$

for the gating variable n,

$$\begin{aligned}\alpha_m(V) &= 0.1\frac{V+16}{1-e^{-(V+16)/10}}\\ \beta_m(V) &= 4e^{-(V+41)/18}\end{aligned}$$

for the gating variable m, and

$$\begin{aligned}\alpha_h(V) &= 0.07e^{-(V+30)/20}\\ \beta_h(V) &= \frac{1.0}{1+e^{-V/10}}\end{aligned}$$

for the gating variable h. Due to the rapid activation of m we replace it by its steady-state value $m_\infty = \frac{\alpha_m}{\alpha_m+\beta_m}$.

The parameter values used throughout this study are those of [Gutfreund 1995]: $g_{\mathrm{K}} = 4.74\ \mu$S, $g_{\mathrm{Na}} = 12.5\ \mu$S and $g_{\mathrm{L}} = 0.025\ \mu$S. The reversal potentials of the different channels are $V_{\mathrm{K}} = -80$ mV, $V_{\mathrm{Na}} = 40$ mV and $V_{\mathrm{L}} = -65$ mV, and the membrane capacitance is $C_{\mathrm{m}} = 0.25$ nF (0.125 nF) for the excitatory (inhibitory) neurons. Values of C_{m} account for the size of the soma (a larger membrane area has more capacitance). The leak conductance defines an effective membrane time constant for the isolated neuron according to the expression $\tau_{\mathrm{m}} = C_{\mathrm{m}}/g_{\mathrm{L}}$, which is taken to be 10 ms for the excitatory neurons and 5 ms for the inhibitory neurons. For a given current, larger C imply slower voltage changes. The temperature factor ϕ is set to 21, which corresponds to $T = 34$°C. These parameter values lead to type I excitability.

In Chapter 4 the membrane capacitance is taken to be $C_{\mathrm{m}} = 0.5$ nF (0.25 nF) for the excitatory (inhibitory) neurons. The leak conductance ($g_{\mathrm{L}} = 0.025\ \mu$S), which is not varied with respect to the aforementioned parameters, defines an effective membrane time constant for the isolated neuron, which is here 20 ms for the excitatory neurons and 10 ms for the inhibitory neurons. Due to these large values, the membrane potential would, in principle, be hardly modulated by inputs with fast fluctuations on the order of the kHz, because a passive filter-like neuron will suppress input frequencies $f > \tau_{\mathrm{m}}$, Figure A.1. However, neurons are rarely in equilibrium and the intense synaptic presynaptic bombardment drives the cell close to the firing threshold, increasing its input conductance. Therefore, an effective membrane time constant can be shorter than 1 ms [Bernander 1991]. Since the membrane capacitances in the neuronal model used in Chapter 4 are twice of those in Chapter 3, firing rates of individual neurons are decreased.

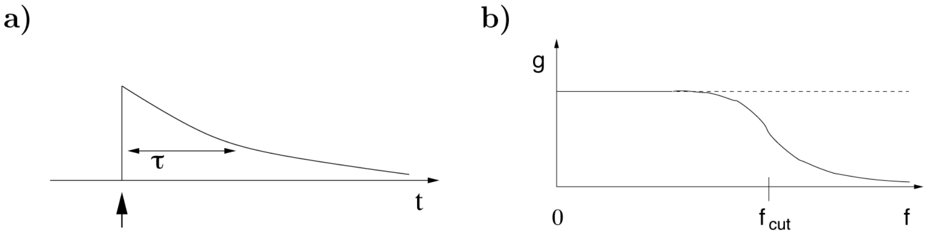

Figure A.1: (a) An input pulse (arrow) triggers a broad response in a low-pass filter characterized by a time constant τ. (b) The gain, g, of this filter shows a cut-off frequency at $f_{\text{cut}} = 1/\tau$. From [Gerstner 2006].

A.2.2 Description of the network model

We consider a network composed of 2000 neurons, 80% of which are excitatory while the remaining 20% are inhibitory [Soriano 2008]. All connections between cells are chemical synapses –no gap junctions are considered– and each neuron connects with 200 other neurons, on average, belonging to both populations. The connections are established following the Watts-Strogatz small-world algorithm [Watts 1998], with a rewiring probability of 1.0 (Chapter 3) and of 0.5 (Chapter 4). After the randomization of the links, in both cases the connectivity still shows a certain degree of clustering, but closest neighbors are further favored in the later case. In the former case the network is closer to a random one. In Chapter 4, the same criteria has been applied for the coupling between networks, where 60% of the excitatory neurons have been randomly chosen as long-range-projecting neurons making synapses to 10% of the neurons belonging to the other population.

We have also introduced a synaptic delay in the transmission of the action potential between neighboring neurons within a network, taken from a gamma distribution, [Vicente 2008], of mean 2 ms and variance 4 ms^2. In Chapter 4 we have used these values for the connectivity between distinct networks and we have assume shorter delays for neurons belonging to the same population (mean 1 ms and variance 1 ms^2).

The synaptic current is described using again a conductance-based formalism [see Equation (1.13)]. For a synapse reversal potential, E_{syn}, greater than the resting potential, the synapse is depolarizing, i.e. *excitatory*, otherwise it is hyperpolarizing, i.e. *inhibitory*. We consider two temporal time constants [see Equation (1.21)], τ_{decay} and τ_{rise} (decay and rise synaptic time respectively, see Table A.1), for the dynamics of the synaptic conductance, which is calculated by

$$g_{\text{syn}}(t) = \frac{g'_{\text{syn}}}{\tau_{\text{decay}} - \tau_{\text{rise}}} \left[e^{\frac{-t-t_j}{\tau_{\text{decay}}}} - e^{\frac{-t-t_j}{\tau_{\text{rise}}}} \right] ,$$

where g'_{syn}, shown in Table A.2, is tuned in order to obtain a balance between excitation and inhibition, given the *f*-*I* relation.

Synapse	τ_{rise}	τ_{decay}	E_{syn}
AMPA	0.5 ms	2 ms	0 mV
GABA	2 ms	5 ms	−70 mV

Table A.1: Synaptic time constants and reversal synaptic potential values. The equilibrium potential at $I_{\text{syn}} = 0$ for Equation (A.4) is $V_{\text{rest}} = -65$ mV.

We have chosen the maximal conductances, g'_{syn}, to maintain the postsynaptic potential (PSP) amplitudes within physiological ranges: the excitatory PSP in the range from 0.42 mV to 0.83 mV, and the inhibitory PSP from 1.54 mV to 1.88 mV.

C_{m}	0.125 nF	0.25 nF	0.25 nF	0.5 nF
Synapse	Conductance on inhibitory neurons		Conductance on excitatory neurons	
GABA	240 nS	325 nS	240 nS	360 nS
Recurrent AMPA	2.5 nS	4.2 nS	2.5 nS	4.2 nS
External AMPA	3.2 nS	4.2 nS	3.2 nS	5.5 nS

Table A.2: Synaptic conductances, g'_{syn}, for all the possible connections and both sets of capacitance C_{m} parameter values.

Additionally, all neurons receive an heterogeneous Poisson train of excitatory presynaptic potentials with a mean event rate that varies following an Ornstein-Uhlenbeck process. This incoming external current mimics the direct input from any other area external to the network considered here. The instantaneous rate, $\lambda(t)$, of the external excitatory train of spikes is generated according to an Ornstein-Uhlenbeck process as considered in [Mazzoni 2008]:

$$\frac{d\lambda}{dt} = -\lambda(t) + \sigma(t)\left(\sqrt{\frac{2}{\tau}}\right)\eta(t) \tag{A.5}$$

where $\sigma(t)$ is the standard deviation of the noisy process and is set to 0.6 spikes/s. τ is set to 16 ms, leading to a *1/f* power spectrum for the λ time series that is flat up to a cut-off frequency $f = \frac{1}{2\pi\tau} = 9.9$ Hz. $\eta(t)$ is a Gaussian white noise.

Excitatory synapses outnumber inhibitory ones, and yet the brain avoids epileptic states because inhibition is able to balance excitation, and thus neurons remain below threshold, firing only occasionally. Inhibitory neurons have higher firing rates than excitatory neurons for any given input current, as can be seen in the *f*-*I* curve of Figure 3.6. Additionally, GABAergic (inhibitory) synapses are stronger than glutamatergic AMPA (excitatory) synapses to compensate their relative small number [Markram 2004].

The model has been integrated using the Heun algorithm, [Garcia-Ojalvo 1999], with a time step of 0.05 ms. All the simulations represent 1.5 seconds of activity and the connectivity, initial conditions, and noise realization were varied from trial to trial.

A.3 Slow UP and DOWN neuronal oscillations

A.3.1 Description of the conductance-based neuronal model

The dynamical equations for the neuronal membrane voltage and for the ionic channels are as in [Compte 2003].

Excitatory neurons The somatic and dendritic voltage of the excitatory neurons follow:

$$\begin{aligned} C_\mathrm{m} A_\mathrm{s} \frac{dV_\mathrm{s}}{dt} &= -A_\mathrm{s}\left(I_\mathrm{L} + I_\mathrm{Na} + I_\mathrm{K} + I_\mathrm{A} + I_\mathrm{KS} + I_\mathrm{KNa}\right) - \\ &\quad -I_\mathrm{syn,s} - g_\mathrm{sd}\left(V_\mathrm{s} - V_\mathrm{d}\right) \qquad \text{(A.6)} \\ C_\mathrm{m} A_\mathrm{d} \frac{dV_\mathrm{d}}{dt} &= -A_\mathrm{d}\left(I_\mathrm{Ca} + I_\mathrm{KCa} + I_\mathrm{NaP} + I_\mathrm{AR}\right) - \\ &\quad -I_\mathrm{syn,d} - g_\mathrm{sd}\left(V_\mathrm{d} - V_\mathrm{s}\right) \qquad \text{(A.7)} \end{aligned}$$

where $I_\mathrm{syn,s}$ is the synaptic current coming from the neighboring inhibitory neurons and $I_\mathrm{syn,d}$ is the synaptic current coming from the neighboring excitatory neurons. The two compartments are joined by an electrical coupling of conductance $g_\mathrm{sd} = 1.75 \pm 0.1\ \mu\mathrm{S}$ such that both voltages are quickly synchronized. Here, the synaptic conductances and g_sd are scaled by the surface of the soma, $A_\mathrm{s} = 0.015\ \mathrm{mm}^2$, and the dendrites, $A_\mathrm{d} = 0.035\ \mathrm{mm}^2$. The membrane capacitance is $C_\mathrm{m} = 1\ \mu\mathrm{F/cm}^2$.

The dynamics of the potassium $[I_\mathrm{K} = g_\mathrm{K} n^4 (V - V_\mathrm{K})]$ and sodium channels $[I_\mathrm{Na} = g_\mathrm{Na} m_\infty^3 h\,(V - V_\mathrm{Na})]$ are represented by the time-varying probabilities, x, that a channel is open:

$$\frac{dx}{dt} = \phi\left[\alpha_x(V)(1-x) - \beta_x(V)x\right] ,$$

where x stands for n in the case of the potassium current, and for m and h in the case of the sodium current. The parameter values used throughout this study are based on [Compte 2003]: $g_{\mathrm{K}} = 10.5$ mS/cm^2, $g_{\mathrm{Na}} = 50$ mS/cm^2 and $g_{\mathrm{L}} = 0.0667 \pm 0.0067$ mS/cm^2.

The rate functions α and β for each gating variable are:

$$\begin{aligned} \alpha_n(V) &= 0.01 \frac{V+34}{1-e^{-(V+34)/10}} \\ \beta_n(V) &= 0.125 e^{-(V+44)/25} \end{aligned}$$

for the gating variable n,

$$\begin{aligned} \alpha_m(V) &= 0.1 \frac{V+33}{1-e^{-(V+33)/10}} \\ \beta_m(V) &= 4 e^{-(V+53.7)/12} \end{aligned}$$

for the gating variable m, and

$$\begin{aligned} \alpha_h(V) &= 0.07 e^{-(V+50)/10} \\ \beta_h(V) &= \frac{1.0}{1+e^{-(V+20)/10}} \end{aligned}$$

for the gating variable h. Due to the rapid activation of m we replace it by its steady-state value $m_\infty = \frac{\alpha_m}{\alpha_m+\beta_m}$. The leak current is a passive channel of the form $I_{\mathrm{L}} = g_{\mathrm{L}}\,(V - V_{\mathrm{L}})$.

The time-varying probabilities x that a channel is open can also be expressed as:

$$\frac{dx}{dt} = \phi\,[x_\infty(V) - x]\,/\tau_x(V).$$

The rest of ionic channels are described in terms of $x_\infty(V)$ and $\tau_x(V)$ and the temperature factor ϕ is set to 1.

The fast A-type K$^+$-channel, $I_{\mathrm{A}} = g_{\mathrm{A}} m_\infty^3 h\,(V - V_{\mathrm{K}})$:

$$\begin{aligned} m_\infty(V) &= \frac{1}{1+e^{-(V+50)/20}} \\ h_\infty(V) &= \frac{1}{1+e^{(V+80)/6}} \\ \tau_h &= 15 \text{ ms} \end{aligned}$$

where $g_{\mathrm{A}} = 1$ mS/cm^2.

The non-inactivating K$^+$-channel, $I_{\mathrm{KS}} = g_{\mathrm{KS}} m \left(V - V_{\mathrm{K}}\right)$:

$$\begin{aligned} m_\infty(V) &= \frac{1}{1 + e^{-(V+34)/6.5}} \\ \tau_m(V) &= \frac{8}{e^{-(V+55)/30} + e^{(V+55)/30}} \end{aligned}$$

where $g_{\mathrm{KS}} = 0.576$ mS/cm^2.

The persistent sodium channel, $I_{\mathrm{NaP}} = g_{\mathrm{NaP}} m_\infty^3 \left(V - V_{\mathrm{Na}}\right)$:

$$m_\infty(V) = \frac{1}{1 + e^{-(V+55.7)/7.7}}$$

where $g_{\mathrm{NaP}} = 0.0686$ mS/cm^2.

The inward rectifying K$^+$-channel, $I_{\mathrm{AR}} = g_{\mathrm{AR}} h_\infty \left(V - V_{\mathrm{K}}\right)$:

$$h_\infty(V) = \frac{1}{1 + e^{(V+75)/4}}$$

where $g_{\mathrm{AR}} = 0.0257$ mS/cm^2.

The high-threshold Ca^{2+}-channel, $I_{\mathrm{Ca}} = g_{\mathrm{Ca}} m_\infty^2 \left(V - V_{\mathrm{Ca}}\right)$:

$$m_\infty(V) = \frac{1}{1 + e^{-(V+20)/9}}$$

where $g_{\mathrm{Ca}} = 0.43$ mS/cm^2.

Two more channels are considered, which depend on ionic concentrations. The Ca^{2+}-dependent K$^+$-channel and the Na$^+$-dependent K$^+$-channel:

$$I_{\mathrm{KCa}} = g_{\mathrm{KCa}} \frac{[\mathrm{Ca}^{2+}]}{[\mathrm{Ca}^{2+}] + K_D} \left(V - V_{\mathrm{K}}\right) \quad \text{, and}$$

$$I_{\mathrm{KNa}} = g_{\mathrm{KNa}} w_\infty([\mathrm{Na}^+]) \left(V - V_{\mathrm{K}}\right)$$

respectively, where $K_D = 30$ mM, $g_{\mathrm{KCa}} = 0.57$ mS/cm^2, $w_\infty([\mathrm{Na}^+]) = 0.37/\left(1 + \left(38.7/([\mathrm{Na}^+])^{3.5}\right)\right)$ and $g_{\mathrm{KNa}} = 1.33$ mS/cm^2. Moreover, the intracellular concentration of calcium follows the dynamical equation:

$$\frac{d[\mathrm{Ca}^{2+}]}{dt} = -\alpha_{\mathrm{Ca}} A_{\mathrm{d}} I_{\mathrm{Ca}} - \frac{[\mathrm{Ca}^{2+}]}{\tau_{\mathrm{Ca}}}$$

where α_{Ca}=5 mM/(mA·ms) and $\tau_{\mathrm{Ca}} = 15$ ms. The intracellular sodium concentration obeys the equation:

$$\begin{aligned} \frac{d[\mathrm{Na}^{+}]}{dt} &= -\alpha_{\mathrm{Na}}\left(A_{\mathrm{s}} I_{\mathrm{Na}} + A_{\mathrm{d}} I_{\mathrm{NaP}}\right) - \\ &\quad -\left(R_{\mathrm{pump}} + D\xi_{\mathrm{OU}}(t)\right)\left(\frac{[\mathrm{Na}^{+}]^{3}}{[\mathrm{Na}^{+}]^{3} + 15^{3}} - \frac{[\mathrm{Na}^{+}]_{\mathrm{eq}}^{3}}{[\mathrm{Na}^{+}]_{\mathrm{eq}}^{3} + 15^{3}}\right) \end{aligned}$$

where $\alpha_{\mathrm{Na}} = 10 \pm 2$ mM/(mA·ms), $R_{\mathrm{pump}} = 0.08 \pm 0.0018$ mM/ms and $[\mathrm{Na}^{+}]_{\mathrm{eq}} = 9.5$ mM. Note that the sodium dynamics considers the Na^{+}-K^{+}-pump which releases three sodium ions for each potassium ion brought inside the neuron [see Section 1.3.1]. The slow kinetics of this pump [Wang 2003] evolve following an Ornstein-Uhlenbeck stochastic process, $\xi_{\mathrm{OU}}(t)$, of amplitude D=0.088 mM/ms. A noisy realization is obtained following [San Miguel 1997, Garcia-Ojalvo 1999]:

$$\begin{cases} \xi_{\mathrm{OU}}(0) = \sqrt{\frac{1}{2\tau}}\,u(0) \\ \xi_{\mathrm{OU}}(t+h) = \xi_{\mathrm{OU}}(t)e^{-h/\tau} + \sqrt{\frac{\left(1-e^{-2h/\tau}\right)}{2\tau}}\,u(t+h) \end{cases}$$

where $u(t)$ is a Gaussian white noise and $\tau = 300$ ms.

The reversal potentials of the different channels are $V_{\mathrm{K}} = -100$ mV, $V_{\mathrm{Na}} = 55$ mV, $V_{\mathrm{Ca}} = 120$ mV and $V_{\mathrm{L}} = -60.95 \pm 0.3$ mV.

Inhibitory neurons Only the somatic compartment is modeled, and its membrane voltage follows:

$$C_{\mathrm{m}} A_{\mathrm{i}} \frac{dV}{dt} = -A_{\mathrm{i}}\left(I_{\mathrm{L}} + I_{\mathrm{Na}} + I_{\mathrm{K}}\right) - I_{\mathrm{SYN,i}} \tag{A.8}$$

where $A_{\mathrm{i}} = 0.02$ mm^2. $I_{\mathrm{SYN,i}}$ stands for the sum of both the excitatory and inhibitory currents coming from the presynaptic neurons. As in the previous Section, here the inhibitory cells are described with the minimum neuronal model for action potential generation. The sodium, potassium and leak current follow the same formalism as in the above excitatory neuronal model with the following α and β rate functions:

$$\begin{aligned}\alpha_n(V) &= 0.05\frac{V+34}{1-e^{-(V+34)/10}}\\ \beta_n(V) &= 0.625e^{-(V+44)/80}\end{aligned}$$

for the gating variable n,

$$\begin{aligned}\alpha_m(V) &= 0.5\frac{V+35}{1-e^{-(V+35)/10}}\\ \beta_m(V) &= 20e^{-(V+60)/18}\end{aligned}$$

for the gating variable m, and

$$\begin{aligned}\alpha_h(V) &= 0.35e^{-(V+58)/20}\\ \beta_h(V) &= \frac{5.0}{1+e^{-(V+28)/10}}\end{aligned}$$

for the gating variable h.

The temperature factor ϕ is set to 1. The maximal conductances are $g_{\mathrm{Na}} = 35$ mS/cm^2, $g_{\mathrm{K}} = 9$ mS/cm^2 and $g_{\mathrm{L}} = 0.1025 \pm 0.0025$ mS/cm^2, and reversal potentials $V_{\mathrm{K}} = -90$ mV, $V_{\mathrm{Na}} = 55$ mV and $V_{\mathrm{L}} = -63.8 \pm 0.15$ mV. All parameters are kept constant for all excitatory neurons except in the cases given as mean ± SD. SD corresponds to the standard deviation of a gaussian distributed parameter over the population.

A.3.2 Potassium reversal potential

The Nernst equation [Equation (1.1)] establishes the relation between the reversal potential of a ionic channel V_{ion} (or equilibrium potential at which there is no net flow of ions across the channel) and the ratio between the external and internal concentration of this particular ionic species $\frac{C_o}{C_i}$. For the potassium ion (z=1) we have set C_i (or $[\mathrm{K}^+]_i$) to 150 mM and varied C_o (or $[\mathrm{K}^+]_o$) from 2.5 mM ($V_{\mathrm{K}} \sim$ -108 mV) to 7.5 mM ($V_{\mathrm{K}} \sim$ -79 mV).

A.3.3 Description of the network model

We consider a network composed of 1280 neurons, 80% of which are excitatory while the remaining 20% are inhibitory [Soriano 2008]. Neurons were arranged in two open one-dimensional chains, one for the excitatory population and another one for the inhibitory population, such that every 4 adjacent excitatory neurons, one inhibitory neuron was placed. All connections between cells are chemical synapses –no gap junctions are considered–, and each

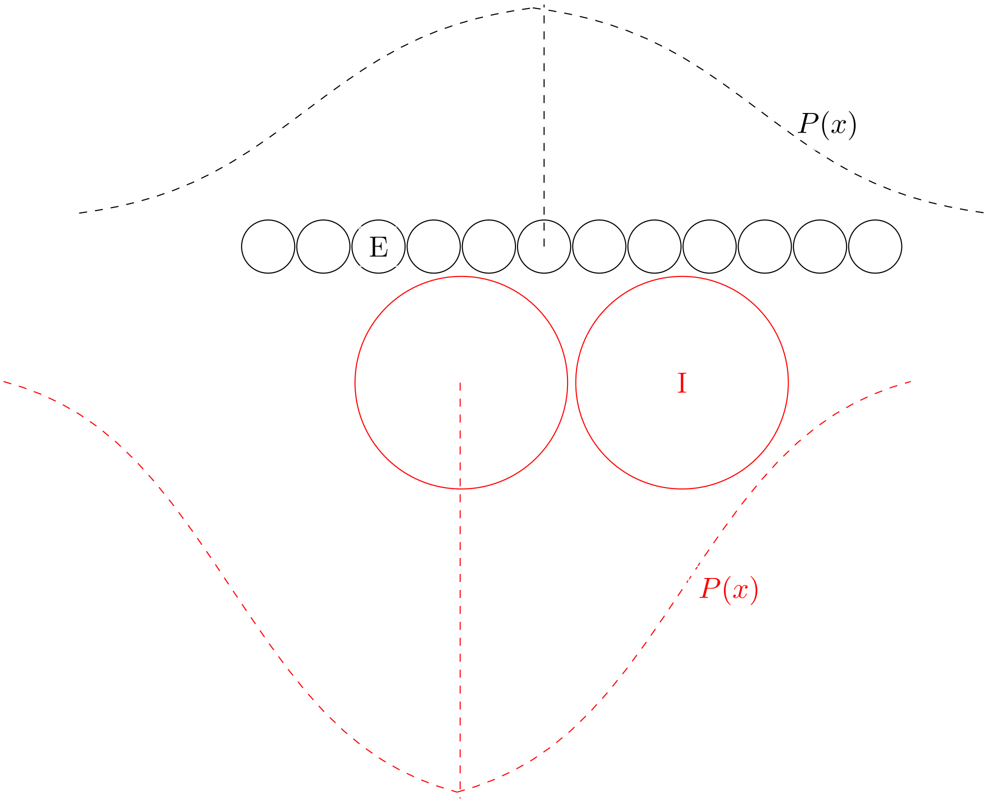

Figure A.2: Schematic connectivity of the circuit exhibiting UP and DOWN dynamics. Excitatory (inhibitory) neurons are shown as black (red) circles. The shape of the probability of connection $P(x)$ centered in two types of neurons is plotted as a dashed line. Only the relative size between the length of neurons and, on the other hand, between the standard deviation of $P(x)$ are representative.

neuron connects with 20±5 other neurons. The two chains are 5 mm long, with neurons touching the two nearest neighbors.

Our interpretation of the microcircuit described in [Compte 2003] is shown schematically in Figure A.2. The probability that two neurons are connected is determined by their distance x according to a Gaussian probability distribution $P(x) = \frac{e^{-x^2/2\sigma^2}}{\sqrt{2\pi\sigma^2}}$. No autapses are allowed and the standard deviation σ is set to 250 μm for the excitatory connection and to 125 μm for the inhibitory connections. In Figure A.2, the relative size between neuron's length and between the σ values of the two populations is maintained. However, note that this comparison cannot be made between the size of a neuron and its corresponding σ. For instance, the size of an excitatory neuron is $\sim$5 μm (50 times smaller than its σ) and of an inhibitory neuron $\sim$19 μm (about 13 times smaller than its σ).

We have considered two types of excitatory synapses, AMPA and NMDA mediated, [Wang 1999]:

$$I_{\text{AMPA}} = g_{\text{AMPA}} s(t)(V - E_{\text{syn}}) \tag{A.9}$$

$$I_{\text{NMDA}} = g_{\text{NMDA}} s(t)(V - E_{\text{syn}}) \left(\frac{1}{1 + [\text{Mg}^{2+}] e^{-0.062V/3.57}} \right) \tag{A.10}$$

where the reversal synaptic potential is $E_{\text{syn}} = 0$ mV and the extracellular magnesium concentration $[\text{Mg}^{2+}] = 1.0$ mM. The g_{AMPA} and g_{NMDA} peak conductances are given in Table A.4 and *s(t)* follows two first-order kinetics:

$$\frac{dx}{dt} = \phi \left(\alpha_x \sum_j \delta(t - t_j) - x/\tau_x \right) \tag{A.11}$$

$$\frac{ds}{dt} = \phi \left(\alpha_s x(1 - s) - s/\tau_s \right) \tag{A.12}$$

where ϕ=1 and the temporal time constants are shown in Table A.3.

Synapse	α_x (dimensionless)	τ_x	α_s	τ_s
AMPA	1.0	0.5 ms	1.0 ms^{-1}	2.0 ms
NMDA	1.0	2.0 ms	1.0 ms^{-1}	80 ms

Table A.3: Synaptic time constants for AMPA and NMDA synapses.

The inhibitory neurons are GABA mediated, $I_{\text{GABA}} = g_{\text{GABA}} s(t)(V - E_{\text{syn}})$ where $E_{\text{syn}} = -70$ mV. The g_{GABA} peak conductance is given in Table A.4 and *s(t)* follows first-order kinetics:

$$\frac{ds}{dt} = \alpha_i \sum_j \delta(t - t_j)(1 - s) - s/\tau_i \tag{A.13}$$

where $\alpha_i = 0.9$ ms^{-1} and $\tau_i = 10$ ms.

Synapse	Conductance on inhibitory neurons	Conductance on excitatory neurons
GABA	240 nS	480 nS
Recurrent AMPA	2.25 nS	7.35 nS
Recurrent NMDA	3.0 nS	8.0 nS
External AMPA	2.25 nS	7.35 nS
External NMDA	2.0 nS	8.0 nS

Table A.4: Synaptic conductances for all the possible connections.

Additionally, all neurons receive an heterogeneous Poisson train of excitatory presynaptic potentials with a an event rate that varies following an Ornstein-Uhlenbeck process [see Equation (A.5)] (mean = 50 spikes/s), that mimics the synaptic input coming from the rest of the cortical slice not being directly simulated by the set of Equations (A.6)-(A.7) and (A.8). The model has been integrated using the Heun algorithm, [Garcia-Ojalvo 1999], with a time step of 0.05 ms.

A.4 Model of local field potential (LFP) and multi-unit activity (MUA)

In Chapters 3-5, we have quantified the activity of the network in different ways. At the single-neuron level we consider the instantaneous firing rate as a measure of the individual spiking dynamics. At the population level we use three observables. First, the time-resolved average firing rate of the whole neuronal population, defined in Chapter 3 as the total number of spikes per unit time in the population divided by the number of neurons. Second the multi-unit activity (MUA), defined in Chapter 4 as the total number of spikes in 5-millisecond windows shifted in steps of 1 millisecond [Buehlmann 2010], and in Chapter 5 as the high-pass filtered local field potential (cut-off frequency 200 Hz) [McCormick 2003]. Finally, the local field potential (LFP), computed as the sum of the absolute values of the excitatory and inhibitory synaptic currents acting upon the excitatory neurons, averaged over this population [Mazzoni 2008, Buzsáki 2012]:

$$\mathrm{LFP} = R_e \left\langle |I_{\mathrm{AMPA}}| + |I_{\mathrm{GABA}}| \right\rangle , \tag{A.14}$$

Here $\langle \cdots \rangle$ denotes an average over all excitatory neurons [Berens 2010]. In particular, for the LFP traces shown in Chapter 5 we have considered only 150 adjacent excitatory neurons from the whole population. The term I_{AMPA} accounts for both the external excitatory heterogeneous Poisson spike train and the recurrent excitatory synaptic current due to network connectivity, while I_{GABA} corresponds to the recurrent inhibitory synaptic current. R_e represents the resistance of a typical electrode used for extracellular measurements, here chosen to be 1 MΩ. In Figures 3.13 and 4.14 the LFP and MUA was filtered with a $4th$ order Butterworth bandpass filter using MATLAB function *filter.m*.

Appendix B
Methods

B.1 Spike triggered average

The spike triggered average (STA) of the LFP and of the inhibitory synaptic current impinging on the neurons represent averages of these signals within a window starting 50 ms prior to a spike and ending 20 ms after it, across the total number of action potentials.

B.2 Multitapered power spectra

The LFP power spectrum was estimated using the multitaper method [Thomson 1982] commonly used to reduce the variance of the spectra of recorded signals, which are usually very noisy. This method is based on the idea that different multitapered data segments give uncorrelated spectral estimates, and when they are averaged, the variance of the mean is reduced. This estimator was implemented in Chronux 2.10 [Bokil 2010]. The multitapered power spectrum, $S(f)$, is the average of the power spectrum of the LFP signal multiplied by K orthogonal Slepian functions (in our case K=5), and further averaged over N trials:

$$S(f) = \frac{1}{N}\sum_{n=1}^{N} s_n(f) = \frac{1}{N}\sum_{n=1}^{N}\left(\frac{1}{K}\sum_{k=1}^{K} \mid \widetilde{LFP}_{n,k}(f) \mid^2\right) \tag{B.1}$$

Here $\widetilde{LFP}_{n,k}(f)$ is the discrete Fourier transform $LFP(t)$ signal of the n-th trial, multiplied by the k-th Slepian function (or taper). We have considered data segments within a 500-ms sliding time window with an overlap of 50 ms, padded with zeros up to a length of 512 in order to obtain an increased sampling rate in the frequency domain. The resolution bandwidth is thus ±6 Hz. The firing rate power spectra are also obtained by the multitaper algorithm, with the same sliding time window, overlap, and padding. In this case the average instantaneous firing rate is obtained from an histogram of the spiking times, with a 1-ms bin. All histograms and power spectra are averaged over 20 trials, taking into account the aforementioned division in time segments $N = 420$.

B.3 Phase coherence

The phase coherence, Figure 4.7, and phase difference plots, Figure 4.8, are obtained with the *coherencyc.m* function for continuous signals implemented in Chronux 2.10, [Bokil 2010]. The normalization convention was taken as in [Womelsdorf 2007]:

$$C_{xy}(f) = \left| \frac{1}{N} \sum_{n=1}^{N} \frac{S_{xy}(f,n)}{|S_{xy}(f,n)|} \right|, \tag{B.2}$$

where x and y denote the two signals whose coherence is being calculated. $S_{xy}(f,n)$ is the cross-spectrum between these two signals. For each trial we have considered data segments within a 500-ms sliding time window with an overlap of 50 ms, padded with zeros up to a length of 512 in order to obtain an increased sampling rate in the frequency domain. All trials represent 1.5 seconds of activity and the connectivity, initial conditions, and noise realization were varied from trial to trial. All phase coherence results are averages over three groups of 200 trials, taking into account the aforementioned division in time segments $N = 4200$ for each group.

Each term within the summation of Equation (B.2) is a unitary complex value, $e^{\Delta\phi(f,n)}$. Each term is obtained as the product of the multitapered power spectrum S of the signals: $S_{xy}(f,n) = S_x^*(f,n) \cdot S_y(f,n)$, where $*$ denotes complex conjugate. Therefore, $\Delta\phi(f,n) = \phi_y - \phi_x$, is the phase lag between signals x and y in the data segment n, at frequency f. Averaging $\Delta\phi(f,n)$ across all the N data segments provides a mean angle $\Delta\phi(f)$. Note that taking the absolute value in Equation (B.2) gives the norm of the resultant vector $\frac{1}{N}\sum_{n=1}^{N} e^{\Delta\phi(f,n)}$ which is the phase coherence $C_{xy}(f)$ itself. Hence $C_{xy}(f)$ quantifies how broad is the distribution of $\Delta\phi(f,n)$ measures within the 2π-cycle. However, the direction of the resultant vector does not correspond to $\Delta\phi(f)$ (the mean of two angles gives the bisector without taking into account the length of the vectors).

In Figure 4.9, $\Delta\phi(f)$ is converted into a time shift by dividing by the corresponding frequency $\tau_e(f) = \frac{\Delta\phi(f)}{2\pi f}$. In all cases x is the fast signal (held at $\tau_{\mathrm{GABA}} = 5$ ms) and y the slow signal (at $\tau_{\mathrm{GABA}} \geq 5$ ms). Negative $\Delta\phi(f)$ indicate a leader-laggard configuration, $\tau_e(f)$ being negative and y following x.

B.4 Experimental methods

The experiments were carried out in the laboratory of Dr. Mavi Sanchez-Vives (IDIBAPS, Barcelona). Brains from anesthetized male young ferrets (5 to 6 months old) were extracted. Coronal slices of 0.4 mm thick were obtained from the prefrontal cortex. Following transfer to the recording chamber, the slices were incubated at 34-35 ^{o}C in a solution containing (in mM) 63NaCl, 126 sacarose; 2.5KCl, 2MgSO4, 1.25Na$_2$HPO$_4$, 2CaCl$_2$, 26NaHCO$_3$. After 15 minutes, the slice solution was modified to contain (in mM) 126NaCl, 2.5KCl, 2MgSO$_4$, 1.25Na$_2$HPO$_4$, 2CaCl$_2$, 26NaHCO$_3$. Finally, after approximately 1 hour and 30 minutes, the solution was replaced by the *oscillatory* solution containing (in mM) 3.5KCl, 1MgSO$_4$, 1CaCl$_2$ (the remaining compounds were left unchanged). 15 minutes later the temperature is increased to 36 ^{o}C. These conditions allow the emergence of spontaneous UP and DOWN states.

The recordings of the extracellular activity were obtained with 2-4 MΩ tungsten electrodes (FHC, Bowdoinham, ME). The LFP potential was defined as the raw data without filtering and amplified (x 1000). The MUA was considered to be well described by the power change of the LFP at high frequencies ($>$ 200 Hz). This assumption relies on the fact that the normalized density of the LFP power spectrum at high frequencies is proportional to the instantaneous firing rate close to the electrode tip [Mattia 2002, Reig 2010]. When this normalization is performed with respect to the averaged power spectrum at the DOWN states, the MUA provides dimensionless values of the relative firing activity in the UP state with respect to the DOWN state. MUAs were logarithmically scaled, log(MUA) to reduce large fluctuations of the nearest elicited spikes to smaller ranges. UP and DOWN states were discriminated by setting a threshold in the log(MUA), Figure B.1.

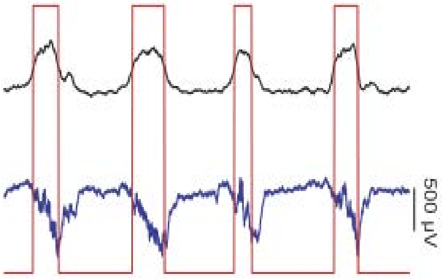

Figure B.1: Relative firing rate (balck) and LFP (blue) register in visual cortex in an anesthetized cat. The red boxes represent the detected UP and DOWN states. From [Ruiz-Mejias 2011].

List of publications

[Sancristóbal 2008] Sancristóbal, B and Sancho, J M and Garcia-Ojalvo, J. *Resonant Spike Propagation in Coupled Neurons with Subthreshold Activity.* Lecture Notes in Computer Science, vol. 5164, page 695, 2008. (Cited on pages 127 and 133.)

[Sancristóbal 2010a] Sancristóbal, B and Sancho, J M and Garcia-Ojalvo, J. *Phase-response approach to firing-rate selectivity in neurons with subthreshold oscillations.* Phys Rev E Stat Nonlin Soft Matter Phys, vol. 82, no. 4 Pt 1, page 041908, Oct 2010. (Cited on pages 45, 49, 55 and 127.)

[Sancristóbal 2010b] Sancristóbal, B and Sancho, J M and Garcia-Ojalvo, J. *Resonant propagation of spike trains in delay-coupled neural subthreshold oscillators.* Eur. Phys. J. Special Topics, vol. 187, pages 189–197, 2010. (Cited on pages 57 and 127.)

[Sancristóbal 2013a] Sancristóbal, B and Vicente, R and Sancho, J M and Garcia-Ojalvo, J. *Emergent bimodal firing patterns implement different encoding strategies during gamma-band oscillations.* Front Comput Neurosci, vol. 7, page 18, 2013. (Cited on pages 81, 86 and 128.)

[Sancristobal2013b] Sancristóbal, B and Vicente, R and Pons, A J and Pipa, G and Garcia-Ojalvo, J *Modulating the phase coherence of neuronal population oscillations in the gamma band.* Proceedings of the 3rd International Conference on Cognitive Neurodynamics, ed. Y Yamaguchi, Springer, 2013. (Cited on page 93.)

[Sancristóbal 2013c] Sancristóbal, B and Vicente, R and Garcia-Ojalvo, J. *Interactions between detuned gamma oscillations: the role of frequency mismatch in neuronal communication through coherence.* Submitted to PLOS Computational Biology, 2013. (Cited on page 105.)

[Sancristóbal 2013d] Sancristóbal, B and Sanchez-Vives, M V and Garcia-Ojalvo, J. *Stochastic coherence in UP and DOWN states.* In preparation, 2013. (Cited on page 121.)

Bibliography

[Albert 2000] R Albert, H Jeong and A-L Barabasi. *Error and attack tolerance of complex networks.* Nature, vol. 406, no. 6794, pages 378–82, Jul 2000. (Cited on page 33.)

[Alonso 1989] A Alonso and R R Llinás. *Subthreshold Na+-dependent theta-like rhythmicity in stellate cells of entorhinal cortex layer II.* Nature, vol. 342, no. 6246, pages 175–7, Nov 1989. (Cited on page 38.)

[Amir 1999] R Amir, M Michaelis and M Devor. *Membrane potential oscillations in dorsal root ganglion neurons: role in normal electrogenesis and neuropathic pain.* J Neurosci, vol. 19, no. 19, pages 8589–96, Oct 1999. (Cited on page 55.)

[Balenzuela 2007] P Balenzuela and J García-Ojalvo. *Spatiotemporal Response of Neuronal Networks to Time-Dependent Spectral Features.* AIP Conference Proceedings, vol. 913, page 178, 2007. (Cited on page 57.)

[Ball 2008] T Ball, E Demandt, I Mutschler, E Neitzel, C Mehring, K Vogt, A Aertsen and A Schulze-Bonhage. *Movement related activity in the high gamma range of the human EEG.* Neuroimage, vol. 41, no. 2, pages 302–10, Jun 2008. (Cited on page 84.)

[Barabási 1999] A-L Barabási and R Albert. *Emergence of scaling in random networks.* Science, vol. 286, no. 5439, pages 509–12, Oct 1999. (Cited on page 33.)

[Barabási 2004] A-L Barabási and Z N Oltvai. *Network biology: understanding the cell's functional organization.* Nat Rev Genet, vol. 5, no. 2, pages 101–13, Feb 2004. (Cited on pages 33 and 34.)

[Barberini 2001] C L Barberini, G D Horwitz and W T Newsome. Motion vision, chapitre A comparison of spiking statistics in motion sensing neurones of flies and monkeys, pages 307–320. Springer, 2001. (Cited on page 67.)

[Barth 2012] A L Barth and J F A Poulet. *Experimental evidence for sparse firing in the neocortex.* Trends Neurosci, vol. 35, no. 6, pages 345–55, Jun 2012. (Cited on page 72.)

[Bastos 2012] A M Bastos, W M Usrey, R A Adams, G R Mangun, P Fries and K J Friston. *Canonical microcircuits for predictive coding.* Neuron, vol. 76, no. 4, pages 695–711, Nov 2012. (Cited on page 104.)

[Benson 1996] D L Benson and P A Cohen. *Activity-independent segregation of excitatory and inhibitory synaptic terminals in cultured hippocampal neurons.* J Neurosci, vol. 16, no. 20, pages 6424–32, Oct 1996. (Cited on page 18.)

[Berens 2010] Ph Berens, N K Logothetis and A S Tolias. *Local field potentials, BOLD and spiking activity-relationships and physiological mechanisms.* Nat. Proc., vol. http://precedings.nature.com/ documents/5216/version/1, 2010. (Cited on pages 90 and 145.)

[Bereshpolova 2011] Y Bereshpolova, C R Stoelzel, J Zhuang, Y l Amitai, J-M Alonso and H A Swadlow. *Getting drowsy? Alert/nonalert transitions and visual thalamocortical network dynamics.* J Neurosci, vol. 31, no. 48, pages 17480–7, 2011. (Cited on page 71.)

[Berman 1998] N J Berman and L Maler. *Distal versus proximal inhibitory shaping of feedback excitation in the electrosensory lateral line lobe: implications for sensory filtering.* Journal of Neurophysiology, vol. 80, no. 6, pages 3214–3232, 1998. (Cited on page 7.)

[Bernander 1991] O Bernander, R J Douglas, K A Martin and C Koch. *Synaptic background activity influences spatiotemporal integration in single pyramidal cells.* Proc Natl Acad Sci U S A, vol. 88, no. 24, pages 11569–73, Dec 1991. (Cited on page 135.)

[Bhattacharjee 2005a] A Bhattacharjee and L K Kaczmarek. *For K+ channels, Na+ is the new Ca2+.* Trends Neurosci, vol. 28, no. 8, pages 422–8, Aug 2005. (Cited on page 130.)

[Bhattacharjee 2005b] A Bhattacharjee, Ch A A von Hehn, X Mei and L K Kaczmarek. *Localization of the Na+-activated K+ channel Slick in the rat central nervous system.* J Comp Neurol, vol. 484, no. 1, pages 80–92, Mar 2005. (Cited on page 118.)

[Bock 2011] D D Bock, W-Ch A Lee, A M Kerlin, M L Andermann, G Hood, A W Wetzel, S Yurgenson, Ed R Soucy, H S Kim and R C Reid. *Network anatomy and in vivo physiology of visual cortical neurons.* Nature, vol. 471, no. 7337, pages 177–182, 03 2011. (Cited on page 32.)

[Bokil 2010] H Bokil, P Andrews, J E Kulkarni, S Mehta and P P Mitra. *Chronux: a platform for analyzing neural signals*. J Neurosci Methods, vol. 192, no. 1, pages 146–51, 2010. (Cited on pages 147 and 148.)

[Bosman 2012] C A Bosman, J-M Schoffelen, N Brunet, R Oostenveld, A M Bastos, T Womelsdorf, B Rubehn, T Stieglitz, P De Weerd and P Fries. *Attentional stimulus selection through selective synchronization between monkey visual areas*. Neuron, vol. 75, no. 5, pages 875–88, Sep 2012. (Cited on pages 93 and 98.)

[Brette 2009] R Brette. *Generation of correlated spike trains*. Neural Comput, vol. 21, no. 1, pages 188–215, Jan 2009. (Cited on page 64.)

[Brillinger 1992] D R Brillinger. *Nerve cell spike train data analysis: a progression of techniques*. J Amer. Stat. Assoc., vol. 87, pages 260–271, 1992. (Cited on page 94.)

[Brillinger 1994] D R Brillinger and A E P Villa. *Examples of the investigation of neural information processing by point process analysis*. Advanced Methods of Physiological System Modeling, vol. 3, page 111, 1994. (Cited on page 94.)

[Brøns 1991] M Brøns and K Bar-Eli. *Canard Explosion and Excitation in a model of the Belousov-Zhabotinsky Reaction*. J. Phys. Chem, vol. 95, pages 8706–8713, 1991. (Cited on page 42.)

[Brunel 2003a] N Brunel, V Hakim and M J E Richardson. *Firing-rate resonance in a generalized integrate-and-fire neuron with subthreshold resonance*. Phys Rev E Stat Nonlin Soft Matter Phys, vol. 67, no. 5 Pt 1, page 051916, May 2003. (Cited on page 39.)

[Brunel 2003b] N Brunel and X-J Wang. *What determines the frequency of fast network oscillations with irregular neural discharges? I. Synaptic dynamics and excitation-inhibition balance*. J Neurophysiol, vol. 90, no. 1, pages 415–30, Jul 2003. (Cited on pages 30, 86 and 87.)

[Bryant 1976] H L Bryant and J P Segundo. *Spike initiation by transmembrane current: a white-noise analysis*. J Physiol, vol. 260, no. 2, pages 279–314, Sep 1976. (Cited on page 67.)

[Buehlmann 2010] A Buehlmann and G Deco. *Optimal information transfer in the cortex through synchronization*. PLoS Comput Biol, vol. 6, no. 9, 2010. (Cited on page 145.)

[Buhl 1994] E H Buhl, K Halasy and P Somogyi. *Diverse sources of hippocampal unitary inhibitory postsynaptic potentials and the number of synaptic release sites.* Nature, vol. 368, no. 6474, pages 823–8, Apr 1994. (Cited on page 88.)

[Bush 1996] P Bush and T Sejnowski. *Inhibition synchronizes sparsely connected cortical neurons within and between columns in realistic network models.* J Comput Neurosci, vol. 3, no. 2, pages 91–110, Jun 1996. (Cited on page 130.)

[Buzsáki 2004] G Buzsáki and A Draguhn. *Neuronal oscillations in cortical networks.* Science, vol. 304, no. 5679, pages 1926–1929, 2004. (Cited on pages 64, 83 and 125.)

[Buzsáki 2006] G Buzsáki. Rhythms of the Brain. Oxford University Press, 2006. (Cited on pages 30, 31, 109 and 124.)

[Buzsáki 2012] G. Buzsáki, C. A. Anastassiou and Ch. Koch. *The origin of extracellular fields and currents - EEG, ECoG, LFP and spikes.* Nat Rev Neurosci, vol. 13, no. 6, pages 407–420, 2012. (Cited on pages 87 and 145.)

[Canolty 2010] R T Canolty, K Ganguly, S W Kennerley, Ch F Cadieu, K Koepsell, J D Wallis and J M Carmena. *Oscillatory phase coupling coordinates anatomically dispersed functional cell assemblies.* Proc Natl Acad Sci U S A, vol. 107, no. 40, pages 17356–61, Oct 2010. (Cited on page 29.)

[Chialvo 1987] D R Chialvo and J Jalife. *Non-linear dynamics of cardiac excitation and impulse propagation.* Nature, vol. 330, no. 6150, pages 749–52, 1987. (Cited on page 54.)

[Compte 2003] A Compte, M V Sanchez-Vives, D A McCormick and X-J Wang. *Cellular and network mechanisms of slow oscillatory activity (<1 Hz) and wave propagations in a cortical network model.* J Neurophysiol, vol. 89, no. 5, pages 2707–25, May 2003. (Cited on pages 109, 130, 131, 138, 139 and 143.)

[Coombes 2000] S Coombes and A H Osbaldestin. *Period-adding bifurcations and chaos in a periodically stimulated excitable neural relaxation oscillator.* Phys Rev E Stat Phys Plasmas Fluids Relat Interdiscip Topics, vol. 62, no. 3 Pt B, pages 4057–66, Sep 2000. (Cited on pages 50 and 54.)

[Cossart 2003] R Cossart, D Aronov and R Yuste. *Attractor dynamics of network UP states in the neocortex.* Nature, vol. 423, no. 6937, pages 283–8, May 2003. (Cited on page 120.)

[de Pittà 2009] M de Pittà. `http://www.mathworks.es/matlabcentral/fileexchange/23076-plotautobd`, February 2009. (Cited on page 62.)

[de Ruyter van Steveninck 1997] R R de Ruyter van Steveninck, G D Lewen, S P Strong, R Koberle and W Bialek. *Reproducibility and variability in neural spike trains.* Science, vol. 275, no. 5307, pages 1805–8, Mar 1997. (Cited on page 67.)

[DeBusk 1997] B C DeBusk, E J DeBruyn, R K Snider, J F Kabara and A B Bonds. *Stimulus-dependent modulation of spike burst length in cat striate cortical cells.* J Neurophysiol, vol. 78, no. 1, pages 199–213, 1997. (Cited on page 71.)

[deCharms 2000] R C deCharms and A Zador. *Neural representation and the cortical code.* Annu Rev Neurosci, vol. 23, pages 613–47, 2000. (Cited on page 20.)

[Deco 2009] G Deco, D Martí, A Ledberg, R Reig and M V Sanchez Vives. *Effective reduced diffusion-models: a data driven approach to the analysis of neuronal dynamics.* PLoS Comput Biol, vol. 5, no. 12, page e1000587, Dec 2009. (Cited on page 130.)

[Desimone 1995] R Desimone and J Duncan. *Neural mechanisms of selective visual attention.* Annu Rev Neurosci, vol. 18, pages 193–222, 1995. (Cited on page 104.)

[Desmaisons 1999] D Desmaisons, J D Vincent and P M Lledo. *Control of action potential timing by intrinsic subthreshold oscillations in olfactory bulb output neurons.* J Neurosci, vol. 19, no. 24, pages 10727–37, Dec 1999. (Cited on pages 45 and 55.)

[Destexhe 1994] A Destexhe, Z F Mainen and T J Sejnowski. *An Efficient Method for Computing Synaptic Conductances Based on a Kinetic Model of Receptor Binding.* Neural Computation, vol. 6, no. 1, pages 14–18, 1994. (Cited on page 16.)

[Destexhe 2001] A Destexhe, M Rudolph, J M Fellous and T J Sejnowski. *Fluctuating synaptic conductances recreate in vivo-like activity in neocortical neurons.* Neuroscience, vol. 107, no. 1, pages 13–24, 2001. (Cited on pages 63 and 65.)

[Destexhe 2003] A Destexhe, M Rudolph and D Paré. *The high-conductance state of neocortical neurons in vivo.* Nat Rev Neurosci, vol. 4, no. 9, pages 739–51, Sep 2003. (Cited on page 67.)

[Destexhe 2004] A Destexhe and M Rudolph. *Extracting information from the power spectrum of synaptic noise.* J Comput Neurosci, vol. 17, no. 3, pages 327–45, 2004. (Cited on page 16.)

[Dierssen 2006] M Dierssen and G J A Ramakers. *Dendritic pathology in mental retardation: from molecular genetics to neurobiology.* Genes Brain Behav, vol. 5 Suppl 2, pages 48–60, 2006. (Cited on page 131.)

[Eguíluz 2005] V M Eguíluz, D R Chialvo, Go A Cecchi, M Baliki and A V Apkarian. *Scale-free brain functional networks.* Phys Rev Lett, vol. 94, no. 1, page 018102, Jan 2005. (Cited on page 33.)

[El Boustani 2007] S. El Boustani, M. Pospischil, M. Rudolph-Lilith and A. Destexhe. *Activated cortical states: experiments, analyses and models.* J Physiol, vol. 101, no. 1-3, pages 99–109, 2007. (Cited on page 61.)

[Engel 2008] T A Engel, L Schimansky-Geier, A V M Herz, S Schreiber and I Erchova. *Subthreshold membrane-potential resonances shape spike-train patterns in the entorhinal cortex.* J Neurophysiol, vol. 100, no. 3, pages 1576–89, Sep 2008. (Cited on page 40.)

[Ermentrout 2002] B Ermentrout. Simulating, Analyzing, and Animating Dynamical Systems: A Guide to XPPAUT for Researchers and Students, volume 56, Issue. SIAM, 2002. (Cited on pages 61 and 62.)

[Fisahn 1998] A Fisahn, F G Pike, E H Buhl and O Paulsen. *Cholinergic induction of network oscillations at 40 Hz in the hippocampus in vitro.* Nature, vol. 394, no. 6689, pages 186–9, 1998. (Cited on pages 70 and 86.)

[Fleming 2010] J J Fleming and P M England. *AMPA receptors and synaptic plasticity: a chemist's perspective.* Nat Chem Biol, vol. 6, no. 2, pages 89–97, Feb 2010. (Cited on page 15.)

[Fries 2001] P Fries, J H Reynolds, A E Rorie and R Desimone. *Modulation of oscillatory neuronal synchronization by selective visual attention.* Science, vol. 291, no. 5508, pages 1560–3, Feb 2001. (Cited on pages 29 and 31.)

[Fries 2005] P Fries. *A mechanism for cognitive dynamics: neuronal communication through neuronal coherence.* Trends Cogn Sci, vol. 9, no. 10, pages 474–80, Oct 2005. (Cited on pages 57, 85, 91, 98, 104 and 125.)

[Fries 2007] P Fries, D Nikolić and W Singer. *The gamma cycle.* Trends Neurosci, vol. 30, no. 7, pages 309–16, Jul 2007. (Cited on page 29.)

[Fries 2009] P Fries. *Neuronal gamma-band synchronization as a fundamental process in cortical computation.* Annu Rev Neurosci, vol. 32, pages 209–224, 2009. (Cited on page 65.)

[Gabbiani 1998] F Gabbiani and C Koch. Principles of Spike Train Analysis. MIT Press, 1998. (Cited on page 21.)

[Galán 2005] R F Galán, G B Ermentrout and N N Urban. *Efficient estimation of phase-resetting curves in real neurons and its significance for neural-network modeling.* Phys Rev Lett, vol. 94, no. 15, page 158101, Apr 2005. (Cited on page 50.)

[Galarreta 2001] M Galarreta and S Hestrin. *Electrical synapses between GABA-releasing interneurons.* Nat Rev Neurosci, vol. 2, no. 6, pages 425–33, Jun 2001. (Cited on page 26.)

[Garcia-Ojalvo 1999] J Garcia-Ojalvo and J M. Sancho. Noise in spatially extended systems. Springer-Verlag, New York, 1999. (Cited on pages 138, 141 and 145.)

[Geisler 2005] C Geisler, N Brunel and X-J Wang. *Contributions of intrinsic membrane dynamics to fast network oscillations with irregular neuronal discharges.* J Neurophysiol, vol. 94, no. 6, pages 4344–61, Dec 2005. (Cited on page 86.)

[Gentet 2000] L J Gentet, G J Stuart and J D Clements. *Direct measurement of specific membrane capacitance in neurons.* Biophys J, vol. 79, no. 1, pages 314–20, Jul 2000. (Cited on page 8.)

[Gerstner 2006] W Gerstner. 23 Problems in Neuroscience. *how can the brain be so fast?* Oxford University Press, 2006. (Cited on page 136.)

[Ghosh 2008] A Ghosh, Y Rho, A R McIntosh, R Kötter and V K Jirsa. *Noise during rest enables the exploration of the brain's dynamic repertoire.* PLoS Comput Biol, vol. 4, no. 10, page e1000196, Oct 2008. (Cited on page 55.)

[Gibson 1999] J R Gibson, M Beierlein and B W Connors. *Two networks of electrically coupled inhibitory neurons in neocortex.* Nature, vol. 402, no. 6757, pages 75–9, Nov 1999. (Cited on page 18.)

[Glass 1988] L Glass and M C Mackey. From clocks to chaos: the rhythms of life. Princeton University Press, 1988. (Cited on page 50.)

[Goense 2008] J B M Goense and N K Logothetis. *Neurophysiology of the BOLD fMRI signal in awake monkeys.* Curr Biol, vol. 18, no. 9, pages 631–40, May 2008. (Cited on page 30.)

[Graf 2003] W Graf, R Spencer, H Baker and R Baker. *Excitatory and inhibitory vestibular pathways to the extraocular motor nuclei in goldfish.* Journal of Neurophysiology, vol. 77, no. 5, pages 2765–2779, 2003. (Cited on page 18.)

[Gray 1989] C M Gray, P König, A K Engel and W Singer. *Oscillatory responses in cat visual cortex exhibit inter-columnar synchronization which reflects global stimulus properties.* Nature, vol. 338, no. 6213, pages 334–7, Mar 1989. (Cited on pages 30 and 125.)

[Gray 989b] C M Gray and W Singer. *Stimulus-specific neuronal oscillations in orientation columns of cat visual cortex.* Proc Natl Acad Sci U S A, vol. 86, no. 5, pages 1698–702, Mar 1989b. (Cited on page 83.)

[Grossenbacher 2001] P G Grossenbacher and C T Lovelace. *Mechanisms of synesthesia: cognitive and physiological constraints.* Trends Cogn Sci, vol. 5, no. 1, pages 36–41, Jan 2001. (Cited on page 131.)

[Gruber 1999] T Gruber, M M Müller, A Keil and T Elbert. *Selective visual-spatial attention alters induced gamma band responses in the human EEG.* Clin Neurophysiol, vol. 110, no. 12, pages 2074–85, Dec 1999. (Cited on page 83.)

[Gutfreund 1995] Y Gutfreund, Y yarom and I Segev. *Subthreshold oscillations and resonant frequency in guinea-pig cortical neurons: physiology and modelling.* J Physiol, vol. 483 (Pt 3), pages 621–40, Mar 1995. (Cited on pages 49, 127 and 135.)

[Gutkin 2005] B S Gutkin, G B Ermentrout and A D Reyes. *Phase-response curves give the responses of neurons to transient inputs.* J Neurophysiol, vol. 94, no. 2, pages 1623–35, Aug 2005. (Cited on page 50.)

[Han 1999] S K Han, T G Yim, D E Postnov and O V Sosnovtseva. *Interacting Coherence Resonance Oscillators.* Physical Review Letters, vol. 83, no. 9, 1999. (Cited on pages 115 and 117.)

[Hansel 1995] D Hansel, G Mato and C Meunier. *Synchrony in excitatory neural networks.* Neural Comput, vol. 7, no. 2, pages 307–337, 1995. (Cited on pages 50 and 61.)

[Hao 2007] J Hao, P R Rapp, W G M Janssen, W Lou, B L Lasley, P R Hof and J H Morrison. *Interactive effects of age and estrogen on cognition and pyramidal neurons in monkey prefrontal cortex.* Proc Natl Acad Sci U S A, vol. 104, no. 27, pages 11465–70, Jul 2007. (Cited on page 3.)

[Harris 2003] K D Harris, J Csicsvari, H Hirase, G Dragoi and G Buzsáki. *Organization of cell assemblies in the hippocampus.* Nature, vol. 424, no. 6948, pages 552–6, Jul 2003. (Cited on page 85.)

[Harsch 2000] A Harsch and H P Robinson. *Postsynaptic variability of firing in rat cortical neurons: the roles of input synchronization and synaptic NMDA receptor conductance.* J Neurosci, vol. 20, no. 16, pages 6181–92, Aug 2000. (Cited on page 26.)

[He 2007] Y He, Z J Chen and A C Evans. *Small-world anatomical networks in the human brain revealed by cortical thickness from MRI.* Cereb Cortex, vol. 17, no. 10, pages 2407–19, Oct 2007. (Cited on page 34.)

[Heistek 2010] T S Heistek, A Jaap Timmerman, S Spijker, A B Brussaard and H D Mansvelder. *GABAergic synapse properties may explain genetic variation in hippocampal network oscillations in mice.* Front Cell Neurosci, vol. 4, page 18, 2010. (Cited on page 70.)

[Henrie 2005] J A Henrie and R Shapley. *LFP power spectra in V1 cortex: the graded effect of stimulus contrast.* J Neurophysiol, vol. 94, no. 1, pages 479–490, 2005. (Cited on pages 65, 87 and 125.)

[Hilborn 2004] R C Hilborn and R J Erwin. *Coherence resonance in models of an excitable neuron with noise in both the fast and slow dynamics.* Physics Letters A, vol. 322.1, pages 19–24, 2004. (Cited on page 115.)

[Hodgkin 1945] A L Hodgkin and A F Huxley. *Resting and action potentials in single nerve fibres.* J Physiol, vol. 104, no. 2, pages 176–95, Oct 1945. (Cited on page 4.)

[Hodgkin 1952] A L Hodgkin and A F Huxley. *A quantitative description of membrane current and its application to conduction and excitation in nerve.* The Journal of Physiology, vol. 117, no. 4, pages 500–544, 1952. (Cited on pages 7 and 10.)

[Holcman 2006] D Holcman and M Tsodyks. *The emergence of Up and Down states in cortical networks.* PLoS Comput Biol, vol. 2, no. 3, page e23, Mar 2006. (Cited on page 109.)

[Horikawa 2001] Y Horikawa. *Coherence resonance with multiple peaks in a coupled FitzHugh-Nagumo model.* Phys Rev E Stat Nonlin Soft Matter Phys, vol. 64, no. 3 Pt 1, page 031905, Sep 2001. (Cited on page 117.)

[Houston 2009] C M Houston, D P Bright, L G Sivilotti, M Beato and T G Smart. *Intracellular chloride ions regulate the time course of GABA-mediated inhibitory synaptic transmission.* J Neurosci, vol. 29, no. 33, pages 10416–23, Aug 2009. (Cited on page 88.)

[Hubel 1959] D H Hubel and T N Wiesel. *Receptive fields of single neurones in the cat's striate cortex.* J Physiol, vol. 148, pages 574–91, Oct 1959. (Cited on page 123.)

[Hutcheon 1996] B Hutcheon, R M Miura and E Puil. *Models of subthreshold membrane resonance in neocortical neurons.* J Neurophysiol, vol. 76, no. 2, pages 698–714, Aug 1996. (Cited on page 49.)

[Hutcheon 2000] B Hutcheon and Y Yarom. *Resonance, oscillation and the intrinsic frequency preferences of neurons.* Trends Neurosci, vol. 23, no. 5, pages 216–22, May 2000. (Cited on pages 38, 39 and 49.)

[Imbihl 2008] R Imbihl. *Chapter 9 Non-linear Dynamics in Catalytic Reactions.* In E. Hasselbrink and B.I. Lundqvist, editeurs, Dynamics, volume 3 of *Handbook of Surface Science*, pages 341 – 428. North-Holland, 2008. (Cited on page 12.)

[Izhikevich 2003] E M Izhikevich, N S Desai, E C Walcott and F C Hoppensteadt. *Bursts as a unit of neural information: selective communication via resonance.* Trends Neurosci, vol. 26, no. 3, pages 161–7, Mar 2003. (Cited on page 57.)

[Izhikevich 2004] E M Izhikevich. *Which model to use for cortical spiking neurons?* IEEE Trans Neural Netw, vol. 15, no. 5, pages 1063–70, Sep 2004. (Cited on page 60.)

[Izhikevich 2007] E M Izhikevich. Dynamical Systems in Neuroscience. Computational Neuroscience. The MIT press, 2007. (Cited on pages 12 and 61.)

[Jacobs 2007] J Jacobs, M J Kahana, A D Ekstrom and I Fried. *Brain oscillations control timing of single-neuron activity in humans.* J Neurosci, vol. 27, no. 14, pages 3839–44, Apr 2007. (Cited on page 125.)

[Jones 2010] A R Jones and C C Overly. *Mapping the Mind: Online Interactive Atlas Shows Activity of 20 000 Brain-Related Genes.* Scientific American, 2010. (Cited on page 2.)

[Kandel 2000] Schwartz J H Kandel E R and Jessell T M. Principles of Neural Science. McGraw Hill, 2000. (Cited on page 22.)

[Kang 1994] Y Kang, T Kaneko, H Ohishi, K Endo and T Araki. *Spatiotemporally differential inhibition of pyramidal cells in the cat motor cortex.* J Neurophysiol, vol. 71, no. 1, pages 280–93, Jan 1994. (Cited on page 88.)

[Kano 2005] T Kano, Y Inaba and M Avoli. *Periodic oscillatory activity in parahippocampal slices maintained in vitro.* Neuroscience, vol. 130, no. 4, pages 1041–53, 2005. (Cited on page 19.)

[Kaplan 1987] E Kaplan, K Purpura and R M Shapley. *Contrast affects the transmission of visual information through the mammalian lateral geniculate nucleus.* J Physiol, vol. 391, pages 267–88, Oct 1987. (Cited on page 87.)

[Kawaguchi 1997] Y Kawaguchi and Y Kubota. *GABAergic cell subtypes and their synaptic connections in rat frontal cortex.* Cereb Cortex, vol. 7, no. 6, pages 476–86, Sep 1997. (Cited on page 88.)

[Klimesch 2007] W Klimesch, P Sauseng and S Hanslmayr. *EEG alpha oscillations: the inhibition-timing hypothesis.* Brain Res Rev, vol. 53, no. 1, pages 63–88, Jan 2007. (Cited on page 31.)

[Knudsen 2007] E I Knudsen. *Fundamental components of attention.* Annu Rev Neurosci, vol. 30, pages 57–78, 2007. (Cited on page 104.)

[Koch 1999] Ch Koch. Biophysics of Computation: Information Processing in Single Neurons, volume 428 of *Computational Neuroscience series.* Oxford University Press, 1999. (Cited on page 25.)

[Kole 2008] M H P Kole, S U Ilschner, B M Kampa, S R Williams, P C Ruben and G J Stuart. *Action potential generation requires a high sodium channel density in the axon initial segment.* Nat Neurosci, vol. 11, no. 2, pages 178–86, Feb 2008. (Cited on page 14.)

[König 1996] P König, A K Engel and W Singer. *Integrator or coincidence detector? The role of the cortical neuron revisited.* Trends Neurosci, vol. 19, no. 4, pages 130–7, Apr 1996. (Cited on pages 20 and 57.)

[Kuhn 2003] A Kuhn, A Aertsen and S Rotter. *Higher-order statistics of input ensembles and the response of simple model neurons.* Neural Computation, vol. 15, no. 1, pages 67–101, 2003. (Cited on page 64.)

[Kumar 2008] A Kumar, S Schrader, A Aertsen and S Rotter. *The high-conductance state of cortical networks.* Neural Comput, vol. 20, no. 1, pages 1–43, Jan 2008. (Cited on page 17.)

[Kumar 2010] A Kumar, S Rotter and A Aertsen. *Spiking activity propagation in neuronal networks: reconciling different perspectives on neural coding.* Nat Rev Neurosci, vol. 11, no. 9, pages 615–27, Sep 2010. (Cited on page 27.)

[Lampl 1993] I Lampl and Y Yarom. *Subthreshold oscillations of the membrane potential: a functional synchronizing and timing device.* J Neurophysiol, vol. 70, no. 5, pages 2181–6, Nov 1993. (Cited on pages 38 and 52.)

[Lampl 1997] I Lampl and Y Yarom. *Subthreshold oscillations and resonant behavior: two manifestations of the same mechanism.* Neuroscience, vol. 78, no. 2, pages 325–41, May 1997. (Cited on pages 7 and 38.)

[Lampl 1999] I Lampl, I Reichova and D Ferster. *Synchronous membrane potential fluctuations in neurons of the cat visual cortex.* Neuron, vol. 22, no. 2, pages 361–74, Feb 1999. (Cited on page 130.)

[Le Van Quyen 2001] M Le Van Quyen, J Foucher, J Lachaux, E Rodriguez, A Lutz, J Martinerie and F J Varela. *Comparison of Hilbert transform and wavelet methods for the analysis of neuronal synchrony.* J Neurosci Methods, vol. 111, no. 2, pages 83–98, 2001. (Cited on page 79.)

[Lindner 2004] B Lindner, J Garcia-Ojalvo, A Neiman and L Schimansky-Geier. *Effects of noise in excitable systems.* Physics Reports, vol. 392, no. 6, pages 321 – 424, 2004. (Cited on page 115.)

[Litwin-Kumar 2012] A Litwin-Kumar and B Doiron. *Slow dynamics and high variability in balanced cortical networks with clustered connections.* Nat Neurosci, vol. 15, no. 11, pages 1498–505, Nov 2012. (Cited on page 127.)

[Liu 2006] J Liu and W T Newsome. *Local field potential in cortical area MT: stimulus tuning and behavioral correlations.* J Neurosci, vol. 26, no. 30, pages 7779–90, Jul 2006. (Cited on page 30.)

[Llinás 1986] R Llinás and Y Yarom. *Oscillatory properties of guinea-pig inferior olivary neurones and their pharmacological modulation: an in vitro study.* J Physiol, vol. 376, pages 163–82, Jul 1986. (Cited on page 55.)

[Maass 1999] W Maass and A M Zador. *Dynamic stochastic synapses as computational units.* Neural Comput, vol. 11, no. 4, pages 903–17, May 1999. (Cited on page 24.)

[MacLeod 1998] K MacLeod, A Bäcker and G Laurent. *Who reads temporal information contained across synchronized and oscillatory spike trains?* Nature, vol. 395, no. 6703, pages 693–8, Oct 1998. (Cited on page 125.)

[Mainen 1995] Z F Mainen and T J Sejnowski. *Reliability of spike timing in neocortical neurons.* Science, vol. 268, no. 5216, pages 1503–6, Jun 1995. (Cited on pages 27, 29 and 67.)

[Makarov 2001] V A Makarov, V I Nekorkin and M G Velarde. *Spiking behavior in a noise-driven system combining oscillatory and excitatory properties.* Physical Review Letters, vol. 86, no. 15, pages 3431–3434, 2001. (Cited on pages 40, 42, 43, 44, 125 and 133.)

[Mann 2010] E O Mann and O Paulsen. *Local field potential oscillations as a cortical soliloquy.* Neuron, vol. 67, no. 1, pages 3–5, Jul 2010. (Cited on page 113.)

[Markram 2004] H Markram, M Toledo-Rodriguez, Y Wang, A Gupta, G Silberberg and C Wu. *Interneurons of the neocortical inhibitory system.* Nat Rev Neurosci, vol. 5, no. 10, pages 793–807, 2004. (Cited on page 138.)

[Mattia 2002] M Mattia and P Del Giudice. *Population dynamics of interacting spiking neurons.* Phys Rev E Stat Nonlin Soft Matter Phys, vol. 66, no. 5 Pt 1, page 051917, Nov 2002. (Cited on page 149.)

[Mazzoni 2008] A Mazzoni, S Panzeri, N K Logothetis and N Brunel. *Encoding of naturalistic stimuli by local field potential spectra in networks of excitatory and inhibitory neurons.* PLoS Comput Biol, vol. 4, no. 12, page e1000239, 2008. (Cited on pages 64, 87, 137 and 145.)

[McCormick 1985] D A McCormick, B W Connors, J W Lighthall and D A Prince. *Comparative electrophysiology of pyramidal and sparsely spiny stellate neurons of the neocortex.* J Neurophysiol, vol. 54, no. 4, pages 782–806, Oct 1985. (Cited on page 26.)

[McCormick 2003] D A McCormick, Y Shu, A Hasenstaub, M V Sanchez-Vives, M Badoual and T Bal. *Persistent cortical activity: mechanisms of generation and effects on neuronal excitability.* Cereb Cortex, vol. 13, no. 11, pages 1219–31, Nov 2003. (Cited on pages 112 and 145.)

[Mejias 2010] J F Mejias, H J Kappen and J J Torres. *Irregular dynamics in up and down cortical states.* PLoS One, vol. 5, no. 11, page e13651, 2010. (Cited on page 109.)

[Migliore 2002] M Migliore and G M Shepherd. *Emerging rules for the distributions of active dendritic conductances.* Nat Rev Neurosci, vol. 3, no. 5, pages 362–70, May 2002. (Cited on page 8.)

[Milner 1974] P M Milner. *A model for visual shape recognition.* Psychol Rev, vol. 81, no. 6, pages 521–35, Nov 1974. (Cited on page 29.)

[Nelson 1995] M Nelson and J Rinzel. *The Hodgkin-Huxley model.* In J. M. Bower and D. Beeman, editeurs, The book of Genesis, chapitre 4, pages 27–51. Springer, New York, 1995. (Cited on page 9.)

[Olshausen 2004] B A Olshausen and D J Field. *Sparse coding of sensory inputs.* Curr Opin Neurobiol, vol. 14, no. 4, pages 481–7, Aug 2004. (Cited on pages 30 and 71.)

[Pike 2000] F G Pike, R S Goddard, J M Suckling, P Ganter, N Kasthuri and O Paulsen. *Distinct frequency preferences of different types of rat hippocampal neurones in response to oscillatory input currents.* J Physiol, vol. 529 Pt 1, pages 205–13, Nov 2000. (Cited on page 49.)

[Pikovsky 1997] A S Pikovsky and J Kurths. *Coherence Resonance in a Noise-Driven Excitable System.* Physical Review Letters, vol. 78, no. 5, 1997. (Cited on page 115.)

[Pikovsky 2001] A Pikovsky, M Rosenblum and J Kurths. Synchronization. a universal concept in nonlinear sciences. Cambridge University Press, 2001. (Cited on pages 86, 91, 92 and 98.)

[Puia 1994] G Puia, E Costa and S Vicini. *Functional diversity of GABA-activated Cl- currents in Purkinje versus granule neurons in rat cerebellar slices.* Neuron, vol. 12, no. 1, pages 117–26, Jan 1994. (Cited on page 88.)

[Puil 1994] E Puil, H Meiri and Y Yarom. *Resonant behavior and frequency preferences of thalamic neurons.* J Neurophysiol, vol. 71, no. 2, pages 575–82, Feb 1994. (Cited on page 49.)

[Pulvermüller 1997] F Pulvermüller, N Birbaumer, W Lutzenberger and B Mohr. *High-frequency brain activity: its possible role in attention, perception and language processing.* Prog Neurobiol, vol. 52, no. 5, pages 427–45, Aug 1997. (Cited on page 83.)

[Purves, D et al. 2004] Purves, D et al., editeur. Neuroscience. Sinauer Associates, Inc., third édition, 2004. (Cited on page 116.)

[Rabinovich 2006] M Rabinovich, P Varona, A Selverston and H Abarbanel. *Dynamical principles in neuroscience.* Reviews of Modern Physics, vol. 78, no. 4, pages 1213–1265, 2006. (Cited on page 40.)

[Rabinovitch 1994] A Rabinovitch, R Thieberger and M Friedman. *Forced Bonhoeffer-van der Pol oscillator in its excited mode.* Phys Rev E Stat Phys Plasmas Fluids Relat Interdiscip Topics, vol. 50, no. 2, pages 1572–1578, Aug 1994. (Cited on page 50.)

[Rakic 2008] P Rakic. *Confusing cortical columns.* Proc Natl Acad Sci U S A, vol. 105, no. 34, pages 12099–100, Aug 2008. (Cited on page 3.)

[Rall 1967] W Rall. *Distinguishing theoretical synaptic potentials computed for different soma-dendritic distributions of synaptic input.* Journal of Neurophysiology, pages 1138–68, 1967. (Cited on page 16.)

[Ray 2010] S Ray and J H R Maunsell. *Differences in gamma frequencies across visual cortex restrict their possible use in computation.* Neuron, vol. 67, no. 5, pages 885–96, Sep 2010. (Cited on pages 87, 93 and 98.)

[Reig 2010] R Reig, M Mattia, A Compte, C Belmonte and M V Sanchez-Vives. *Temperature modulation of slow and fast cortical rhythms.* J Neurophysiol, vol. 103, no. 3, pages 1253–61, Mar 2010. (Cited on pages 120 and 149.)

[Richardson 2003] M J E Richardson, N Brunel and V Hakim. *From subthreshold to firing-rate resonance.* J Neurophysiol, vol. 89, no. 5, pages 2538–54, May 2003. (Cited on page 39.)

[Riehle 1997] A Riehle, S Grün, M Diesmann and A Aertsen. *Spike synchronization and rate modulation differentially involved in motor cortical function.* Science, vol. 278, no. 5345, pages 1950–3, Dec 1997. (Cited on page 27.)

[Rinzel 1989] J Rinzel and G B Ermentrout. Analysis of neural excitability and oscillations. Methods in Neuronal Modeling. MIT Press, 1989. (Cited on page 60.)

[Roberts 2013] M J Roberts, E Lowet, N M Brunet, M Ter Wal, P Tiesinga, P Fries and P De Weerd. *Robust Gamma Coherence between Macaque V1 and V2 by Dynamic Frequency Matching.* Neuron, vol. 78, no. 3, pages 523–536, 2013. (Cited on page 100.)

[Roxin 2011] A Roxin, N Brunel, D Hansel, G Mongillo and C van Vreeswijk. *On the distribution of firing rates in networks of cortical neurons.* J Neurosci, vol. 31, no. 45, pages 16217–16226, 2011. (Cited on pages 63, 69 and 71.)

[Rué 2011] P Rué and J Garcia-Ojalvo. *Gene circuit designs for noisy excitable dynamics.* Math Biosci, vol. 231, no. 1, pages 90–97, 2011. (Cited on page 61.)

[Ruiz-Mejias 2011] M Ruiz-Mejias, L Ciria-Suarez, M Mattia and M V Sanchez-Vives. *Slow and fast rhythms generated in the cerebral cortex of the anesthetized mouse.* J Neurophysiol, vol. 106, no. 6, pages 2910–21, Dec 2011. (Cited on page 149.)

[Salinas 2000] E Salinas and T J Sejnowski. *Impact of correlated synaptic input on output firing rate and variability in simple neuronal models.* J Neurosci, vol. 20, no. 16, pages 6193–209, Aug 2000. (Cited on page 24.)

[Salinas 2001] E Salinas and T J Sejnowski. *Correlated neuronal activity and the flow of neural information.* Nat Rev Neurosci, vol. 2, no. 8, pages 539–50, Aug 2001. (Cited on pages 27 and 28.)

[San Miguel 1997] M San Miguel and R Toral. *Stochastic Effects in Physical Systems.* http://arxiv.org/abs/cond-mat/9707147, 1997. (Cited on page 141.)

[Sanchez-Vives 2000] M V Sanchez-Vives and D A McCormick. *Cellular and network mechanisms of rhythmic recurrent activity in neocortex.* Nat Neurosci, vol. 3, no. 10, pages 1027–34, Oct 2000. (Cited on pages 109, 110, 120 and 130.)

[Sanchez-Vives 2010] M V Sanchez-Vives, M Mattia, A Compte, M Perez-Zabalza, M Winograd, V F Descalzo and R Reig. *Inhibitory modulation of cortical up states.* J Neurophysiol, vol. 104, no. 3, pages 1314–24, Sep 2010. (Cited on page 112.)

[Sancristóbal 2008] B Sancristóbal, J M Sancho and J Garcia-Ojalvo. *Resonant Spike Propagation in Coupled Neurons with Subthreshold Activity.* Lecture Notes in Computer Science, vol. 5164, page 695, 2008. (Cited on pages 127 and 133.)

[Sancristóbal 2010a] B Sancristóbal, J M Sancho and J Garcia-Ojalvo. *Phase-response approach to firing-rate selectivity in neurons with subthreshold oscillations.* Phys Rev E Stat Nonlin Soft Matter Phys, vol. 82, no. 4 Pt 1, page 041908, Oct 2010. (Cited on pages 45, 49, 55 and 127.)

[Sancristóbal 2010b] B Sancristóbal, J M Sancho and J Garcia-Ojalvo. *Resonant propagation of spike trains in delay-coupled neural subthreshold oscillators.* Eur. Phys. J. Special Topics, vol. 187, pages 189–197, 2010. (Cited on pages 57 and 127.)

[Sancristóbal 2013a] B Sancristóbal, R Vicente and J Garcia-Ojalvo. *Interactions between detuned gamma oscillations: the role of frequency mismatch in neuronal communication through coherence.* in preparation, 2013. (Cited on page 105.)

[Sancristóbal 2013b] B Sancristóbal, R Vicente, J M Sancho and J Garcia-Ojalvo. *Emergent bimodal firing patterns implement different encoding strategies during gamma-band oscillations.* Front Comput Neurosci, vol. 7, page 18, 2013. (Cited on pages 81, 86 and 128.)

[Schmitt 2008] J E Schmitt, R K Lenroot, G L Wallace, S Ordaz, K N Taylor, N Kabani, D Greenstein, J P Lerch, K S Kendler, M C Neale and J N Giedd. *Identification of genetically mediated cortical networks: a multivariate study of pediatric twins and siblings.* Cereb Cortex, vol. 18, no. 8, pages 1737–47, Aug 2008. (Cited on page 34.)

[Schoffelen 2005] J-M Schoffelen, R Oostenveld and P Fries. *Neuronal coherence as a mechanism of effective corticospinal interaction.* Science, vol. 308, no. 5718, pages 111–3, Apr 2005. (Cited on pages 93 and 125.)

[Shadlen 1994] M N Shadlen and W T Newsome. *Noise, neural codes and cortical organization.* Curr Opin Neurobiol, vol. 4, no. 4, pages 569–79, Aug 1994. (Cited on pages 24 and 25.)

[Shadlen 1998] M N Shadlen and W T Newsome. *The variable discharge of cortical neurons: implications for connectivity, computation, and information coding.* J Neurosci, vol. 18, no. 10, pages 3870–96, May 1998. (Cited on pages 19 and 67.)

[Shapley 2011] R Shapley and M J Hawken. *Color in the cortex: single- and double-opponent cells.* Vision Res, vol. 51, no. 7, pages 701–17, Apr 2011. (Cited on page 124.)

[Shih 2011] J Y Shih, C A Atencio and Ch E Schreiner. *Improved stimulus representation by short interspike intervals in primary auditory cortex.* J Neurophysiol, vol. 105, no. 4, pages 1908–1917, 2011. (Cited on page 71.)

[Shinomoto 1999] S Shinomoto, Y Sakai and S Funahashi. *The Ornstein-Uhlenbeck process does not reproduce spiking statistics of neurons in prefrontal cortex.* Neural Comput, vol. 11, no. 4, pages 935–951, 1999. (Cited on page 63.)

[Shinomoto 2005] S Shinomoto, K Miura and S Koyama. *A measure of local variation of inter-spike intervals.* Bio Systems, vol. 79, no. 1-3, pages 67–72, 2005. (Cited on page 63.)

[Shu 2003] Y Shu, A Hasenstaub and D A McCormick. *Turning on and off recurrent balanced cortical activity.* Nature, vol. 423, no. 6937, pages 288–93, May 2003. (Cited on pages 108, 120 and 130.)

[Silva 1991] L R Silva, Y Amitai and B W Connors. *Intrinsic oscillations of neocortex generated by layer 5 pyramidal neurons.* Science, vol. 251, no. 4992, pages 432–5, Jan 1991. (Cited on page 31.)

[Singer 1993] W Singer. *Synchronization of cortical activity and its putative role in information processing and learning.* Annu Rev Physiol, vol. 55, pages 349–74, 1993. (Cited on page 31.)

[Singer 1999] W Singer. *Neuronal synchrony: a versatile code for the definition of relations?* Neuron, vol. 24, no. 1, pages 49–65, 1999. (Cited on pages 65 and 125.)

[Smith 2009] Ch Smith. Biology of sensory systems. Wiley, 2nd édition, 2009. (Cited on page 6.)

[Snider 1998] R K Snider, J F Kabara, B R Roig and A B Bonds. *Burst firing and modulation of functional connectivity in cat striate cortex.* J Neurophysiol, vol. 80, no. 2, pages 730–744, 1998. (Cited on page 71.)

[Softky 1993] W R Softky and C Koch. *The highly irregular firing of cortical cells is inconsistent with temporal integration of random EPSPs.* J Neurosci, vol. 13, no. 1, pages 334–50, Jan 1993. (Cited on pages 21, 22, 23, 25, 63 and 86.)

[Soriano 2008] J Soriano, M Rodríguez Martínez, T Tlusty and E Moses. *Development of input connections in neural cultures.* Proc Natl Acad Sci, vol. 105, no. 37, pages 13758–13763, 2008. (Cited on pages 136 and 142.)

[Sporns 2010] O Sporns. Networks of the Brain, volume 1. MIT Press, 2010. (Cited on page 33.)

[Stam 2004] C J Stam. *Functional connectivity patterns of human magnetoencephalographic recordings: a 'small-world' network?* Neurosci Lett, vol. 355, no. 1-2, pages 25–8, Jan 2004. (Cited on page 32.)

[Steriade 1984] M Steriade and M Deschenes. *The thalamus as a neuronal oscillator.* Brain Res, vol. 320, no. 1, pages 1–63, Nov 1984. (Cited on page 31.)

[Steriade 1993a] M Steriade, D Contreras, R Curró Dossi and A Nuñez. *The slow (< 1 Hz) oscillation in reticular thalamic and thalamocortical neurons: scenario of sleep rhythm generation in interacting thalamic and neocortical networks.* J Neurosci, vol. 13, no. 8, pages 3284–99, Aug 1993. (Cited on page 83.)

[Steriade 1993b] M Steriade, A Nuñez and F Amzica. *A novel slow (< 1 Hz) oscillation of neocortical neurons in vivo: depolarizing and hyperpolarizing components.* J Neurosci, vol. 13, no. 8, pages 3252–65, Aug 1993. (Cited on pages 83, 107, 108 and 130.)

[Sterratt 2011] David Sterratt, Bruce Graham, Andrew Gillies and David Willshaw. Principles of Computational Modelling in Neuroscience. Cambridge University Press, 2011. (Cited on page 17.)

[Stevens 1998a] C F Stevens and A M Zador. *Input synchrony and the irregular firing of cortical neurons.* Nat Neurosci, vol. 1, no. 3, pages 210–7, Jul 1998. (Cited on page 26.)

[Stevens 1998b] C F Stevens and A M Zador. *Input synchrony and the irregular firing of cortical neurons.* Nat Neurosci, vol. 1, no. 3, pages 210–7, Jul 1998. (Cited on page 86.)

[Szymon 2013] L Szymon, H Lindén, T Tetzlaff, K H Pettersen and G T Einevoll. *Frequency dependence of signal power and spatial reach of the local field potential.* arXiv preprint arXiv:1302.4559, 2013. (Cited on page 65.)

[Takinoue 2009] M Takinoue, Y Ma, Y Mori and K Yoshikawa. *Extended continuous-flow stirred-tank reactor (ECSTR) as a simple model of life under thermodynamically open conditions.* Chemical Physics Letters, vol. 476, no. 4–6, pages 323 – 328, 2009. (Cited on page 12.)

[Tallon-Baudry 1997] C Tallon-Baudry, O Bertrand, C Delpuech and J Permier. *Oscillatory gamma-band (30-70 Hz) activity induced by a visual search task in humans.* J Neurosci, vol. 17, no. 2, pages 722–34, Jan 1997. (Cited on page 83.)

[Thomson 1982] D J Thomson. *Spectrum estimation and harmonic analysis.* Proceedings of the IEEE, vol. 70, no. 9, pages 1055–1096, 1982. (Cited on page 147.)

[Tuckwell 1988] H C Tuckwell. THEORETICAL NEUROBIOLOGY Volume 2. Cambridge University Press, 1988. (Cited on page 21.)

[Uhlhaas 2009] P J Uhlhaas, G Pipa, B Lima, L Melloni, S Neuenschwander, D Nikolić and W Singer. *Neural synchrony in cortical networks: history, concept and current status.* Front Integr Neurosci, vol. 3, page 17, 2009. (Cited on page 125.)

[van Vreeswijk 1996] C van Vreeswijk and H Sompolinsky. *Chaos in neuronal networks with balanced excitatory and inhibitory activity.* Science, vol. 274, no. 5293, pages 1724–6, Dec 1996. (Cited on page 26.)

[Verechtchaguina 2004] T Verechtchaguina, L Schimansky-Geier and I M Sokolov. *Spectra and waiting-time densities in firing resonant and nonresonant neurons.* Phys Rev E Stat Nonlin Soft Matter Phys, vol. 70, no. 3 Pt 1, page 031916, Sep 2004. (Cited on page 40.)

[Verechtchaguina 2007] T Verechtchaguina, I M Sokolov and L Schimansky-Geier. *Interspike interval densities of resonate and fire neurons.* Biosystems, vol. 89, no. 1-3, pages 63–8, 2007. (Cited on page 40.)

[Verheijck 1998] E E Verheijck, R Wilders, R W Joyner, D A Golod, R Kumar, H J Jongsma, L N Bouman and A C G van Ginneken. *Pacemaker Synchronization of Electrically Coupled Rabbit Sinoatrial Node Cells.* The Journal of General Physiology, vol. 111, no. 1, pages 95–112, 01 1998. (Cited on page 85.)

[Vicente 2008] R Vicente, L L Gollo, C R Mirasso, I Fischer and G Pipa. *Dynamical relaying can yield zero time lag neuronal synchrony despite long conduction delays.* Proc Natl Acad Sci U S A, vol. 105, no. 44, pages 17157–62, Nov 2008. (Cited on page 136.)

[Volgushev 1998] M Volgushev, M Chistiakova and W Singer. *Modification of discharge patterns of neocortical neurons by induced oscillations of the membrane potential.* Neuroscience, vol. 83, no. 1, pages 15–25, Mar 1998. (Cited on page 45.)

[Von Der Malsburg 1981] Ch Von Der Malsburg. *The correlation theory of brain function. Internal Report 81-2, MPI Biophysical Chemistry.* Reprinted in E Domany JL van Hemmen and K Schulten editors Models of Neural Networks II chapter 2 pages 95119 Springer Verlag Berlin, 1981. (Cited on page 29.)

[Wang 1996] X-J Wang and G Buzsáki. *Gamma oscillations by synaptic inhibition in a hippocampal interneuronal network.* J. Neurosci, vol. 16, pages 6402–6413, 1996. (Cited on page 61.)

[Wang 1998] X-J Wang. *Calcium Coding and Adaptive Temporal Computation in Cortical Pyramidal Neurons.* J Neurophysiol, vol. 79, no. 3, pages 1549–1566, 1998. (Cited on page 71.)

[Wang 1999] X-J Wang. *Synaptic basis of cortical persistent activity: the importance of NMDA receptors to working memory.* J Neurosci, vol. 19, no. 21, pages 9587–603, Nov 1999. (Cited on page 144.)

[Wang 2003] X-J Wang, Y Liu, M V Sanchez-Vives and D A McCormick. *Adaptation and temporal decorrelation by single neurons in the primary visual cortex.* J Neurophysiol, vol. 89, no. 6, pages 3279–93, Jun 2003. (Cited on page 141.)

[Watts 1998] D J Watts and S H Strogatz. *Collective dynamics of 'small-world' networks.* Nature, vol. 393, no. 6684, pages 440–2, Jun 1998. (Cited on pages 32, 34 and 136.)

[Whittington 1995] M A Whittington, R D Traub and J G Jefferys. *Synchronized oscillations in interneuron networks driven by metabotropic glutamate receptor activation.* Nature, vol. 373, no. 6515, pages 612–5, Feb 1995. (Cited on pages 31, 86 and 87.)

[Wierenga 2008] C J Wierenga, N Becker and T Bonhoeffer. *GABAergic synapses are formed without the involvement of dendritic protrusions.* Nat Neurosci, vol. 11, no. 9, pages 1044–52, Sep 2008. (Cited on page 25.)

[Williams 2002] S R Williams and G J Stuart. *Dependence of EPSP efficacy on synapse location in neocortical pyramidal neurons.* Science, vol. 295, no. 5561, pages 1907–1910, 2002. (Cited on page 24.)

[Winfree 2001] A T Winfree. The geometry of biological time. Springer, 2nd ed. 2001. (Cited on page 50.)

[Wolfe 2010] J Wolfe, A R Houweling and M Brecht. *Sparse and powerful cortical spikes.* Curr Opin Neurobiol, vol. 20, no. 3, pages 306–12, Jun 2010. (Cited on pages 30, 66 and 71.)

[Womelsdorf 2007] T Womelsdorf, J-M Schoffelen, R Oostenveld, W Singer, R Desimone, A K Engel and P Fries. *Modulation of neuronal interactions through neuronal synchronization.* Science, vol. 316, no. 5831, pages 1609–12, Jun 2007. (Cited on pages 57, 93 and 148.)

[Yague 2006] J G Yague, A Muñoz, P de Monasterio-Schrader, J Defelipe, L M Garcia-Segura and I Azcoitia. *Aromatase expression in the human temporal cortex.* Neuroscience, vol. 138, no. 2, pages 389–401, 2006. (Cited on page 3.)

[Yamaguchi 2003] S Yamaguchi, H Isejima, T Matsuo, R Okura, K Yagita, M Kobayashi and H Okamura. *Synchronization of Cellular Clocks in the Suprachiasmatic Nucleus.* Science, vol. 302, no. 5649, pages 1408–1412, 11 2003. (Cited on page 85.)

[Yuste 2005] R Yuste, J N MacLean, J Smith and A Lansner. *The cortex as a central pattern generator.* Nat Rev Neurosci, vol. 6, no. 6, pages 477–83, Jun 2005. (Cited on page 38.)

[Zacksenhouse 2008] M Zacksenhouse and S Nemets. Methods for neural ensemble recordings. Chapter 4: *Strategies for Neural Ensemble Data Analysis for Brain–Machine Interface (BMI) Applications.* Boca Raton (FL). CRC Press, 2008. (Cited on page 64.)


UPC